From single atoms to magnetic chains: Fe atoms on $2H$-$NbSe_2$

Dissertation

zur

Erlangung des Grades eines Doktors der Naturwissenschaften

(Dr. rer. nat.)

Eingereicht am Fachbereich Physik

der

Freien Universität Berlin

vorgelegt von

Eva-Maria Rudisch

Berlin, 2021

Erstgutachterin Katharina Franke
Fachbereich Physik
Freie Universität Berlin

Zweitgutachter Kirill Bolotin
Fachbereich Physik
Freie Universität Berlin

Tag der Disputation: 23.09.2021

Abstract

Superconductivity and magnetism are two phenomena which seem to be incompatible on macropscopic view. Microscopically, this can be traced back to the different spin-orders of both phases: Spin-singlet Cooper pairs versus ferromagnetic spin order. In this thesis we investigate magnetic Fe atoms on the quasi-2D superconductor $2H$-$NbSe_2$ by means of combined scanning tunneling microscopy and spectroscopy. The magnetic moment of the Fe atoms locally interacts with the Cooper pair condensate and gives rise to in-gap quasiparticle states - the so-called Yu-Shiba-Rusinov (YSR) states. The peculiar properties of $NbSe_2$ manifest in versatile features of the YSR states which we explore in detail. Capable of atomic manipulation we assemble customized structures - atomic dimers and extended chains - and investigate the hybridization within these structures.

We start by characterizing the pure substrate which exhibits an incommensurate charge-density wave (CDW) that coexists with superconductivity at low temperatures. Both correlated phases are driven by electron-phonon coupling yielding a highly anisotropic superconducting order parameter which appears as a peculiar quasiparticle peak distribution in differential conductance spectra around the superconducting gap.

Fe atoms adsorbed on the surface exhibit multiple YSR resonances with extended wave functions due to the quasi-2D nature of the substrate. The CDW wave induces local variations of the density of states which affect the energy and symmetry of the YSR states. Hence, apart from the two different crystalline hollow sites, the incommensurate CDW creates a multitude of inequivalent sites for Fe atoms. The influence of the CDW on the YSR states was systematically investigated and could be qualitatively modeled in collaboration with theorists.

We study the influence of the CDW on the hybridization between the long-ranged YSR states within the versatile energetic landscape arising from the incommensurate CDW. We assemble various dimers and show that equal positions relative to the CDW are a prerequisite for substantial hybridization. Further, we detect signatures of the quantum spin nature in the coupling of atomic dimers.

We go beyond dimers and stepwise assemble a dilute chain where the coupling between adjacent atoms is entirely mediated via the substrate. We track the formation of YSR bands which are identified by tunneling into their van Hove singularities. In longer chains, the incommensurate CDW induces band bending of the YSR bands. As a last step we investigate chains consisting of densely packed Fe atoms in which direct exchange between d orbitals drives the formation of Fe_2 molecules on the surface.

Kurzfassung

Supraleitung und Magnetismus sind zwei sehr interessante physikalische Phänomene, welche aufgrund ihrer unterschiedlichen Spinstruktur - Spin-Singulett Cooperpaare und ferromagnetische Spinordnung - widersprüchlich erscheinen. Im Zuge dieser Arbeit untersuchen wir die Wechselwirkung zwischen magnetischen Fe Atomen und dem quasi-2D Supraleiter $2H$-$NbSe_2$ mittels Rastertunnelmikroskopie und -spektroskopie. Das magnetische Moment der Eisenatome schwächt lokal die Supraleitung und führt zu lokalen Quasiteilchenzuständen, so genannten Yu-Shiba-Rusinov-(YSR-)Zuständen, welche von den besonderen Eigenschaften des Substrats beeinflusst werden. Zudem haben wir die Möglichkeit, Atome auf der Oberfläche zu manipulieren, wodurch die Untersuchung der Kopplung zwischen YSR-Zuständen in diversen Strukturen ermöglicht wird.

Anfangs gehen wir auf die vielfältigen Eigenschaften des Substrats ein, welches bei tiefen Temperaturen neben Supraleitung eine inkommensurable Ladungsdichtewelle (LDW) aufweist. Beide Phasen beruhen auf stark anisotroper Elektron-Phonon-Kopplung. Dies spiegelt sich in dem hochanisotropen Paarpotenzial wieder, welches wir in differenziellen Leitfähigkeitsspektren als Multi-Peak-Struktur der supraleitenden Quasiteilchenzustandsdichte auflösen.

Einzelne Fe Atome induzieren mehrere YSR-Zustände, welche aufgrund der 2D-Eigenschaften des Substrats sehr langreichweitig sind. Die LDW kreiert periodische Schwankungen der lokalen Zustandsdichte, was zu vielen inäquivalenten Adsorptionsplätzen führt. Durch eine systematische Studie vieler Fe Atome konnten wir den Einfluss der LDW auf die Symmetry, sowie auf die Energie der YSR-Zustände nachweisen. Die Ergebnisse konnten im Rahmen einer Zusammenarbeit mit Theoretikern qualitativ reproduziert werden.

Die vielfältige Oberfläche und die Langreichweitigkeit der YSR-Zustände nutzen wir, um den Einfluss der LDW auf the Kopplung zwischen Fe Atomen in diversen, gezielt zusammengesetzten atomaren Dimeren zu untersuchen. Hierbei wählen wir den Abstand zwischen Fe Atomen so groß, dass die Wechselwirkung ausschließlich durch das Substrat vermittelt wird und enthüllen gleiche Positionen der einzelnen Atome relativ zur LDW als Voraussetzung für Hybridsierung ihrer Wellenfunktionen.

In den Dimeren finden wir Signaturen des Quanten-Charakters der Spins, welche in längeren Ketten bestehen bleiben. Durch den schrittweisen Aufbau längerer Ketten untersuchen wir die Entstehung von YSR-Bändern, welche wir durch Tunneln in ihre Van-Hove-Singularitäten identifizieren. Die LDW prägt langen Ketten ein kontinuierliches Hintergrundpotenzial auf, was Bandverbiegungen hervorruft. Zu guter Letzt analysieren wir die direkte Kopplung zwischen den d-Orbitalen in Ketten aus dicht-gepackten Fe Atomen, wo wir Anzeichen für die Ausbildung von Fe_2-Molekülen auf der Kristalloberfläche finden.

Contents

List of abbreviations

AFM - Antiferromagnetic
BCS - Bardeen-Cooper-Schrieffer
BdG - Bogoliubov-de Gennes
BZ - Brillouin Zone
CC - Chalcogenide-Centered
CDW - Charge-Density Wave
CP - Cooper Pair
CPD - Contact Potential Difference
DFT - Density Functional Theory
DOS - Density of States
FM - Ferromagnetic
HC - Hollow-Centered
JT - Joule-Thomson
MC - Metal-Centered
MZM - Majorana Zero Mode
NDC - Negative Differential Conductance
NN - Nearest Neighbor
NNN - Next Nearest Neighbor
PSD - Phase-Sensitive Detector
QPT - Quantum Phase Transition
RKKY - Ruderman-Kittel-Kasuya-Yosida
SCDFT - Superconducting Density Functional Theory
STM - Scanning Tunneling Microscope/Scanning Tunneling Microscopy
STS - Scanning Tunneling Spectroscopy
vdW - van der Waals
YSR - Yu-Shiba-Rusinov

1 Introduction

1.1 Motivation

> *Die Technik von heute ist das Brot von morgen – die Wissenschaft von heute ist die Technik von morgen.*
>
> **— Richard von Weizsäcker**
> Federal president of Germany 1981-1984

Today's technology is tomorrow's cash cow - today's science creates future technologies. There are indeed various examples showing that Weizäcker was right. One of them is the development of the transistor.

In the beginning of the 20th century, vacuum triodes - being fragile and consuming substantial power - have been widely employed to amplify currents for radio and telecommunication applications. Already back then first patents by J. E. Lilienfeld [Lil30; Lil32; Lil33] and O. Heil [Hei35] of field-effect transistors were filed intending to be a solid state replacement of the triode. However, being decades away of the capability to produce high-quality semiconducting thin films, the concept of the field-effect transistor remained completely unattended [FBM12; Arn98].

„Creative failures" in the attempts to develop a field-effect transistor - as Shockley himself later called it - led to the point-contact transistor as the first experimental realization of a transistor [Sho84]. Although the point-contact transistor itself never made it to commercial application, the discovery of the transistor effect gained the 1956 Nobel Prize and initiated a lot of activity in the field [Arn98].

The first field-effect transistor that showed the desired characteristics was presented in 1962 by P. K. Weimer [Wei62; FBM12]. Shortly thereafter, the first implementation of multiple transistors on a single chip - a 4-bit microprocessor - was announced by Intel in 1971 [Int]. Thus, the journey of the field-effect transistor - from the first idea in the 1920's to the basic element of 21st century digital electronics - lasted several decades [Arn98; FBM12]. In retrospect, one could place Lilienthal, Heil, Shockly, Weimer and all researchers working in this field over decades in the development of modern microprocessors. However, back then their research was motivated by other perspectives - the development of a novel current amplifying device.

In that sense the research of this thesis might be placed in the far-fetched field of topologically protected quantum computation and the concomitant race for Majorana

fermions.[1] The solid state version of the Majorana fermion emerges as zero-energy excitation in topological superconductors. Such Majorana zero modes are predicted to serve - if localized in space - as qubits for decoherence-free quantum computation [SA17; LF12; Ali12]. There are various routes toward the realization of Majorana zero modes including topological insulators [FK08; SA17; Ali12; LF12] or Weyl and Dirac semimetals [SA17]. Besides, semiconductors with strong spin-orbit coupling exposed to external magnetic fields [Mou+12; LF12; LSD10] or chains of magnetic atoms [ORO10; PGO13; Nad+14; Nad+13; Kli+13; BS13; VF13], both proximity-coupled to ordinary s-wave superconductors are considered as promising platforms for the search of Majorana zero modes. The latter - adatom chains on superconductors - establishes the connection between quantum computation and the research of this thesis.

> *The journey with a 1000 miles begins with one step.*
>
> **— Confucius**
> Chinese philosopher and politician

The main motivation of the author of this thesis is the study of the intriguing physics arising from the interplay between magnetism and superconductivity - both of them being interesting phenomena. As a magnetic field is expelled by a superconductor - known as the Meissner-Ochsenfeld effect[2] - both phenomena seem to be incompatible on macroscopic sight. Microscopically, a single magnetic atom on a superconducting surface locally perturbs the superconducting condensate and thereby induces so-called Yu-Shiba-Rusinov (YSR) bound states named after L. Yu, H. Shiba and A. I. Rusinov [Yu65; Shi68; Rus69] who predicted their appearance already in the late 1960's. However, there was no experimental technique to investigate surfaces on the atomic level back then. This changed in the 1980's with the development of the first scanning tunneling microscope (STM) by the pioneering work of G. Binnig et al. [Bin+82b; Bin+82a], which enabled real-space atomic-resolution investigation of surfaces for the first time and thereby revolutionized the field of surface science. After the successful implementation of the STM it took another 15 years for scanning tunneling spectroscopy to reach the required energy resolution to observe YSR states [Yaz+97].

Since the pioneering work of A. Yazdani et al. [Yaz+97], YSR states are subject to intense research and there have been remarkable efforts in the investigation of their properties. Meanwhile, STMs reach base temperatures of less than $1\,\mathrm{K}$. Furthermore, the use of superconducting tunneling tips increases the energy resolution beyond the Fermi-Dirac limitation. This enabled the resolution of multiple YSR resonances within the superconducting energy gap, which arise from the orbital structure of the impurity [Ji+08; Rub+16; Cho+17a] or from magnetic anisotropy [Hat+15] revealing the exact geometry

[1] Named after E. Majorana who first introduced the theoretical concept [MM06].
[2] Superconductors act as perfect diamagnets and expel magnetic fields up to a certain critical field strength as found by W. Meissner and R. Ochsenfeld (Meissner-Ochsenfeld effect) in 1933 [MO33].

of the adsorption site to largely impact the YSR states. Moreover, the symmetry of the YSR wave function is related to the anisotropy of the Fermi surface [SBS97; FB97; Mén+15; Rub+16]. The total spin state of the system is governed by the intriguing relation between superconducting pairing and the local exchange interaction between the magnetic moment and the bath electrons (Kondo screening) [FSP11]. YSR states give us insight into the interaction between the spin moment and the superconducting condensate and play a key role in understanding the interplay between superconductivity and magnetism.

Beside the already interesting physics of a single magnetic impurity, we can go beyond and study the coupling between quantum spins on a superconductor. The capability of reliable atom manipulation opens access to create customized adatom assemblies. The natural interplay between spin exchange interactions, Kondo screening and superconducting order yields a rich phase diagram of competing ground states [Yao+14b] which we can explore using the STM. Hybridization between adjacent YSR states was already investigated using atoms and molecules on a variety of 3D superconductors [Ji+08; Cho+18b; Rub+18; Bec+21; Din+21] and interpreted within classical models [Rub+18; Yao+14a; Hof+15; FR00; Bec+21; Din+21].

In 2015, G. C. Ménard et al. [Mén+15] observed extremely long-ranged YSR states of buried Fe impurities in the quasi-2D supercondcutor $2H$-$NbSe_2$ showing that the decay of the YSR wave function is related to the dimensionality of the substrate. Since then, $NbSe_2$ is considered as a promising substrate not only for the study of single YSR states, but it should also facilitate coupling between adjacent impurities. Dimers consisting of CoPc molcules showed fingerprints of hybridized YSR excitations up to separations of $\sim 2\,\mathrm{nm}$ putting forward $NbSe_2$ as a well-suited platform to study hybridization between YSR states [Kez+18]. Another remarkable property of $NbSe_2$ is an incommensurate charge-density wave (CDW) which coexists with superconductivity at low temperature. The impact of such a charge-ordered state on YSR states was not addressed before.

In this thesis we use $2H$-$NbSe_2$ as a substrate for detailed studies of Fe atoms adsorbed on the surface. We characterize single Fe atoms, for which the CDW turns out to have a dramatic effect on the YSR states. Within the rich energetic landscape created by the incommensurate CDW we study YSR hybridization in different dimers. We observe signatures of the quantum spin nature which are not captured by classical models [Rub+18; Yao+14a; Hof+15; FR00; Bec+21; Din+21].

We also investigate to what extent the 2D-character of $NbSe_2$ and the CDW affect hybridization between YSR states in larger atom assemblies. Multiple experiments investigate (self-assembled or artificially constructed) adatom chains with direct exchange between the d orbitals [Nad+14; Rub+15b; Fel+17; Paw+16; Rub+17; Kim+18; Sch+20; Sch+21a; Sch+21b; Mie+21]. In contrast, the limit of dilute atom chains, where the interaction is entirely mediated via the substrate has not been extensively addressed so far. Very recent studies investigate dilute chains on 3D superconductors [Sch+21a; Sch+21b; Mie+21]. Motivated by the long-range YSR states, we assemble an extended adatom chain in the

dilute limit and monitor the development of YSR bands which are identified by tunneling into their Van Hove singularities. In the right parameter regime, such dilute chains are predicted to host Majorana zero modes [PGO13; PGO14; Nad+13; Kli+13; AS17].

1.2 Thesis structure

The thesis is organized as follows. We get started in the field of scanning tunneling microscopy and spectroscopy and outline the experimental setup in **chapter 2**. In the following we desist from a pure theory chapter and rather deliver the required theory in smaller portions at the beginning of each chapter.

We acquire a basic understanding of the microscopic physics of superconductivity by outlining the key aspects of the BCS theory in the beginning of **chapter 3**. Subsequently, we introduce the physical properties of the of $2H$-$NbSe_2$ which we use as substrate for all experiments presented in this thesis. Due to its layered nature it gains 2D electronic character to some extent which makes it a promising substrate for the investigation of YSR states [Mén+15]. Further, the coexistence of different charge-ordered phases at low temperature - CDW and superconductivity - and their entanglement across the Fermi surface yields a complex superconducting order parameter far beyond the simple BCS s-wave scenario.

Chapter 4 is dedicated to the investigation of single Fe atoms adsorbed on $2H$-$NbSe_2$. Therefore, we first provide all basics of the interaction between magnetic atoms with a metal and superconductor. Then, we investigate YSR states of single Fe atoms on $NbSe_2$. The local variations of the density of states imposed by the incommensurate CDW create a manifold energetic landscape for the YSR states. We further find fingerprints of magnetic anisotropy in the YSR states of Fe atoms.

One task during this thesis was the successful implementation of superconducting Nb tips for atomic manipulation on the $NbSe_2$ surface. Fe atoms could be reliably manipulated, thereby allowing the assembly of customized adatom arrangements while retaining the high energy resolution of a SC tip. After a short theory introduction, we go beyond single atoms and investigate multiple atomic dimers assembled with the STM tip in **chapter 5**. The quasi-2D character of the substrate yields long-range YSR wave functions and thus, facilitates pure substrate-mediated coupling between adatoms being several crystal sites apart from each other [Mén+15; Kez+18] - the dilute limit. We exploit the hybridization between YSR states in the framework set by the CDW superimposed on the crystal lattice which offers great diversity of different dilute dimer arrangements.

In **chapter 6** we increase the atom number and assemble atomic chains. We outline different models of magnetic chains on ordinary superconductors in the beginning of the chapter. By stepwise bottom-up assembly of a chain we explore YSR band formation. We realize an extended YSR chain in the dilute limit with > 50 atoms. The incommensurate

CDW imposes a smoothly varying background potential which leads to band bending within the extended chain. We further address the other coupling limit in a densely packed adatom chain where the atoms couple via direct exchange. We find abrupt changes in the electronic structure of the Fe atoms which points to the formation of covalently bound Fe_2 molecules on the crystal surface.

2 A brief introduction to the field of scanning tunneling microscopy and spectroscopy

All measurement presented in this thesis are performed with a low-temperature scanning tunneling microscope (STM). This chapter provides an introduction in the basic principles of this technique and an overview of the experimental setup.

2.1 Scanning tunneling microscopy

There are various spectroscopic techniques such as angle-resolved photoemission spectroscopy (ARPES), low-energy electron diffraction (LEED) or X-ray absorption spectroscopy (XAS) which provide information of structural and electronic properties of surfaces. However, all these techniques average over μm-size sample areas and are thus limited in their spatial resolution. The development of STM in the 1980s by the pioneering work of G. Binnig et al. [Bin+82b; Bin+82a] provided a milestone in surface science as it enables the real-space investigation of sample surfaces beyond the optical Abbe diffraction limit.

2.1.1 The tunneling current

The key element of an STM is the tunnel junction consisting of an atomically sharp metal tip in close vicinity to a conducting surface as schematically depicted in Fig. 2.1a. The distance between tip and sample sets a potential barrier of thickness z whose height is determined by the work functions of tip and sample, Φ_t and Φ_s (Fig. 2.1b). Classically, electrons in tip or sample cannot overcome this barrier unless their energy is sufficiently high. However, due the quantum nature of electrons there is a finite probability for electrons to propagate through the barrier. In thermal equilibrium without any applied bias, the chemical potentials of both electrodes align and there is no net current as electrons travel equally in both directions between tip and sample (red arrow in Fig. 2.1b). However, we expect a non-vanishing tunneling current if we apply a voltage V to the tunnel junction. In the following we derive the tunneling current following J. Bardeen [Bar61], J. Tersoff and D. R. Hamann [TH85; TH83].

We describe the tip and sample states independently by non-orthogonal wave functions ψ_t and ψ_s, respectively. The total tunneling current I consists of electrons tunneling

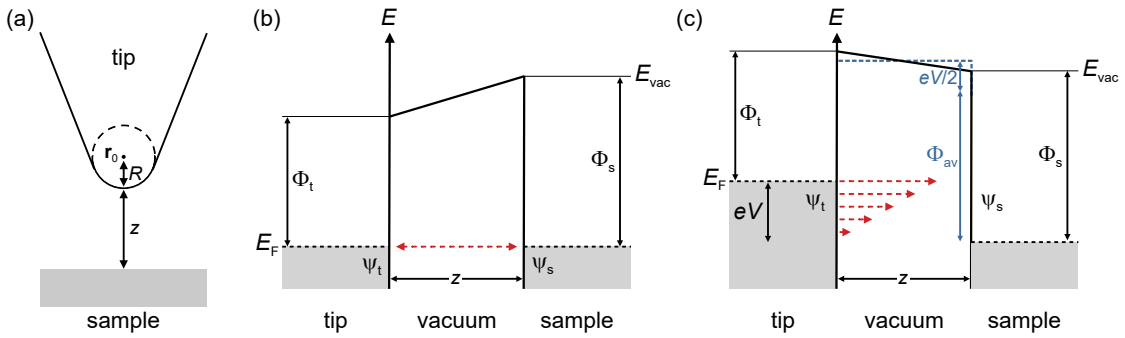

Fig. 2.1.: (a) Schematic model of the spherical tip with curvature R located at $\mathbf{r}_0$. The vacuum barrier has width z. Inspired by [TH85]. (b) Schematic energy diagram of a metal-vacuum-metal tunnel junction in thermal equilibrium. $\psi_{\mathrm{s,t}}$ and $\Phi_{\mathrm{s,t}}$ are the tip and sample wave and work functions, respectively. The Fermi energy and the vacuum level are indicated by E_{F} and E_{vac}. The net electron transfer is zero (dark red arrow). (c) Same junction as in (b) with an applied voltage V. The average barrier approximation is illustrated in blue. There is non-zero current as indicated by the dark red arrows.

from tip to sample ($I_{\mathrm{t}\to\mathrm{s}}$) and vice versa ($I_{\mathrm{s}\to\mathrm{t}}$). As obtained by J. Bardeen [Bar61], the tunneling current I to first order can then be expressed as [SK93]

$$\begin{aligned} I_{\mathrm{t}\to\mathrm{s}} &= \frac{2\pi e}{\hbar}\sum_{\mathrm{ts}} f(E_{\mathrm{t}})\left[1-f(E_{\mathrm{s}})\right]|M_{\mathrm{ts}}|^2\delta(E_{\mathrm{t}}-E_{\mathrm{s}}+eV), \\ I_{\mathrm{s}\to\mathrm{t}} &= \frac{2\pi e}{\hbar}\sum_{\mathrm{ts}} f(E_{\mathrm{s}})\left[1-f(E_{\mathrm{t}})\right]|M_{\mathrm{ts}}|^2\delta(E_{\mathrm{t}}-E_{\mathrm{s}}+eV), \\ I = I_{\mathrm{t}\to\mathrm{s}} - I_{\mathrm{s}\to\mathrm{t}} &= \frac{2\pi e}{\hbar}\sum_{\mathrm{ts}} \left[f(E_{\mathrm{t}})-f(E_{\mathrm{s}})\right]\,|M_{\mathrm{ts}}|^2\delta(E_{\mathrm{t}}-E_{\mathrm{s}}+eV). \end{aligned} \tag{2.1}$$

Above, $f(E)$ is the Fermi-Dirac distribution function. $|M_{\mathrm{ts}}|$ is the tunneling matrix element for tunneling between state ψ_{t} at energy E_{t} and ψ_{s} at energy E_{s} and captures the transmission probability between tip and surface. Assuming low temperatures and small voltages we can simplify the above equation to [TH83; TH85]

$$I = \frac{2\pi}{\hbar}e^2V\sum_{\mathrm{ts}}|M_{\mathrm{ts}}|^2\delta(E_{\mathrm{t}}-E_{\mathrm{F}})\delta(E_{\mathrm{s}}-E_{\mathrm{F}}). \tag{2.2}$$

As shown by Bardeen the tunneling matrix element yields [Bar61]

$$M_{\mathrm{ts}} = \frac{\hbar^2}{2m}\int \mathrm{d}\mathbf{S}\left(\psi_{\mathrm{t}}^*\vec{\nabla}\psi_{\mathrm{s}} - \psi_{\mathrm{s}}\vec{\nabla}\psi_{\mathrm{t}}^*\right). \tag{2.3}$$

The integral contains the probability current operator and has to be evaluated over any surface S lying entirely in the vacuum barrier between tip and surface. Thus, the essential problem is to calculate the tunneling matrix element. In order to evaluate the integral, Tersoff and Hamann assumed a perfectly spherical tip centered at $\mathbf{r}_0$ with radius R as depicted in Fig. 2.1a. The tip states ψ_{t} are described by spherical s-wave functions decaying into the vacuum thereby neglecting any angular dependence of the tip states.

Further, Tersoff and Hamann expand the sample's surface states ψ_s by Bloch states which exponentially decay into the vacuum [SK93]:

$$\psi_\mathrm{s}(\mathbf{r}) = \int \mathrm{d}\mathbf{k}\, a_\mathbf{k} e^{-\kappa z} e^{i\mathbf{k}\cdot\mathbf{r}_\parallel}, \tag{2.4}$$

where $\mathbf{r}_\parallel$ is the in-plane component of the tip position. In the average barrier approximation with $\Phi_\mathrm{av} = (\Phi_\mathrm{t} + \Phi_\mathrm{s})/2$ (indicated in blue in Fig. 2.1c) the decay constant κ is given by [ZH09; SK93]

$$\kappa = \sqrt{\frac{2m}{\hbar^2}\left(\Phi_\mathrm{av} + \frac{eV}{2} - E_\mathrm{s}\right) + k_\parallel^2}\,. \tag{2.5}$$

Thus, we obtain [TH85; TH83]

$$|M_\mathrm{ts}|^2 \propto |\psi_\mathrm{s}(\mathbf{r}_0)|^2 \propto e^{-2\kappa z}. \tag{2.6}$$

$|\psi_\mathrm{s}(\mathbf{r}_0)|^2$ is the probability of sample state ψ_s at the position $\mathbf{r}_0$ of the tip. From this we already note that the tunneling current depends exponentially on the tip-sample separation. Taking all of above's simplifications together, Eq. 2.3 can be evaluated and we arrive at [TH83; TH85]

$$I \propto \nu_\mathrm{t}(E_\mathrm{F}) V \sum_\mathrm{s} |\psi_\mathrm{s}(\mathbf{r}_0)|^2 \delta(E_\mathrm{s} - E_\mathrm{F}), \tag{2.7}$$

where $\nu_\mathrm{t}(E_\mathrm{F})$ is the density of states (DOS) of the tip at the Fermi energy. The sum over the sample states in Eq. 2.7 simply represents the local DOS at E_F of the surface [TH85; SK93].

2.1.2 Imaging on the atomic scale

As seen above, the tunneling current at a fixed voltage is proportional to the local DOS which exponentially depends on the thickness z of the vacuum barrier (typically a few Å for tunneling currents in the pA-regime). Thus, very small variations in the tip-sample separation cause a sizeable change in the tunneling current around one order of magnitude per Å. This characteristic is exploited in order to reach sub-nanometer spatial resolution with an STM.

Figure 2.2a schematically depicts an STM. The position of the STM tip is precisely controlled with piezoelectric elements in all dimensions. An image of the surface can be achieved by laterally scanning the surface with the (atomically sharp) tip. There are two fundamental operation modes. In the **constant-current mode** the position of the tip is readjusted at each scan pixel by the feedback loop such that a fixed tunneling current is maintained. Therefore, the tip's vertical position carries the topographic information of the surface as depicted in Fig. 2.2b. Due to the feedback loop, this imaging mode is relatively slow. This limitation can be overcome in the **constant-height mode** where the tip scans the surface at a fixed height. The topographic information is then stored

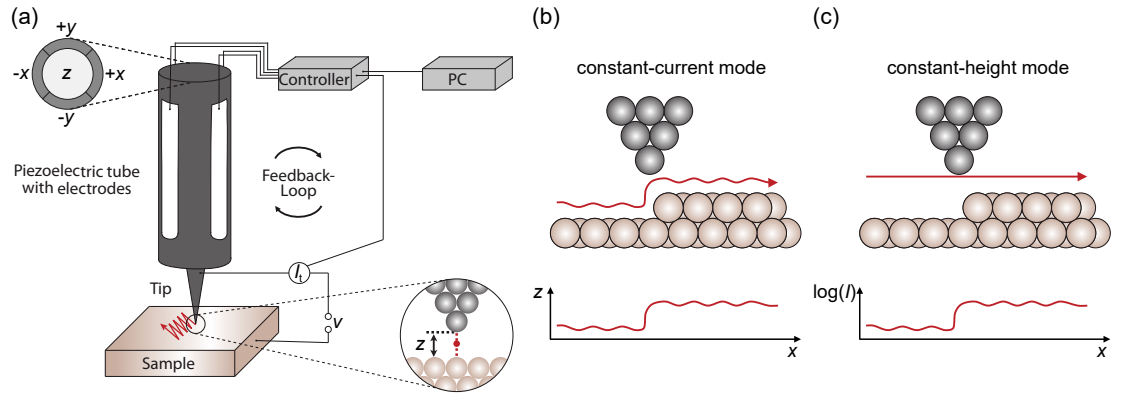

Fig. 2.2.: (a) Simplified working principle of an STM. The tip-sample distance z is controlled via the feedback loop. The position of the tip is controlled with piezoelectric elements in all three dimensions. (b) Constant-current operation mode: The vertical tip position is regulated by the feedback loop such that the tunneling current is constant while scanning the surface. (c) Constant-height operation mode: The vertical tip position is constant while scanning the surface. Figure taken from [Rol18].

in the tunneling current signal (Fig. 2.2c). However, this operation mode bears the risk of crashing the tip into the surface for non-flat samples which are either tilted or have strong surface corrugations. As the tunneling current is proportional to the local DOS of the sample (*c.f.* Eq. 2.7), STM images are always convolution of topographic information and electronic structure of the surface states as we will explicitly see in section 3.2.1.

2.1.3 Manipulation of single atoms

In the early 1990s, shortly after the successful implementation of the STM as powerful tool offering atomic-resolution surface imaging, IBM researchers demonstrated the capability of the STM to manipulate single atoms on surfaces [SE91; ELR91; ES90; LA91].

In order to manipulate single atoms we can exploit the short-range interactions existing between the tip and the sample [LRT05; Hla05; BMR97]. There are several possible mechanisms: (1) The use of electric fields strong enough to pick up an atom (by applying rather large biases $\sim$ V) and subsequent release at the desired position. (2) When the tip is really close to surface, one can make use of attractive van der Waals (vdW) and Pauli repulsion forces to pull or push the atoms across the surface [LRT05; Hla05; BMR97]. This regime can be achieved with low voltages (a few mV) and high currents (of several nA). The exact mechanism to successfully move atoms across the surface as well as the reliability, reproducibility and stability of atomic manipulation sensitively depend on the material system under investigation meaning that not every material system facilitates atomic manipulation.

As we will see below, the use of superconducting tips offers drastically increased energy resolution well beyond the Fermi-Dirac broadening (*c.f.* section 2.2.2). However, the well-established Pb-coated tungsten tips [Rub+15a] are not stable enough for the controlled manipulation of single atoms on metal surfaces due to the soft nature of the tip apex.

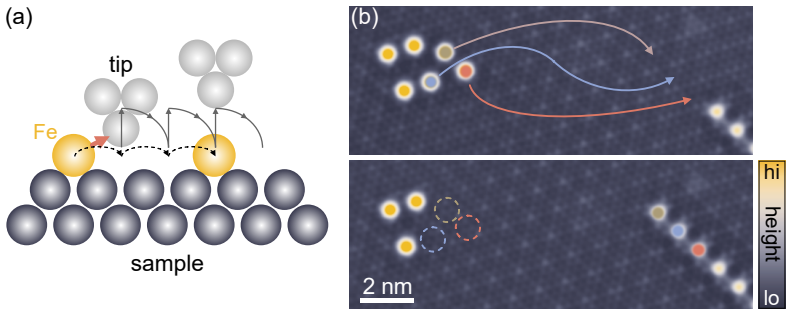

Fig. 2.3.: (a) Mechanism to manipulate Fe atoms on the $NbSe_2$ surface by attractive vdW forces. (b) Constant-current topographies acquired during the build-up sequence of an extended Fe chain on $NbSe_2$. Constant-current set point is $100\,\mathrm{pA}, 10\,\mathrm{mV}$.

One task during this thesis was the successful realization of atomic manipulation of Fe atoms on the $NbSe_2$ surface. In this scope, the fabrication procedure of Nb coated tips was implemented. The more stiff Nb tips offer controlled manipulation of Fe atoms while maintaining the desired energy resolution of a superconducting tip. Using a Nb tip the Fe atoms could be reliably dragged across the $NbSe_2$ surface as schematically depicted in Fig. 2.3 at set points of $1\text{-}5\,\mathrm{nA}$ at $\sim 4\,\mathrm{mV}$ (exact values vary for different tip preparations). With active feedback loop the tip is brought in close vicinity sideways to the atom until the vdW forces cause the atom to hop to the next adsorption site. As soon as the atom is following, the tip is withdrawn by the feedback in order to maintain the current. Using this approach the atoms could be dragged over large distances ($\sim 50\,\mathrm{nm}$) and reliably placed in any desired adsorption site. Figure 2.3 shows constant-current topographies recorded during the build-up sequence of an extended chain of Fe atoms on the $NbSe_2$ surface (*c.f.* chapter 6). The Fe atoms are visible as circular elevations.

2.2 Scanning tunneling spectroscopy

2.2.1 Insight into the density of states

As can be seen already from Eq. 2.7 the STM current bears information about the local DOS of the sample. Thus, STM not only faciliates real-space imaging with atomic resolution, but further allows us to get insight into the sample's DOS.

We can rewrite Eq. 2.1 by replacing the discrete summation over all sample and tip states by integration over the continuous DOSs $\nu_\mathrm{t}(E_\mathrm{t})$ and $\nu_\mathrm{s}(E_\mathrm{s})$ of tip and sample [Che93]:

$$I(V) \propto \iint_{-\infty}^{+\infty} \mathrm{d}E_\mathrm{t}\mathrm{d}E_\mathrm{s}\; \nu_\mathrm{t}(E_\mathrm{t})\nu_\mathrm{s}(E_\mathrm{s})\,[f(E_\mathrm{t}) - f(E_\mathrm{s})]\,|M_\mathrm{ts}|^2\delta(E_\mathrm{t} - E_\mathrm{s} + eV)\,. \tag{2.8}$$

By evaluating the δ-distribution and renaming $E_\mathrm{s} \to E$ the above integral simplifies to

$$I(V) \propto \int_{-\infty}^{+\infty} \mathrm{d}E\; \nu_\mathrm{t}(E - eV)\nu_\mathrm{s}(E)\,[f(E - eV) - f(E)]\,|M_\mathrm{ts}|^2, \tag{2.9}$$

which is a convolution of the DOS of tip and sample with additional Fermi-Dirac broadening. We see that at low temperatures ($T \approx 0\,\mathrm{K}$) only states within the energy window of eV between the Fermi levels of tip and sample contribute to the tunneling current as sketched in Fig. 2.4a. For metallic tips we can assume a constant DOS around the Fermi energy. Further, we neglect the energy dependence of the tunneling matrix element. With these assumptions we obtain

$$I(V) \propto |M_{\mathrm{ts}}|^2 \nu_{\mathrm{t}}(E_{\mathrm{F}}) \int_{E_{\mathrm{F}}}^{E_{\mathrm{F}}+eV} \mathrm{d}E \; \nu_{\mathrm{s}}(E), \tag{2.10}$$

and differentiating according to the bias voltage yields the differential conductance

$$\frac{\mathrm{d}I(V)}{\mathrm{d}V} \propto |M_{\mathrm{ts}}|^2 \nu_{\mathrm{t}}(E_{\mathrm{F}}) \nu_{\mathrm{s}}(E_{\mathrm{F}} + eV). \tag{2.11}$$

Thus, by measuring the voltage-dependent differential-conductance signal we can directly access the energy-dependence of the sample's DOS. Such a $\mathrm{d}I/\mathrm{d}V$ spectrum is achieved by sweeping the bias voltage while recording the $\mathrm{d}I/\mathrm{d}V$ signal at a specific point of interest above the sample. Commonly, we do not access the $\mathrm{d}I/\mathrm{d}V$ signal by a numerical derivative of the tunneling current, but using a lock-in amplifier which offers superior noise performance as discussed in section 2.3.2. Thus, we can also record the spatially resolved $\mathrm{d}I/\mathrm{d}V$ signal at a fixed voltage yielding so-called $\mathrm{d}I/\mathrm{d}V$ maps. In the following, all different measurement modes employed in this thesis are introduced.

As with the topographies there are different operation modes for spectroscopy. A so-called **constant-height $\mathbf{d}I/\mathbf{d}V$ spectrum** is obtained by opening the feedback at the position of interest above the sample at pre-defined set point parameters for current and bias. Subsequently, the bias voltage is swept in the range of interest while the $\mathrm{d}I/\mathrm{d}V$ signal is recorded without any movement of the tip. A **constant-current $\mathbf{d}I/\mathbf{d}V$ spectrum** is obtained by sweeping the bias and recording the $\mathrm{d}I/\mathrm{d}V$ signal while the feedback remains active and regulates the tip height in order to maintain a constant current. This allows to investigate the DOS over a large voltage range within a single spectrum (*e.g.* $0.2\,\mathrm{V} < V < 3\,\mathrm{V}$). However, since the tip-sample distance changes during the bias sweep the sample states appear at slightly shifted energies due to variations of the tunneling matrix element. Further, this mode requires non-vanishing DOS as otherwise the feedback drives the tip into the sample in order to maintain the set point current. Thus, this mode is not suitable in the small energy window around the Fermi level (especially when superconducting materials with an energy gap are involved).

Since we directly obtain the $\mathrm{d}I/\mathrm{d}V$ signal using the lock-in technique, we can combine imaging and spectroscopy in the so-called $\mathrm{d}I/\mathrm{d}V$ maps which capture the spatial variation of the $\mathrm{d}I/\mathrm{d}V$ signal at a certain bias within an area of interest. Depending on the requests of sample and tip we can in turn employ different modes. The simplest mode is again a **constant-height $\mathbf{d}I/\mathbf{d}V$ map**. As with a constant-height $\mathrm{d}I/\mathrm{d}V$ spectrum, the feedback is opened at the set point (at a certain lateral position), but instead of sweeping the bias

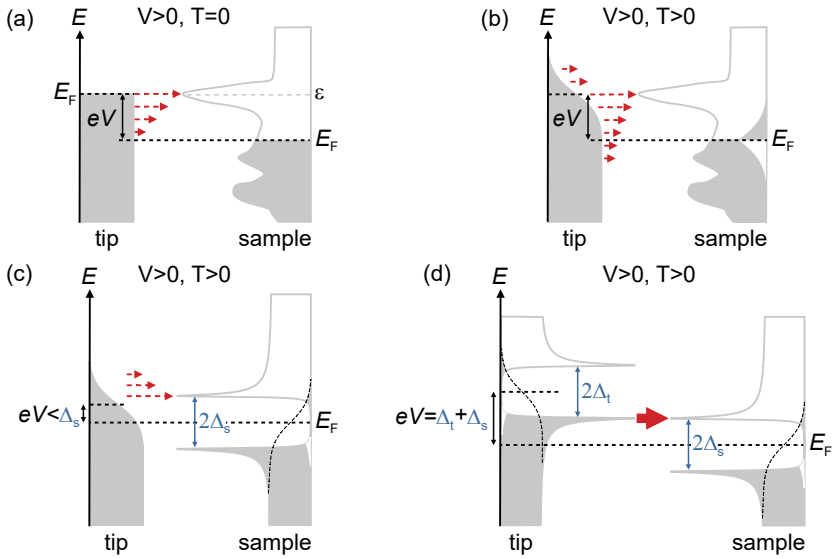

Fig. 2.4.: (a) Schematic of the DOS of tip and sample illustrating the tunneling processes between normal metals and superconductors. (a) Tunneling between two normal materials at $T = 0\,\mathrm{K}$. A constant DOS is assumed for the tip. (b) Tunneling between two normal materials at $T > 0$. The Fermi-Dirac broadening causes energetic smearing around E_F. (c) Tunneling between a metallic tip and a superconducting sample with energy gap $2\Delta_\mathrm{s}$. (d) Tunneling between two superconducting materials. tunneling current is suppressed for energies $eV < \Delta_\mathrm{t} + \Delta_\mathrm{s}$. Sample states appear shifted by Δ_t.

the tip lateral scans across the surface at a fixed bias (not necessarily the set point bias) while the $\mathrm{d}I/\mathrm{d}V$ signal is recorded. As discussed along with the imaging modes, this method is not suitable for non-flat samples. For example, due to the 3D-character of adatoms, the $\mathrm{d}I/\mathrm{d}V$ signal will be more intense above the adatom while lacking intensity on pristine parts of the surface. Here, the method of choice is a so-called **constant-contour $\mathrm{d}\boldsymbol{I}/\mathrm{d}\boldsymbol{V}$ map**. First, the constant-current z-profile at a suitable set point is recorded and then retraced by the tip while recording the $\mathrm{d}I/\mathrm{d}V$ signal at the desired bias voltage. This mode is especially suitable to image the so-called YSR states of magnetic atoms on superconducting surfaces and will be widely employed throughout this thesis (chapters 4,5 and 6).

We can further investigate the DOS of 3D adsorbates by regulating the tip's z-position directly on the $\mathrm{d}I/\mathrm{d}V$ signal in the so-called **constant-$\mathrm{d}\boldsymbol{I}/\mathrm{d}\boldsymbol{V}$ maps**. Similarly to topography images obtained in the constant-current mode, the $\mathrm{d}I/\mathrm{d}V$ magnitude is then stored in the variations in tip height and the map displays a constant-DOS contour. Like constant-current spectra, this technique can only be applied at energies for which there is a finite DOS above the whole area of interest as the feedback drives the tip into the sample otherwise. Hence, it is not suitable to image local states within the energy gap of a superconductor. As introduced in [Ree+17], this technique is well-suited to image molecular orbitals as it reduces artefacts caused by other measurement modes (as for example constant-contour $\mathrm{d}I/\mathrm{d}V$ maps).

2.2.2 Spectroscopy beyond the Fermi-Dirac limit

As schematically depicted in Fig. 2.4b the energy window of eV in which electrons contribute to the tunneling current is smeared by the Fermi-Dirac distribution around the Fermi energy. Mathematically, this is included in Eq. 2.9. At a measurement temperature of $1.2\,\mathrm{K}$ the Fermi edge limits the energy resolution to $3.5k_\mathrm{B}T \approx 360\,\mu\mathrm{eV}$ hindering the investigation of electronic features in the sub-meV range as, for example, the peculiar quasiparticle DOS of $NbSe_2$ (*c.f.* section 3.2.2).

A constant-height $\mathrm{d}I/\mathrm{d}V$ spectrum recorded on $NbSe_2$ using a metallic Au tip is presented in Fig. 2.5. The superconducting energy gap of the substrate can be discerned. Despite the presence of the superconducting energy gap in the substrate which prevents thermal broadening in the substrate, the sharp DOS of the superconducting coherence peaks appears broadened due to the thermal smearing in the tip as discussed above. The situation is schematically depicted in Fig. 2.4c.

By implementing superconducting tips we can significantly increase the energy resolution. First, we can overcome the thermally limited energy resolution as depicted in Fig. 2.4d [FSP11]. The energy gap prevents thermal smearing of electrons around the Fermi level in the tip such that the energy resolution is now limited by other experimental broadening effects. Second, the fact that we probe the sample DOS with the sharp coherence peaks of the tip DOS instead of a flat metallic DOS further increases the energy resolution. The difference between the use of a metallic and superconducting tip becomes evident when comparing Fig. 2.5a,b. The spectrum obtained with a Nb tip reveals rich features of the $NbSe_2$ which are not resolved with the Au tip. The substrate features will be discussed in detail in section 3.2.2. Note that all sample states appear shifted by Δ_t (*c.f.* Fig. 2.4d).

However, the DOS of superconducting tips is clearly not constant around the Fermi level such that we should reconsider above's approximations resulting in Eq. 2.11. In the following, we neglect the tunneling matrix element. Deriving Eq. 2.9 leads to the differential conductance:

$$\frac{\partial I(V)}{\partial V} \propto \int_{-\infty}^{+\infty} \mathrm{d}E\, \frac{\partial \nu_\mathrm{t}(E-eV)}{\partial V} \nu_\mathrm{s}(E,T)[f(E-eV,T)-f(E,T)] + \int_{-\infty}^{+\infty} \mathrm{d}E\, \nu_\mathrm{t}(E-eV)\nu_\mathrm{s}(E,T)\frac{\partial f(E-eV,T)}{\partial V}\,. \tag{2.12}$$

We see that both DOSs are entangled. As already mentioned, the major feature is that all sample states appear shifted by Δ_t. In the following section we deduce a numerical approach to calculate the sample DOS from the $\mathrm{d}I/\mathrm{d}V$ spectra based on Eq. 2.12.

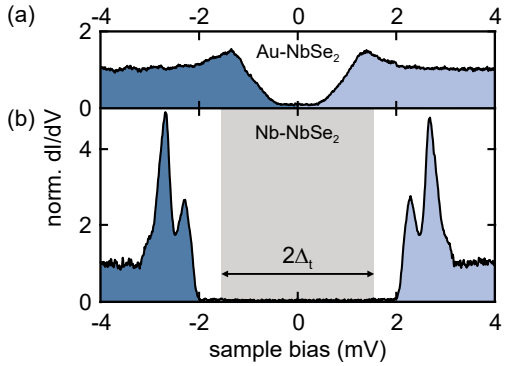

Fig. 2.5.: Normalized constant-height $\mathrm{d}I/\mathrm{d}V$ spectra obtained with (a) a Au tip and (b) a Nb tip on the pristine $NbSe_2$ surface (set point: $200\,\mathrm{pA}, 4\,\mathrm{mV}$ and $700\,\mathrm{pA}, 5\,\mathrm{mV}$). The tip gap is indicated by the gray box. Filled and empty states are indicated in dark and bright blue.

2.2.3 Numerical deconvolution

In order to deduce the DOS from the $\mathrm{d}I/\mathrm{d}V$ signal we can numerically deconvolve the spectra as described in the following (similar to the procedure described in [Cho+17a]). Equation 2.12 can be discretized into matrix form and then reads:

$$\overrightarrow{\frac{\partial I}{\partial V}}(V) \propto \mathbf{K}(E,V,T)\,\vec{\nu_{\mathrm{s}}}(E)\,. \tag{2.13}$$

The vector on the left hand side contains the differential conductance data. $\vec{\nu_{\mathrm{s}}}(E)$ is the local DOS of the sample to extract. The matrix $\mathbf{K}$ can be determined by comparing Eq. (2.12) and Eq. (2.13) to

$$\begin{aligned}\mathbf{K}_{ij}(E_j,V_i,T) = &\,\mathrm{d}E\;\frac{\partial \nu_{\mathrm{t}}(E_j-eV_i)}{\partial V}[f(E_j-eV_i,T)-f(E_j,T)]\\ &+\mathrm{d}E\;\nu_{\mathrm{t}}(E_j-eV_i)\frac{\partial f(E_j-eV_i,T)}{\partial V}\,.\end{aligned} \tag{2.14}$$

Therefore, with the knowledge of the DOS of the tip, we can calculate $\nu_{\mathrm{s}}\,(E)$ by finding the pseudoinverse of $\mathbf{K}$.

2.3 Experimental setup

2.3.1 Joule-Thomson scanning tunneling microscope

Data presented in this thesis were acquired with a commercially available Joule-Thomson (JT) STM manufactured by SPECS[1] that operates at a base temperature of $1.2\,\mathrm{K}$ and a base pressure of $\sim 1\cdot 10^{-10}\,\mathrm{mbar}$. The system is equipped with a heating stage for temperature dependent measurements and an out-of-plane magnetic field of up to $3\,\mathrm{T}$.

[1] SPECS Surface Nano Analysis GmbH.

Figure 2.6a is a 3D drawing of the experimental setup. To ensure mechanical stability of the tunnel junction, the whole system is placed on pneumatic feet with pressurized air damping and the STM head is suspended by springs. The ultra high vacuum conditions are reached with several pumps (Turbo, Ion-Getter and Titan-sublimation pumps) and allow the investigation of pristine surfaces without contamination of ambient molecules. In order to allow in-situ sample preparation, the STM is directly connected to the preparation chamber by a gate valve. Samples can be transferred between both chambers with the manipulator. Further, the STM is equipped with evaporation ports that allow in-situ evaporation of adsorbates on samples directly in the STM.

The low temperatures ensure stable adsorption of adsorbates (no thermally activated cluster formation), increase the energetic resolution and reduce thermal fluctuations of the tip sample-distance. Elaborate radio-frequency filtering at all input lines permits to reach an energy resolution in the order of $\approx 50\,\mu\mathrm{eV}$ (in combination with the lock-in amplifier, *c.f.* section 2.3.2). In order to achieve the low temperatures, the system consists of several cooling stages including a liquid nitrogen and a liquid helium reservoir which pre-cool the system to $4.5\,\mathrm{K}$ (Fig. 2.6b) and an additional cooling stage as outlined in the following.

Joule-Thomson cooling

To reach the base temperature of $1.2\,\mathrm{K}$ a Joule-Thomson cooling stage is integrated in the system (Fig. 2.6c). At very low temperatures, further energy can be removed from the system by adiabatic expansion of He. In our setup, high-purity pressurized He gas ($\lesssim 2\,\mathrm{bar}$) is first passed through a liquid-nitrogen cold trap to remove residual contaminations. Within the cryostat it is pre-cooled by the liquid helium reservoir and a back streaming heat exchanger. Subsequently, it passes a small capillary (indicated by the red star) and adiabatically expands into a small reservoir, the so-called $1\,\mathrm{K}$-pot which is pumped to low vacuum and thermally coupled to the STM head.

2.3.2 Lock-in amplifier in a nutshell

Of course, one could directly calculate the differential conductance from the voltage-dependend tunneling current $I(V)$. However, using a lock-in amplifier a superior signal-to-noise ratio can be achieved. The lock-in amplifier is a widely used technique which enables detection of small signals hidden within a broad noise spectrum several orders of magnitude larger. The trick is to excite the system at a known reference frequency. The lock-in amplifier then filters noise at all frequencies except for the reference frequency, which carries the signal of interest as outlined in the following based on [SRS].

The key principle is to add a small sinusoidal AC component with a known reference frequency ω_{ref} to the DC bias voltage which is applied to the tunnel junction. Such a time-dependent bias $V_{\mathrm{ac}}(t) = V_{\mathrm{mod}}\sin(\omega_{\mathrm{ref}}t)$ will cause a response of the tunneling current

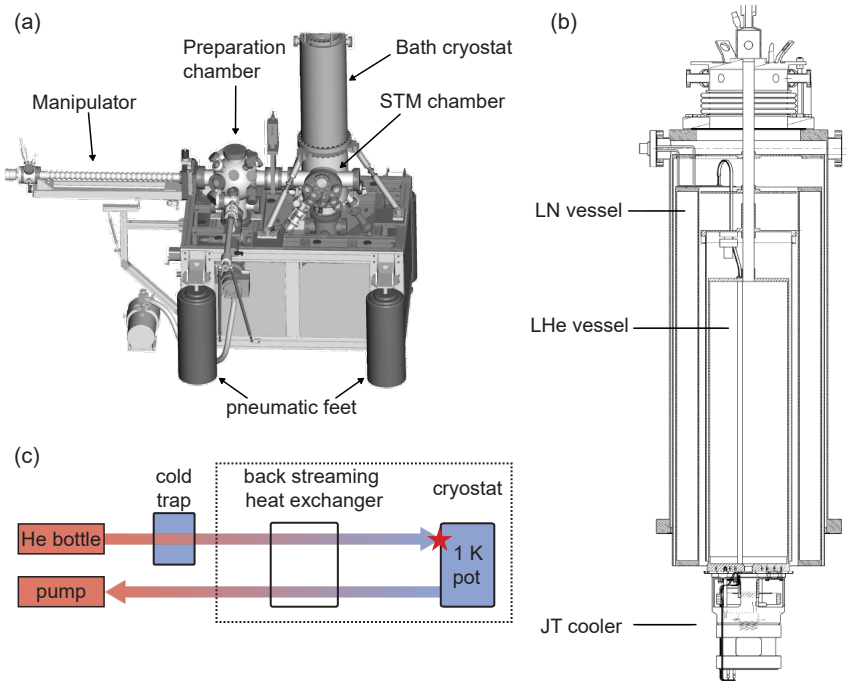

Fig. 2.6.: Drawing of the combined vacuum system with STM and preparation chamber. Some components are indicated in the sketch. (b) Design of the JT-STM bath cryostat with different cooling stages. (c) Simplified scheme of the JT-cycle. Red indicates high temperatures, whereas blue indicates low temperatures. Figure taken and adapted from [Hat16].

as schematically depicted in Fig. 2.7. As the AC amplitude is small, we can expand the response of the tunneling current as a Taylor series yielding:

$$I(V + V_{\mathrm{mod}} \sin(\omega_{\mathrm{ref}} t)) \approx I(V) + \frac{\mathrm{d}I(V)}{\mathrm{d}V} V_{\mathrm{mod}} \sin(\omega_{\mathrm{ref}} t) + \mathcal{O}(2). \tag{2.15}$$

Here, the first term is the normal bias-dependent tunneling current (DC response). The second term is the linear response (1^{st} harmonic) of the junction to the AC bias and proportional to the desired $\mathrm{d}I/\mathrm{d}V$ magnitude. Note that one can in principle also detect the 2^{nd} harmonic in order to increase the sensitivity for very faint signals.

Generally, the junction's response at the reference frequency ω_{ref} is hidden in broad-band white noise of the current signal. The current signal is passed through a low-noise current-voltage-amplifier which returns an amplified voltage signal being proportional to the input current:

$$V_{\mathrm{signal}}(V) = \alpha I(V) + \alpha \frac{\mathrm{d}I(V)}{\mathrm{d}V} V_{\mathrm{mod}} \sin(\omega_{\mathrm{ref}} t + \theta) + \sum_i V_i \sin(\omega_i t + \theta_i). \tag{2.16}$$

Above, α denotes the gain of the pre-amplifier (units $\mathrm{V\,A^{-1}}$) and θ is the phase of the junction's response. The last term represents the white noise which obscures the desired signal (*c.f.* Fig. 2.7). V_{signal} is then passed to the lock-in amplifier and multiplied with

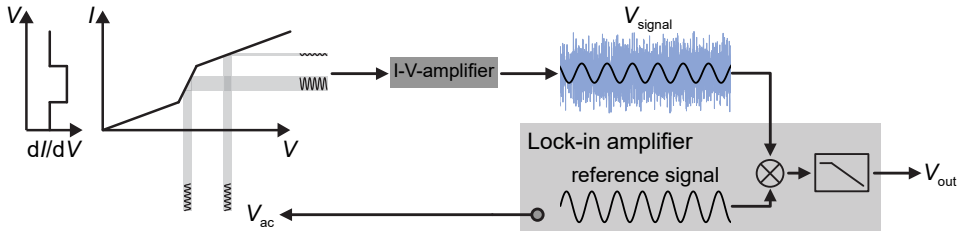

Fig. 2.7.: Working principle of a lock-in amplifier. Figure taken and adapted from [Far19].

the reference signal $V_{\mathrm{ref}}\sin(\omega_{\mathrm{ref}}t+\theta_{\mathrm{ref}})$ by the central unit of the lock-in amplifier, the phase-sensitive detector (PSD), yielding:

$$\begin{aligned} V_{\mathrm{psd}}(V) &= \alpha I(V) V_{\mathrm{ref}}\sin(\omega_{\mathrm{ref}}t+\theta_{\mathrm{ref}}) \\ &+ \alpha\frac{\mathrm{d}I(V)}{\mathrm{d}V}V_{\mathrm{mod}}V_{\mathrm{ref}}\sin(\omega_{\mathrm{ref}}t+\theta)\sin(\omega_{\mathrm{ref}}t+\theta_{\mathrm{ref}}) \\ &+ V_{\mathrm{ref}}\sum_i V_i\sin(\omega_i t+\theta_i)\sin(\omega_{\mathrm{ref}}t+\theta_{\mathrm{ref}}), \end{aligned} \tag{2.17}$$

which we can rewrite[2] as

$$\begin{aligned} V_{\mathrm{psd}}(V) &= \alpha I(V) V_{\mathrm{ref}}\sin(\omega_{\mathrm{ref}}t+\theta_{\mathrm{ref}}) \\ &+ \frac{\alpha}{2}\frac{\mathrm{d}I(V)}{\mathrm{d}V}V_{\mathrm{mod}}V_{\mathrm{ref}}\cos(\theta-\theta_{\mathrm{ref}}) - \frac{\alpha}{2}\frac{\mathrm{d}I(V)}{\mathrm{d}V}V_{\mathrm{mod}}V_{\mathrm{ref}}\cos(2\omega_{\mathrm{ref}}t+\theta+\theta_{\mathrm{ref}}) \\ &+ \frac{1}{2}V_{\mathrm{ref}}\sum_i V_i\big[\cos\big((\omega_i-\omega_{\mathrm{ref}})t+\theta_i-\theta_{\mathrm{ref}}\big) - \cos\big((\omega_i+\omega_{\mathrm{ref}})t+\theta_i+\theta_{\mathrm{ref}}\big)\big]. \end{aligned} \tag{2.18}$$

Thus, the output of the PSD unit yields a DC component proportional to the component of the current signal whose frequency is exactly ω_{ref}. The PSD unit is followed by a low-pass filter which performs time-averaging over the signal and thus removes all time-dependent components resulting in

$$V_{\mathrm{out}}(V) = \frac{\alpha}{2}\frac{\mathrm{d}I(V)}{\mathrm{d}V}V_{\mathrm{mod}}V_{\mathrm{ref}}\cos(\theta-\theta_{\mathrm{ref}}), \tag{2.19}$$

which is a DC voltage being proportional to the desired $\mathrm{d}I/\mathrm{d}V$ signal. As the lock-in amplifier filters all signals at frequencies which do not *exactly* match ω_{ref}, it provides a superior signal-to-noise ratio.

The phase of the reference signal has to be adjusted in order to maximize the amplitude of the output signal. The reference frequency has to be chosen as high as possible within the filtering scheme and the cut-off of the current-voltage amplifier in order to not perturb the feedback control of the STM and to allow efficient averaging. Moreover, it should be chosen well off typical noise frequencies and their harmonics, as for example the $50\,\mathrm{Hz}$ utility frequency. Further care has to be taken when considering the amplitude of the modulation. On one hand, the signal intensity scales with V_{mod}. On the other

[2] Using the trigonometric identity $2\sin(x)\sin(y) = \cos(x-y) - \cos(x+y)$.

hand it should be small enough to avoid additional broadening of the spectral features [Kle+73]. Lock-in amplifiers commonly measure the magnitude of the modulation by the root-mean-square value V_{rms} corresponding to a modulation amplitude of $V_{\mathrm{mod}} = \sqrt{2}V_{\mathrm{rms}}$ (and a peak-to-peak amplitude of $2\sqrt{2}V_{\mathrm{rms}}$).

2.3.3 Sample preparation

Preparation of SC tips

Before we prepare the $NbSe_2$ sample we have to prepare and characterize the STM tips. In the scope of this thesis we use superconducting Pb and Nb tips. Both SC crystals are cleaned by repeated sputtering and annealing processes as described elsewhere [Rub+15a; Odo+19]. In order to reach annealing temperatures of $\gtrsim 2000\,^{\circ}\mathrm{C}$ required for the Nb crystal a home made high-temperature e-beam heating stage was developed and attached to the preparation vacuum chamber in the scope of this thesis.

We obtain a superconducting tip by indenting the tip in the corresponding superconductor until a stable atomically sharp tip apex and a bulk-like superconducting gap is achieved. The Pb tips are obtained with an electro-chemically etched W wire on a clean Pb(111) surface, the Nb tips by indenting a cut NbTi wire into a Nb(111) crystal (see [Rub+15a] for more details of the tip preparation process). Spectra recorded on bare Pb(111) and Nb(111) surfaces after preparation of the tip are shown in Fig. 2.8. Pb is a two-band superconductor exhibiting two superconducting gaps arising from different Fermi surface sheets [Rub+15a; Flo+07]. The corresponding two pairs of coherence peaks are well resolved in Fig. 2.8a. The tips are characterized by the fit procedure described in detail in Ref. [Rub+15a] where a BCS-like DOS is assumed for the tip:

$$\nu_{\mathrm{t}}(E) = \mathrm{sgn}(E)\,\Re\left(\frac{E - i\Gamma}{\sqrt{(E - i\Gamma)^2 - \Delta_{\mathrm{t}}^2}}\right). \tag{2.20}$$

From this fitting procedure we determine the values of the superconducting order parameter Δ_{t} and the depairing factor Γ. For Pb tips, we reliably achieve bulk-like values of $\Delta_{\mathrm{t}} \approx 1.35\,\mathrm{meV}$ while the superconducting order parameter obtained for Nb tips varies from the bulk value of $\Delta_{\mathrm{t}} \approx 1.55\,\mathrm{meV}$ to smaller values. The depairing factors that are found typically vary between 5-20 μeV.[3]

[3] Note that the spectrum recorded with the Nb tip on the Nb(111) surface shows increased smearing at the low-energy edges of the coherence peaks indicating short quasiparticle lifetimes and thus, a big depairing factor Γ. The Nb tips exhibit as good energy resolution as the Pb tips on the $NbSe_2$. Therefore, we attribute this broadening to the inhomogenity of the Nb(111) crystal surface we used for tip preparation and characterization as achieving atomically clean Nb surfaces is demanding (and not required for tip preparation) [Odo+19].

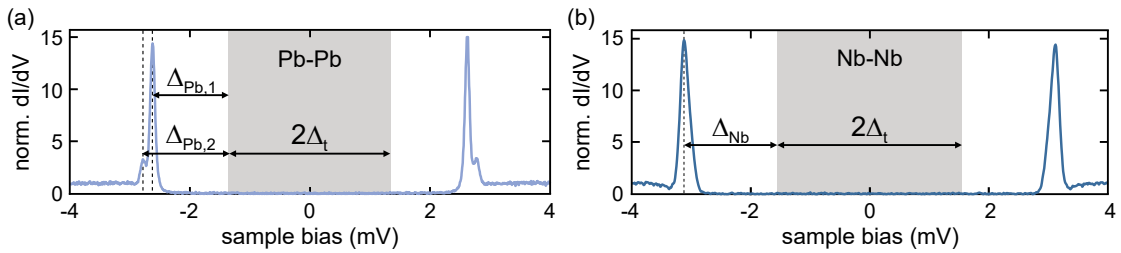

Fig. 2.8.: Normalized constant-height spectra obtained (a) with a Pb tip on a Pb(111), and (b) with a Nb tip on a Nb(111) sample (set point: $200\,\mathrm{pA}, 4\,\mathrm{mV}$ and $250\,\mathrm{pA}, 5\,\mathrm{mV}$). The tip gap is indicated by the gray box.

Preparation of the $NbSe_2$ sample

After preparing the tip we can turn towards the sample preparation. The bulk $NbSe_2$ crystals (grown by iodine vapor transport [Rah+12]) are supplied by K. Rossnagel.[4] A clean surface is achieved by cleaving the crystal in UHV and transferring it into the STM. Afterwards we evaporate Fe atoms directly into the STM at temperatures below $15\,\mathrm{K}$ using a commercially available electron-beam metal evaporator by Omicron.[5] Dilute coverages of ≈ 100 atoms$/(100 \times 100\,\mathrm{nm}^2)$ are achieved with a flux of $1\,\mathrm{nA}$ for 2-3 s.

[4] Institut für Experimentelle und Angewandte Physik, Christian-Albrechts-Universität zu Kiel and Ruprecht-Haensel-Labor, Deutsches Elektronen-Synchrotron DESY, Hamburg.
[5] Scienta Omicron AB.

2*H*-$NbSe_2$ as a substrate

3

In the scope of this thesis the most important property of $NbSe_2$ is its superconductivity below $T_c = 7.2\,\mathrm{K}$ which is required for the investigation of the Yu-Shiba-Rusinov states. Therefore, a brief introduction to superconductivity is provided in the next section as basis to understand the more complex superconducting pairing in $NbSe_2$. Beside its complex superconductivity, $NbSe_2$ exhibits a CDW that coexists with superconducting pairing at low temperatures. We introduce the rich substrate properties in the second part of this chapter.

3.1 Introduction to superconductivity

In some metals the resistivity drops to zero below a certain critical temperature. This was first observed by H. Kamerlingh Onnes in 1911[1] by cooling Hg down to $4.2\,\mathrm{K}$. Some years later, W. Meissner and R. Ochsenfeld revealed superconductors to be perfect diamagnets (Meissner-Ochsenfeld effect) [MO33] meaning that superconductors expel magnetic fields up to a certain critical field strength. Shortly after, J. N. Rjabinin and L. W. Shubnikov discovered the existence of a second type of superconductivity, the so-called type II superconductors where a magnetic field can penetrate the material without destroying superconductivity within some range [RS35]. There were many different approaches in order to explain the phenomena.[2] However, it took more than 40 years until J. Bardeen, L. N. Cooper and J. R. Schrieffer developed the first microscopic model explaining superconductivity, the so-called BCS theory in 1957 [BCS57a; BCS57b].

3.1.1 BCS theory

In a superconductor, the supercurrent is carried by pairs of electrons, the so-called Cooper pairs (CPs). As shown by L. N. Cooper in 1956 [Coo56] the Fermi sea of a metal is unstable against the formation of electron pairs if there is a net attractive interaction between the electrons. This attractive interaction is based on the exchange of virtual phonons, *i.e.* on electron-phonon coupling and is schematically illustrated in Fig. 3.1. If an electron is traveling through the lattice, it tends to attract the positive ion cores leading to a small lattice deformation (Fig. 3.1a,b). Subsequently, this positively charged region attracts another electron traveling in the opposite direction (Fig. 3.1c). Due to the long lifetime of a phonon, the distance between both interacting electrons is large (in

[1] Shortly after the first liquefaction of Helium [Kam08].

[2] In 1935, the London brothers came up with a phenomenological electrodynamic model that could explain both fundamental properties, zero resistance and perfect diamagnetism [LL35]. In 1950 V. L. Ginzburg and L. D. Landau developed a macroscopic theory based on thermodynamic arguments [GL09] which was

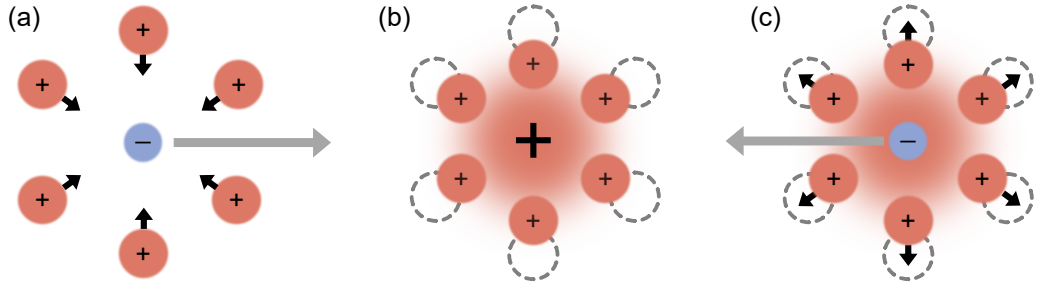

Fig. 3.1.: Intuitive model of the phonon-mediated electron-electron interaction. (a) An electron traveling through the lattice attracts the positive ion cores leading to a positive space charge as shown in (b). (c) This space charge attracts a second electron traveling in opposite direction. Inspired by [GM12].

the order of the superconducting coherence length[3]). Therefore, this phonon-mediated interaction can overcome the short-ranged Coulomb repulsion [Tin04]. The momenta of both participating electrons after the exchange of a virtual phonon with momentum $\mathbf{q}$ are [GM12]

$$\mathbf{k}_1' = \mathbf{k}_1 + \mathbf{q} \quad \text{and} \quad \mathbf{k}_2' = \mathbf{k}_2 - \mathbf{q}\,. \tag{3.1}$$

Since the Debye frequency $\hbar\omega_\mathrm{D} << E_\mathrm{F}$ is the limiting factor for the phonon energy, the interaction takes place in a narrow shell around the Fermi sphere in the order of $\delta k \simeq m\omega_D/\hbar k_\mathrm{F}$. The pairing is most effective if $\mathbf{k}_1 = -\mathbf{k}_2 =: \mathbf{k}$ as follows from momentum conservation (see Fig. 3.2a,b) [GM12] and leads to a condensation of multiple CPs.

The total wave function describing a CP has to be antisymmetric with respect to the exchange of two fermions. Thus, there are different possible combinations between orbital and spin wave functions. The two spins can either be coupled to a singlet (antisymmetric, antiparallel spins) or to a triplet (symmetric, parallel spins) and be combined with a symmetric (*i.e.* s-type, d-type) or antisymmetric (p-type, f-type) orbital wave function. The simplest case of superconductivity is the so-called s-wave superconductivity, where an s-wave orbital function is combined with the spin singlet: $(\mathbf{k}\uparrow, -\mathbf{k}\downarrow)$ [GM12]. Such a singlet CP can be described by [Tin04]:

$$|\Psi_0\rangle = \sum_{\mathbf{k}=\mathbf{k}_\mathrm{F}}^{\mathbf{k}_\mathrm{F}+\delta\mathbf{k}} g_\mathbf{k} c^\dagger_{\mathbf{k}\uparrow} c^\dagger_{-\mathbf{k}\downarrow} |F\rangle\,, \tag{3.2}$$

where $c^\dagger_{\mathbf{k}\sigma}(c_{\mathbf{k}\sigma})$ are the fermionic creation (annihilation) operators, $|F\rangle$ is the Fermi sea and $g_\mathbf{k}$ is the weighting coefficient. As this is a many-particle problem it is most convenient

able to broadly explain the observed phenomena. In 1957 A. A. Abrisokov was able to explain type I and II superconductors based on the findings of Ginzburg and Landau [Abr57].

[3] Assuming a typical metallic Fermi velocity of $v_\mathrm{F} \approx 10^6\,\mathrm{m\,s^{-1}}$, the lower limit of the lifetime $\tau = 1/\omega_\mathrm{D} \approx 10^{-14}\,\mathrm{s} - 10^{-13}\,\mathrm{s}$ yielding superconducting coherence lengths from a few nm to hundreds of nm depending on the material [GM12].

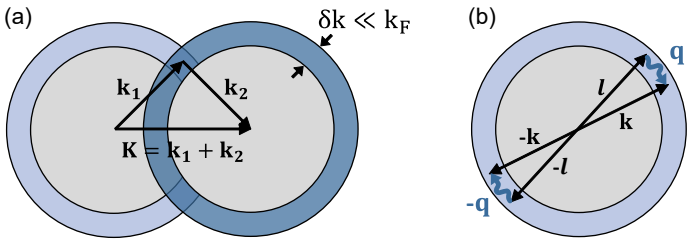

Fig. 3.2.: (a) Illustration of the momentum conservation upon exchange of a virtual phonon. As the momentum $\mathbf{K} = \mathbf{k_1} + \mathbf{k_2} = \mathbf{k_1'} + \mathbf{k_2'} = \mathbf{K'}$, has to be conserved, the interaction is limited to the cross section of the two shells around the Fermi spheres (marked in bright and dark blue). (b) When $\mathbf{K} = 0$, *i.e.* $\mathbf{k_1} = -\mathbf{k_2}$ the overlap of the two shells is maximized and the pairing most effective. Inspired by [GM12].

to describe the BCS ground state (condensation of multiple CPs) as a grand canonical ensemble by [Tin04]

$$|\Psi_G\rangle = \prod_{\mathbf{k}=\mathbf{k}_1,\ldots,\mathbf{k}_M} (u_\mathbf{k} + v_\mathbf{k} c^\dagger_{\mathbf{k}\uparrow} c^\dagger_{-\mathbf{k}\downarrow}) |\phi_0\rangle\,, \quad \text{where} \quad |u_\mathbf{k}|^2 + |v_\mathbf{k}|^2 = 1\,. \tag{3.3}$$

Above, $|\phi_0\rangle$ denotes the vacuum state. We see that, $|u_\mathbf{k}|^2$ and $|v_\mathbf{k}|^2$ represent the probability for a CP $(\mathbf{k}\uparrow, -\mathbf{k}\downarrow)$ to be unoccupied or occupied, respectively.

The BCS Hamiltonian (in the notation of 2nd quantization) [Tin04]

$$\mathcal{H}_\text{BCS} = \sum_{\mathbf{k}\sigma} \xi_\mathbf{k} n_{\mathbf{k}\sigma} + \sum_{\mathbf{kl}} V_\mathbf{kl} c^\dagger_{\mathbf{k}\uparrow} c^\dagger_{-\mathbf{k}\downarrow} c_{-\mathbf{l}\downarrow} c_{\mathbf{l}\uparrow}\,, \quad \text{with} \quad n_{\mathbf{k}\sigma} = c^\dagger_{\mathbf{k}\sigma} c_{\mathbf{k}\sigma}\,, \tag{3.4}$$

describes the scattering from the occupied paired state $(\mathbf{l}\uparrow, \mathbf{l}\downarrow)$ to the empty one $(\mathbf{k}\uparrow, -\mathbf{k}\downarrow)$ by the effective attractive interaction $V_\mathbf{kl}$, with $\mathbf{k} = \mathbf{l} + \mathbf{q}$. $\xi_\mathbf{k} = \varepsilon_\mathbf{k} - \mu = (\hbar\mathbf{k})^2/2m - \mu$ is the normal state kinetic energy dispersion. The interaction is attractive $(V_\mathbf{kl} < 0)$ only for initial $(\mathbf{l})$ and final $(\mathbf{k})$ wave vectors for which $\mathbf{q}$ lies within the small shell around the Fermi sphere (set by the Debye frequency) as discussed before (Fig. 3.2b) and vanishes elsewhere. For a net attractive interaction the mean value $\langle c_{-\mathbf{l}\downarrow} c_{\mathbf{l}\uparrow}\rangle \neq 0$ (the same holds for its complex conjugate counterpart) implying non-vanishing pairing correlations.

With this in mind, one can define the superconducting order parameter

$$\Delta_\mathbf{k} = -\sum_\mathbf{l} V_\mathbf{kl} \langle c_{-\mathbf{l}\downarrow} c_{\mathbf{l}\uparrow}\rangle\,, \tag{3.5}$$

which can be understood as the statistical mean value of the pairing interaction [GM12]. By considering only terms linear in $\langle c^\dagger_{-\mathbf{k}\downarrow} c^\dagger_{\mathbf{k}\uparrow}\rangle$ the Hamiltonian (Eq. 3.4) can be transformed into the following form [Tin04]:

$$\mathcal{H}_\text{BCS} = \sum_{\mathbf{k}\sigma} \xi_\mathbf{k} n_{\mathbf{k}\sigma} - \sum_\mathbf{k} (\Delta_\mathbf{k} c^\dagger_{\mathbf{k}\uparrow} c^\dagger_{-\mathbf{k}\downarrow} + \Delta^*_\mathbf{k} c_{-\mathbf{k}\downarrow} c_{\mathbf{k}\uparrow} - \Delta_\mathbf{k} \langle c^\dagger_{-\mathbf{k}\downarrow} c^\dagger_{\mathbf{k}\uparrow}\rangle). \tag{3.6}$$

From that we can pass to the more convenient matrix notation [GM12]

$$\mathcal{H}_{\mathrm{BCS}} = \sum_{\mathbf{k}} \left\{ \xi_{\mathbf{k}} + \Delta_{\mathbf{k}} \langle c^{\dagger}_{-\mathbf{k}\downarrow} c^{\dagger}_{\mathbf{k}\uparrow} \rangle + \left(c_{\mathbf{k}\uparrow}, c^{\dagger}_{-\mathbf{k}\downarrow} \right) \begin{pmatrix} \xi_{\mathbf{k}} & -\Delta_{\mathbf{k}} \\ -\Delta^{*}_{\mathbf{k}} & -\xi_{\mathbf{k}} \end{pmatrix} \begin{pmatrix} c_{\mathbf{k}\uparrow} \\ c^{\dagger}_{-\mathbf{k}\downarrow} \end{pmatrix} \right\}. \tag{3.7}$$

This Hamiltonian illustrates the coupling between electrons and holes of opposite spin directions ($\Delta_{\mathbf{k}}$ on the off diagonal terms). In order to obtain the excitation spectrum of the superconductor, this Hamiltonian can be diagonalized by the Bogoliubov transformation (which is an unitary transformation) [Bog58; Tin04; Val58] by introducing the quasiparticle operators $\gamma^{\dagger}_{\mathbf{k}}$ and $\eta^{\dagger}_{\mathbf{k}}$ [GM12]

$$\left(c_{\mathbf{k}\uparrow}, c^{\dagger}_{-\mathbf{k}\downarrow} \right) = \begin{pmatrix} u^{*}_{\mathbf{k}} & v_{\mathbf{k}} \\ -v^{*}_{\mathbf{k}} & u_{\mathbf{k}} \end{pmatrix} \begin{pmatrix} \gamma_{\mathbf{k}} \\ \eta_{\mathbf{k}} \end{pmatrix} \text{ and } \left(c^{\dagger}_{\mathbf{k}\uparrow}, c_{-\mathbf{k}\downarrow} \right) = \begin{pmatrix} u_{\mathbf{k}} & -v_{\mathbf{k}} \\ v^{*}_{\mathbf{k}} & u^{*}_{\mathbf{k}} \end{pmatrix} \begin{pmatrix} \gamma^{\dagger}_{\mathbf{k}} \\ \eta^{\dagger}_{\mathbf{k}} \end{pmatrix}. \tag{3.8}$$

$\gamma_{\mathbf{k}}$ participates in creating an electron with $-\mathbf{k}\downarrow$ and destroying one with $\mathbf{k}\uparrow$ and hence, reduces the system's momentum by $\mathbf{k}$ and the spin S_z by $\hbar/2$. Similarly, $\eta_{\mathbf{k}}$ increases the momentum by $\mathbf{k}$ and the spin by $\hbar/2$ (decreases by $-\mathbf{k}$ and $-\hbar/2$). By choosing

$$|v_{\mathbf{k}}|^2 = \frac{1}{2}\left[1 - \frac{\xi_{\mathbf{k}}}{E_{\mathbf{k}}}\right] \text{ and } |u_{\mathbf{k}}|^2 = \frac{1}{2}\left[1 + \frac{\xi_{\mathbf{k}}}{E_{\mathbf{k}}}\right], \tag{3.9}$$

which satisfies the normalization condition $|u_{\mathbf{k}}|^2 + |v_{\mathbf{k}}|^2 = 1$, we finally arrive at [Tin04; GM12]

$$\mathcal{H}_{\mathrm{BCS}} = \sum_{\mathbf{k}} (\xi_{\mathbf{k}} - E_{\mathbf{k}} + \Delta_{\mathbf{k}} \langle c^{\dagger}_{-\mathbf{l}\downarrow} c^{\dagger}_{\mathbf{l}\uparrow} \rangle) + \sum_{\mathbf{k}} E_{\mathbf{k}} (\gamma^{\dagger}_{\mathbf{k}} \gamma_{\mathbf{k}} + \eta^{\dagger}_{\mathbf{k}} \eta_{\mathbf{k}}) \text{ with } E_{\mathbf{k}} = \sqrt{\xi^2_{\mathbf{k}} + \Delta^2_{\mathbf{k}}}\,. \tag{3.10}$$

The first term is a constant which indicates the condensation energy, hence the net energy gain upon transition in the superconducting state (at $T = 0$). The second sum describes the elementary (fermionic) excitations of the system as it contains the number operators $\gamma^{\dagger}_{\mathbf{k}}\gamma_{\mathbf{k}}$ and $\eta^{\dagger}_{\mathbf{k}}\eta_{\mathbf{k}}$ of the quasiparticle operators defined in Eq. 3.8. The excitation spectrum is gapped by $\Delta_{\mathbf{k}}$ compared to the normal state excitations (*c.f.* Eq. 3.10 and Fig. 3.3a). In general, since $\gamma_{\mathbf{k}}$ and $\eta_{\mathbf{k}}$ are linear combinations of the creation and annihilations operators (Eq. 3.8), the excitations are superpositions of electrons and holes.[4] As the particle number is conserved we can assume $\nu_{\mathrm{N}}(\xi_{\mathbf{k}})\mathrm{d}\xi_{\mathbf{k}} = \nu_{\mathrm{SC}}(E_{\mathbf{k}})\mathrm{d}E_{\mathbf{k}}$ (where ν_{N} and ν_{SC} are the normal and superconducting DOS, respectively). For a narrow energy range around the Fermi energy we can consider the normal DOS to be constant within this range, *i.e.* $\nu_{\mathrm{N}}(\xi_{\mathbf{k}}) \approx \nu_0$. For simplicity, we further assume a $\mathbf{k}$-independent attractive interaction $V_{\mathbf{kl}} = -V$ which yields also a constant value of the superconducting order parameter $|\Delta_{\mathbf{k}}| = \Delta$ (this is the

[4] At the Fermi level the excitation has equal electron- and hole-character as the quasiparticles are equal-weight superpositions of the creation and annihilation operators ($u_{\mathbf{k}} = v_{\mathbf{k}}$). For excitations far above (below) the Fermi energy the nature of the excitation is purely hole-like (electron-like) as $v_{\mathbf{k}} \to 0$, $u_{\mathbf{k}} \to 1$ ($v_{\mathbf{k}} \to 1$, $u_{\mathbf{k}} \to 0$) implying that the particles are not affected by the pairing potential.

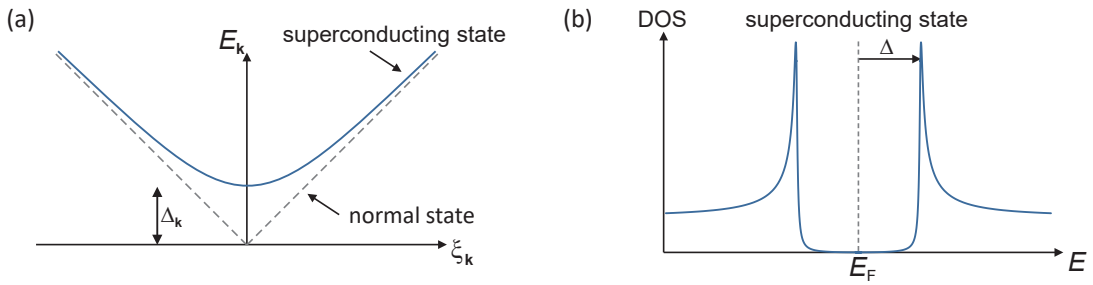

Fig. 3.3.: (a) Comparison between the quasiparticle excitation energy $E_{\mathbf{k}}$ and the normal state excitation energy $\xi_{\mathbf{k}}$. For $\xi_{\mathbf{k}} < 0$ (> 0) the excitations are hole- (electron-) like. (b) Quasiparticle DOS of a normal metal (top) and a superconductor (bottom). Taken and adapted from [Kle17].

case for isotropic s-wave superconductors). With this and Eq. 3.10 the superconducting DOS can be deduced to be [Tin04]

$$\frac{\nu_{\mathrm{SC}}(E)}{\nu_0} = \begin{cases} \frac{E}{(E^2-\Delta^2)^{1/2}} & (E > \Delta) \\ 0 & (E < \Delta) \end{cases} . \tag{3.11}$$

The DOS of a normal metal and a superconductor is depicted in Fig. 3.3b. An energy gap of 2Δ opens in the quasiparticle DOS around the Fermi level with the narrow coherence peaks at its boundaries. Hence, 2Δ is the minimum energy required in order to break a CP and the CPs are protected against (small) perturbations explaining the vanishing resistance in the superconducting state. Such external perturbations can be, for example, temperature, but also external forces which lift the electron-hole-symmetry, as for example current density (as the CPs acquire a net momentum) or a magnetic field (spin polarization). The corresponding critical quantities are denoted as T_{c}, j_{c} and B_{c}, respectively. As anticipated in Eq. 2.20, the so-called depairing-factor Γ which accounts for the finite lifetime of the quasiparticles is commonly introduced in Eq. 3.11 $(E \to E - i\Gamma)$ yielding a broadening of the divergent DOS at $E = \pm\Delta$. In the following we briefly introduce the BdG formalism as it will be useful later in the thesis.

3.1.2 Bogoliubov-de Gennes formalism

We briefly introduce the so-called Bogoliubov-de Gennes (BdG) formalism [Bog58; De 99] which is very convenient to include superconductivity when it is not necessary to precisely account for the microscopic origin of the pairing interaction. In the previous section we have seen that the elementary excitations of a superconductor, the quasiparticles, are no longer single particles as electrons or holes, but rather superpositions of the former. Therefore, we introduce the Nambu-Spinor $\Psi_{\mathbf{k}} = \left(c_{\mathbf{k}\uparrow}, c_{\mathbf{k}\downarrow}, c^{\dagger}_{-\mathbf{k}\downarrow}, -c^{\dagger}_{-\mathbf{k}\uparrow}\right)^{\mathrm{T}}$ which spans the 4×4-Nambu space, whereby two dimensions describe the electron-hole degree of freedom

while the remainding 2D subspace is assigned to the spin direction. Up to a constant, we can express the 2$^{\text{nd}}$ quantized BCS Hamiltonian [BH13; PGO13] as

$$\mathcal{H}_{\text{BCS}} = \frac{1}{2}\sum_{\mathbf{k}} \Psi_{\mathbf{k}}^{\dagger} H_{\text{BdG}}(\mathbf{k})\Psi_{\mathbf{k}}, \quad \text{where} \quad H_{\text{BdG}} = \xi_{\mathbf{k}}\,\tau_z \otimes \sigma_0 + \Delta\,\tau_x \otimes \sigma_0\,. \tag{3.12}$$

H_{BdG} is the BdG Hamiltonian. τ_i (σ_i) act on particle-hole (spin) subspace, Δ is the isotropic s-wave superconducting order parameter and $\xi_{\mathbf{k}}$ is as above the normal electron dispersion. By introducing the Nambu spinor we doubled the degrees of freedom as it spans a 4×4 space (two dimensions for particle-hole and spin subspace). In order to describe an s-wave superconductor this seems to be redundant,[5] however, the BdG formalism will turn out to be very useful when it comes to more complex systems.

For systems where the momentum is not a good quantum number anymore, it is favorable to pass to real space and replace the standard momentum operators acting in $\mathbf{k}$-space with field operators acting in real space by $\Psi(\mathbf{r}) = \int \frac{\mathrm{d}\mathbf{k}}{(2\pi)^3}\Psi_{\mathbf{k}} e^{i\mathbf{k}\cdot\mathbf{r}}$. The Nambu-Spinor reads $\Psi(\mathbf{r}) = \left(\psi_{\uparrow}(\mathbf{r}), \psi_{\downarrow}(\mathbf{r}), \psi_{\downarrow}^{\dagger}(\mathbf{r}), -\psi_{\uparrow}^{\dagger}(\mathbf{r})\right)^{\mathrm{T}}$, where $\psi_{\sigma}^{\dagger}(\mathbf{r})$ and $\psi_{\sigma}(\mathbf{r})$ create and annihilate a quasiparticle with spin σ at position $\mathbf{r}$, respectively. In this case the transformation is carried out by [OPP17; PGO13]

$$\mathcal{H}_{\text{BCS}} = \frac{1}{2}\int \mathrm{d}\mathbf{r}\, \Psi^{\dagger}(\mathbf{r}) H_{\text{BdG}} \Psi(\mathbf{r}), \tag{3.13}$$

with the same BdG Hamiltonian as above.

3.2 $2H$-$NbSe_2$ - not a simple BCS superconductor

Beside superconductivity, $NbSe_2$ exhibits another correlated electronic phase, a charge-density wave (CDW) that forms below $33\,\mathrm{K}$ and coexists with superconductivity at low temperatures. In the following we introduce all relevant aspects of CDW ordering and the superconducting pairing and their entanglement.

3.2.1 Crystal structure and charge density wave

Due to its intriguing properties $2H$-$NbSe_2$ is a widely studied material. It belongs to the class of the transition-metal dichalcogenides (TMDCs) and crystallizes in a double trilayer structure whereby each trilayer consists of a Nb layer sandwiched between two Se layers. One unit cell is depicted in Fig. 3.4a. Each Nb atom is surrounded by six Se atoms in a hexagonal coordination. The arrangement of the Se atoms is rotated by $180°$ between both trilayers ($2H$-configuration). Successive trilayers are coupled by weak vdW interactions between adjacent Se layers. The lattice constants are $a = 3.44\,\text{Å}$ and $c = 12.54\,\text{Å}$ [Mar+72]. In the top view (Fig. 3.4a) the different lattice sites are labeled as

[5] The unit matrix in spin state, σ_0, was still included for clarity. We have actually performed this transformation already along with Eq. 3.7, but in the sufficient 2×2-particle-hole subspace.

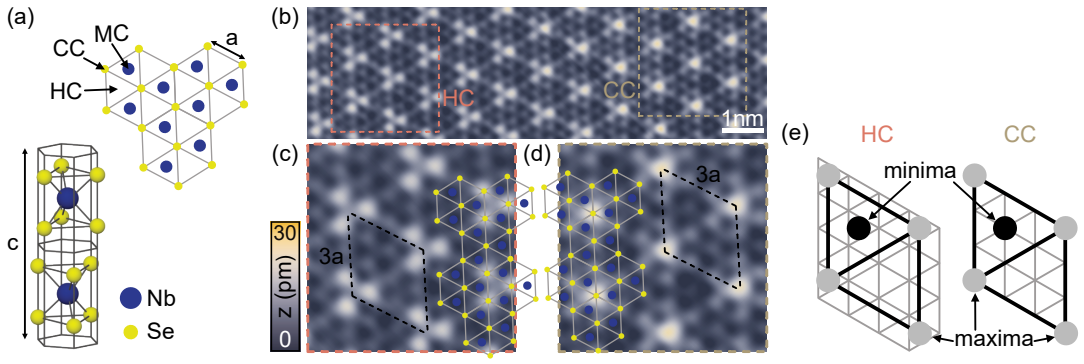

Fig. 3.4.: (a) Top view and 3D view of the unit cell of $2H$-$NbSe_2$. Crystal sites are labeled as metal-centered (MC), chalcogen-centered (CC) and hollow-centered (HC). (b) Constant-current topography of a clean $NbSe_2$ surface with a set point of $100\,\mathrm{pA}, 10\,\mathrm{mV}$ (recorded with a Nb tip). Areas with HC (CC) CDW pattern are highlighted in red (brown). (c,d) Zooms in the areas indicated in (b). Black lines outline the CDW superstructure. Atomic grids are overlaid as guides to the eye. (e) Sketch of the alignment between CDW and atomic lattice for the HC and CC structure. The CDW is depicted by the black rhombus, where gray (black) dots indicate CDW maxima (minima). Additionally, the Se grid is overlaid in gray (Se atoms located at vertices of the triangles).

metal-centered (MC), chalcogen-centered (CC) and hollow-centered (HC) which will be important for the CDW characterization and the adsorption of Fe atoms.

Below $33\,\mathrm{K}$, $NbSe_2$ exhibits an incommensurate two-dimensional CDW. This CDW is driven by strong anisotropic electron-phonon coupling [Kis+07; LSD18; Ler+15; Rah+12; Web+11; Ros+01; Ros11; MK13; Val+04; JMH06; JM08; Arg+14; Zhu+15] which causes periodic lattice distortions in the order of a few percent of the unperturbed lattice [MK13; Zhe+18; LSD18; San+21] accompanied by a periodic modulation of the local DOS. Figure 3.4b shows an atomic-resolution constant-current topography of the clean $NbSe_2$ surface. We find different patterns across the surface as highlighted by the colored boxes. In the topographies the CDW-induced local variations of the DOS appear superimposed to the atomic corrugation of the terminating Se layer (*c.f.* section 2.1.2). The periodicity of the (incommensurate) CDW is $\gtrsim 3a$ [MAD75; Fen+12; Sou+13; McM76] and thus, the CDW periodicity does not exactly match an integer multiple of the atomic lattice constant leading to the emergence of different patterns across the surface which smoothly transform into each other. Figure 3.4c,d show scale-ups of the colored boxes in (b) with overlaid atomic grids serving as guides to the eye. In (c) the CDW maxima coincide with a HC site leading to triangular patterns with three bright Se atoms (HC structure of the CDW). In (d) the CDW maxima align with a Se site corresponding to the CC-CDW structure with one bright Se atom. The CDW creates a superlattice as indicated with the black rhombi in Fig. 3.4c,d with maxima on its edges and a minimum and local minimum in the interior. Fig. 3.4e schematically illustrates the alignment between CDW and atomic lattice for both structures. The CDW lattice is outlined by black lines with CDW maxima (minima) as gray (black) circles. The Se grid is shown in gray with Se atoms sitting on intersections of the lines.

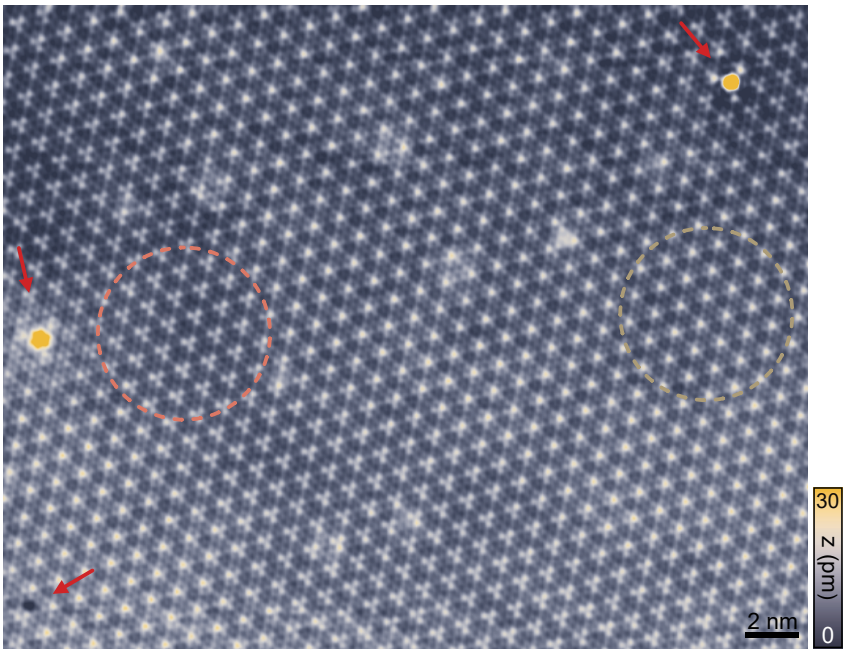

Fig. 3.5.: Constant-current topography of a clean $NbSe_2$ surface with a set point of $100\,\mathrm{pA}, 10\,\mathrm{mV}$ (recorded using a Nb tip). Areas with HC (CC) CDW wave pattern are highlighted in red (brown). Red arrows point out distortions of the CDW in the vicinity of lattice defects.

Interestingly, while the HC and CC structures continuously evolve across the surface, we do not find regions where the CDW maxima coincide with Nb atoms (MC-structure), as can be verified in the large-scale topography in Fig. 3.5. The MC-configuration is energetically disfavored as shown by DFT calculations (on single-layer $NbSe_2$) and hence, does not occur on the surface [GOY19; Zhe+18; Gus+19; LSD18; Cos+18]. HC and CC structure form a continuous network in which the absence of the MC structure is resolved by domain boundaries [GOY19]. Without any defects we expect a change from HC to CC domain (shift of half a lattice site) after $10a_{\mathrm{CDW}} \approx 10\,\mathrm{nm}$. However, in real crystals the CDW can be pinned by crystal defects [Cos+18; Lan+14; FW15; Cha+15; Arg+14]. Examples, where defects perturb the CDW in their vicinity are marked by red arrows in Fig. 3.5. Therefore, the exact configuration of the CDW is dictated by the complex interplay of lattice defects and natural long-range order of the CDW.

3.2.2 Superconductivity and CDW - coexistence of correlated phases

Results presented in this section were achieved in collaboration with A. Sanna[6] et al. within a combined STM and *ab inintio* study of the anisotropic superconductivity of bulk $2H$-$NbSe_2$ in the CDW phase and are published in [San+21]. All DFT calculations and

[6]Max-Planck-Institut für Mikrostrukturphysik, Halle.

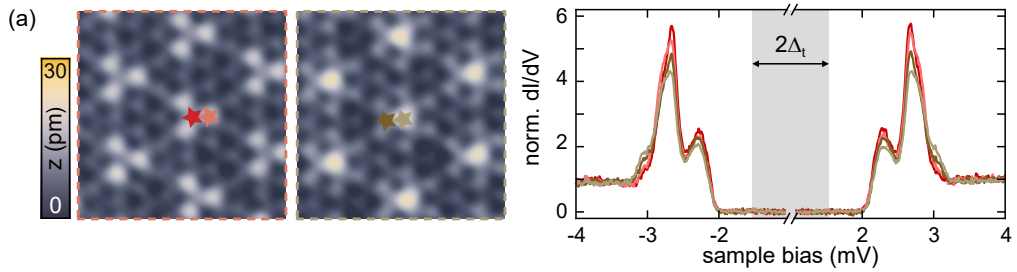

Fig. 3.6.: Constant-height $\mathrm{d}I/\mathrm{d}V$ spectra at the positions indicated with the colored stars in the topographies in the left (reproduced from Fig. 3.4c,d) (feedback was opened at the position of the bright brown spectrum for all traces at $250\,\mathrm{pA}, 5\,\mathrm{mV}$ and a modulation of $V_{\mathrm{rms}} = 15\,\mu\mathrm{V}$ was used). The Nb tip gap is indicated by the gray box ($\Delta_{\mathrm{t}} \approx 1.55\,\mathrm{meV}$).

modeling were performed by A. Sanna and his colleagues. The author of this thesis contributed the experimental part.

As introduced in section 2.2.2 we can investigate the quasiparticle DOS by $\mathrm{d}I/\mathrm{d}V$ spectroscopy employing superconducting tips (Fig. 3.6). Around the Fermi energy we find a fully gapped region enclosed by a peculiar peak distribution in the range $2.1\,\mathrm{mV} < \Delta/e < 3.1\,\mathrm{mV}$. Comparing Fig. 3.6 and Fig. 3.3b we note that the DOS of $NbSe_2$ does not reflect a pure BCS-like DOS with a single pair of coherence peaks. All spectra recorded at different positions on the surface exhibit a similar quasiparticle DOS with two main peaks and further shoulders. Comparing dark and bright spectra of each color, which are taken on a Se atom and a hollow site, respectively, we discern small variations of the relative intensities of the different peaks and shoulders on the atomic scale. There are also intensity variations on the scale of the CDW (HC vs CC structure) which can be discerned by comparing the dark (bright) traces of different color. Additional positions with respect to the CDW (spectra recorded on minima and local minima of the CDW) are compiled in Fig. A.2.

Superconductivity in $NbSe_2$ has been discussed in terms of multiband or anisotropic superconductivity [HRW90; Yok+01; Noa+10; Noa+15; RV04; Boa+03; Fle+07; Gui+08a; Gui+08b]. Furthermore, the interplay between CDW an superconductivity in $NbSe_2$ is still under debate. Both coexisting charge-ordered phases are driven by strong momentum-dependent electron-phonon interactions [Kis+07; LSD18; Ler+15; Rah+12] and it remains a valid question if they boost or compete with each other [Kis+07; Xi+15; Cho+18a; LSD18; Zhe+18; Sou+13; Ler+15; Uge+16; Yan+18].

First-principles simulations based on superconducting density functional theory (SCDFT) enable full $\mathbf{k}$- and real-space resolution revealing the strongly anisotropic character of the superconducting pairing ruling out the scenario of multiband superconductivity. The overall structure of the quasiparticle DOS probed by STM (Fig. 3.6) could be well reproduced [San+21]. In the following we briefly outline the main outcomes of the calculations (see [San+21] for details).

The CDW is approximated to be commensurate with the lattice, *i.e.* $a_{\mathrm{CDW}} = 3a$, as otherwise calculations would require an exceedingly large unit cell. From experimental point of view this is justified as the main peak structure (beside slight intensity variations) does not significantly vary between different positions across the surface (*c.f.* Fig. 3.6). Interestingly, calculations predict a unit cell with two crystallographically inequivalent trilayers exhibiting the pure HC and CC CDW reconstruction. To recall, both structures coexist on the surface (*c.f.* Figs. 3.4 and 3.5). This confirms them as the energetically favored phases in agreement with prior DFT studies on single-layer $NbSe_2$ [GOY19; Zhe+18; Gus+19; LSD18; Cos+18].

The band structure and the DOS of the undistorted and CDW-ordered crystal is shown in Fig. 3.7a in black and red, respectively. The latter was achieved by a backfolding procedure to the original Brillouin zone (BZ). Note that the BZ is reduced due to the CDW-induced superstructure. The key features of the CDW is the opening of a broad dip in the DOS slightly above the Fermi level yielding a reduction of the DOS of $\approx 10\,\%$ and a band gap opening along MK (blue and orange arrow). Panel (b) shows a $k_z = 0$-cut of the Fermi surface. The unperturbed Fermi surface is outlined in blue. It consists of two sets of double-walled cylinders around K and Γ arising from two Nb-4d-derived bands that cross the Fermi level several times and a pancake-like Se pocket having 4p-character around Γ (innermost feature). The CDW reconstruction of the Fermi surface obtained from the unfolding procedure is shown in white-red-black. The outer pair of Nb-cylinders (around K) appear more blurred indicating a stronger influence of the CDW on this part of the Fermi surface. The band gap opening along MK is indicated by the orange circle.

While the CDW wave leaves the phonon DOS largely unaffected it significantly alters the momentum-dependent electron-phonon coupling. The electron-phonon coupling strength obtained for the unfolded BZ within a small slice around $k_z = 0$ are presented in Fig. 3.8a. We observe a complex pattern of strong- (light) and weak-coupling (dark) regions (*c.f.* [San+21] for more details). Superconductivity is implemented within this CDW state from first-principles using SCDFT facilitating fully anisotropic calculations of the superconducting gap in both reciprocal and real space. Note that the calculations yield a critical temperature of $T_{\mathrm{c,DFT}} = 10.2\,\mathrm{K}$ (*c.f.* experimental value of $T_{\mathrm{c}} = 7.2\,\mathrm{K}$) and hence, overestimate the total gap size.[7] The obtained superconducting state exhibits a complex gap distribution that considerably varies within and across the different Fermi surface sheets. This is in contrast to true multiband superconductors as MgB_2 or Pb which exhibit sheet-dependent gap anisotropies [Rub+15a; BY01; Flo+07].

The manifold superconducting order parameter is depicted in Fig. 3.8b,c. Panel (b) shows the distribution of gap values computed over the full BZ and within a small slice around the BZ center $(k_z < 0.1\pi/c)$ in green and red, respectively. Panel (c) shows

[7] This can be attributed to neglection of anharmonic corrections to the lattice dynamics and limits on the precision in computing the phonon properties and dielectric screening imposed by the large size of the CDW cell. See [San+21] for details.

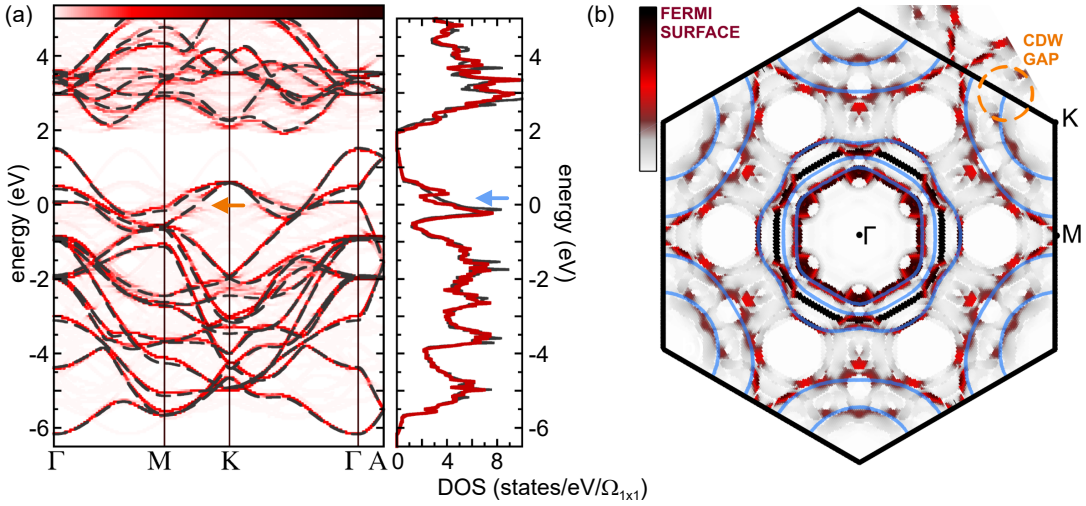

Fig. 3.7.: (a) Unfolded band structure (left) and electronic DOS (right) of the CDW (red) and undistorted phase (black). (b) Cut of the Fermi surface (at $k_z = 0$) obtained by unfolding the reduced BZ. Color scale indicates the relative spectral weight. Blue curves represent the unperturbed Fermi surface sheets. Arrows and circles highlight features in the data (see text). Figure reproduced from [San+21].

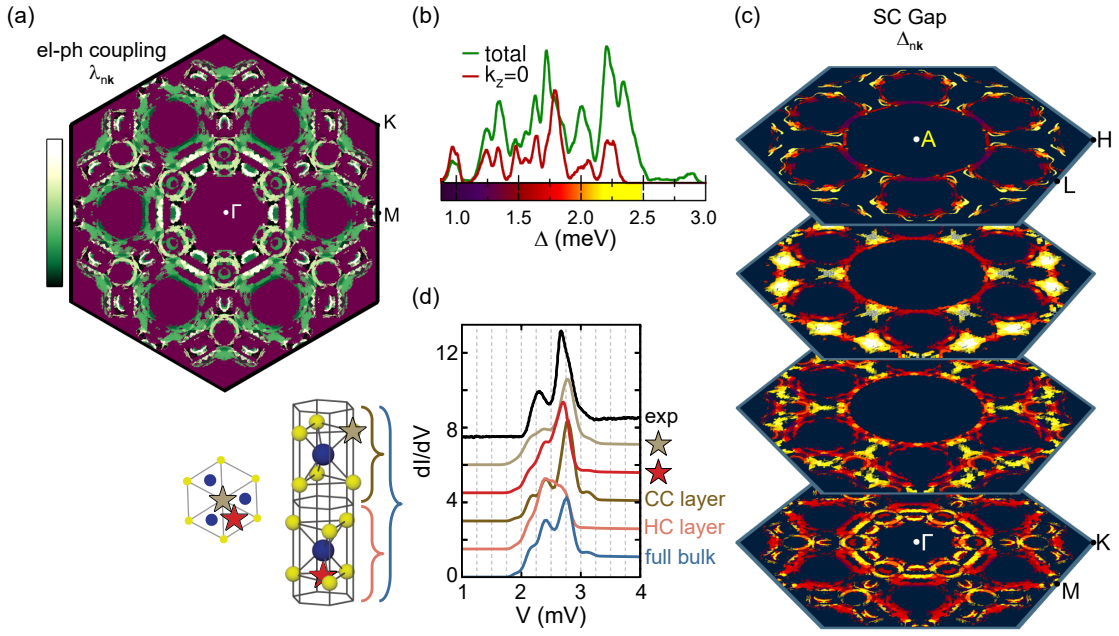

Fig. 3.8.: (a) Electron-phonon coupling computed in the unfolded BZ at random points within a slice of $k_z < 0.1\pi/c$ around the BZ center and within $\pm 0.1\mathrm{mR_y}$ from the Fermi level. (b) Distribution of gap values computed over the full BZ (green) and a $k_z < 0.1\pi/c$ slice (red). (c) Superconducting gap computed in the unfolded BZ at random points on constant-k_z-slices of width $0.1\pi/c$ and within $\pm 0.1\mathrm{mR_y}$ from the Fermi level. (d) Simulated $\mathrm{d}I/\mathrm{d}V$ spectra for the full bulk (blue), the layer with HC-CDW (bright red), the layer with CC-CDW (dark brown) and at two specific positions as indicated in the left (dark red and bright brown, both positions resemble the experimental positions of Fig. 3.6 of corresponding color). Experimental spectrum (black) obtained by averaging over multiple data traces (*c.f.* Fig. A.2). Tunneling currents are computed from the real-space distributions of gap values which are scaled by the factor $T_\mathrm{c}/T_{\mathrm{c,DFT}}$ to correct for the overestimation of the critical temperature. Figure reproduced from [San+21].

several cuts through the BZ with the gap size indicated by the color scale. Note that the high energy gap values mainly arise from hot spots at the K-cylinders at $2/3$ of the ML-line exhibiting significant out-of-plane, but also sizeable $k_{\|}$-character. The lower energy features are mainly governed by the inner Fermi surface sheets around Γ within the $k_z = 0$-slice. Remarkably, the high energy values originate from the same Fermi surface sheet that is gapped by the CDW (*c.f.* Fig. 3.7b, orange circle). We like to point out that the gap distribution closely resembles the structure of the electron-phonon coupling across the Fermi surface (*c.f.* Fig. 3.8a,c). The electron-phonon coupling is, in turn, considerably affected by the CDW, constituting the connection between CDW order and superconductivity in $NbSe_2$ ([San+21] for details).

In order to directly compare the results to the STM spectra the superconducting DOS of the sample was computed from the real-space projection of the gap distribution (see [San+21] for details). To match the experimental energies the gap size was downscaled by a factor of $T_c/T_{c,DFT}$ and a superconducting s-wave tip (with the bulk value of the superconducting order parameter of Nb) was assumed. Fig. 3.8c shows the computational dI/dV conductance spectra obtained for the full bulk, the HC and CC layer (remember, that the two structures appear in two distinct layers in the simulations) and two specific tip positions mimicking the experimental positions of Fig. 3.6 on the maxima of the CDW. For comparison, an experimental dI/dV spectrum obtained from averaging multiple traces on different positions across the surface (see Appendix Fig. A.2) is shown in black. In contrast to the experimental spectra, that only exhibit slight intensity variations across the surface, the simulations reveal strong variations depending on the exact position of the tip. While some theory traces reproduce the data (two main peaks with additional shoulders) quite well, others differ strongly. The most intense STM peak can be identified with the superconducting gap values arising from the K-cylinder hot spots at $2/3$ML. Due to its strong out-of-plane character it appears intense in the STM spectra (strong overlap with the tip).

The deviations between data and simulation can be explained considering two aspects: (1) The different CDW structures that are mapped on different layers actually exist on one layer smoothly evolving into each other leading to additional hybridization of the electronic states of the HC and CC CDW structure that is not captured by the calculations. (2) The simulated spectra are acquired within the 3D crystal structure with periodic boundary conditions. Hence, the tip is placed "within" the atomic layers and not above the surface and the momentum sensitivity of the STM ($\mathbf{k}_{\|}$ in Eq. 2.5) due to the decay of the wave functions into vacuum is not captured. The second consideration can be checked by height-dependent measurements depicted in Fig. 3.9. We observe variations of the relative peak intensities with tip height. While the largest peak is reduced in intensity upon tip approach to the surface, the high-energy shoulders gain intensity. Especially the highest gap values are found to exhibit (beside k_z) significant $k_{\|}$-character (*c.f.* Fig. 3.8b) and hence, they decay faster into the vacuum than the low-gap values which mainly originate from around Γ. Considering these issues we find nice agreement between simulated spectra and STM

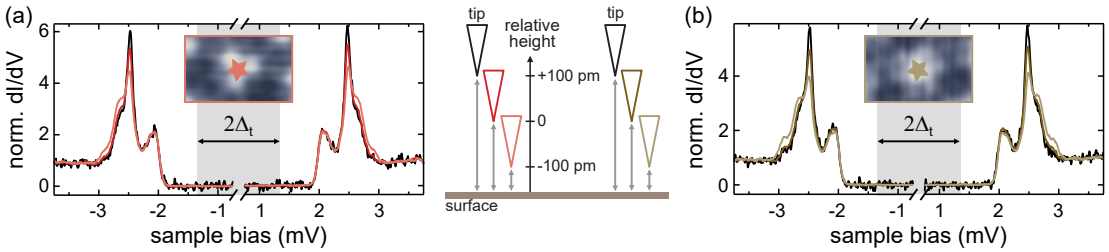

Fig. 3.9.: Constant-height $\mathrm{d}I/\mathrm{d}V$ spectra recorded at different tip-sample distances (a) on the maximum of the CDW in the HC, and (b) on the maximum of the CC structure. The tip's lateral position is indicated in the inset topographies (constant-current mode with set point: $200\,\mathrm{pA}, 4\,\mathrm{mV}$). Feedback was opened at $200\,\mathrm{pA}, 4\,\mathrm{mV}$ before adding an additional offset of $0\,\mathrm{pm}$, $\pm 100\,\mathrm{pm}$ to the tip's z-position. A modulation of $V_{\mathrm{rms}} = 15\,\mu\mathrm{V}$ was used. The Pb tip gap is indicated by the gray box ($\Delta_{\mathrm{t}} \approx 1.35\,\mathrm{meV}$).

measurements. We assign the slight intensity variations found across the surface in the experimental $\mathrm{d}I/\mathrm{d}V$ spectra to spatial variations of the quasiparticle wave functions which manifest in changes in the tunneling matrix element (*c.f.* section 2.1.1).

Concluding, the calculations performed by A. Sanna settle the long-standing discussion about the superconducting nature of $NbSe_2$ revealing the highly anisotropic nature of the superconducting pairing arising from the momentum anisotropy of the electron-phonon coupling across the Fermi surface. Further, it shines light onto the exact entanglement between both correlated phases: the formation of the CDW affects the momentum-dependent electron-phonon coupling which then governs the anisotropy of the superconducting pairing strength across the different Fermi surface sheets.

3.2.3 Additional properties of $2H$-$NbSe_2$

To close the chapter we briefly comment on further characteristics of $2H$-$NbSe_2$. Due to its layered structure bulk $NbSe_2$ has partially 2D electronic properties which are reflected in the critical quantities for superconductivity. Note that $NbSe_2$ is a type II superconductor and vortices penetrate the material for $B_{\mathrm{c1}} < B < B_{\mathrm{c2}}$ [HRW90]. We find upper critical out of-plane and in-plane magnetic fields of $B_{\mathrm{c2}\perp} \approx 4\,\mathrm{T}$ and $B_{\mathrm{c2}\parallel} \approx 14\,\mathrm{T}$, respectively [FM73]. The lower critical fields at which vortices start to penetrate the bulk crystal are very small[8] around $B_{\mathrm{c1}\perp,\parallel} \approx 10\text{-}20\,\mathrm{mT}$ for both directions [ZW10]. For the superconducting coherence length we find in-plane and out of-plane values of $\zeta_{\parallel} \approx 90\,\text{Å}$ and $\zeta_{\perp} \approx 27\,\text{Å}$ [FM73].

For completeness, we present $\mathrm{d}I/\mathrm{d}V$ data covering higher energy ranges in Fig. 3.10. The negative energies reveal a broad featureless DOS in agreement with the presence of multiple bands below E_{F} (*c.f.* Fig. 3.7a). A resonance found at $\gtrsim 0.2\,\mathrm{V}$ could emerge from the flat band edges at Γ and K at these energies. We further find a broad region of low DOS between $0.5\text{-}2.0\,\mathrm{V}$ which we associate with the region of low DOS in Fig. 3.7a. Above $2\,\mathrm{V}$ we find again increased DOS arising from multiple high-energy bands.

[8] The in-plane lower magnetic field is greatly enhanced in few layer samples [Dvi+18].

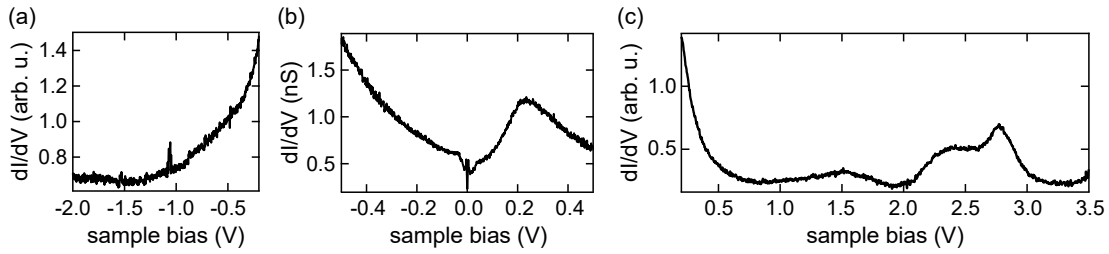

Fig. 3.10.: Spectra covering different voltage ranges recorded on the clean $NbSe_2$-surface recorded with a Pb tip. (a,c) Constant-current spectra (set point: $100\,\mathrm{pA}, V_{\mathrm{rms}} = 5\,\mathrm{mV}$). (b) Constant-height spectrum (set point: $500\,\mathrm{pA}, -0.5\,\mathrm{V}, V_{\mathrm{rms}} = 2\,\mathrm{mV}$).

4 Single magnetic impurities on 2*H*-$NbSe_2$

In this chapter we first set the essential theoretical basics of magnetic impurities on metals and superconductors. After introducing the two stable species of Fe atoms we find on the surface after evaporation, we will study the effect of the CDW on Yu-Shiba-Rusinov (YSR) states focusing on one species. In the following we address the excitations arising from the quantum nature of the impurity spin also focusing on this species. We close the chapter with the study of the second Fe atom species which show tip-induced spatial variations of their YSR excitations.

4.1 Magnetic adsorbates on a metal

4.1.1 Crystal field and magnetic anisotropy

In general, the magnetic moment is given by the number of unpaired electrons in d orbitals. In gas phase, the ground state of an Fe atom (electron configuration of [Ar] $3d^6 4s^2$) is determined by Hund's rule to ${}^5D_4$ within the usual terminology ${}^{2S+1}L_J$, where S is the total spin, L the orbital angular momentum and J the total angular momentum The total spin of $S = 2$ is carried by the electrons occupying degenerate d levels as illustrated in Fig. 4.1a. Fig. 4.1b shows the usual representation of the unperturbed d orbitals ($d_{x^2-y^2}, d_{xy}, d_{xz}, d_{yz}, d_{z^2}$) in cartesian coordinates.[1]

If an atom is adsorbed on a surface, *i.e.* in an anisotropic environment, the gas phase representation of the atomic orbitals does not hold anymore. The atomic orbitals hybridize with the states of the surface atoms (ligands) and form new hybrid orbitals which (partially) keep the symmetry of the unperturbed d levels. Depending on the magnitude of their overlap with the ligands different d levels can experience different Coulomb repulsion and hence, different energy shifts such that their degeneracy is lifted. The (qualitative) energetic configuration of the d-block - called crystal field splitting - depends on the geometry of the adsorption site. Being in the same order of magnitude as the spin pairing energy, the crystal field splitting competes with Hund's rule which tends to maximize the spin. Thus, adsorption on the surface can change the spin configuration compared to the atom in gas phase. A detailed derivation of crystal field splitting in transition metal complexes can be found in [Jea05]. In the following we discuss different trigonal ligand

[1] These are linear combinations of the angular momentum eigenstates with $m_l = \pm 2, m_l = \pm 1$ and $m_l = 0$ [Dem16].

fields which are relevant for the adsorption of single atoms in hollow sites of the $NbSe_2$ surface (MC and HC, *c.f.* section 3.2.1).

Figure 4.1c-e illustrate three examples of the crystal field split d-block in different trigonal ligand fields. In (c) the atom is adsorbed between three in-plane ligands and two out of-plane ligands. In (d) the out of-plane ligands are removed. In (e) the atom is slightly lifted out of-plane compared to (d) such that the symmetry is further reduced. The levels are named according to their symmetry class (a detailed derivation of the symmetry classes can be found in [Jea05]). For the trigonal-bipyramidal and trigonal-planar configurations with and without the vertical ligands (Fig. 4.1c,d) the state a_1 inherits the characteristic symmetry of the former d_{z^2}. Comparing Fig. 4.1c and d we see how the presence or absence of the vertical ligands affects the energy of a_1 (blue arrow, Fig. 4.1c,d). The levels labeled e'' resemble the former d_{xz} and d_{yz} orbitals (*c.f.* Fig. 4.1b). The d_{xy} and $d_{x^2-y^2}$ can lower their energy by mixing with the atom's p_x and p_y-levels, respectively, resulting in symmetry class e'. Hence, they do not keep the symmetry of the unperturbed d orbitals. Similar findings hold for the pyramidal ML_3-complexes (Fig. 4.1e), where the symmetry is further reduced due to the out of-plane adsorption geometry. $1a_1$ can be traced back to d_{z^2}. The states $1e$ have the typical four-lobe shape of d_{xz}, d_{yz}, but are rotated with respect to the orbitals of Fig. 4.1b as this adsorption geometry is easier described within a rotated basis. The states labeled $2e$ arise from admixtures of former rotated d orbitals with p-states. Usually pure s- and p-states are not relevant as they are too high in energy. However, here the state $2a_1$ which originates from an admixture of the former s- and p_z-orbitals is found close to the d-block.

The final spin configuration, *i.e.* the occupation of the crystal field split levels is determined by the competition between energy gain due to parallel spin alignment (Hund's energy) and the energy splitting between the levels. For Fe atoms adsorbed on $NbSe_2$ DFT calculations predict a total magnetic moment of $\approx 3.8\mu_B$ [Yan+20], *i.e.* the spin of the d-shell remains largely unquenched upon adsorption on the surface (high-spin configuration).[2] Possible occupations of the d-block are depicted schematically in Fig. 4.1c-e by the red arrows.

On first sight, this high-spin state with a total spin of $S = 2$ is five-fold degenerate ($m_s = \pm 2, \pm 1, 0$) as there is no preferred spin direction. However, considering the orbital angular momentum, this degeneracy can be lifted. The angular momentum couples to the spin via spin-orbit interaction. The spin-orbit Hamiltonian reads $H_{\mathrm{SO}} = \lambda \mathbf{L} \cdot \mathbf{S}$, where λ is the spin-orbit coupling constant and $\mathbf{L}$ the total angular orbital momentum.

The unperturbed five d orbitals (Fig. 4.1b) are constructed such that they all exhibit zero angular momentum (as they are linear combinations of the $m_l = \pm 2, m_l = \pm 1$ and $m_l = 0$ states). Hence, the orbital angular momentum of transition metal atoms is usually largely quenched and spin-orbit coupling can be treated as perturbation leading to a small energy

[2] Similar results were obtained for Mn, Co adsorbed on $NbSe_2$ [Cos+18].

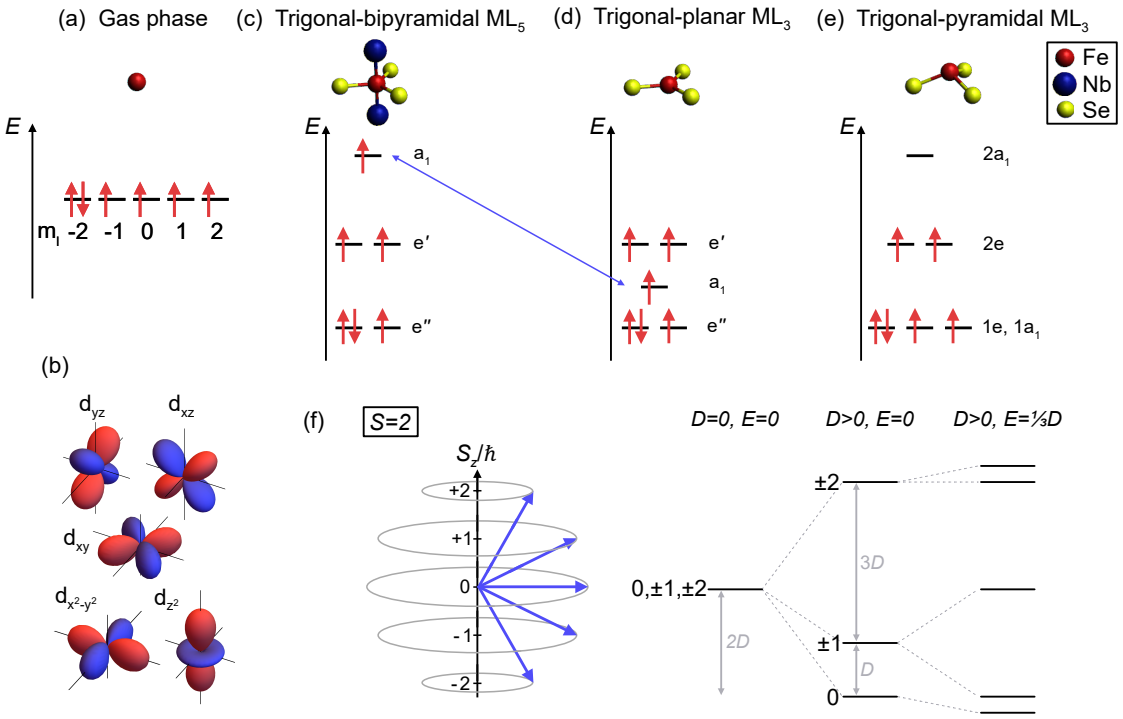

Fig. 4.1.: (a,c-e) Lifting of the degeneracy of the d-block in different crystal fields. (a) Gas phase (isotropic environment). (c) Trigonal-bipyramidal ML_5. (d) Trigonal-planar ML_3. (e) Trigonal-pyramidal ML_3. (b) Representation of the d orbitals in cartesian coordinates. (f) Schematic illustration of the different spin projections along the z-axis for a system with $S = 2$ in the left. Right: Effect of the magnetic anisotropy on the spin-system. Without anisotropy, all levels are degenerate. The degeneracy is successively lifted by axial and transverse anisotropies. The energetic order of the levels is determined by the signs of D and E.

correction in the Hamiltonian. It is convenient to only use the spin angular momentum to describe the system. The spin-orbit coupling term can be mapped into the so-called effective spin Hamiltonian which reads (up to a constant) [DXW08; GSV06]:

$$H_{\text{eff}} = DS_z^2 + E(S_x^2 - S_y^2)\,, \tag{4.1}$$

and only contains the spin quantum numbers. The parameter $D \propto \lambda^2(L_z - L_\perp)$ represents the difference between the unquenched out of-plane (L_z) and in-plane ($L_\perp$) orbital angular momentum. Likewise, $E \propto \lambda^2(L_x - L_y)$ accounts for the in-plane components of the unquenched orbital angular momentum. Thus, the parameters D and E are called axial and transverse magnetic anisotropy, respectively.

Therefore, any unquenched orbital angular momentum lifts the degeneracy of the high-spin ground state inducing a preferred spin orientation within the crystal field. Figure 4.1f illustrates schematically the effect of axial and transverse magnetic anisotropies for a total spin of $S = 2$. Positive axial magnetic anisotropy ($D > 0$) energetically favors in-plane spin alignment. Thus, $m_s = 0$ is the ground state followed by the $m_s = \pm 1$ and $m_s = \pm 2$ doublets. Analogously, $D < 0$ favors high out-of-plane spin projections reversing the order of the levels. Non-zero transverse magnetic anisotropy further lifts the degeneracy and mixes states with $\Delta m_s = \pm 2$ [GSV06].

This splitting of the ground state multiplet occurs without the application of an external magnetic field and is therefore often referred to as zero-field splitting. In an external magnetic field, the split levels shift in energy due to the Zeeman effect. Magnetic anisotropy is only relevant for spins exceeding $S = 1/2$ as the ground state remains doubly degenerate for half-integer spins due to time-reversal symmetry (Kramer's theorem).

4.1.2 Interaction with the substrate - Anderson model and Kondo effect

In this section we will outline how a magnetic moment on a metal surface interacts with the conduction electrons of the host before extending the problem to a superconducting substrate in the next section. For simplicity, we consider a single spin of $S = 1/2$. A magnetic moment remains unquenched, if the singly occupied d orbital lies below the Fermi energy ($\varepsilon_d < E_{\text{F}}$) while the Coulomb repulsion U shifts the doubly occupied level above ($\varepsilon_d + U > E_{\text{F}}$) as illustrated in Fig. 4.2a.

We can describe the system within the so-called Anderson-model [And61]. Within this model, all interactions between the substrate and the localized magnetic moment are summarized within the mean-field Hamiltonian [And61; Hew93]

$$\mathcal{H} = \mathcal{H}_0 + \mathcal{H}_d + \mathcal{H}_{sd}\,. \tag{4.2}$$

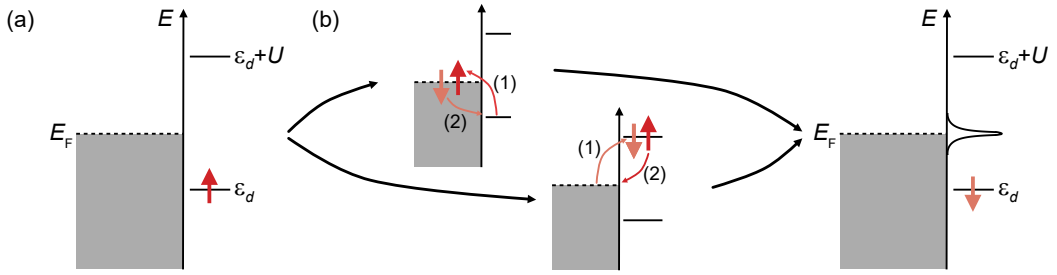

Fig. 4.2.: (a) Anderson model for a spin-1/2 impurity: the singly occupied level is at ε_d below the Fermi energy while the doubly occupied level is at $\varepsilon_d + U$ above E_F. U is the Coulomb repulsion energy. (b) Different spin-exchange scattering processes of the impurity with the bath electrons. Virtual excitations involve the impurity level being empty (top) or doubly occupied (bottom). The Kondo resonance is outlined at the Fermi level.

The first part describes the energy of the unperturbed electrons in the metal,

$$\mathcal{H}_0 = \sum_{\mathbf{k}\sigma} \varepsilon_\mathbf{k} n_{\mathbf{k}\sigma}\,, \quad \text{with} \quad n_{\mathbf{k}\sigma} = c^\dagger_{\mathbf{k}\sigma} c_{\mathbf{k}\sigma}. \tag{4.3}$$

Here, $\varepsilon_\mathbf{k}$ is the energy of the electron state with momentum $\mathbf{k}$ and $n_{\mathbf{k}\sigma}$ is the number operator for momentum $\mathbf{k}$ and spin σ which contains the creation $(c^\dagger_{\mathbf{k}\sigma})$ and annihilation $(c_{\mathbf{k}\sigma})$ operators of the Bloch states. The second term

$$\mathcal{H}_d = \sum_\sigma \varepsilon_d n_{d\sigma} + U n_{d\uparrow} n_{d\downarrow}, \quad \text{with} \quad n_{d\sigma} = d^\dagger_\sigma d_\sigma \tag{4.4}$$

contains the unperturbed energy ε_d of the d orbital relative to the Fermi energy and a term that accounts for the Coulomb repulsion of electrons localized at the impurity site. $d^\dagger_\sigma$ (d_σ) act on the impurity, *i.e.* create (annihilate) an electron at the impurity site. The last term $\mathcal{H}_{sd}$ inherits the scattering between the conduction electrons and the impurity:

$$\mathcal{H}_{sd} = \sum_{\mathbf{k}\sigma} (V_\mathbf{k} d^\dagger_\sigma c_{\mathbf{k}\sigma} + V^*_\mathbf{k} c^\dagger_{\mathbf{k}\sigma} d_\sigma), \text{ where } V_\mathbf{k} = \sum_j e^{i\mathbf{k}\cdot\mathbf{r}_j} \langle \phi_d | H | \psi_{\mathbf{r}_j} \rangle \,. \tag{4.5}$$

Above, ϕ_d is the atomic d level wave function and $\psi_{\mathbf{r}_j}$ are the Wannier functions describing the conduction electrons at site $\mathbf{r}_j$. It further contains the 1st quantization Hamiltonian H which reads:

$$H = \sum_{i=1}^{N_0} \left(\frac{\mathbf{p}_i^2}{2m} + \tilde{U}(\mathbf{r}_i) + V_\mathrm{imp}(\mathbf{r}_0) \right) + \frac{1}{2} \sum_{i \neq j}^{N_0} \frac{e^2}{\mathbf{r}_i - \mathbf{r}_j} + \sum_{i=1}^{N_0} \lambda(\mathbf{r}_i)\, \mathbf{l}_i \cdot \boldsymbol{\sigma}_i \,. \tag{4.6}$$

It accounts for kinetic energy terms, the periodic potential $\tilde{U}(\mathbf{r}_i)$ of all ion cores of the substrate, the additional potential $V_\mathrm{imp}(\mathbf{r}_0)$ at the impurity site, the Coulomb interaction between the electrons and spin-orbit coupling.

The Anderson Hamiltonian (Eq. 4.2) can be transformed to the so-called sd-model via the Schrieffer-Wolff transformation [SW66] and then reads [Hew93]:[3]

$$\mathcal{H} = \sum_{\mathbf{k},\mathbf{k}'} J_{\mathbf{k}\mathbf{k}'} \left(S^+ c^\dagger_{\mathbf{k}\downarrow} c_{\mathbf{k}'\uparrow} + S^- c^\dagger_{\mathbf{k}\uparrow} c_{\mathbf{k}'\downarrow} + S_z (c^\dagger_{\mathbf{k}\uparrow} c_{\mathbf{k}'\uparrow} - c^\dagger_{\mathbf{k}\downarrow} c_{\mathbf{k}'\downarrow}) \right) + \sum_{\mathbf{k},\mathbf{k}',\sigma,\sigma'} K_{\mathbf{k}\mathbf{k}'}\, c^\dagger_{\mathbf{k}\sigma} c_{\mathbf{k}'\sigma}\,. \tag{4.7}$$

Here, S_z and $S^\pm = S_x \pm i S_y$ are the spin operators of the impurity's d level and $J_{\mathbf{k}\mathbf{k}'}$ ($K_{\mathbf{k}\mathbf{k}'}$) are the exchange (potential) scattering strengths:

$$J_{\mathbf{k}\mathbf{k}'} = V^*_{\mathbf{k}} V_{\mathbf{k}'} \left(\frac{1}{U + \varepsilon_d - \varepsilon_{\mathbf{k}'}} + \frac{1}{\varepsilon_{\mathbf{k}} - \varepsilon_d} \right) \tag{4.8}$$

$$K_{\mathbf{k}\mathbf{k}'} = \frac{V^*_{\mathbf{k}} V_{\mathbf{k}'}}{2} \left(\frac{1}{\varepsilon_{\mathbf{k}} - \varepsilon_d} - \frac{1}{U + \varepsilon_d - \varepsilon_{\mathbf{k}'}} \right) \tag{4.9}$$

If we assume isotropic exchange and potential scattering we can transform Eq. 4.7 (similarily to the BdG formalism, *c.f.* section 3.1.2) to matrix notation with the spinor $\Psi_{\mathbf{k}} = (c_{\mathbf{k}\uparrow}, c_{\mathbf{k}\downarrow})^{\mathrm{T}}$. As we are on a metal (and not on a superconductor), a 2×2 representation is sufficient (no particle-hole, only spin-subspace). The Hamiltonian of Eq. 4.7 then yields:

$$\mathcal{H} = \frac{1}{2} \sum_{\mathbf{k}} \Psi^\dagger_{\mathbf{k}} H \Psi_{\mathbf{k}}, \quad \text{where} \quad H = \left[K\sigma_0 + J\mathbf{S} \cdot \boldsymbol{\sigma} \right], \tag{4.10}$$

where J and K are the isotropic exchange and potential scattering strengths at the impurity site. σ_0 is the identity matrix in spin space and $\boldsymbol{\sigma} = (\sigma_x, \sigma_y, \sigma_z)^{\mathrm{T}}$ denotes the vector of Pauli matrices.

Kondo effect

The exchange scattering J with the continuum electrons gives rise to the so-called Kondo effect which was first theoretically treated by J. Kondo in 1964 [Kon64]. Due to Heisenbergs uncertaincy relation an electron can hop off the impurity into a free substrate level at the Fermi energy for a short time. The empty d level can then be reoccupied by a substrate electron as depicted in the top panel of Fig. 4.2b, thereby effectively inducing a spin-flip of the impurity level. A different scattering process involves the meanwhile doubly occupied d orbital and the removal of the former electron of the impurity (bottom panel). Both virtual processes induce a new many-body ground state in which the spins of the conduction electrons coherently couple to the impurity spin. This coupling is usually antiferromagnetic and thus, the impurity is screened by the bath electrons (Kondo cloud). The correlated state gives rise to the so-called Kondo-resonance at the Fermi energy (*c.f.* Fig. 4.2b) with a characteristic lineshape arising from the interference of the different tunneling paths involving the Kondo cloud and unperturbed substrate electrons [Fan61; THS08]. Its width Γ is a measure of the energy scale of the magnetic interaction and is usually quantified

[3] A detailed deviation can be found in [Hew93].

by the Kondo temperature T_K by $\Gamma = k_\mathrm{B} T_\mathrm{K}$. The Kondo temperature is related to the exchange scattering strength J by [Hew93]

$$k_\mathrm{B} T_\mathrm{K} \propto \sqrt{J} e^{-1/(2J\nu_0)}, \tag{4.11}$$

where k_B is the Boltzmann constant and ν_0 the DOS at the Fermi energy.

4.2 Magnetic impurities on a superconductor - Yu-Shiba-Rusinov states

Equipped with the fundamental understanding of the interaction between magnetic impurities on a metal we can study what happens in the case of a superconducting substrate. Beside the Kondo effect which arises due to the exchange coupling between the impurity and the electron sea, the impurity also couples to the Cooper pair (CP) condensate. As first predicted in the late 1960's by L. Yu, H. Shiba and A. I. Rusinov [Yu65; Shi68; Rus69], a magnetic moment on or in a superconductor induces a local bound state, a so-called Yu-Shiba-Rusinov (YSR) state. Experimentally, YSR states have first been observed using Mn atoms on Nb(110) by [Yaz+97] in 1997.

4.2.1 Derivation of the YSR ground state

If a magnetic impurity is placed on a superconductor, its localized magnetic moment interacts with the CPs of the superconductor. Let us, for simplicity consider a classical spin-$1/2$-impurity (*e.g.* a singly occupied d level of an adatom). Assuming antiferromagnetic exchange, the impurity spin attracts the electron of the CP with opposite spin and repels the second electron of the CP. Hence, the magnetic moment locally reduces the binding energy of the CP creating a localized quasiparticle state - the YSR state - within the superconducting energy gap. Depending on the interaction strength this quasiparticle state can be empty or occupied. This is schematically illustrated in Fig. 4.3a,b.

Treating the impurity classical and assuming antiferromagnetic exchange we can describe the system in real space by the following BdG Hamiltonian in the Nambu space spanned by the 4×4 spinor $\Psi(\mathbf{r}) = \left(\psi_\uparrow(\mathbf{r}), \psi_\downarrow(\mathbf{r}), \psi_\downarrow^\dagger(\mathbf{r}), -\psi_\uparrow^\dagger(\mathbf{r})\right)^\mathrm{T}$ [PGO13; OPP17]:[4]

$$H_\mathrm{BdG} = \xi_\mathbf{k}\, \tau_z + \Delta\, \tau_x + [K\tau_z + J\mathbf{S}\cdot\boldsymbol{\sigma}]\delta(\mathbf{r}) \tag{4.12}$$

This Hamiltonian is simply obtained by combining the BdG Hamiltonians of the s-wave BCS superconductor (Eq. 3.12) and the s-d model (Eq. 4.10). τ_i (σ_i) act on particle-hole (spin) space and $\boldsymbol{\sigma} = (\sigma_x, \sigma_y, \sigma_z)^\mathrm{T}$ denotes the vector of Pauli matrices. $\xi_\mathbf{k} = \varepsilon_\mathbf{k} - \mu$ is the normal electron dispersion and Δ is the isotropic superconducting order parameter. K and

[4] For clarity, if we write down all (redundant) unit matrices, the BdG Hamiltonian reads $H_\mathrm{BdG} = [\xi_\mathbf{k}\,\tau_z + \Delta\,\tau_x + K\delta(\mathbf{r})\,\tau_z] \otimes \sigma_0 + \tau_0 \otimes [J\delta(\mathbf{r})\,\mathbf{S}\cdot\boldsymbol{\sigma}]$.

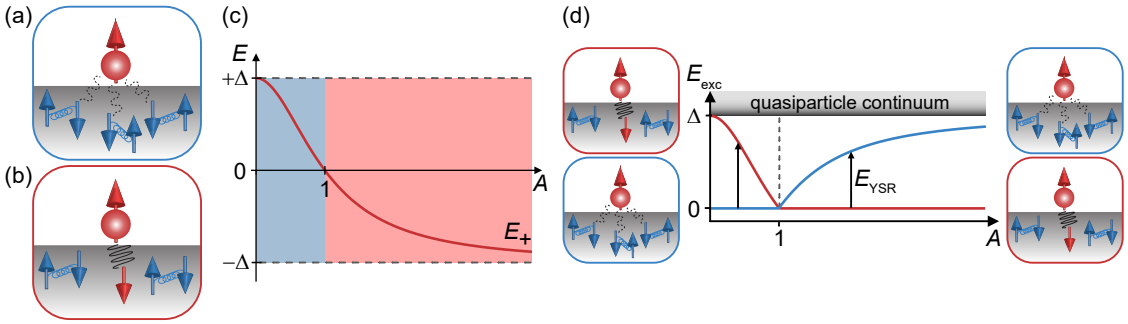

Fig. 4.3.: Schematic illustration of the interaction between a classical spin and the CP condensate. (a) Free-spin regime: the spin-up electron attracts the electrons of the CPs with spin-down while repelling the others. The bound state is unoccupied. (b) Screened-spin regime. The interaction is strong enough to bind one quasiparticle to the impurity. (c) YSR energy as a function of coupling strength $A = \pi\nu_0 JS$. For $A < 1$ (small exchange coupling strength), the bound states energy is above E_F and, hence, is unoccupied corresponding to the situation sketched in (a). At $A = 1$, the energy of the YSR state crosses the Fermi level and the system undergoes a quantum phase transition to a screened-spin ground state ($A > 1$), *i.e.* one quasiparticle is bound to the impurity. (d) Illustration of possible excitations by tunneling with one electron. For $A < 1$ the excitation includes the occupation with a quasiparticle. For $A > 1$ we remove the occupied quasiparticle. Figure taken and adapted from [Far19; Far+18].

J are the (isotropic) potential and exchange scattering strengths. The δ-function restricts the interaction to the impurity site (isotropic point-like scatterer at $\mathbf{r} = 0$).

Choosing the impurity spin to point along the z-axis (*i.e.* $\mathbf{S} \cdot \boldsymbol{\sigma} = S\sigma_z$) separates the above 4×4 Hamiltonian into two independent 2×2 matrices [PGO13],

$$H_{\mathrm{BdG},\pm} = \xi_{\mathbf{k}}\,\tau_z + \Delta\,\tau_x + [K\tau_z \pm JS\tau_0]\,\delta(\mathbf{r})\,, \tag{4.13}$$

for the spin-up and the spin-down subspace which are related by particle-hole symmetry. Focusing on the $\Psi_+ = \left(0, \psi_\downarrow, 0, -\psi_\uparrow^\dagger,\right)^\mathrm{T}$ subspace we can solve the eigenvalue problem for Eq. 4.13 and obtain the following subgap solution [PGO13; OPP17; Rus69]:

$$E_+ = \Delta \frac{1 - A^2 + B^2}{\sqrt{(1 - A^2 + B^2)^2 + 4A^2}}\,. \tag{4.14}$$

Here, A and B are dimensionless parameters for the exchange and potential scattering with $A = \pi\nu_0 JS$ and $B = \pi\nu_0 K$. The corresponding eigenstate at the position of the impurity are found to be [PGO13; OPP17]

$$\Psi_+(\mathbf{0}) = \begin{pmatrix} u(\mathbf{0}) \\ v(\mathbf{0}) \end{pmatrix} = C \begin{pmatrix} \sqrt{1 + (A - B)^2} \\ -\sqrt{1 + (A + B)^2} \end{pmatrix}, \tag{4.15}$$

or in the original four-Spinor representation $\Psi = \left(\psi_\uparrow, \psi_\downarrow, \psi_\downarrow^\dagger, -\psi_\uparrow^\dagger\right)^{\mathrm{T}}$

$$\Psi_+(\mathbf{0}) = C \begin{pmatrix} 0 \\ \sqrt{1+(A-B)^2} \\ 0 \\ -\sqrt{1+(A+B)^2} \end{pmatrix}. \tag{4.16}$$

In the above equations, C is a normalization constant. We note that the bound state consists of an electron and hole component, representing the quasiparticle nature. Fig. 4.3c visualizes the dependence of the corresponding eigenenergy E_+ on the parameter $A = \pi\nu_0 JS$ for $B = 0$. Note that there is no subgap solution for vanishing exchange coupling ($A = 0$). For $A < 1$, *i.e.* small exchange coupling J, the ground state is empty (blue region) and no quasiparticle is bound to the impurity, called *free-spin* regime (Fig. 4.3a). At a critical exchange coupling J_c ($A = 1$) the energy crosses zero. The system changes its ground state from even to odd parity to the so-called *screened-spin* regime, in which the YSR state is occupied by a quasiparticle for $A > 1$ (red region, Fig. 4.3b,c). In other words, the interaction between impurity and CPs is strong enough to bind a quasiparticle to the impurity.

When investigating such a system with STM, we do not probe the ground state. Instead, we excite the system by tunneling with single electrons. As depicted in Fig. 4.3d the excitation involves the creation of the quasiparticle in the free-spin regime, while the quasiparticle is annihilated by the excitation in the screened-spin regime. Hence, single-electron tunneling changes the parity of the system from odd to even or vice versa (depending on the ground state). Because the YSR state has both, a hole-like and an electron-like component, we detect such excitation processes as two peaks at $\pm E_\mathrm{YSR}$. Thus, we cannot directly determine the ground state of the system (free-spin or screened-spin). The potential scattering strength B induces an asymmetry between electron and hole components, such that the resonances at $\pm E_\mathrm{YSR}$ do in general have different spectral weight, *i.e.* asymmetric intensities.

The quantum phase transition (QPT) was observed in various STM studies [FSP11; Hat+15; Far+18; Mal+18; Hua+20; Odo+20; Cha+21] in which variations of the coupling strength between impurity and substrate leads to the zero-energy crossing.

4.2.2 Spatial extent of the YSR wave functions

The full spatial extent of the electron- and hole-components of the YSR wave functions depends on the dimensionality of the substrate. By introducing $\tan\delta^\pm = (K\nu_0 \pm JS\nu_0)$ the YSR energy can be written as $E_\mathrm{YSR} = \Delta\cos(\delta^+ - \delta^-)$. In the continuum limit (*i.e.* fully isotropic environment) the YSR wave functions can be evaluated to be [Mén+15; Rus69]

$$u(r), v(r) = \frac{1}{\sqrt{N}k_\mathrm{F}r}\sin(k_\mathrm{F}r + \delta^\pm)e^{-\Delta\sin(\delta^+-\delta^-)r/\hbar v_\mathrm{F}}\ (\mathrm{3D}) \tag{4.17}$$

for three-dimensional substrates, and

$$u(r), v(r) = \frac{1}{\sqrt{N\pi k_{\mathrm{F}} r}} \sin(k_{\mathrm{F}} r - \frac{\pi}{4} + \delta^{\pm}) e^{-\Delta \sin(\delta^{+} - \delta^{-}) r / \hbar v_{\mathrm{F}}} \text{ (2D)} \tag{4.18}$$

for two-dimensional substrates. N is a normalization factor. Independent of the dimensionality, the YSR wave functions have oscillatory character which is determined by the Fermi wave vector k_{F}. The exponential decay is mainly governed by the superconducting coherence length as it is defined by $\zeta_0 = \frac{\hbar v_{\mathrm{F}}}{\pi \Delta}$ [Tin04; GM12]. In general, electron- and hole-components oscillate with different phases. In tunnel experiments we observe this spatial extent of the electron- and hole- components ($|u|^2$ and $|v|^2$) at opposite bias polarities.

The important difference between 2D and 3D substrates is that the YSR wave function decays (beside the exponential part) with $1/r$ for 3D, while it is decreases with $1/\sqrt{r}$ in the case of 2D materials. Hence, the YSR states on 2D materials are more extended than in 3D superconductors. Indeed, buried Fe impurities in $NbSe_2$ showed extreme long-ranged YSR wave functions in the order of tens of nanometers [Mén+15]. Hence, due to its strong 2D electronic character, $NbSe_2$ is a very promising candidate to study the interaction between YSR wave functions in larger magnetic structures as will be addressed in detail in chapters 5 and 6.

In the above calculations an isotropic scattering environment was assumed. In real materials, the geometry of the long-range decay of the YSR wave function is governed by the anisotropy of the Fermi surface [SBS97; FB97]. Experimentally, this was observed, *e.g.* for Mn impurities on Pb(111) surface [Rub+16] or for buried Fe impurities in $NbSe_2$ [Mén+15] where the observed YSR wave functions reflected the threefold and sixfold geometries of the Fermi surface, respectively.

Besides the impact of the Fermi surface which mainly governs the long-range oscillations the geometry of the orbital hosting the spin can affect the spatial appearance of the YSR wave function. Various studies observed the presence of multiple YSR states (*e.g.* [Ji+08; Rub+16; Cho+17a]) being related to the orbital structure of the impurity. Transition metals can have several singly occupied d levels which are split in energy due to the local crystal field (partially) lifting the degeneracy (*c.f.* section 4.1.1). This in turn yields orbital-dependent potential and exchange coupling strengths, which are imprinted on the YSR states [Moc+08]. The orbital character mainly influences the YSR wave function in direct vicinity of the impurity.

Another reason for the presence of multiple YSR peaks is magnetic anisotropy in systems with $S \geq 1$ which energetically splits the different spin projections along the z-axis as introduced in section 4.1.1. As this energy splittings are usually in the order of $\sim \mathrm{meV}$ there can be several excitation channels of one YSR state within the SC energy gap involving different spin projections S_z. Magnetic anisotropy split YSR excitations have been theoretically studied in [ŽBP11] and experimentally observed in MnPc molecules

on Pb(111) [Hat+15]. The YSR wave functions of such multiplets should exhibit similar patterns (neglecting spin-orbit coupling) [OF21].

After setting the theoretical framework we can now move on to experimental findings of single Fe atoms on $NbSe_2$ in the remainder of the chapter.

4.3 Adsorption of Fe atoms on $2H$-$NbSe_2$

Figure 4.4a shows an atomic resolution STM topography of a clean $NbSe_2$ surface after deposition of Fe atoms. In order to study single magnetic impurities we evaporate a dilute coverage of Fe atoms of approximately $100\,\mathrm{atoms}/(100 \times 100\,\mathrm{nm}^2)$ directly into the STM at temperatures below $12\,\mathrm{K}$ (*c.f.* section 2.3.3). With such a preparation, we find two stable species of Fe atoms with different apparent heights. One atom of each species appears in the topography in Figure 4.4b. The corresponding height profiles can be found in Fig. 4.4d exhibiting apparent heights of $\approx 140\,\mathrm{pm}$ and $\approx 100\,\mathrm{pm}$ for the large and small species, respectively.

In order to identify the precise adsorption sites we overlay atomic grids on various atomic-resolution STM images. An example is shown in Fig. 4.4c which is the same image as in (b) with a reduced z-scale in order to resolve the atomic background (the surface Se atoms are located on intersections of the gray grid). We find that all Fe atoms are adsorbed in hollow sites of the terminating Se layer (HC or MC as introduced in section 3.2.1, see also Fig. 4.4e) as indicated by the colored triangles (pointing in different directions). One species is reliably found in one type of hollow sites while atoms of the other species always sit on the other. Refering back to section 3.2.1 we know that the CDW maxima do not coincide with MC sites [GOY19; Gus+19]. As we find Fe atoms with low apparent height coinciding with maxima and minima of the CDW we identify these to be adsorbed in HC sites. Examples of HC atoms located on a maximum and minimum of the CDW will be extensively discussed later in this chapter along with Fig. 4.6 (atoms labeled with I and III). Consequently, we identify the large species to be adsorbed in MC sites.

Low-energy constant-height $\mathrm{d}I/\mathrm{d}V$ spectra recorded on the two atoms of Fig. 4.4b (blue, red) can be found in Fig. 4.5a (substrate in black). The tip energy gap is indicated in gray. For both species the data reveal multiple intense YSR resonances with energies ranging from deep within the superconducting energy gap of the substrate up to energies within the range of the coherence peaks. The presence of YSR multiplets presumably originates from several singly occupied d orbitals exhibiting different exchange- and potential-scattering strengths with the substrate [Rub+16; Cho+17a] and is further addressed in section 4.5. Note that there are resonances within the tip energy gap (gray shaded area). These can be attributed to the excitation of thermally occupied YSR resonances (see Appendix A.3.1 or [Rub+15c] for an extensive study). Their intensity scales with their energy, being most intense for resonances at the Fermi level. The strong negative differential conductance (NDC) present at the high-bias flank of some YSR resonances can be explained by the

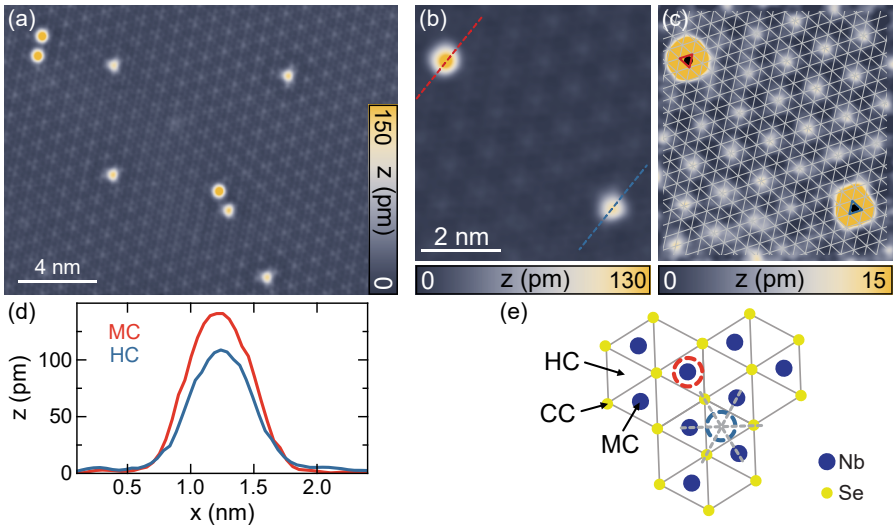

Fig. 4.4.: (a) Atomic-resolution STM image showing the surface after deposition of Fe atoms (constant-current set point: $100\,\mathrm{pA}, 10\,\mathrm{mV}$, recorded with a Nb tip). (b,c) Topography showing two adatoms in different crystalline adsorption sites with different z-scales (set point: $200\,\mathrm{pA}, 4\,\mathrm{mV}$, recorded with a Pb tip). In (c), the atomic lattice of the top Se layer is overlaid in gray (Se atom at intersections). Blue (red) triangles indicate a HC (MC) adsorption site and black dots mark the atoms' center. (d) Line profiles across the atoms shown in (b). (e) Top view of $2H$-$NbSe_2$, with different lattice sites labeled as HC, CC and MC. Gray dashed lines indicate mirror axes (exemplary shown for a HC site).

convolution of the superconducting DOS of tip and sample leading to the observed negative $\mathrm{d}I/\mathrm{d}V$ signal when energetically sharp resonances are probed (*c.f.* section 2.2.2).

Data of the higher energy ranges can be found in Fig. 4.5b,c. Possible d levels of each species are indicated with colored arrows. Resonances found at positive bias presumably originate from tunneling via empty or half filled d orbitals ($\varepsilon_d + U > E_\mathrm{F}$, *c.f.* section 4.1.2). Peaks at negative energy belong to filled or half filled d levels. We note that the two species differ in their d level resonances. The adsorption sites of both species are identified as MC and HC sites and therefore differ in the presence or absence of a Nb atom beneath. Therefore, they sense a different crystal field leading to a different energy splitting of the d-block as discussed in section 4.1.1 [Jea05].

The Fe atoms are presumably in a high-spin configuration ($S = 2$) [Yan+20] in agreement with the number of YSR resonances as we discuss in more detail in section 4.5. Therefore, we expect - depending on the degree of degeneracy of the d levels - at least three resonances at $V > 0$ and up to five at $V < 0$ (*c.f.* Fig. 4.1c-e). At $V < 0$ we identify one resonance for MC atoms and two resonances for HC atoms. It is possible that resonances at negative biases are not detected as they strongly hybridize with the filled substrate bands inducing substantial broadening. For $V > 0$ we detect three resonances for MC atoms and four resonances for HC atoms. Slight changes in the adsorption geometry of a few pm can lift the remaining degeneracy of the d levels in the crystal field (*c.f.* Fig. 4.1c-e). In $NbSe_2$, lattice distortions induced by the CDW which lie in the order of a few percent of the undistorted lattice [MK13; Zhe+18; LSD18] could further reduce the

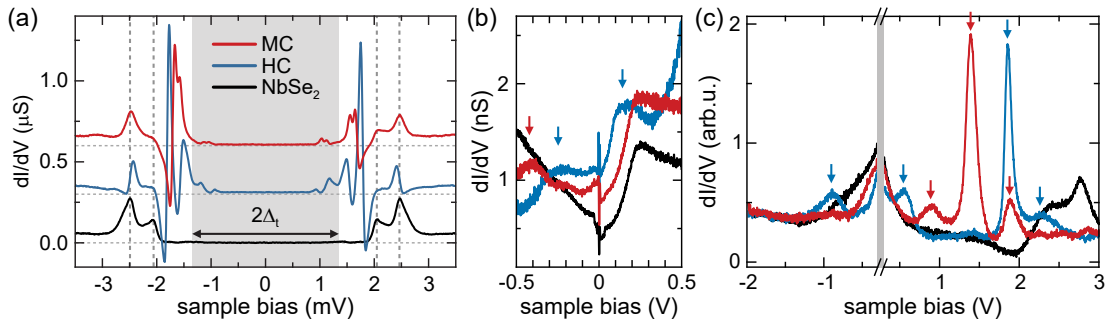

Fig. 4.5.: (a) Constant-height $\mathrm{d}I/\mathrm{d}V$ spectra taken on the substrate (black) and on the atoms shown in Fig. 4.4b (set point: $200\,\mathrm{pA}, 4\,\mathrm{mV}$; $V_{\mathrm{rms}} = 15\,\mu\mathrm{eV}$, spectra offset by $0.3\,\mu\mathrm{S}$). $2\Delta_{\mathrm{t}}$ is indicated by the shaded area. (b) Constant-height spectra (set point: $500\,\mathrm{pA}, -0.5\,\mathrm{V}, V_{\mathrm{rms}} = 2\,\mathrm{mV}$) of $NbSe_2$ (black) and on Fe adatoms in a HC (blue) and a CC (red) site. (c) Constant-current spectra ($100\,\mathrm{pA}, V_{\mathrm{rms}} = 5\,\mathrm{mV}$) of $NbSe_2$ (black) and on Fe adatoms in a HC (blue) and a CC (red) site.

trigonal symmetry of the HC sites yielding more than three d level resonances at $V > 0$. In agreement with the findings at higher energies, the presence of multiple YSR states also suggests several singly occupied d orbitals.

While the signal probed in the higher energy ranges (Fig. 4.5b,c) exhibits only minor differences within atoms of one type, the YSR states differ strongly across atoms of the same species, even though they sit on equal crystalline adsorption sites. This can be linked to the local variations of the DOS imposed by the CDW and will be addressed in detail in the following section. The exact number of YSR resonances is addressed further in section 4.5.

4.4 Influence of the CDW on YSR states

Results presented in this section were achieved in collaboration with S. Acero González and F. von Oppen who performed the theoretical modeling and are published in [Lie+20]. The author of this thesis was involved in the experimental part. Results with focus on the theoretical work are further published in the dissertation of S. Acero González [Ace20].

As already mentioned above, HC adatoms can coincide with CDW maxima and minima while this is not possible for MC adatoms as the CDW avoids MC domains. Therefore, we focus on HC adatoms in order to elucidate the role of the CDW on the YSR states. MC atoms will be addressed in section 4.6.

Topographies of six different Fe atoms labeled with I-VI all adsorbed on a HC site can be found in Fig. 4.6a. The z-range is chosen such that the atomic background is resolved. Note already, that the CDW is in the HC phase (CC phase) for atoms I,III and VI (II,IV and V) as can be discerned in the atomic background. Thus, even though atoms I-VI are all adsorbed in equivalent atomic lattice sites they can differ in their position relative to the CDW.

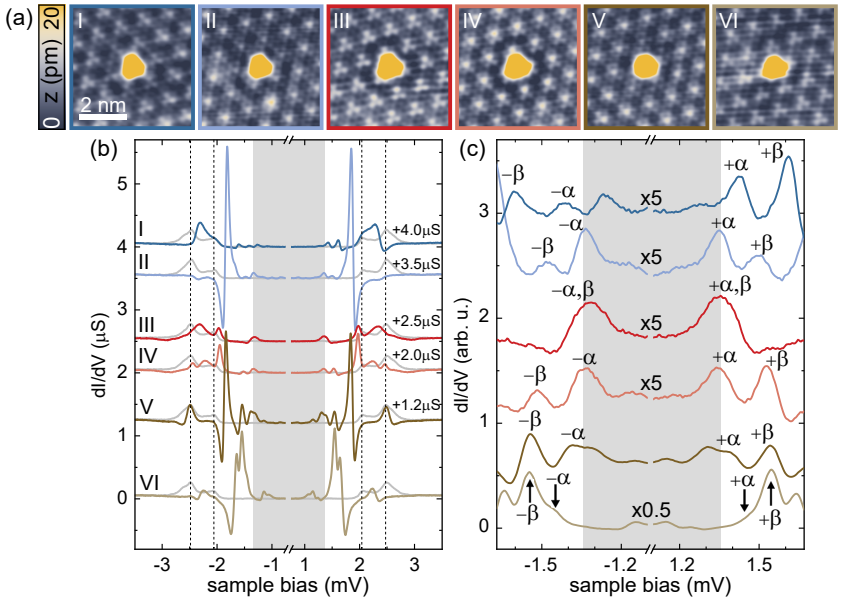

Fig. 4.6.: (a) Constant-current STM images of several HC Fe atoms labeled by I-VI. The z-scale is reduced in order to resolve the atomic background (set point: $200\,\mathrm{pA}, 4\,\mathrm{mV}$). (b) Constant-height $\mathrm{d}I/\mathrm{d}V$ spectra taken at the center of atoms I-VI (color) and on the substrate (gray). Spectra offset as indicated (set point: $200\,\mathrm{pA}, 4\,\mathrm{mV}; V_{\mathrm{rms}} = 15\,\mu\mathrm{eV}$). The Pb tip gap is indicated in gray. (c) Close-ups of the spectra in (b). YSR resonances are labeled by $\pm\alpha, \pm\beta$. Some spectra are scaled up/down in intensity as indicated.

For all HC atoms, low-energy spectroscopy reveals the presence of several YSR resonances with their energies ranging from deep within the gap up to the substrate's coherence peaks. Interestingly, we find rich differences in energy and intensity of the YSR resonances found on the different atoms (Fig. 4.6b). YSR resonances that fall in the range of the superconducting coherence peaks are rather broad and short-ranged and are thus hard to disentangle from the background (*c.f.* section 4.5 and [Sen+19]). We therefore focus on the two low-energy YSR resonances which are found deep inside the superconducting energy gap on all atoms. They are labeled as α- and β-states in Fig. 4.6c which is a low-energy zoom of Fig. 4.6b. Note that the α- and β-resonances exhibit their main intensity away from the atoms' center and thus appear with rather low intensity in the spectra taken on the atoms' center (Fig. 4.6b,c). In order to gain insight into the YSR wave functions we examine $\mathrm{d}I/\mathrm{d}V$ maps (Fig. 4.7a) of the β- and α-states of atoms I-VI in the top and bottom panel, respectively. Scale-ups ($2 \times 2\,\mathrm{nm}$) of the atoms' center can be found in the bottom right of each map. All maps show a long-range (several nm) oscillatory decay of the YSR wave functions which is associated with the Fermi wavelength and the shape of the Fermi surface (*c.f.* Fig 3.7b) as introduced in section 4.2.2. In detail, the electrons/holes scattered at an impurity are focused into directions, which originate from flat parts of the Fermi surface [Wei+09] leading to beam-like patterns reflecting the symmetry of the Fermi surface [Mén+15]. The short-range pattern ($\sim 1\,\mathrm{nm}$, insets) is expected to be dominated by the geometry of the crystal-field split d orbitals [Rub+16; Cho+17a]. Therefore, considering the sixfold symmetry of the Fermi surface and the

threefold symmetric adsorption site we expect D_3-symmetry (3-fold rotational and mirror symmetry) for adatoms located on both hollow sites as indicated in Fig. 4.4e exemplary for a HC site by the gray dashed lines.

4.4.1 CDW-induced symmetry reduction

Comparing the YSR patterns of the different atoms one realizes that they obey different degrees of symmetry. The α- and β- maps of atom I and III show three mirror axes with the predicted orientation (the directions of the lattice symmetry axes are indicated as gray dashed lines in the bottom panel for each atom). On the contrary, the symmetry, both in the direct vicinity and in the long-range oscillations is reduced to one-fold symmetry (D_1, one rotation and mirror axis) for atoms II, IV and V. Here, the single mirror axis present in the $\mathrm{d}I/\mathrm{d}V$ data is indicated by the thick axis while the remaining two crystal symmetry axes are plotted as thin lines. On atom VI no symmetry is observed neither in the direct vicinity of the atom nor in the long-range decay. In order to identify the origin of the observed symmetry reductions we study the location of the six atoms with respect to the CDW as this is their main difference.

Figure 4.8a contains the same topographies as already presented in Fig. 4.6a. The red cross indicates the center (maximum of the atoms, placed with a different z-scale, not shown) of each atom. The black grids illustrate the CDW „lattice“ with gray (black) dots indicating maxima (minima) of the CDW. Atom I (atom III) coincide with a CDW maximum (minimum). For these positions, the CDW respects the atomic D_3-symmetry (indicated by white dashed lines) in agreement with the symmetry observed in the $\mathrm{d}I/\mathrm{d}V$ maps. All other atoms are not located on such a high symmetry point. By close inspection of Fig. 4.8a one remaining symmetry axis relative to the CDW grid can be discerned for atoms II,IV and V and is indicated by the white dashed lines. Again, the orientation of the mirror axis found in the $\mathrm{d}I/\mathrm{d}V$ maps exactly matches the prediction from the topographies. For atom VI no symmetry is found in the maps in accordance with Fig. 4.8a. Concluding, the detected degree of symmetry agrees with the symmetry of the adsorption sites relative to the CDW.

One can now classify all HC sites regarding their different positions relative to the CDW which is schematically depicted in Fig. 4.8b. This classification will be important thoughout the thesis as the CDW also affects the hybridization of YSR states as we will see in chapter 5. As in Fig. 4.8a the CDW is illustrated by the black grid with gray (maxima) and black (minima) dots. Additionally, the Se atoms of the surface are indicated by the gray grid (Se atoms located on the intersections), where triangles pointing upwards (downwards) represent HC (MC) sites. The top panel shows the HC structure of the CDW, *i.e.* the CDW maxima/minima are aligned with atomic HC sites. The high symmetry HC sites are indicated in dark blue/red in agreement with the coloring of atom I and III. All sites marked in bright brown exhibit no symmetry with respect to the CDW lattice as atom VI. Note, that there is a third site with expected D_3-symmetry (uncolored). However, we do

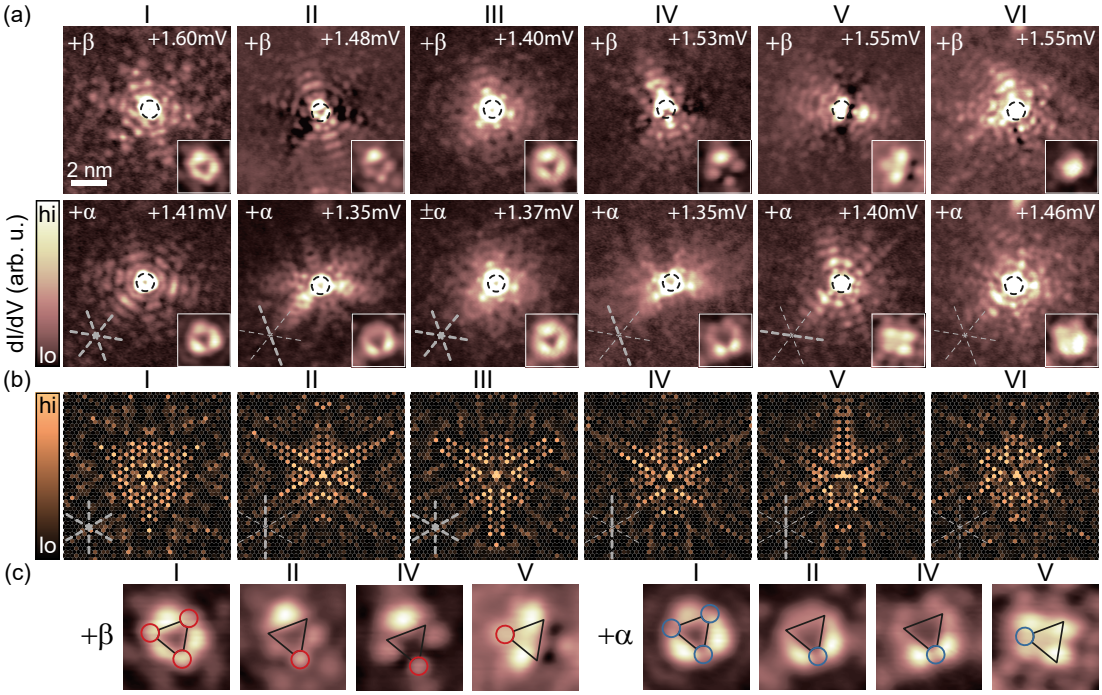

Fig. 4.7.: Constant-contour $\mathrm{d}I/\mathrm{d}V$ maps of the YSR (α-,β-) states of HC atoms I-VI (set point: $200\,\mathrm{pA}, 4\,\mathrm{mV}; V_{\mathrm{rms}} = 15\text{-}25\,\mu\mathrm{eV}, V_{\mathrm{bias}}$ as indicated). Black dashed circles (diameter $1\,\mathrm{nm}$) outline the atoms' position. The insets show a $2 \times 2\,\mathrm{nm}$ close-up view around the center of the atoms. Thick (thin) gray lines in the maps indicate the presence (absence) of mirror axes. On atom III, α- and β-states overlap; on atom VI there is no symmetry. Data of thermal resonances and the other bias polarity can be found in Figs. A.3 and A.4. (b) Numerical results of the electronic probability density $|u(\mathbf{r})|^2$ of the YSR state in the presence of the CDW potential for band 2 for adatoms located at positions equivalent to those of atoms I-VI (field of view: $40a \times 40a$ around the atom). The parameters are $JS/2 = 120\,\mathrm{meV}, K = 0, V_0 = 30\,\mathrm{meV}$. (c) Close-up views of the α- and β-states around the center of the atoms I, II, IV, and V with superimposed triangles illustrating the presence (red circles) and absence (blue circles) of intensity at their vertices.

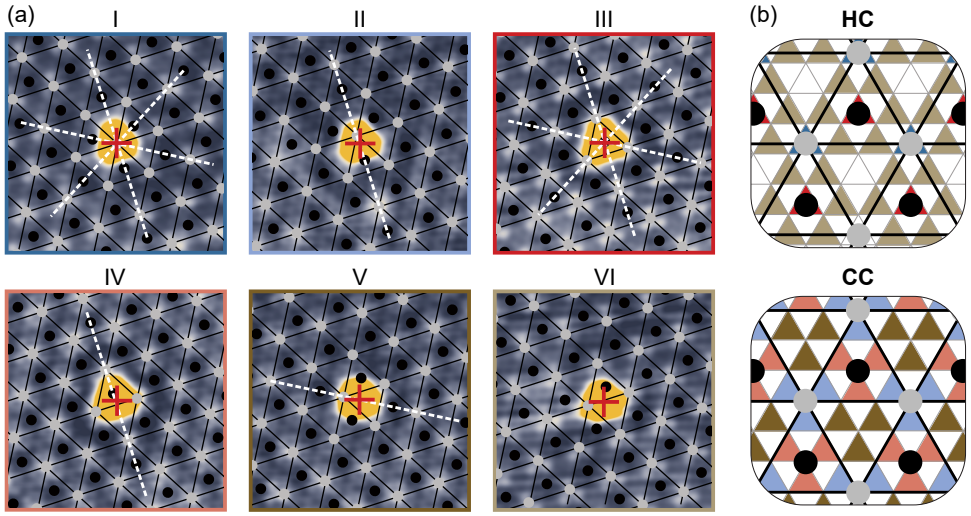

Fig. 4.8.: (a) Same topographies as in Fig. 4.6a. The CDW is depicted by the black grid, where gray (black) dots indicate CDW maxima (minima). The center of each atom is marked by the red cross. The from the position of the atoms' center relative to the CDW grid expected symmetry axes are indicated by the white dashed lines. (b) Sketch of the different possible adsorption sites of HC adatoms for the two CDW structures (HC and CC). The CDW grid is the same as in (a), *i.e.* maxima (minima) as gray (black) dots. Additionally, the Se grid is overlaid in gray (Se atoms located at vertices of the triangles). The HC (MC) adsorption sites correspond to triangles pointing up (down). Colors indicate different adsorption sites (chosen such that they indicate the positions of atoms I-VI) relative to the CDW.

not find Fe atoms adsorbed in this third symmetric site.[5] The bottom panel contains the same grids, but illustrates the CDW CC structure where the maxima/minima coincide with Se atoms. All adsorption sites are located on one of the symmetry axis of the CDW (*i.e.* obey one-fold symmetry) and differ by their exact location within the CDW lattice. All bright blue (bright red) HC sites are situated $a/\sqrt{3}$ apart from a CDW maximum (minimum). The dark brown sites are located close to $(a/\sqrt{3})$ the local minimum of the CDW. Again, the colors are chosen such to reflect the adsoprtion sites of atoms II, IV and V. Remember, that the CDW maxima/minima are not found on MC sites (MC structure of the CDW is not observed in experiment, see section 3.2.1). Furthermore, the CDW varies smoothly across the surface transforming between the HC and the CC structure which will become important later in this section. Therefore, the six sites discussed here are limiting cases appearing in regions with pure HC and CC CDW structure.

Summarizing so far, the symmetry reduction of the YSR wave function observed in experiment can be linked to the position of the atoms relative to the CDW which breaks the

[5] The CDW varies smoothly between the HC and CC structure across the surface as they are energetically very similar [Gus+19; GOY19; Cos+18; LSD18]. Hence, Fe atoms are found in a broad range of positions relative to the CDW. As discussed in great detail in this section, the CDW affects the YSR states. On the other hand it is known that the CDW can be pinned/influenced by defects [Cos+18; Lan+14; FW15; Cha+15; Arg+14]. We can also flip/switch the phase of the CDW - especially in areas high density of intrinstic defects - by manipulation of Fe atoms with the tip to a different energetically similar configuration. Hence, the Fe atoms (being surface defects) also affect the CDW to some extent. Attempts to place an Fe atom in this third symmetric HC site always induces a local switch of the CDW phase.

D_3-symmetry expected for adsorption in HC lattice sites. In the following section we will introduce a theoretical model capturing the microscopic origin behind these findings.

4.4.2 Modeling the role of the CDW

The microscopic origin behind these findings can be modeled within a phenomenological mean-field description of the CDW incorporated in the classical YSR model (*c.f.* Eq. 4.12) foregoing a realistic description of the d level physics. The essentials of the substrate's band structure are covered within a tight-binding model of $NbSe_2$. Thus, the model aims at a qualitative understanding of the microscopic physics rather than a quantitative comparison to the experiment. The basic aspects of the model will be outlined in the following. A more complete elaboration can be found along with [Lie+20] and also in the PhD thesis of S. Acero González [Ace20], who was carrying out all calculations.

The $NbSe_2$ is described within an effective tight-binding model following [SKD85; Ros+05; Ino+08; Ino+09; Rah+12; Mén+15]. As the relevant states near the Fermi energy have mostly Nb character, the Se-derived band around the Γ-point is neglected reducing the band-structure problem to the triangular Nb sublattice. Focusing on one d orbital per Nb atom and including hopping up to five nearest neighbors reproduces the band structure symmetries and the approximate shape of the Fermi surface and hence, captures the essential physics of $NbSe_2$ (two Nb derived bands forming the two paired cylinders around the K- and Γ-points of the Fermi surface, *c.f.* section 3.2.2). The model neglects intralayer couplings making it purely two-dimensional. Considering the strong 2D electronic character of $2H$-$NbSe_2$ and the fact that the Fe predominantly couples to the top layer, the simplified model should still capture all relevant physics in order to give a qualitative understanding of the involved processes.

Superconductivity is included by the usual BdG Hamiltonian (*c.f.* Eq. 3.12) assuming isotropic s-wave pairing of $\Delta = 1\,\mathrm{meV}$ which is not capturing the strongly anisotropic nature of $NbSe_2$, but, as we focus on the low-energy YSR states this simplification should again be fair enough to provide qualitative insights.

As previously used in [Mén+15], the YSR states in $NbSe_2$ are considered by treating the magnetic impurity as classical spin S interacting with the substrate electrons via the (isotropic) exchange interaction $JS\sigma_z/2$ and the (isotropic) potential scattering K. As we consider Fe atoms in HC sites, the impurity possesses equal hopping amplitudes to its three Nb neighbors. Furthermore, it is necessary to consider non-local exchange coupling between the three Nb sites in order to obtain only one YSR state per impurity. Assuming equal hopping amplitudes and the impurities spin aligned along the z-direction yields

$$\mathcal{H}_{\mathrm{YSR}} = -\frac{JS/2}{3}\sum_{i,j}\sum_{s,s'} c^\dagger_{is}\sigma^z_{ss'}c_{js'} + \frac{K}{3}\sum_{i,j}\sum_{s} c^\dagger_{is}c_{js}\,, \tag{4.19}$$

which includes exchange and potential scattering terms. The sums over i and j run over the three nearest-neighbor Nb sites of the impurity, σ^z denotes a Pauli matrix, and $c_{is}^\dagger$ (c_{is}) creates (annihilates) an electron on site i with spin s.

Finally, we need to find a way to account for the CDW. The CDW in $NbSe_2$ manifests as tiny lattice distortions (*c.f.* section 3.2.1). Hence, the CDW sets an additional periodic potential which couples to the electrons via electron-phonon interaction. Therefore, we can incorporate the CDW by a small additional modulation of the on-site potential

$$\mathcal{H}_{\mathrm{CDW}} = \sum_{\mathbf{r},\sigma} c_{\mathbf{r}\sigma}^\dagger V(\mathbf{r}) c_{\mathbf{r}\sigma} \,, \tag{4.20}$$

where the sum runs over the Nb lattice sites of the triangular lattice. The CDW potential is described by

$$V(\mathbf{r}) = V_0 \sum_{i=1,2,3} \cos(\mathbf{Q}_i \cdot \mathbf{r} + \phi_i), \tag{4.21}$$

where the $\mathbf{Q_i}$ (ϕ_i) are the CDW wave vectors (phases) in real space (see below) and V_0 denotes the amplitude of the CDW potential. In order to reproduce the CDW's symmetry and shape, one possible choice of the phases ϕ_i is $\phi_1 = \phi_2 = 0$ and $\phi_3 = \pi/3$. An appropriate set of wave vectors is given by

$$\begin{aligned} \mathbf{Q}_1 &= q(1-\delta)(\sqrt{3}/2, -1/2), \\ \mathbf{Q}_2 &= q(1-\delta)(0, 1), \\ \mathbf{Q}_3 &= q(1-\delta)(-\sqrt{3}/2, -1/2) = -(\mathbf{Q}_1 + \mathbf{Q}_2), \end{aligned} \tag{4.22}$$

where $q = \frac{4\pi}{\sqrt{3}\,3a}$ and $\delta \ll 1$ accounts for the fact that the CDW is not exactly commensurate with the lattice.[6] The length of the (commensurate) wave vector q is achieved using $q = \frac{2\pi}{\lambda_{\mathrm{CDW}}}$ and $\lambda_{\mathrm{CDW}} = \frac{\sqrt{3}}{2} 3a$ (a is the lattice constant).[7]

Numerical results showing the electronic probability density $|u(\mathbf{r})|^2$ of the YSR state in the presence of the CDW are displayed in Fig. 4.7b for different positions relative to the CDW according to those of atoms I-VI. The displayed result is achieved by considering scattering with one Nb band only (see [Lie+20; Ace20] for results of the other band). The results obtained considering the other Nb band yield qualitatively similar results, although details of the band structure (*e.g.* anisotropic character) affect the YSR wave functions. In any case, the effect of the CDW potential on the symmetries of the YSR wave functions should be captured correctly. Indeed, we find that positions I and III exhibit D_3-symmetry. For positions II,IV and V we find one symmetry axis while no symmetry is left for position VI, in agreement with the experiment. Note that the theoretical plots are rotated differently than the $\mathrm{d}I/\mathrm{d}V$ maps in Fig. 4.7a, the symmetry axes are indicated in gray. Again, thick (thin) lines denote the presence (absence) of symmetry in the probability density plots.

[6] The periodicity of the CDW is $\gtrsim 3a$ yielding a slightly reduced wave vector.
[7] $a_{\mathrm{CDW}} \gtrsim 3a$ and λ_{CDW} are indicated in Fig. 4.9a (left panel).

Concluding, the CDW can be modeled by an additional periodic potential included in a simple tight-binding model of $NbSe_2$ in combination with a classical magnetic impurity reproducing the symmetry-reduction observed in the experiment.

4.4.3 Effect on the YSR energies

Up to now we understand how the CDW reduces the symmetry of the YSR wave function. However, we find that atoms I-VI - beside their different degrees of symmetry - further differ in the energies at which the YSR resonances are probed (Fig. 4.6b,c). So far the α- and β-states were simply assigned to the two resonances lowest in energy. In the following we track their energetic evolution by analyzing similarities in their wave function patterns. Note that the strong locally variating NDC complicates the assignment. In particular, the β-maps of atoms II, IV and V are strongly affected by the NDC of the energetically close α-resonances. We thus focus on the direct vicinity around the atoms' center (close-ups of both states around the center of atom I,II,IV and V in Fig. 4.7c). Starting with atom I we find that both, the α- and β-state, are characterized by a triangular pattern with three intense lobes at its sides. However, the β-resonance additionally exhibits intensity at its vertices (red circles) while the α-state does not (lack of intensity in blue circles). Fingerprints of these characteristics are also present in the reduced symmetry cases of atoms II,IV and V. Among them, we find enhanced intensity in at least one of the three vertices for the β-state (red circles) while the α-state still lacks intensity at all vertices (blue circles). Note that both resonances overlap at zero energy for atom III (*c.f.* dark red data trace in Fig. 4.6c) and hence, the $\mathrm{d}I/\mathrm{d}V$ maps cannot be interpreted individually (in terms of seperate α- and β-wave functions) in this case.

The above identification of the α- and β- states is further supported by the similarity found across the $\mathrm{d}I/\mathrm{d}V$ images of the thermally activated duplicates (at energies within the tip energy gap) which are less affected by NDCs. Extensive data and discussion can be found in the Appendix A.3.1. With the above assignments we can now track the energy of the α- and β-excitations along the CDW. Remember, as the CDW transforms smoothly between the HC and CC structures we can find adatoms covering a broad range of positions relative to the CDW (adsorption sites in between the ones of atoms I-VI).

Therefore, we analyze more than 90 different HC atoms (acquired across several sample/tip preparations) which are adsorbed along (or close to) a symmetry axis. One complete period of the CDW along one symmetry axis (with length $2\lambda_{\mathrm{CDW}} = \sqrt{3}\,a_{\mathrm{CDW}}$, *c.f.* Eq. 4.22) is indicated in Fig. 4.9a (left panel) in yellow starting at a maximum, reaching a minimum at $2/3\lambda_{\mathrm{CDW}}$ and a local minimum at $4/3\lambda_{\mathrm{CDW}}$. The center of the Fe atoms along the symmetry axis can be determined from the STM images (see superimposed CDW grid on the STM topographies in Fig. 4.8a). The error in finding the position relative to the CDW is estimated to be $\delta x = \pm 0.05\lambda_{\mathrm{CDW}}$, which accounts for the inaccuracy in placing the CDW grid and finding the center of the atom as well as possible drift effects.

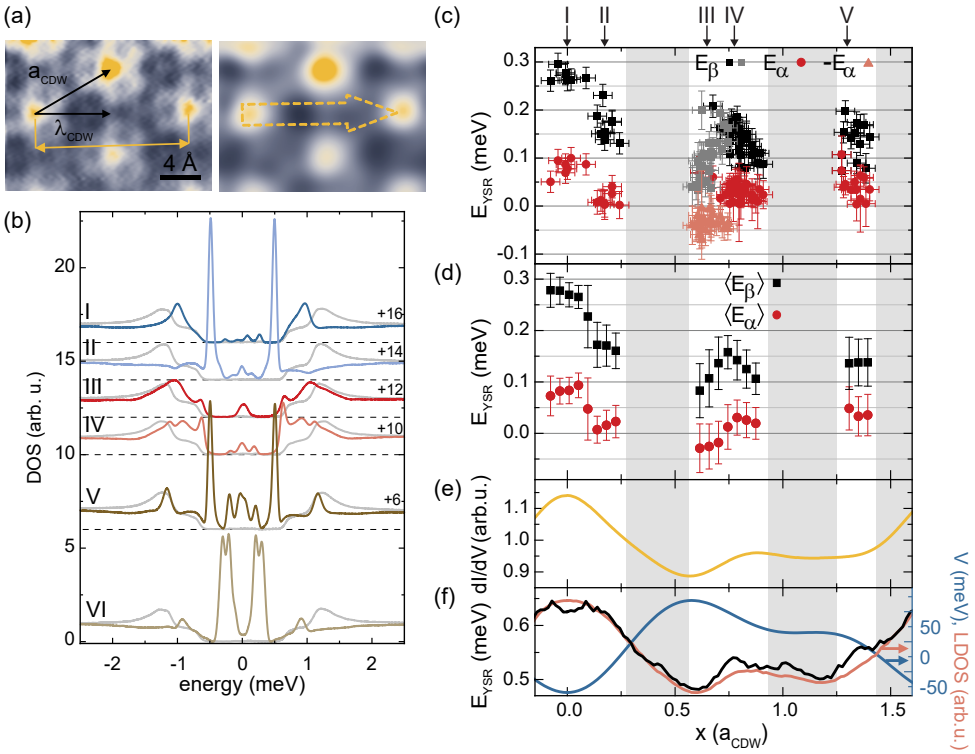

Fig. 4.9.: (a) Constant-height $\mathrm{d}I/\mathrm{d}V$ map recorded at $T = 8\,\mathrm{K}$ and $V_{\mathrm{bias}} = 0\,\mathrm{mV}$ (set point: $200\,\mathrm{pA}, 4\,\mathrm{mV}$; $V_{\mathrm{rms}} = 100\,\mu\mathrm{eV}$; some z-drift is visible). a_{CDW}, λ_{CDW} and one complete period along one symmetry axis of the CDW are indicated with the black and yellow arrows, respectively. The right panel shows the FFT-filtered data of the left panel. (b) Deconvolved data of atoms I-VI (substrate data is shown in gray). Offsets are indicated on each trace. (c) Evolution of YSR excitation energies E_α and E_β of approximately 90 atoms with position relative to the CDW (measured on several samples with several Pb tips) obtained by fitting the deconvolved spectra as described in the text. Error bars are also discussed in the text. Black and gray show the evolution of E_β. Dark and bright red data points correspond to E_α. For the bright red data points a negative E_α is assumed as the excitation changes bias side. Corridors with no data points are marked in gray. (d) Evolution of the α- and β-YSR energy obtained from averaging the the data from (c) within intervals of $\pm 0.05\lambda_{\mathrm{CDW}}$. Error bars include standard deviation from the averaging method and experimental errors from (c). (e) Linecut along the yellow-dashed arrow in the right panel of (a). The signal is averaged over the radius of influence ($125\,\mathrm{pm}$ corresponding to one covalent radius of Fe). (f) Calculated CDW potential (blue), local DOS (bright red), and YSR excitation energies (black) using the tight-binding model discussed in the text for $JS/2 = 360\,\mathrm{meV}$ and $K = 0$ which corresponds to the strong-coupling regime.

In order to obtain the local DOS, all data were deconvolved as described in sections 2.2.3 and A.1. Exemplary deconvolved data (of atoms I-VI) can be found in Fig. 4.9b. Subsequently, the energy at which we probe the α- and β-states is determined by fitting the low-energy region with a set of four Gaussian curves as follows:

$$\begin{aligned}\mathrm{LDOS}(E) = \nu_0 &+ A_1 e^{-(E-E_\alpha)^2/(2\sigma^2)} + A_2 e^{-(E+E_\alpha)^2/(2\sigma^2)} \\ &+ B_1 e^{-(E-E_\beta)^2/(2\sigma^2)} + B_2 e^{-(E+E_\beta)^2/(2\sigma^2)}.\end{aligned} \tag{4.23}$$

Here, ν_0 is an offset, E_α and E_β are the YSR energies, $A_{1,2}$ and $B_{1,2}$ are four amplitudes and σ is the width of the Gaussian peaks. In addition to the standard deviation of the fit routine errors of the YSR energy include the uncertainty in the exact value of the tip energy gap Δ_t, the lock-in modulation of the bias voltage and the sampling interval. Additionally, an error of $\pm\sigma/2$ was added to the energy uncertainty if the peaks are not well separated (*i.e.* $E_\alpha - E_\beta \leq 2\sigma$). This is mainly the case for atoms around the CDW minimum (such as atom III), where the α- and β-resonances overlap as they are both very close to zero energy. Some of these atoms can be fitted with only one pair of Gauss peaks as the YSR states coincide. In this case both energies have the same value ($E_\alpha = E_\beta$).

Figure 4.9c shows the extracted energies of the YSR excitations (of the set of approximately 90 atoms) with respect to their location relative to the CDW (including all energy errors as discussed above and $\pm 0.05\lambda_\mathrm{CDW}$ for the position along the CDW). Note that for atoms close to position III negative values of E_α (bright red data points) are assumed as will be explained in the following.

Starting at the maximum the energy of both resonances drop with increasing distance relative to the CDW maximum (position I $\rightarrow$ position II). By default, the fit outputs for the excitation energies E_α and E_β are positive. Assuming that E_α and E_β follow a similar trend, we suggest a zero-energy crossing of the α-excitation (meaning that we find the $+\alpha$-resonance at negative bias). Hence, $E_\alpha < 0$ was assumed for the atoms in close vicinity to the CDW minimum (the set of atoms with $E_\alpha < 0$ is marked in bright red and gray). This implies a change from the screened-spin to the free-spin regime or vice versa [FSP11; Mal+18; Far+18]. Remember, that we a priori cannot discern the ground state of the α- and β-states (*c.f.* section 4.2.1). Having passed the minimum (*i.e.* position IV) the α- and β-peaks are separated and can be identified again in the $\mathrm{d}I/\mathrm{d}V$ maps (see Fig. 4.7a), *i.e.* $E_\alpha > 0$.

We note, that there are regions not covered by adatoms (gray shaded in Fig. 4.9c-f). These regions correspond to the energetically unfavorable MC phase of the CDW (*c.f.* section 3.2.1) and are not observed in experiment.[8] A schematic illustration of the alignment between CDW and atomic lattice within one complete period can be found in Appendix A.3.2.

[8] Also the third symmetric adsorption site at $4/3\lambda_\mathrm{CDW}$ which could not be achieved in experiment contributes to the gray areas.

In Fig. 4.9d we average over all atoms which are found within the error interval of $\pm 0.05 \lambda_{\mathrm{CDW}}$. In the previous section the symmetry-reduction could be explained by the presence of the CDW which imposes a spatial variation of the DOS. Furthermore, we notice that the YSR energy depends on the normal state DOS at the Fermi-energy (*c.f.* Eq. 4.14). Experimentally, we access the CDW-imposed DOS in a constant-height $\mathrm{d}I/\mathrm{d}V$ map recorded at zero bias and $T = 8\,\mathrm{K}$ (*i.e.* above T_c) after FFT-filtering. The filtering is necessary to isolate the CDW-induced DOS from the atomic corrugation. Both maps (non-filtered and FFT-filtered) can be found in Fig. 4.9a. The CDW-induced variation of the LDOS along one symmetry axis can be found in Fig. 4.9e which is extracted along the big arrow in the FFT-filtered map. In fact, comparing Fig. 4.9d and e one realizes that both YSR excitation energies follow the trend of the CDW-induced LDOS. Therefore, we can not only link the observed symmetry reduction of the YSR wave functions to the CDW, but also correlate their energy shifts to the variations of the DOS induced by the CDW.

Now after establishing the correlation between YSR excitation energies and CDW-DOS experimentally we can interpret the results by considering the simplified classical picture (neglecting the potential scattering K in Eq. 4.14). As already mentioned, the YSR energy depends (beside the exchange coupling strength J and the spin S) on the normal DOS at the Fermi energy ν_0. Thus, one indeed expects the YSR ground state energy to depend on the exact location of the adsorption site relative to the CDW.

The direction of the energy shift of the YSR excitations depends on the value of the exchange coupling strength J between impurity and substrate, being correlated (anticorrelated) to the LDOS in the screened-spin (free-spin) regime, respectively (*c.f.* Fig. 4.3c). Hence, within this simple picture, the data suggests both YSR states to be in the screened-spin regime meaning that the α- and β-YSR states have negative ground state energies (*c.f.* Fig. 4.3b, red region), except the α-resonance at the minimum of the CDW, where it crosses the QPT to the free-spin regime.

Turning towards the more sophisticated model calculations introduced above we find that the CDW influences the YSR energies in general via two mechanisms. First, the CDW potential (Eq. 4.21 and Fig. 4.9f, blue trace) causes an anticorrelated LDOS (bright red) which affects the YSR energy as discussed already. Beside this DOS effect, the CDW potential can be rationalized as additional (spatially variating) contribution to the potential scattering (neglected in the simplified picture). The CDW potential shifts K to $K + V(\mathbf{r})$, where $\mathbf{r}$ denotes the adsorption site of the impurity relative to the CDW. Considering only the DOS effect we expect the YSR excitation energy to anticorrelate with the LDOS in the weak coupling regime. However, rather strong potential scattering can overcome the DOS effect and reverse the correlation yielding YSR excitation energies being correlated with the LDOS. On the contrary, no such reversal is found for a strongly coupled impurity as the impact of K is generally weaker. We thus expect correlation between LDOS and YSR excitation energy for all values of K.

Concluding, unless the impurity is a surprisingly strong potential scatterer[9] (in the free-spin regime) the model suggests strong coupling between the impurity and the substrate - in agreement with the simplified model discussed above. Figure 4.9f (black trace) contains the calculated excitation energies for a strongly coupled impurity ($K = 0$) confirming the experimental trend. A more detailed elaboration and plots with different parameter sets can be found in [Lie+20; Ace20].

4.4.4 Observations at higher energies

Before closing the section we comment on the d level resonances observed on the different HC atoms. Spectra of atoms I-VI covering a broad energy range can be found in Fig. 4.10. Possible d-resonances are marked by the gray-shaded areas. Some resonances shift across atoms I-VI (marked by arrows) and, hence, seem to be affected by the CDW. On the CDW maximum (atom I) the intense resonance just above $1.8\,\mathrm{V}$ (zoom in the inset) is about $50\,\mathrm{mV}$ lower in energy compared to atom III (minimum on CDW). On the contrary, the resonance located below $0.2\,\mathrm{V}$ exhibits an opposite trend, *i.e.* the resonance appears at lower energies on atom III (minimum) than atom I (maximum). For the other resonances no shift is resolved. As discussed in section 3.2.1, the origin of the CDW is a slight lattice distortion coupling to the electronic degrees of freedom via electron-phonon interaction. The atomic displacements are expected to be in the order of a few percent of the undistorted lattice constants and, hence (should be well below) $< 10\,\mathrm{pm}$ [MK13; Zhe+18; LSD18; San+21]. However, such deviations of the local crystal field can lead to the small energetic shifts observed for some d-resonances. Depending on the exact shape of the orbital, the overlap with the Se-ligands might be enhanced, non-affected or decreased and therefore lead to the observed energetic shifts in different directions.

To close the section, the reduction of expected D_3-symmetry of the YSR-resonances on HC atoms can be explained by simply symmetry arguments considering the crystalline adsorption sites relative to the CDW. The experimentally observed YSR energies follow the CDW-induced LDOS which can be explained in the simple classical YSR model indicating a strongly coupled impurity. Both experimental findings are qualitatively reproduced within a general tight-binding approach where the CDW is included in the model by an additional (incommensurate) on-site potential which affects the YSR energy via the CDW-induced DOS, but there is also a contribution via the potential scattering channel.

The experimental and theoretical results presented in this section are quite general as they are also valid for a broad range of other material systems exhibiting periodic DOS modulations. Examples include other materials exhibiting CDWs, but DOS modulations are also found in Moiré structures which is a growing field in the context of topological phase engineering using 2D materials [Kez+20b; Kez+20a; Cao+18]. Especially, one

[9] As we do not observe strong intensity asymmetry between the electron- and hole-like YSR resonances, this scenario is unlikely.

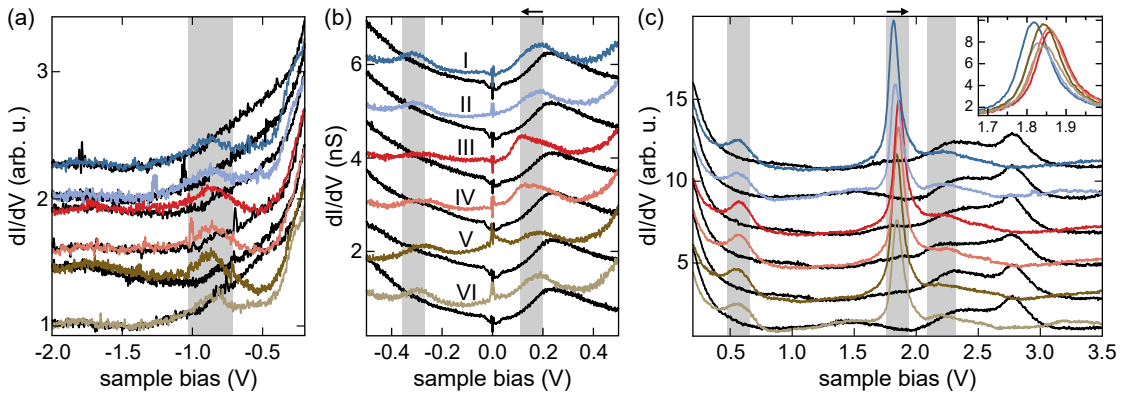

Fig. 4.10.: (a) Constant-current spectra (set point: $100\,\mathrm{pA}, V_{\mathrm{rms}} = 5\,\mathrm{mV}$) of atom I-VI (top to bottom) and the substrate (black). Traces stacked with offsets of 0.25. (b) Constant-height spectra (set point: $500\,\mathrm{pA}, -0.5\,\mathrm{V}, V_{\mathrm{rms}} = 2\,\mathrm{mV}$) of atom I-VI (top to bottom) and the substrate (black). Traces stacked with offsets of $1\,\mathrm{nS}$. (c) Constant-current spectra (set point: $100\,\mathrm{pA}, V_{\mathrm{rms}} = 5\,\mathrm{mV}$) of atom I-VI (top to bottom) and the substrate (black). Traces stacked with offsets of 2. The inset shows a zoom to the intense resonance (traces without offsets).

needs to consider above findings when coupling magnetic impurities to larger structures as chain or lattices one substrates exhibiting a modulated DOS.

4.5 Excitations in the presence of multiple Yu-Shiba-Rusinov states

In the previous sections we could deduce a correlation between the CDW-induced DOS and the YSR energies of the two low-energy resonances (α and β) by investigating various Fe atoms on different positions within the CDW. However, we did not pay attention to the YSR resonances at higher energies as they overlap with the substrates coherence peaks and are not featured by such characteristic wave functions as the long-ranged in-gap resonances. Therefore, it was not possible to trace their energy along the CDW. Furthermore, we did not comment in detail on the exact number of YSR resonances and their possible origin.

Fig. 4.11a,b contains spectra recorded on an Fe atom on a maximum (a, blue, type I) and minimum (b, red, type III) of the CDW. A substrate spectrum is shown in gray in each panel. (c,d) show stacked false-color plots of $\mathrm{d}I/\mathrm{d}V$ spectra recorded along a line across both atoms as indicated in the inset topography (white arrow). The horizontal dashed lines indicate the precise location of the spectra of (a,b). The data were acquired using Nb tips. Beside small intensity deviations the data is in full agreement to the data acquired with Pb tips (*c.f.* Fig. 4.6b). The gap is indicated as the gray box and dashed lines in (a,b) and (c,d), respectively. On the HC atom on the CDW maximum, we can discern four resonances. The largely discussed α- and β-states and two more states within the substrates coherence peaks which are labeled γ and δ. One is easy to identify as it is intense, the other manifests

as a shoulder with asymmetric intensity at the low-energy flank of the former. All four states are labeled and indicated by the white dotted lines in (c).

$\mathrm{d}I/\mathrm{d}V$ maps of all states can be found in Fig. 4.11e. In the corresponding panels we identify the specific oscillatory patterns of the α- and β-resonances and the expected overall D_3-symmetry as discussed in section 4.4 and [Lie+20] (*c.f.* corresponding Pb tip data in Fig. 4.7a, atom I). Similary to the patterns acquired with the Pb tip, the near-field pattern of the β-state exhibits intensity at the sides and vertices of a triangular shape. The α-state has largest intensity at the sides of the triangle and only small residual intensity at the vertices.

We further note that all four resonances exhibit different $\mathrm{d}I/\mathrm{d}V$ patterns. As already mentioned, the states at higher energies (γ, δ) are short-ranged and featureless (compared to their in-gap counterparts) which we attribute to scattering with the quasiparticle continuum reducing their lifetimes [Sen+19]. Both states have their maximum intensity on the atom center (opposed to α and β). δ is dominated by a circular shape while we can discern a more triangular shape for γ.

From the previous section we know that the α- and β-state are both found close to zero energy on the HC atom at the minimum of the CDW (type III, Fig. 4.11b). Beside these two resonances we identify three additional peaks as indicated in the linespectra (Fig. 4.11d) by the white dashed lines. We label them with γ, δ and β' for reasons that will become clear below. Note that the overall weak β'-resonance has no intensity directly on the atom's center and hence, does barely appear in the spectrum in (b). In the $\mathrm{d}I/\mathrm{d}V$ maps (Fig. 4.11f) we find signatures of the overlapping α- and β-resonances close to zero energy. At $+1.80\,\mathrm{mV}$ we find a resonance which exhibits striking similarity with the $+\beta$-resonance (*c.f.* map at $1.35\,\mathrm{mV}$). At negative bias the signal of the β-resonance is largely suppressed by the NDC which makes a comparison challenging. Note that the two highest-energy resonances are labeled as $\tilde{\gamma}$ and $\tilde{\delta}$ ascending in energy as we are not able to identify clear signatures (Fig. 4.11e).

Thus, the data reveals different numbers of YSR resonances for atoms placed on different positions relative to the CDW. The Fe atoms presumably carry a spin $S = 2$, *i.e.* four singly occupied d orbitals. In materials with non-zero interband scattering, each d level induces one YSR bound state, disregarding the presence of multiple superconducting energy gaps [Moc+08; Rub+16; Cho+17a]. Thus, we expect maximum four resonances per bias polarity, which is true for the atoms of type I, but not the case for the atoms on the CDW minimum. From the previous sections we further know that the CDW induces slight energetic shifts of the d levels (Fig. 4.10), but we do not find significant changes, such as a resonance crossing the Fermi level which would lead to a different d level occupation and hence to a changed spin configuration.

In section 4.1.1 we introduced the concept of magnetic anisotropy within a crystal field. For magnetic impurities with a spin $S \geq 1$ the quantum nature of the spin yields multiple

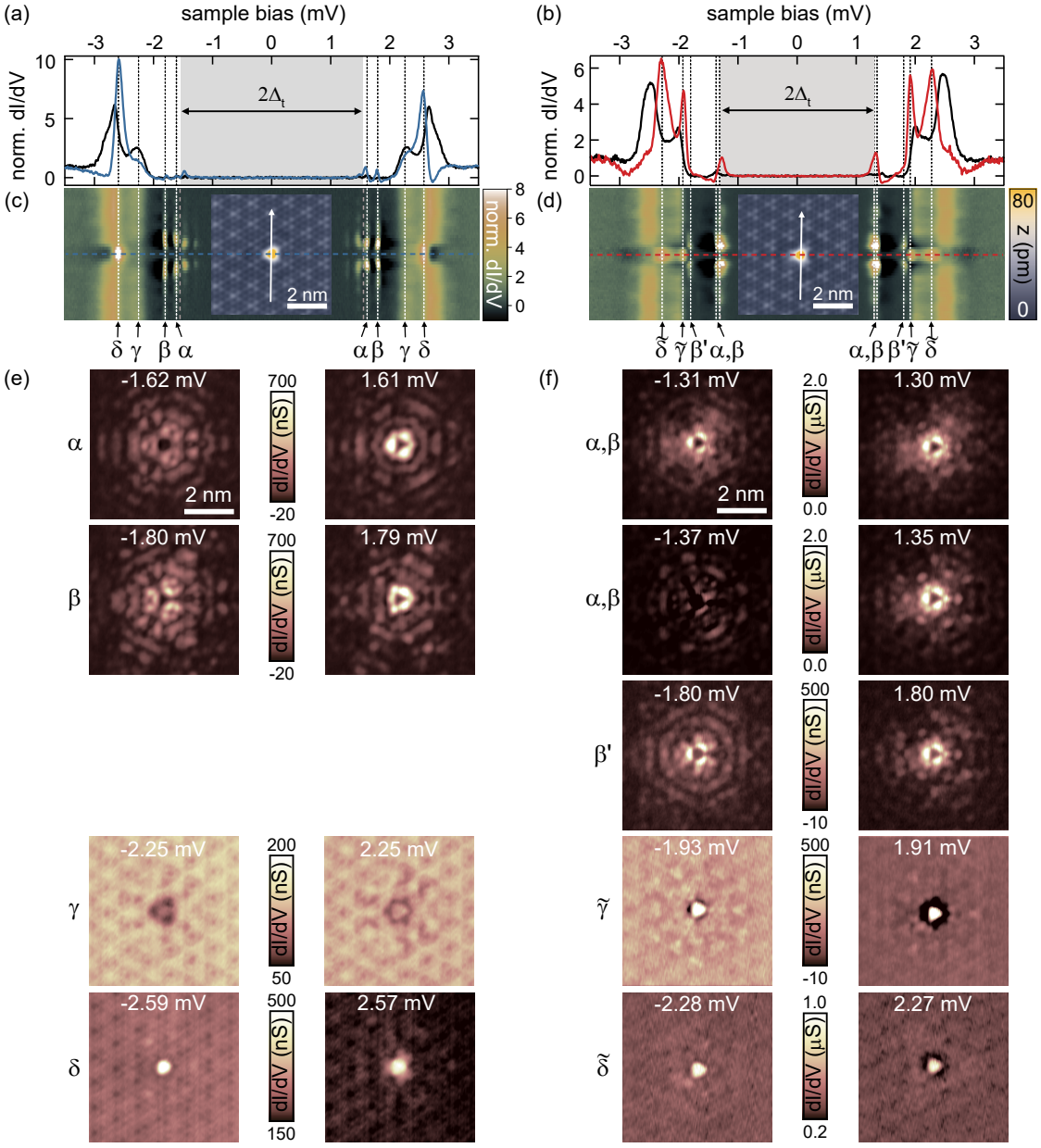

Fig. 4.11.: (a,b) Normalized differential conductance spectra recorded on an Fe atom (color) and the substrate (gray) of a type I (a) and a type III (b) HC atom. Feedback was opened at $250\,\mathrm{pA}, 5\,\mathrm{mV}$ in (a) and $750\,\mathrm{pA}, 5\,\mathrm{mV}$ in (b) and a modulation of $15\,\mu\mathrm{V}$ was used. The (Nb) tip gap of $\Delta_t \approx 1.55\,\mathrm{meV}$ in (a) and $\Delta_t \approx 1.30\,\mathrm{meV}$ in (b) are indicated in gray. (c,d) Stacked spectra recorded across the atoms from (a,b) as illustrated in the inset topographies (constant-current mode with set point $100\,\mathrm{pA}, 10\,\mathrm{mV}$). Horizontal dashed lines indicate the precise location of the spectra from (a,b). Vertical gray dashed lines indicate Δ_t. All YSR resonances are indicated by dotted lines and labeled below the panels. (e,f) Constant-contour $\mathrm{d}I/\mathrm{d}V$ maps recorded on all energies marked in (c,d) by the dotted lines. Bias voltages are given above each panel. Constant-contour feedback set point and modulation same than for spectra in (a,b).

YSR excitations involving different spin projections S_z. YSR excitations on Mn-phthalocyanine molecules revealed magnetic anisotropy splitting of YSR resonances [Hat+15]. Here, the molecular spin of $S = 1$ arises from unpaired spins in the d_{z^2} and d_{xy} orbitals of the Mn center. As it points towards the surface only the spin of the d_{z^2}-orbital couples to the superconducting condensate. The spin $S = 1$ is subject to magnetic anisotropy yielding rich YSR excitation spectra as modeled in [ŽBP11]. However, there is no general model accounting for the presence of multiple singly occupied d orbitals coupling to the CP condensate which also incorporates magnetic anisotropy effects. Such a model is presented in [OF21]. In this thesis, we outline the basic concepts in the following and discuss the possible manifestations in our material system. A detailed discussion can be found in [OF21].

We describe the high-spin quantum impurity (spin S_{imp}) subject to a crystal field by expanding the Hamiltonian of a classical $S = 1/2$-impuritiy (*c.f.* Eq. 4.12). The impurity can couple to $2S_{\mathrm{imp}}$ electron channels (indexed by i) which are represented by individual single-site superconductors [OF21]:

$$\mathcal{H} = \sum_i \Delta(c^\dagger_{i\downarrow}c^\dagger_{i\uparrow} + c_{i\uparrow}c_{i\downarrow}) + \sum_{\sigma\sigma'}\sum_i c^\dagger_{i\sigma}[K_i\tau_z\delta_{\sigma\sigma'} + J_i\mathbf{S}_{\mathrm{imp}}\cdot\mathbf{s}_{\sigma\sigma'}]c_{i\sigma'} \tag{4.24}$$

$$+DS^2_{\mathrm{imp},z} + E(S^2_{\mathrm{imp},x} - S^2_{\mathrm{imp},y}). \tag{4.25}$$

$\mathbf{s} = 1/2\boldsymbol{\sigma}$ is the electron spin in terms of the Pauli vector $\boldsymbol{\sigma}$. As in Eq. 4.1 D and E are the axial and transverse magnetic anisotropies. J_i and K_i are the exchange and potential scattering strengths which can be different for all i channels. States arising from a subset of degenerate d orbitals have identical J_i and K_i.

For simplicity, we assume vanishing transverse anisotropy, *i.e.* $E = 0$. Furthermore, we assume $T = 0$, such that magnetic anisotropy splitting of the ground state does not lead to thermal occupation of the split levels (which would further complicate the excitation picture). The total spin of the system (impurity and substrate) $\mathbf{S} = \mathbf{S}_{\mathrm{imp}} + \sum_{\sigma\sigma'}\sum_i c^\dagger_{i\sigma}\mathbf{s}_{\sigma\sigma'}c_{i\sigma'}$ depends on the number of screened channels. In the absence of transverse anisotropy (*i.e.* $E = 0$) the projection of the total spin along the z-axis S_z remains a good quantum number. To recall $D < 0$ favors out-of-plane spin alignment (maximizing S_z) while $D > 0$ tends to align the spin in plane (minimizing S_z). Furthermore, we can classify the ground state of the system by the number of bound quasiparticles (occupied substrate channels) Q. Thus, the ground state can be specified by the set of quantum numbers (Q, S_z). If Q is even the ground state has even parity while odd Q indicates an odd parity ground state.

Figure 4.12 shows the phase diagram (ground state of the Hamiltonian in Eq. 4.25) of an $S_{\mathrm{imp}} = 2$ impurity coupled to the superconductor with different exchange coupling strengths J_i for the four channels depending on the superconducting pairing strength Δ and the axial magnetic anisotropy D. For simplicity, we neglect potential scattering by setting $K_i = 0$ for all channels. We know first discuss the different phases/ground states and then consider different excitation spectra in the next step.

In the top (brown, gray) of the diagram (Fig. 4.12), the pairing strength is larger than all exchange couplings J_i. Hence, all spin channels are unscreened implying a total spin (impurity and substrate) of $S = 2$ and the number of occupied quasiparticles is zero, *i.e.* $Q = 0$. For $D < 0$, large spin protections are favored yielding $(Q, S_z) = (0, \pm 2)$ (brown) while for $D > 0$ the spin is aligned in-plane yielding $(Q, S_z) = (0, 0)$ (gray). For decreasing Δ, the spin channel with the highest J_i will change its ground state to be screened while the other three states remain unscreened ($Q = 1$, bright and dark red). Hence, one quasiparticle is bound to the impurity and the total spin of the system is reduced by $1/2$ to $S = 3/2$. The ground state is $(Q, S_z) = (1, \pm 3/2)$ for $D < 0$ (bright red) and $(Q, S_z) = (1, \pm 1/2)$ for $D > 0$ (dark red).

If Δ is further decreased (relative to the coupling strengths) a second state undergoes the quantum phase transition. Then, two quasiparticles are bound to the impurity decreasing the total spin by 1 to $S = 1$, such that $(Q, S_z) = (2, \pm 1)$ for $D < 0$ (bright blue) and $(Q, S_z) = (2, 0)$ for $D > 0$ (dark blue). Further decreasing Δ leads to three bound quasiparticles and a left over total spin of $S = \pm 1/2$. Therefore the ground state is $(Q, S_z) = (3, \pm 1/2)$. As spin-$1/2$ systems are not subject to magnetic anisotropy (Kramer's degenerate), there is no phase boundary at $D = 0$.

We note that large positive axial anisotropies suppress states with uneven parity as those do not have zero spin projection, but the minimum achievable spin along z is $S_z = \pm 1/2$. This manifests in the phase diagram in the rapid closing of the dark red and dark yellow regions at $D > 0$.

Finally, when the pairing strength (compared to the exchange couplings) is small enough, also the 4^{th} channel is screened and hence, $(Q, S_z) = (4, 0)$ which is also not further affected by magnetic anisotropy (bright yellow).

Let us now consider possible excitations. One tunneling event, *i.e.* adding/removing a single electron to/from the sample will change the the parity of the system by $\Delta Q = \pm 1$ and the spin along the z-axis by $\Delta S_z = \pm 1/2$. With these selection rules we can determine all possible excitations.

As discussed in section 4.4, the α- and β-states are likely in the screened-spin regime on the maximum HC-atom, but α crosses over to the free-spin regime on minimum HC atoms. Careful analysis of how the γ- and δ-resonances shift as a function of the position relative to the CDW suggest that one of them is in the screened-spin as it downshifts in energy along with α and β when moving away from the CDW maximum. Thus, three resonances are presumably in the screened-spin regime and one remains unscreened, when the Fe atom is located at the CDW maximum. However, as already discussed we cannot trace γ and δ along one complete period of the CDW and therefore an unambiguous assignment to one regime is not possible. Hence, as we cannot definitely access the number of screened channels, we discuss different possible scenarios in the following.

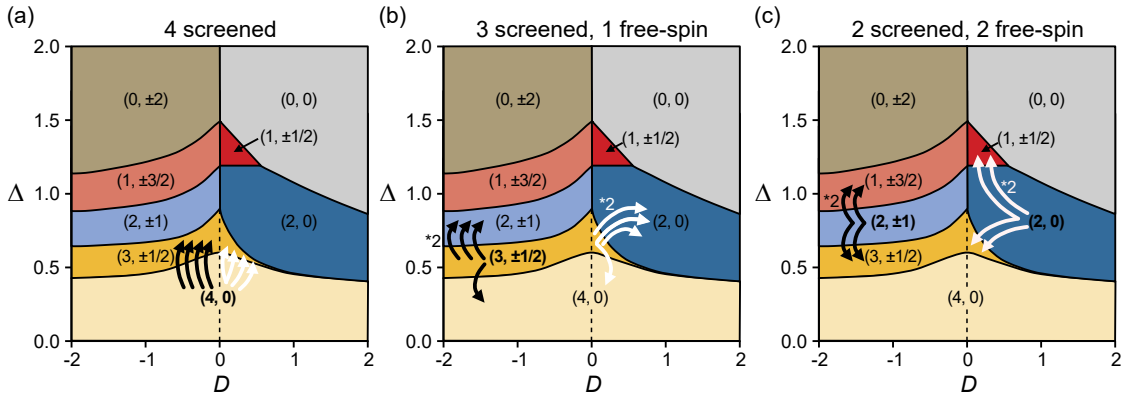

Fig. 4.12.: Phase diagrams for a $S_{\mathrm{imp}} = 2$-impurity depending on the uniaxial anisotropy D and the pairing strength Δ for different exchange coupling strengths of $J_1 = 1, J_2 = 0.8, J_3 = 0.6, J_4 = 0.4$. All $K_i = 0$ and $E = 0$, for simplicity. The different ground states are labeled according their quantum numbers (Q, S_z). All possible tunnel excitations are indicated by black and white arrows for the case of 4 screened (a), 3 screened (b) and 2 screened (c) YSR states. The factor on the left indicates magnetic anisotropy split levels that can be excited (see text for detailed discussion). The figure is taken and adapted from [OF21].

If γ and δ are in the screened-spin regime, we have four screened YSR resonances on the maximum of the CDW. Possible excitations in this case are illustrated in Fig. 4.12a. When all channels are screened, the ground state is $(Q, S_z) = (4, 0)$ as indicated in bold (bright yellow). We can excite the system to $(3, \pm 1/2)$ by emptying one of the bound quasiparticle states for $D < 0$ and also $0 < D \lesssim 1$. As we assumed four different exchange couplings J_i we expect four YSR resonances (per bias side) at different energies (indicated by the black and white arrows for $D < 0$ and $D > 0$, respectively). There are no further excitations allowed considering the selection rules for single-electron tunneling. This scenario is in agreement with the observations on the HC atom on the CDW maximum, where we discerned four YSR resonances with different spatial appearance.

Starting with three screened states and one free spin, *i.e.* $(Q, S_z) = (3, \pm 1/2)$, the excitation scheme becomes more complex (Fig. 4.12b). This scenario could apply for an HC atom on the minimum of the CDW with γ and δ screened or to a maximum atom where one of γ or δ is unscreened. For $D < 0$ we can excite the system to $(4, 0)$ (bright yellow) by occupying the empty quasiparticle state or to $(2, \pm 1)$ (bright blue) by removing one quasiparticle from the substrate. As there are three different J_i involved, the latter produces three peaks at different energies (indicated by black arrows). Furthermore, magnetic anisotropy splits the latter excitations to $S_z = \pm 1$ and $S_z = 0$ doublets each, separated by D. Similar findings hold for $D > 0$ with the difference that the magnetic anistropy split reverses the energetic order of the $S_z = \pm 1$ and $S_z = 0$ doublets (white arrows). Thus, possible excitations include one channel without further splitting by magnetic anisotropy and three magnetic anisotropy split doublets. This scenario could explain the appearance of the β'-resonance detected on the minimum atom which is not as intense, but very similar to the β-state, and hence, these two states constitute a magnetic

anisotropy split doublet. Note, that it is not surprising that we do not observe all possible 7 resonances (which include three doublets) as resonances may coincide within our energy resolution, be very unintense or be shifted outside the superconducting gap.

Finally, we discuss the scenario of two screened and free-spin channels each which could apply for the minimum atom if - additional to α - one of γ or δ is in the free-spin regime (Fig. 4.12c). The ground state is characterized by $(Q, S_z) = (2, \pm 1)$ for $D < 0$ (bright blue) and $(Q, S_z) = (2, 0)$ for $D > 0$ (dark blue). For $D < 0$ excitations now involve two channels (two J_i) emptying occupied quasiparticle states, *i.e.* to $(1, \pm 3/2)$ and two channels tunneling into empty substrate channels, *i.e.* to $(3, \pm 1/2)$. The former two excitations each split into doublets $(1, \pm 3/2), (1, \pm 1/2)$ by magnetic anisotropy. $D > 0$ yields a similar spectrum with the energetic order of the doublets reversed as $(1, \pm 1/2)$ is favored. Thus, also in this scenario we find YSR doublets which can expain the experimental findings.[10]

Concluding, the presence of more than four resonances for an impurity with $S_{\mathrm{imp}} = 2$ cannot be explained considering four singly occupied d orbitals acting as individual classical spins. We introduced a quantum model where multiple scattering channels as well as magnetic anisotropy is considered [OF21]. Even though we cannot unambiguously deduce the exact amount of screened channels for the HC atoms from experiment, several scenarios (considering pure axial anisotropy) explain the presence of > 4 YSR resonances originating from magnetic anisotropy split doublets as found on minimum HC atoms.

Having extensivley studied Fe atoms adsorbed on HC sites we dedicate the next section to Fe atom on MC sites.

4.6 The MC adsorption site - spatially varying YSR states

As discussed already in section 4.3 MC sites do not coincide with CDW maxima and minima. But nevertheless there are differences in their positions relative to the CDW. Fig. 4.13a,b show data obtained on two MC atoms (within the HC phase of the CDW) which are located close to a CDW maximum (a) and minimum (b) and labeled type (i) and type (ii) in the following.[11] The position of the MC sites relative to the CDW is indicated in Fig. 4.13e using the same scheme as for HC atoms by the thick triangles (*c.f.* Fig. 4.8b). Topographies with overlaid CDW grids can be found in Fig. A.7.

[10] For completeness, also if both, γ and δ, are in the free-spin regime, we can explain the experimental findings. This corresponds to a ground state of $(Q, S_z) = (1, \pm 3/2)$ and $(Q, S_z) = (1, \pm 1/2)$ for $D < 0$ and $D > 0$, respectively. Possible excitations involve once $(0, \pm 2)$ and triply $(2, \pm 1)$ which are further split by magnetic anisotropy into a triplet and three doublets. Again, for $D > 0$ we find similar excitations with the energetic order of the multiplets reversed.

[11] To make a clear difference to the HC atoms which we labeled with capital roman numbers, we choose small roman numbers (i), (ii) for the MC atoms.

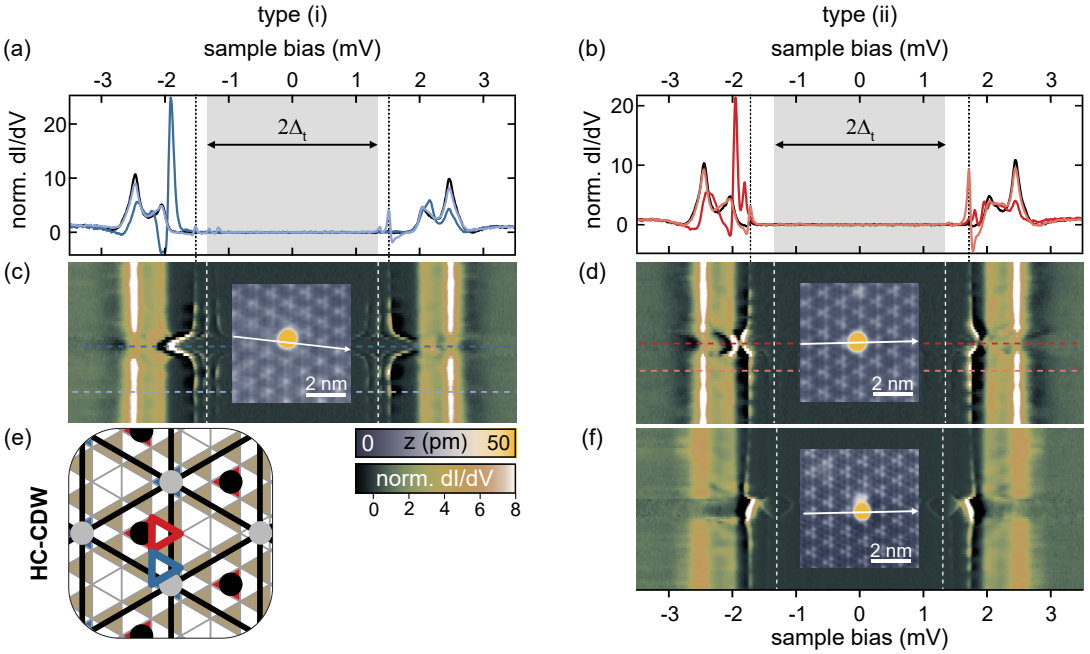

Fig. 4.13.: (a,b) Normalized differential conductance spectra recorded centrally on (dark) and in the vicinity (bright) of MC Fe atoms of type (i) in (a) and type (ii) in (b). The precise positions of the spectra are indicated in panels (c,d) in the corresponding color. Reference $NbSe_2$ spectrum in black. Vertical black dotted lines mark the YSR energy of the intense in-gap YSR excitation away on the atoms' center. Feedback was opened at $250\,\mathrm{pA}, 5\,\mathrm{mV}$ and a modulation of $15\,\mu\mathrm{V}$ was used. (c,d) Stacked spectra recorded across the atoms from (a,b) as illustrated in the inset topographies (constant-current mode with set point $100\,\mathrm{pA}, 10\,\mathrm{mV}$). The (Nb) tip gap of $\Delta_t \approx 1.34\,\mathrm{meV}$ is indicated by the gray box and white dashed lines). Horizontal dashed lines indicate the precise location of the spectra from (a,b). (e) Adsorption positions relative to the CDW of both atoms in the equivalent scheme as Fig. 4.8b. The MC sites of atom (i) and (ii) are indicated by the thick triangles in blue and red, respectively. (f) Stacked spectra recorded across an atom of type (ii) with a different tip as illustrated in the inset topography (constant-current mode with set point $100\,\mathrm{pA}, 10\,\mathrm{mV}$). Feedback was opened at $750\,\mathrm{pA}, 5\,\mathrm{mV}$ and a modulation of $15\,\mu\mathrm{V}$ was used. The (Nb) tip gap of $\Delta_t \approx 1.30\,\mathrm{meV}$ is indicated by white dashed lines.

Both atoms differ in their YSR resonances in agreement with the effect of the CDW on YSR energies explained for HC atoms before. There are short-ranged resonances in the energy range of the substrates coherence peaks as well as long-range in-gap resonances as can be seen in the stacked spectra recorded along lines across both atoms in Fig. 4.13c,d. Interestingly, the YSR excitation energies spatially vary. In particular, the intense in-gap resonance is found further away from the Fermi level directly on the atom and smoothly shifts into the gap away of the atom's center until it saturates in energy (marked by vertical black dotted lines in Fig. 4.13a,b). There are also resonances exhibiting an opposite trend as can be discerned, for example, close to the coherence peaks across atom (ii). Thus, we find resonances that are up- or down- shifted in energy when the tip comes close to the atom. Such a behavior is not observed for HC atoms.

Fundamentally, YSR states have one specific energy defined by Eq. 4.14 at which we observe the extended wave function (in the $\mathrm{d}I/\mathrm{d}V$ maps, *c.f.* Fig. 4.11e,f). Thus, something

must perturb the YSR excitations in our system. Actually, the STM tip itself can modify electronic states and hence, the YSR excitation energies. Indeed, we find that the exact shape of the tip apex largely affects the observed magnitude and trend of the spatial energy shifts of the YSR states of MC atoms. As an example we show data obtained on another type (ii) MC atom measured with a different tip. Comparing Fig. 4.13d,f we find that the dispersion of the YSR resonances strongly differs even though both atoms are on equal positions relative to the CDW. Importantly, the YSR energy far away from the atoms saturates to a similar value for both atoms.

To further establish the influence of the tip on the YSR states we can compare data obtained on identical lateral positions, but at different relative tip heights above the surface. In Fig. 4.14 we show spectra recorded across both atoms with the same tip apex but with the tip height increased by $200\,\mathrm{pm}$ (a,d), $100\,\mathrm{pm}$ (b,e) and $0\,\mathrm{pm}$ (c,f) relative to the usual set point before sweeping the bias as sketched in the left of Fig. 4.14. Mainly visible for the in-gap states we find that the resonances shift stronger, the closer the tip is to the surface. This observation confirms that the presence of the tip affects the YSR excitation energies. Note that we find spatially varying YSR resonances also with Pb tips. The geometry of the tip apex seems to be important rather than the tip material. Exemplary data recorded with Pb tips can be found in Fig. A.8.

Recalling Eq. 4.14 the YSR energy depends on the spin state S, the exchange coupling strength with the substrate J and the DOS at the Fermi level ν_0. There are different tip-induced mechanisms that could modify one of these parameters and therefore cause the observed spatial variations of the YSR excitation energies: (1) Influence of the local electric field between tip and sample, and, (2) slight displacement of the atoms within their adsorption site by attractive van der Waals (vdW) forces between the Fe atom and the tip. In the following we explain and discuss both mechanisms in more detail and elucidate how they influence the YSR energy.

To start with, even at zero bias there is always a local strongly inhomogeneous electric field in the junction caused by the contact potential difference (CPD) between tip and sample [Gir+93] (*c.f.* Fig. 2.1b). Literature values of the work function for $NbSe_2$ yield $\Phi_{NbSe_2} = 5.6\text{-}5.9\,\mathrm{eV}$ [SOP94; LSW16]. The work functions of Nb and Pb are very similar being $\Phi_{\mathrm{Pb,Nb}} \approx 4.2\text{-}4.3\,\mathrm{eV}$ [Mic77; Wil66; Eas70; Tra71]. Thus, for both tip materials the CPD caused by the work function difference is in the order of $> 1\,\mathrm{V}$.

In metals, the electric field is screened by the surface electrons. Thus, the tip can locally perturb the carrier density and basically acts as a local (top-)gate. In materials with relatively low carrier density such as semiconductors or in purely 2D materials the screening cloud significantly perturbs the electronic states. For example, STM measurements on graphene revealed a large tip-induced screening cloud of $r \approx 50\,\mathrm{nm}$ [Zha+15]. Furthermore, for poor screening the electric field penetrates the sample resulting in band bending near the surface [McE+93; Zhe+94; Fee94]. Recently, spatially varying YSR states of subsurface impurities have been observed in $FeTe_{0.55}Se_{0.45}$ and explained by the

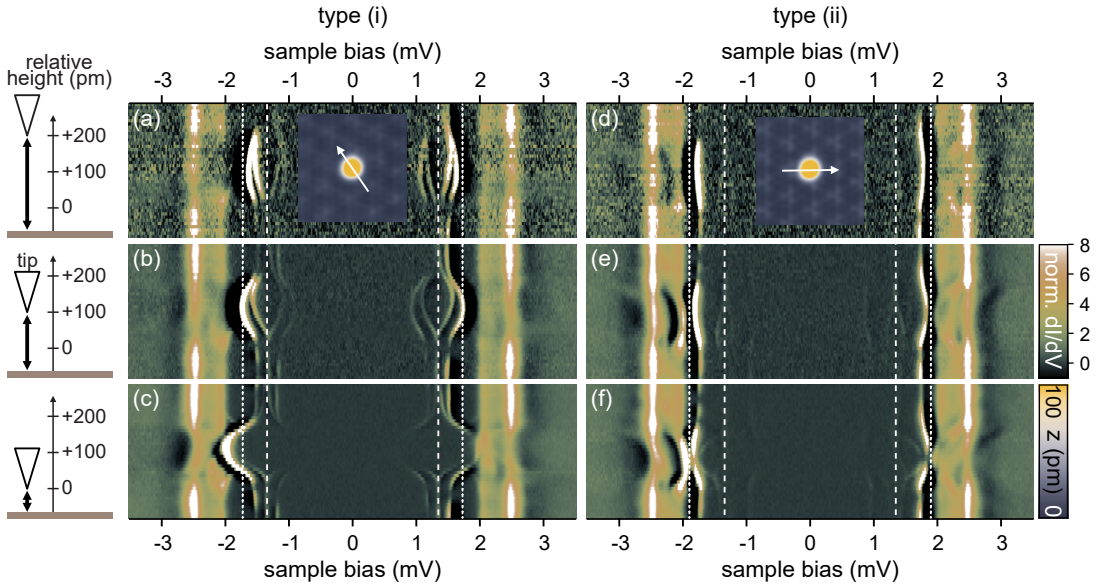

Fig. 4.14.: Stacked spectra recorded across atom (i) in (a-c) and atom (ii) in (d-f) of Fig. 4.13a-d as illustrated in the inset topographies (constant-current mode with set point $100\,\mathrm{pA}, 10\,\mathrm{mV}$). Feedback was opened at $250\,\mathrm{pA}, 5\,\mathrm{mV}$ and a modulation of $15\,\mu\mathrm{V}$ was used. The feedback is opened at the same parameters for each (constant-height) spectrum, however, the tip is withdrawn by $200\,\mathrm{pm}$ (a,d), $100\,\mathrm{pm}$ (b,e) and $0\,\mathrm{pm}$ (c,f) before sweeping the bias as sketched in the left of the figure. The (Nb) tip gap of $\Delta_\mathrm{t} \approx 1.34\,\mathrm{meV}$ is indicated by white dashed lines. White dotted lines serve as guides to the eye.

low carrier density yielding a large screening length which enables the electric field to penetrate the sample inducing energetic shifts of the d orbitals [Cha+21].

However, $NbSe_2$ has a considerable DOS at the Fermi level and thus the perturbation by the tip potential should be negligible. Hence, a screening cloud exhibiting a sizeable change of the LDOS and hence, causing the observed substantial energy shifts ($\lesssim \Delta$) is unlikely. Furthermore, such a tip-induced variation of the substrate's LDOS should affect HC and MC atoms in a similar manner which is clearly not observed in experiment.

Recalling the Anderson-model (*c.f.* ε_d in Eq. 4.9) energetic shifts of the YSR states can originate from shifted d orbitals. Such energy shifts of atomic/molecular levels have been observed if adsorbates are sufficiently decoupled from the surface as there is a sizeable potential drop between the impurity and the surface. Such double barrier junctions are achieved, for example, by molecules decoupled from the surface by their extended ligands or by insulating/semiconducting buffer layers [Mar+08; Tei+08; Wu+04; Pra+05; NQH05; Fer+12] However, the Fe atoms are clearly not decoupled from the surface.

As a further mechanism which can impose energy shifts on the d orbitals we consider the Stark effect. The strong inhomogeneous electric field beneath the STM tip induces small variations in the energy of surface states in the order of a few meV for currents in the nA-regime [Gir+93; Lim+03; Krö+04]. Thus, the strong electric field of the tip can polarize the d orbitals shifting them in energy. Generally, the Stark effect is stronger

the further the states decay into the vacuum [Krö+04]. As the electric field beneath the STM tip is strongly inhomogeneous [Gir+93] and depends on the tip apex, this could explain the experimental findings. However, even though MC atoms stick out the surface more compared to the HC atoms, one would expect a detectable Stark shift also for HC atoms. Furthermore, similar materials systems including various adsorbates on metallic substrates do not observe significant Stark shifts. Hence, even though we cannot exclude Stark-shifted d orbitals as the origin of the dispersing YSR states this scenario remains unlikely.[12]

Beside the effects caused by the electric field between tip and sample, we discuss the attractive vdW forces between tip and sample in the following. Recent experiments showed the tunability of the YSR energy exploiting the vdW forces between tip and magnetic molecules adsorbed on a superconductor. The substrate-molecule distance could be reliably altered by the vertical tip-sample distance thereby controlling the exchange coupling J between the molecule and the substrate [Far+18; Hua+20; Mal+18]. In our case, attractive vdW forces between the tip and the MC atoms can slightly displace the atoms in their adsorption site when the tip laterally or vertically approaches the atom. This changes the crystal field leading to different d orbital splitting. This in turn affects the exchange and potential coupling strengths and thus, the YSR energies. Manipulation experiments revealed that the HC atoms are more stable in their adsorption site than MC atoms. Indeed, for some (reactive) tips using the usual set point (250-$750\,\mathrm{pA}, 5\,\mathrm{mV}$) we observe unintended atom manipulations as the MC atoms tend to follow the tip. An example is given in the appendix Fig. A.9. Importantly, such unintended manipulations do not happen for HC atoms. Hence, this could explain why the variations of YSR energies only occur for MC atoms.

Concluding, we cannot unambiguously discern attractive vdW forces as the origin of the dispersing YSR states, however, this scenario appears to be most likely at the current level of data interpretation. If the atom is (partially) decoupled from the surface by vdW forces also the influence of the electric field could become valuable as discussed above, such that probably both effects are entangled. Further measurements using an atomic force microscope could be performed in order to get insight into the attractive forces necessary for atom manipulation for both species [Ter+08].

Although tip dependent effects make an unambiguous interpretation challenging, we can still gain insight into some basic properties of the MC atoms and compare them to the properties of HC atoms.

[12] Performing spectroscopy at higher voltages ($\sim \mathrm{V}$), we could not resolve any spatial variations of the d level energies. Constant-current measurements with set points up to $\lesssim 1\,\mathrm{nA}$ were tested. However, such measurements are still in a different regime with higher tip-sample distances. For example, the lateral difference between set points of $1\,\mathrm{nA}, 1\,\mathrm{V}$ and $250\,\mathrm{pA}, 5\,\mathrm{mV}$ on an MC Fe atom is $\approx 250\,\mathrm{pm}$. Moreover, the work function difference between tip and surface is (partially) compensated at positive bias yielding reduced electric field strengths.

The spatially shifting YSR resonances observed in the line spectra translate in ring-like features in $\mathrm{d}I/\mathrm{d}V$ maps (*c.f.* Fig. 4.15). The diameter of the rings increases (decreases) with decreasing energy if the corresponding resonance shifts towards (away from) E_F away from the atoms' center (two left $\mathrm{d}I/\mathrm{d}V$ maps in Fig. 4.15a,b). The rings transform to YSR wave functions with the typical oscillatory decay when the resonance reaches its saturation energy, as can be seen in the panels at $1.51\,\mathrm{mV}$ for atom (i) and $1.73\,\mathrm{mV}$ for atom (ii). Extended $\mathrm{d}I/\mathrm{d}V$ maps at various energies for both atoms can be found in Figs. A.10 and A.11. As their wave functions have very similar spatial appearance the intense in-gap resonance on type (i) and (ii) atoms originates from the same YSR state. It exhibits the opposite trend as the α- and β-states of HC atoms and anticorrelates with the CDW-induced DOS as the excitation is at lower energy on the maximum of the CDW. Thus, at least for this in-gap resonance we can conclude that the YSR state is in the free-spin regime. In agreement with the CDW-induced symmetry reduction of the YSR wave functions of HC atoms we find mirror symmetry indicated by the white dashed lines for both MC atoms.

Before we close the section we comment on one last aspect. Close inspection of the line spectra in Fig. 4.13c yields the presence of a second less intense in-gap resonance with the same oscillatory decay as the intense one of atom (i) saturating to $\approx 1.4\,\mathrm{mV}$. The $\mathrm{d}I/\mathrm{d}V$ maps reveal striking similar wave functions of both in-gap resonances (compare the panels at $1.51\,\mathrm{mV}$ and $1.39\,\mathrm{mV}$ in Fig. 4.13a). Similarly, although not discernable from the line spectrum (Fig. 4.13d) as it is faint, we find a low-energy replica of the intense in-gap resonance also for atom (ii) (compare the panels at $1.73\,\mathrm{mV}$ and $1.41\,\mathrm{mV}$ in Fig. 4.13b). These duplicates likely arise from excitations channels of the same YSR state energetically split by magnetic anisotropy as already discussed for HC atoms in the previous section. As can be seen from Fig. 4.14 the resonances of the doublets do not shift parallel in energy. This is naturally expected, as the tip-induced change of the d orbitals (either via the electric field or the slight movement of the atoms in their adsorption site as discussed above) affects the magnetic anisotropy parameter D and, hence the energetic split of the doublets.

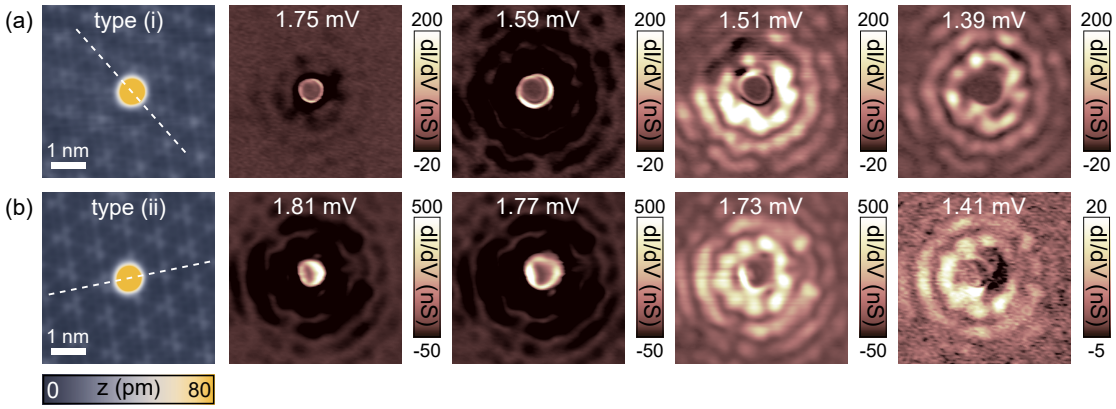

Fig. 4.15.: Constant-contour $\mathrm{d}I/\mathrm{d}V$ maps of atom (i) in the top row (a) and atom (ii) in the bottom row (b). Same atoms as in Fig. 4.13a-d. Voltages are indicated above each panel. Constant-contour feedback parameters are $250\,\mathrm{pA}, 5\,\mathrm{mV}$ and a modulation of $15\,\mu\mathrm{V}$ is used. Topography of the map area in the left panels (constant-current set point $100\,\mathrm{pA}, 10\,\mathrm{mV}$). The symmetry axis is indicated by the white dashed line. The (Nb) tip gap is $\Delta_\mathrm{t} \approx 1.34\,\mathrm{meV}$.

5 Beyond single impurities - coupling in magnetic dimers on 2*H*-$NbSe_2$

After studying the properties of single Fe atoms adsorbed on the $NbSe_2$ surface, we now investigate the hybridization in atomic dimers. As introduced in section 2.1.3, the use of superconducting Nb tips facilitates atomic manipulation and hence, opens access to assemble customized adatom structures. As we have seen in the previous chapter, the CDW is an important factor that has to be considered when creating hybrid structures as it affects YSR energies and wave functions of the Fe atoms. As MC adatoms showed tip-dependent variations and are less stable we focus on HC adatoms from now on. The chapter is organized as follows. We introduce the basic concepts of coupling between spins on a surface and YSR hybridization in section 5.1. Afterwards we demonstrate that there is substantial YSR hybridization in dimers which sit on appropriate positions relative to the CDW (section 5.2). Subsequently we will study the influence of the CDW on the hybridization in section 5.3 by exploring dimers with different spacings.

5.1 Basic concepts of YSR hybridization

5.1.1 Interaction between spins on a metal or superconductor

Spins on a surface may interact via different mechanisms. To start with, the magnetic dipoles of both spins can directly interact leading to antiferromagnetic (AFM) coupling. However, this dipole-dipole interaction is overall small in magnitude and further scales with $\propto 1/d^3$, where d is the separation between the impurities [AM07] resulting in small interaction energies. Thus, one can usually safely neglect direct spin exchange even for short distances [WZW11].[1]

The interaction between two spins on a metallic surface can significantly be enhanced by their mutual interaction with the conduction electrons as first shown by M. A. Ruderman, C. Kittel, T. Kasuya and K. Yosida in the 1950s [RK54; Kas56; Yos57]. In particular, one impurity (partially) polarizes the spin of the bath electrons. This spin density is then sensed by the second impurity and vice versa, thereby generating long-range interactions mediated by the conduction electrons - the so-called RKKY interaction. Considering only

[1] Note that while direct dipole-dipole interaction is usually small compared to the substrate-mediated RKKY interaction on metallic surfaces it was shown to be the dominating interaction between spins on insulating surfaces as revealed by electron spin resonance measurements carried out with a specially equipped STM [Cho+17b].

isotropic exchange,[2] we can describe the RKKY interaction by the following Hamiltonian [WZW11]:

$$H_{\mathrm{RKKY}} = I(\mathbf{d}_{ij})\,\mathbf{S}_i \cdot \mathbf{S}_j\,, \tag{5.1}$$

where $\mathbf{S}_i$ and $\mathbf{S}_j$ are the spins of the two interacting magnetic atoms at positions $\mathbf{r}_i$ and $\mathbf{r}_j$ separated by $\mathbf{d}_{ij} = \mathbf{r}_i - \mathbf{r}_j$. The exchange constant $I(\mathbf{d}_{ij})$ generally depends on the distance and the lattice direction. For an isotropic electronic environment with dimensionality D we can describe $I(\mathbf{d}_{ij})$ by the following oscillatory decay [FK75; Yaf87]:

$$I(d) \propto \frac{\cos(2k_{\mathrm{F}}d + \delta)}{(2k_{\mathrm{F}}d)^D}\,. \tag{5.2}$$

Above, δ denotes the scattering phase. Depending on the sign of $I(d)$ the RKKY coupling between two impurities can be ferromagnetic (FM) or AFM. The RKKY interaction is boosted in systems with reduced dimensionality. In Fig. 5.1 we plot $I(d)$ for $D = 2$ and a Fermi wave vector of $k_{\mathrm{F}} = 5\,\mathrm{nm}^{-1}$ which approximately corresponds to the inner pair of Γ-cylinders (of the $NbSe_2$'s Brillouin zone [Rah+12], *c.f.* Fig. 3.7b) for two different phases δ. For example, assuming an atomic separation of $1\,\mathrm{nm}$ depending on the exact phase δ next nearest neighbor (NNN) contributions can be of comparable magnitude than nearest neighbor (NN) interactions. Thus, in materials with relatively long Fermi wavelengths (relatively small k_{F}) compared to interatomic spacings relevent for experiments, NNN contributions can play a significant role in linear structures with more than 2 atoms (which will be important in section 6.2).

Experimentally, the oscillatory nature of the RKKY interaction was probed in different systems involving magnetic adsorbates on metal surfaces [Zho+10; Mei+08; Kha+12] and superconducting surfaces [Din+21]. Since the RKKY coupling arises from the continuum states, the opening of the small superconducting gap does not significantly modify the RKKY interaction [HMK15; Kli+13; GL02; AMY97]. Generally, the presence of local YSR states gives rise to an AFM contribution as adjacent impurities with opposite spin favor the condensation of a singlet CP. This AFM correction can be significant within specific parameter regimes (especially at $k_{\mathrm{F}}r > \zeta_0/r$) [Yao+14a; Hof+15], but for interatomic distances relevant for our experiments (sections 5.2.1 to 6.3) conventional RKKY interaction should dominate the coupling.

5.1.2 Excitations of a magnetic dimer

There are various classical models addressing the hybridization between YSR states which could successfully explain many experimental findings of coupled impurities on superconductors [Rub+18; Yao+14a; Hof+15; FR00; Bec+21; Din+21]. Classically, YSR

[2] For simplicity, we neglect the anisotropic Dzyaloshinskii–Moriya interaction [Dzy57; Mor60], which yields a contribution $\propto \mathbf{D}(\mathbf{d}_{ij}) \cdot (\mathbf{S}_i \times \mathbf{S}_j)$ including the Dzyaloshinskii-Moriya vector to the RKKY Hamiltonian [WZW11; Wie09].

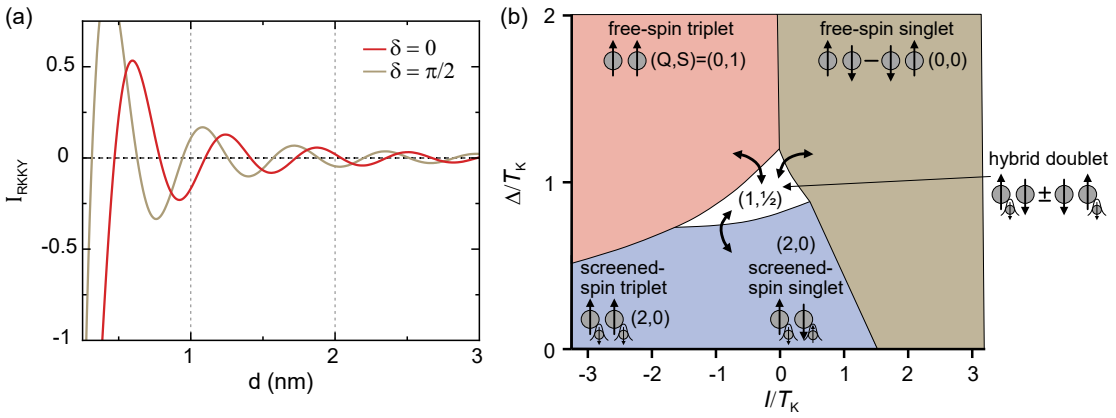

Fig. 5.1.: (a) Plot of the oscillatory decay of the RKKY interaction constant for $k_\mathrm{F} = 5\,\mathrm{nm}^{-1}$ and $\delta = 0$ (red) and $\delta = \frac{\pi}{2}$ (brown). (b) Phase diagram for an overlap of $\mathcal{S} = 0.1$ depending on the relative magnitudes of the Kondo temperature T_K, superconducting pairing Δ and RKKY interaction strength I. Background colors correspond to different ground states labeled within each region. All excitations possible by single electron tunneling are indicated by the black arrows. Panel (b) taken and adapted from [Yao+14b].

states hybridize only for (partially) FM alignment between the impurity spins of both atoms (no splitting of the resonances if their wave functions are orthogonal) while AFM interaction induces energy shifts, but the YSR states remain degenerate. Since Fe atoms on $NbSe_2$ show Kondo fingerprints[3] (*c.f.* section 4.1.2), we consider our impurities as quantum spins in the following foregoing the classical approaches.

We introduce the rich phase diagram of two interacting magnetic moments with $S_i = 1/2$ arising from the interplay between RKKY and Kondo exchange interactions with superconductivity following [Yao+14b] based on a semi-classical calculation. Within this approach, YSR and RKKY terms are considered separately as follows:[4]

$$\mathcal{H} = \int d\mathbf{r}\, \Psi^\dagger(\mathbf{r}) \left(\frac{-\hbar^2}{2m}\nabla^2 - \mu \right) \Psi(\mathbf{r}) + \int d\mathbf{r} \left(\Delta \psi_\uparrow^\dagger(\mathbf{r}) \psi_\downarrow^\dagger(\mathbf{r}) + h.c. \right) + \frac{J}{2}\mathbf{S_1} \cdot \Psi^\dagger(\mathbf{r}_1)\boldsymbol{\sigma}\Psi(\mathbf{r}_1) + \frac{J}{2}\mathbf{S_2} \cdot \Psi^\dagger(\mathbf{r}_2)\boldsymbol{\sigma}\Psi(\mathbf{r}_2) + I\mathbf{S_1} \cdot \mathbf{S_2}\,. \tag{5.3}$$

Above, $\Psi(\mathbf{r}) = (\psi_\uparrow(\mathbf{r}), \psi_\downarrow(\mathbf{r}))$. The Hamiltonian contains kinetic energy, BCS pairing and YSR terms of both impurities which are located at $\mathbf{r}_1$ and $\mathbf{r}_2$. The RKKY interaction is captured by the last term containing both spin operators. The system is solved within the numerical renormalization group approach (see [Yao+14b] for details) revealing the existence of five competing subgap solutions which can be labeled (similar to the

[3] Not shown in this thesis.

[4] Note, that the YSR states and the RKKY interaction both result from exchange interaction of the magnetic moment with the substrate. The different interactions are beared in the energy dependence of the exchange interaction $\tilde{J}(\varepsilon)$. The YSR states are governed by the exchange coupling strength at the Fermi level while the the RKKY interaction is mediated by continuum states (also well above/below the Fermi energy) [HMK15; Yao+14b]. Thus, one can approximate both as separate contributions to the Hamiltonian with the corresponding constant values $J = \tilde{J}(\varepsilon = 0)$ for the YSR states and $I = \tilde{J}(|\varepsilon| >> 0)$ for the RKKY interaction.

approach in section 4.5) by the quantum numbers (Q, S) being the number of occupied quasiparticle states and the total spin of the system S. The ground state depends on the relative strengths of the superconducting pairing Δ, the RKKY interaction I and the exchange coupling J. To recall, the connection between Kondo temperature and YSR states is given by $T_\mathrm{K} \propto e^{-1/J}$ (*c.f.* Eq. 4.11). Also, the overlap $\mathcal{S}$ between the YSR wave functions plays an important role.

Figure 5.1b shows the phase diagram obtained for an overlap of $\mathcal{S} = 0.1$ (reproduced from [Yao+14b]). For large values of Δ/T_K both substrate channels are empty corresponding to the free-spin regime. The coupled moments can form a singlet $(0, 0)$ or a triplet $(0, 1)$ state. For negative I (FM coupling) the free-spin triplet is the ground state while the free-spin singlet is energetically favored for $I > 0$ (red and brown regions in Fig. 5.1b). For large positive I the free-spin singlet phase extends down to $\Delta = 0$. For small positive and negative values of I and decreasing pairing Δ both impurities pass over to the screened-spin regime and are individually screened by quasiparticles (blue region). For large negative I they form a screened-spin triplet while the spins are antiparallel for $I \gtrsim 0$ (screened-spin singlet), both characterized by $(2, 0)$. Finally, there is a phase with only one quasiparticle state occupied with $(1, 1/2)$ which we call *hybrid doublet* in the following. As each of the impurities can bind the quasiparticle the YSR wave functions hybridize and form symmetric and antisymmetric linear wave function combinations if there is non-zero overlap $\mathcal{S}$ between the wave functions (white region). The splitting between both levels depends on the size of the overlap $\mathcal{S}$.

As largely discussed already we do not probe the ground state by tunneling with a single electron, but we excite the system with the selection rules $\Delta Q = \pm 1$ and $\Delta S = \pm 1/2$. All possible STM-excitations are indicated by black arrows in Fig. 5.1. For all ground states except the hybrid doublet, the only possible excitations are those involving the symmetric and antisymmetric wave functions of the hybrid doublet. For example, if the free-spin triplet is the ground state we can probe both states of the hybrid doublet (which are split in energy) by tunneling into the empty quasiparticle states.

YSR hybridization in magnetic dimers was observed in different material systems [Ji+08; Cho+18b; Rub+18; Kez+18; Bec+21; Din+21] including atoms and molecules on different superconductors. For $NbSe_2$ hybridization between surface impurities is predicted to be strong if the impurities are adsorbed along the same atomic row and weak otherwise [Kez+18]. Dimers consisting of CoPc molcules showed fingerprints of split YSR excitations up to separations of $\sim 2\,\mathrm{nm}$ putting forward $NbSe_2$ as a well-suited platform to study the interactions between magnetic atoms [Kez+18; FR00; KTK18].

5.2 Fe dimers respecting the CDW periodicity

Considering the results of section 4.4, we have to elucidate how to efficiently couple YSR states of two Fe atoms in the framework of the CDW. Hybridization leads to the

largest energy split, when the states obey the same symmetry and have the same energy [Rub+18]. In this section we investigate the hybridization in Fe dimers with a separation of $3a \approx 1\,\mathrm{nm}$ which places such dimers well within the dilute coupling regime (*c.f.* section 6.1.2). Because the atoms sit on quasi-identical positions relative to the CDW (as the smooth transition between the CDW structures happens on a larger scale), YSR energies should be similar for both atoms and this should facilitate efficient coupling. Again, we focus on the two low-energy resonances, labeled as α- and β-states above as their wave function patterns are easy to resolve. Furthermore, they are more long-range than resonances within the quasiparticle continuum and thus, should exhibit sizeable overlap which is one main requirement for hybridization.

5.2.1 Hybridization starting from well separated states

Results presented in this section are published in [Lie+21].

Considering the findings from section 4.4 we choose two atoms sitting on a CDW maximum (like atom I) as building blocks for the dimer. The α- and β-resonances are well separated here. Furthermore, the wave functions exhibit the full D_3-symmetry which makes these atoms a good starting point to study the coupling between HC atoms.

Figure 5.2a contains spectra obtained on a single Fe atom (black) located on a CDW maximum and on the substrate (gray) recorded with a Nb tip. In (b) the corresponding line profile across the atom (as indicated in the inset topography) can be found (same atom/data as in Fig. 4.11). For better comparison, the differential conductance maps of the positive α- and β-resonances are reproduced in Fig. 5.3a (corresponding topography in the left panel).

In the next step we precisely place a second Fe atom at a distance of $3a$ next to the first atom in order to form an atomic dimer - without moving the first Fe atom. The $\mathrm{d}I/\mathrm{d}V$ spectra at the center of the two atoms (black and blue) and the complete set of spectra along a line across the Fe dimer are shown in Fig. 5.2c,d. Compared to the monomer we observe an increased number of YSR states in the $\mathrm{d}I/\mathrm{d}V$ spectra, which can be verified by comparing the low-energy zooms of the line profiles across the monomer and the dimer in Fig. 5.2e,f (all resonances are indicated by white dotted lines). In particular, we find four resonances ($\pm\alpha, \pm\beta$) along the monomer, while there are eight resonances (four YSR states) within in the energy gap of the $NbSe_2$ on the dimer, *i.e.* we observe a doubling of states within the energy region of the original α- and β-states. The oscillating intensity distribution of the four dimer states exhibits horizontal mirror symmetry with respect to the center of the dimer (Fig.5.2d,f). We further identify two states which lack intensity at the center between the atoms, while the other two do not. These observations suggest the formation of hybrid states formed by the symmetric and antisymmetric linear combinations of the monomer YSR states.

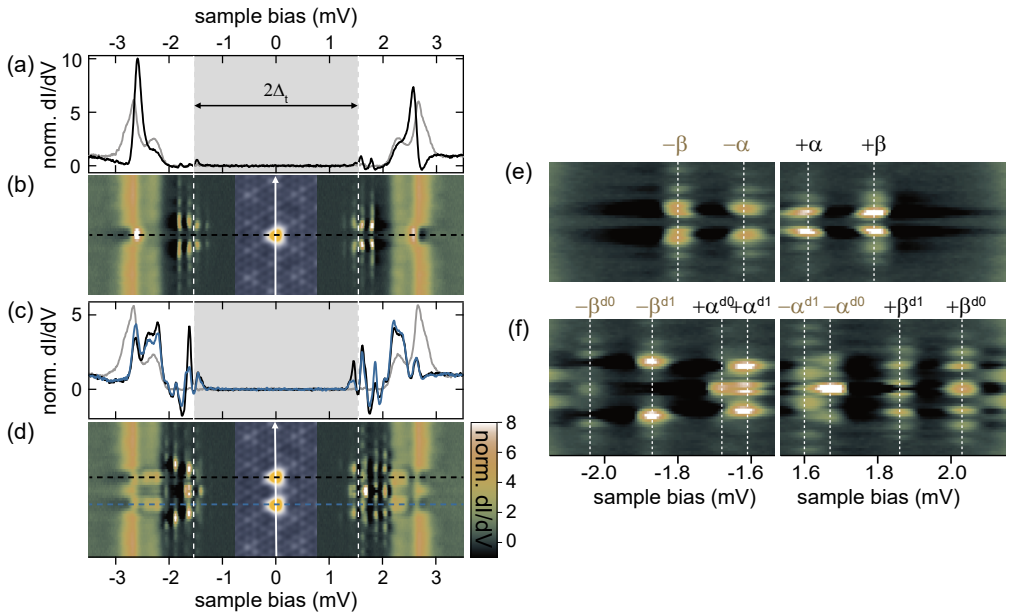

Fig. 5.2.: (a,c) Normalized differential conductance spectra recorded on the atom(s) (black, blue) of the monomer (a) and dimer (c) and on the bare $NbSe_2$ (gray). Feedback was opened at $250\,\mathrm{pA}, 5\,\mathrm{mV}$ and a modulation of $15\,\mu\mathrm{V}$ was used. The (Nb) tip gap of $\Delta_t \approx 1.55\,\mathrm{meV}$ is indicated in gray. (b,d) Stacked spectra recorded across the monomer (b) and the dimer (d) as illustrated in the inset topographies (constant-current mode with set point $100\,\mathrm{pA}, 10\,\mathrm{mV}$). Horizontal dashed lines serve mark the position of the spectra from (a,c). Vertical dashed lines indicate Δ_t. (e,f) Zoom into the energy gap of the substrate of (b,d). The (hybrid) α- and β-states are indicated by the dotted lines and labeled on the top of each graph. Data of the single Fe atom reproduced from Fig. 4.11a,c.

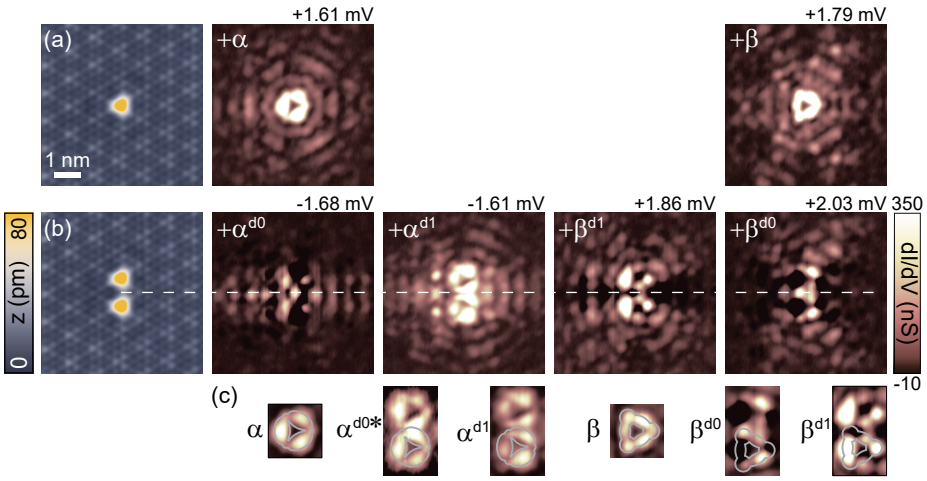

Fig. 5.3.: (a,b) STM topographies (constant-current mode with set point $100\,\mathrm{pA}, 10\,\mathrm{mV}$) of the single Fe atom (a) and a Fe dimer (b) with spacing of $3a$ in the left. Corresponding constant-contour $\mathrm{d}I/\mathrm{d}V$ maps of the (hybridized) YSR states in the monomer (a) and dimer (b) in the right. Constant-contour feedback was opened at $250\,\mathrm{pA}, 5\,\mathrm{mV}$ and a modulation of $15\,\mu\mathrm{V}$ was used. Bias voltages are given above each panel and are indicated in Fig. 5.2e,f by the white dotted lines ($\Delta_\mathrm{t} \approx 1.55\,\mathrm{meV}$). (c) Close-ups around the atoms' center for the monomer and dimer α- and β-states. Gray lines serve as guide to the eye. For α^{d0} the thermally activated resonance ($\alpha^{\mathrm{d0}*}$) is shown. Data of the single Fe atom reproduced from Fig. 4.11e.

To gain further insight, we examine $\mathrm{d}I/\mathrm{d}V$ maps at the corresponding peak energies in Fig. 5.3b (topography of the dimer in the left panel, only one polarity of the $\mathrm{d}I/\mathrm{d}V$ data shown, for clarity). Data of the opposite polarity can be found in Appendix A.5. In agreement with the line profiles, the maps recorded at $+1.86\,\mathrm{mV}$ and $-1.61\,\mathrm{mV}$ clearly exhibit suppressed intensity all along the line perpendicular to the dimer axis, *i.e.* a nodal plane (horizontal dashed line as a guide to the eye), while the resonances recorded at $+2.03\,\mathrm{mV}$ and $-1.68\,\mathrm{mV}$ do not. Thus, the wave functions indeed seem to be symmetric and antisymmetric linear combinations.

As done in the previous chapter we can analyze the shape of the hybrid states to discern their origin (hybrid α- or β-state). The near-field shapes of the YSR patterns are shown as close-up views in Fig. 5.3c. The monomer β-state exhibits intensity at the sides and vertices of a triangular shape (outlined by gray lines) while the monomer α-state has largest intensity at the sides of the triangle and only small residual intensity at the vertices. Note that the states at $-1.68\,\mathrm{mV}$ and $+2.03\,\mathrm{mV}$ are strongly affected by the negative differential conductance (NDC) of the adjacent resonances at lower energy. Because of this we present data recorded at the energy of the thermal duplicate (indicated with a star) of the state at $-1.68\,\mathrm{mV}$ in the scale-up (Fig. 5.3c). As being too far away from the Fermi level, no thermal data for the state at $+2.03\,\mathrm{mV}$ is available. The patterns of the dimer recorded at $-1.61\,\mathrm{mV}$ and $-1.68\,\mathrm{mV}$ closely resemble the one of the original α-state at positive bias (for comparison of the shape at the different polarity, see Fig. A.12). Therefore, these states are identified as symmetric (antisymmetric) hybrid α-states and labeled - according to the number of nodal planes - as α^{d0} (α^{d1}). Note already that the hybrid states of the

$+\alpha$-resonance are found at negative bias, *i.e.* undergo a quantum phase transition (QPT) upon hybrid state formation [Din+21]. Beside the similarity of the hybrid states with the monomer wave function, the assignment of both hybrid α-states to be on the same side of the Fermi level is supported by the fact that the hybrid states resemble linear wave function combinations within our $\mathrm{d}I/\mathrm{d}V$ maps corresponding to the hybrid doublet (*c.f.* section 5.1.2). As discussed in section 5.1.2, we expect different excitations if both hybrid states are on different sides of the Fermi level. In this case, the lower energy state of the *hybrid doublet* is the ground state and we cannot excite the other state of the hybrid doublet by single electron tunneling. Hence, we do not expect to find both linear combinations within the maps. Possible excitations (by tunneling with a single electron) involve wave functions with different spatial fingerprints [Yao+14b].

Similarly - albeit with strong intensity deviations from the monomer due to the hybridization and NDC effects - the states at $+2.03\,\mathrm{mV}$ and $+1.86\,\mathrm{mV}$ can be identified to be β-like. The antisymmetric combination, labeled β^{d1} exhibits large intensity at one of the vertices (right). The assignment of β^{d0} to the resonance at $+2.03\,\mathrm{mV}$ is more difficult as this state is strongly affected by the NDC of β^{d1}. However, despite the suppression of intensity by the adjacent resonance (β^{d1}) it still exhibits fingerprints of intensity at both left vertices. Furthermore, the energetic location (being within the energy gap) and the nature of the long-range scattering pattern of the negative counterparts (data and discussion can be found in Appendix A.5) further support this assignment.

Thus, we observe the formation of hybrid α- and β-states. From section 4.4 we know that the α- and β-states are in the screened-spin regime for single HC atoms on the maximum of the CDW implying a negative ground state energy (*c.f.* Fig. 4.3c, red region). In the dimer, both α-resonances have crossed zero energy while both β-resonances stay on the same bias side implying a transition to the free-spin regime for the α-states. Figure 5.4a compiles the ground state energies of monomer and dimer extracted from deconvolved data. Details on the data evaluation are provided in section 6.2.1 when we extend the dimer by an atom and evaluate the hybrid trimer states.

As discussed in section 5.1.2 we can excite the symmetric and antisymmetric wave functions of the hybrid doublet from different singlet and triplet ground states. Thus, in the dimer, β is probably in the screened-spin singlet or triplet ground state depending on the RKKY interaction I. As we find both hybrid doublet α-excitations on the other bias side (free-spin regime, *c.f.* Fig. 4.3c, blue region) the ground state of the coupled α-state is presumably one of the free-spin phases (*c.f.* Fig. 5.1b).

From Fig. 5.4a we extract splittings of $D_\alpha = (69 \pm 33)\,\mu\mathrm{eV}$ and $D_\beta = (173 \pm 33)\,\mu\mathrm{eV}$. Note that the energetic order of the symmetric and antisymmetric states of the α- and β-states is reversed: β^{d0} is found at lower energies than β^{d1} while α^{d0} is at higher energies than α^{d1}. The hybridization between YSR wave functions depends on their overlap whose sign and magnitude is governed by the oscillatory nature of the YSR wave functions

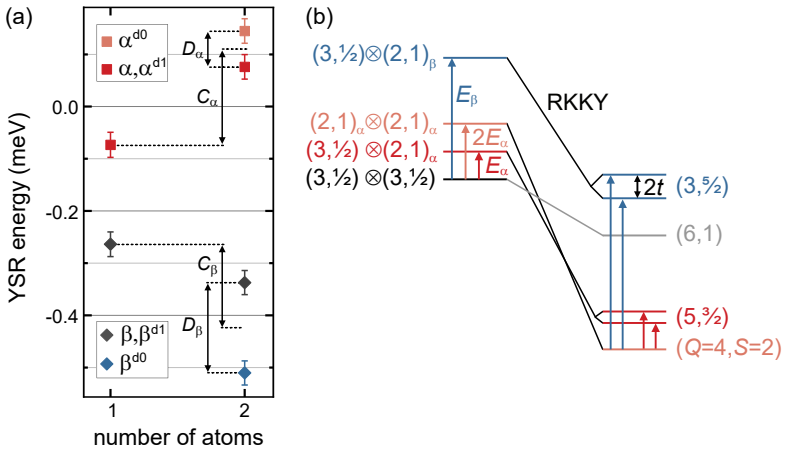

Fig. 5.4.: (a) Energies of the (hybrid) α- and β-states of the monomer and dimer obtained by fitting multiple deconvolved DOS traces as described in detail in section 6.2.1. (b) Schematic level diagram showing the effect of the RKKY interaction upon dimer formation. Details are discussed in the text.

[Rub+18]. Thus, the energetic order of the symmetric and antisymmetric hybrid states can be reversed.

Moreover, we note that both, α- and β-hybrid states exhibit large center of mass shifts in different directions of $C_\alpha = (184 \pm 29)\,\mu\text{eV}$ and $C_\beta = (-160 \pm 29)\,\mu\text{eV}$ which cannot be explained in the classical models [Rub+18; Din+21] which predict small shifts with the same trend for all YSR resonances. Indeed, the substantial shift even drives α to the free-spin ground state upon dimerization yielding a different spin state of the individual atoms within the dimer as compared to the monomer. We can qualitatively explain these observations by considering quantum-spin impurities interacting via RKKY interaction. To recall, the energy contributions of the RKKY interaction of two coupled spins scale with the total spin ($\propto I(d)\,\mathbf{S}_1 \cdot \mathbf{S}_2$, *c.f.* Eq. 5.1)

For the single Fe atoms we assume a total spin of $S = 1/2$ resulting from one of the higher energy YSR states, γ or δ, being in the free-spin regime and all other channels being screened, *i.e.* $(Q, S) = (3, 1/2)$. The situation without coupling is indicated in the left of Fig. 5.4b, with $(3, 1/2) \otimes (3, 1/2)$ being the ground state of two non-interacting impurities. α- and β-excitations annihilate a quasiparticle and increase the total spin, leading to $(2, 1)$ for the excited single atom (indicated in dark red and blue). With coupling (right) the levels are downshifted by the RKKY interaction. While the former ground state is only slightly downshifted due to its small total spin (gray), the RKKY-induced shifts of levels with higher total spin are stronger.

The α-states of both atoms in the dimer undergo the QPT to $(2, 1)$ leading to a new ground state with $(4, 2)$ for the dimer when assuming FM coupling. Hence, we can understand the QPT from monomer to dimer as being due to a larger gain in RKKY energy, which overcompensates the cost in YSR energy for unscreening the α-states of both atoms ($2E_\alpha$, bright red). The two states (shown in dark red and blue) in which one of the

monomers is in an excited state are further split by hybridization (t). In the dimer, exciting the α-channel which is now in the free-spin regime creates a bound quasiparticle and reduces the total spin $(5, 3/2)$, while excitation of the β-channel annihilates a quasiparticle and increases the total spin to $(3, 5/2)$. These YSR excitations are indicated by red and blue colored arrows for α and β states, respectively. Other excitations are not possible by single electron tunneling. Thus, the large shifts (C) arise from the RKKY interaction, the splitting (D) originates from the hybridization t.

Concluding, we identify clear symmetric and antisymmetric linear wave function combinations of the α- and β-states on the dimer with its atoms on adjacent maxima of the CDW. We explain the large shifts upon dimerization by the RKKY interaction which even drives the α-state through the QPT. In section 6.2 we will expand the dimer by stepwise increasing the atom number and track the evolution of the hybrid YSR states. Before that we investigate different dimers in the next two sections.

5.2.2 Hybridization starting from overlapping states

Before moving to dimers with different interatomic spacings which offer a rich playground to examine the influence of the CDW on YSR hyridization we compare the result of the previous section with a dimer with equal spacing of $3a$, but consisting of atoms sitting on minima of the CDW (*c.f.* atom III, section 4.4). Hence, we again expect effective hybridization as the YSR states induced by both atoms (individually) have equivalent energies. In contrast to HC atoms on a maximum, where both resonances are well separated, the α- and β-states already strongly overlap in single HC atoms placed on a minimum of the CDW (*c.f.* sections 4.4 and 4.5). Hence, this dimer (min-min) provides a different starting point for hybridization.

Figure 5.5a,b accommodates spectra recorded on the atom's center (black) and spectra recorded across a single Fe atom sitting on the minimum of the CDW (data reproduced from Fig. 4.11b,d, but still shown here for better comparison). The α- and β- resonances are found very close to zero energy, *i.e.* at $|\pm V_{\mathrm{bias}}| \gtrsim \Delta_{\mathrm{t}}/e$ as discussed before (see also the zoom to the energy gap of the substrate provided in Fig. 5.5e). Note that there is a third state within the substrates energy gap (white arrow) which was discussed in terms of a magnetic anisotropy-induced excitation of the β-state in section 4.5.

Without moving the first atom, we precisely place the second atom in a distance of $3a$ on the adjacent minimum of the CDW. We note an enormous change in the spectra from monomer to dimer (Fig. 5.5c,d,f). In particular, we detect four states within the low-energy window (energy gap of the substrate) as indicated by the white dotted lines in Fig. 5.5f. In turn, all resonances are mirror symmetric around the dimer center and exhibit either increased or suppressed intensity centrally between both atoms which points towards hybridization.

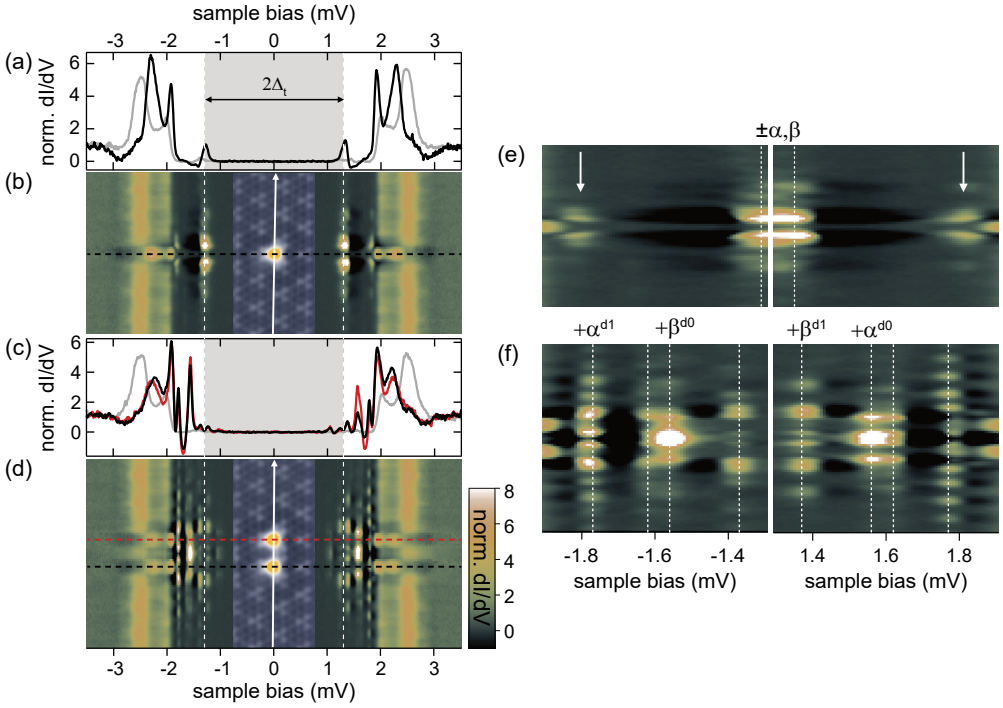

Fig. 5.5.: (a,c) Normalized differential conductance spectra recorded on the atom(s) (black, red) of the monomer (a) and dimer (c) and on the substrate (gray). Feedback was opened at $750\,\mathrm{pA}, 5\,\mathrm{mV}$ and a modulation of $15\,\mu\mathrm{V}$ was used. (b,d) Stacked spectra recorded across the monomer (b) and the dimer (d) as illustrated in the inset topographies (constant-current mode with set point $100\,\mathrm{pA}, 10\,\mathrm{mV}$). Horizontal dashed lines display the precise location of the spectra in (a,c). Vertical dashed lines and gray box indicate the Nb tip gap $\Delta_t \approx 1.30\,\mathrm{meV}$. (e,f) Zoom into lower energies of (b,d). The hybrid states are indicated by the white dotted lines and partially labeled on the top of each graph. The white arrow points out an additional YSR resonance of the single atom within the substrate's energy gap. Data of the single Fe atom reproduced from Fig. 4.11b,d.

As before, we inspect the wave functions in more detail in the $\mathrm{d}I/\mathrm{d}V$ maps recorded on the monomer and dimer (Fig. 5.6) in order to identify symmetric and antisymmetric hybrid states. As discussed in section 4.4 the $\mathrm{d}I/\mathrm{d}V$ map of the monomer close to zero energy inherits signatures of the α- and the β-state as they nearly coincide. Analyzing the patterns found across the dimer one clearly identifies symmetric and antisymmetric states exhibiting none and one nodal plane, respectively. In particular, the states found at $\pm 1.77\,\mathrm{mV}$ and $\pm 1.37\,\mathrm{mV}$ display a nodal plane while the state at $\pm 1.56\,\mathrm{mV}$ has enhanced intensity between both atoms, *i.e.* at the dimer center. At odds, the state at $\pm 1.62\,\mathrm{mV}$ has symmetric character at positive bias while there seems to be a nodal plane at the negative counterpart. However, as this state is in close vicinity to the one at $\pm 1.56\,\mathrm{mV}$, it could be affected by its NDC presumably suppressing intensity at the dimer's center.

Turning towards the α- and β-characteristics - intensity on triangle sides and vertices for the β-states versus main intensity at the triangle sides for α-like states - we try to classify the hybrid wave functions in terms of their origin (α- or β-like). The near-field structures found at $-1.77\,\mathrm{mV}$ and $+1.37\,\mathrm{mV}$ inherit α- and β-characteristics, respectively, as is illustrated in the close-ups in Fig. 5.6c and are therefore labeled as $+\alpha^{\mathrm{d}1}$ and $+\beta^{\mathrm{d}1}$ (as above the number pertains to the number of nodal planes). However, the patterns found at $\pm 1.56\,\mathrm{mV}$ do not inherit clear α- or β-fingerprints as can be seen in Fig. 5.6c, black box. While one could find residual intensity at the right vertex (of each atom) mimicking a β-like state at negative energies (labeled as $+\beta^{\mathrm{d}0}$), the state lacks intensity at its vertices at positive energies rather pointing toward an α-like resonance (labeled $+\alpha^{\mathrm{d}0}$). Thus, while the number of states matches the expectations (four resonances at each bias side), it is not possible to assign all hybrid states to be α- or β-derived (as in section 5.2.1, max-max dimer).

As both states largely overlap in the monomer, it is probable that the simplified tight-binding approach considering the α- and β-channels individually and expecting the hybrid wave functions to be pure linear combinations of them fails here. As shown in the previous section this model is adequate for the max-max dimer where both channels remain separated, but seems to fail here when the (multiple) states overlap. When the states are close in energy, they can mix (leading to a different set of basis wave functions) and with that the hybrid states loose their α- and β-attributes. Furthermore, as already mentioned above, if one of the α- or β-derived hybrid doublet phases is the ground state, symmetric and antisymmetric combinations are located on different sides of the Fermi level and there are different excitations involved (section 5.1.2) which do not necessarily inherit characteristic (anti)symmetric wave function patterns. Thus, this can further complicate the excitations probed with STM.

To conclude this section, we observe hybridization in dimers consisting of two atoms on adjacent CDW minima. Identification of the hybrid states in terms of α- and β-signatures as for the max-max dimer (section 5.2.1) is not possible due to possible mixing effects. Similar findings hold for other dimers with spacing of $3a$ consisting of atoms on other

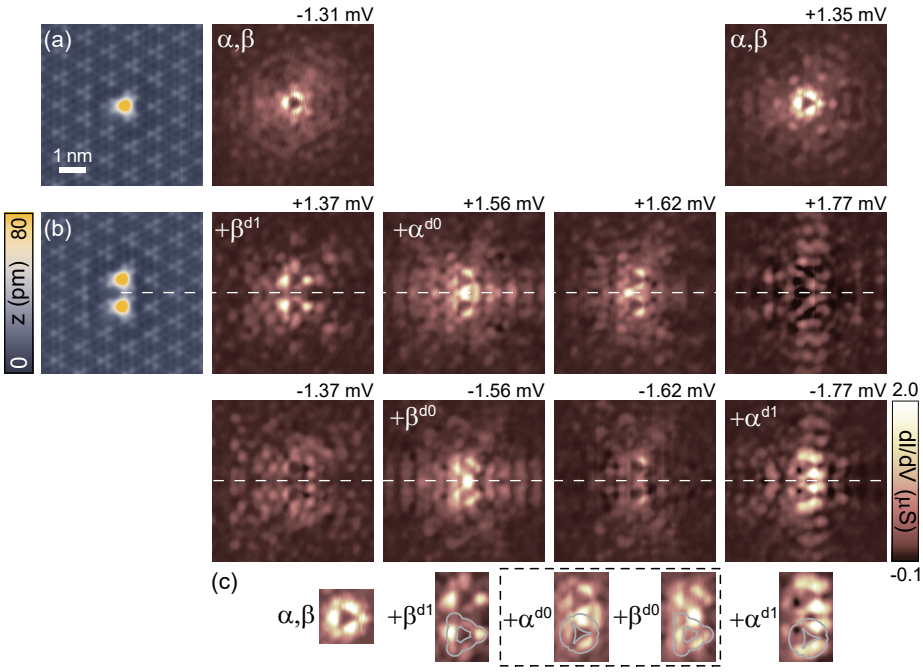

Fig. 5.6.: (a,b) STM topographies (constant-current mode with set point $100\,\mathrm{pA}, 10\,\mathrm{mV}$) of the single Fe atom and a Fe dimer with spacing of $3a$ in the left. Corresponding constant-contour $\mathrm{d}I/\mathrm{d}V$ maps of the (hybridized) YSR states in the monomer (a) and dimer (b). Constant-contour feedback was opened at $750\,\mathrm{pA}, 5\,\mathrm{mV}$ and a modulation of $15\,\mu\mathrm{V}$ was used. Bias voltages are given above each panel and are indicated in Fig. 5.5e,f by the white dotted lines ($\Delta_\mathrm{t} \approx 1.30\,\mathrm{meV}$). (c) Close-ups around the atoms center of selected monomer and dimer states. Gray/white lines serve as guide to the eye. Data of the single Fe atom reproduced from Fig. 4.11f.

positions relative to the CDW like atoms II or IV in section 4.4 (not shown). From that we conclude that the magnetic moment of Fe atoms with spacing of $3a$ couple via the RKKY interaction. However, we cannot access the sign on the RKKY interaction from our tunneling experiment. Moreover, we observe clear fingerprints of YSR wave function hybridization as the YSR states are sufficiently similar in dimers with interatomic separation of $3a \approx a_{\mathrm{CDW}}$.

After having studied dimers which respect the CDW periodicity, we can go a step further. We exploit the rich framework set by the CDW and study dimers with different interatomic separations in the next section.

5.3 Hyridization within the landscape of the incommensurate CDW

The slight mismatch between the CDW periodicity ($\gtrsim 3a$) and the lattice causes a landscape of alternating areas with the HC- and CC-CDW structure (which smoothly transform into each other on the order of $\sim 10\,\mathrm{nm}$). The two different phases of the CDW are schematically illustrated in Fig. 5.7a,b using the same coloring as in section 4.4. To recall, the high symmetry positions (HC structure) on the maximum and minimum are colored in dark blue and dark red. The bright brown sites do not have any symmetry. In the CC structure all sites have mirror symmetry, but different colored sites differ in their position within the CDW lattice. As the position within the CDW lattice affects the YSR energy and wave functions, the CDW creates different landscapes for coupling of the YSR states.

Figure 5.7c,d show topographies of two different series of dimers with interatomic spacings ranging from $4a$ to $1a$ (the single atom shown in the left panel, for clarity). Such building sequences within a pure CDW domain are possible as the CDW transforms between the two phases on a larger scale. The approach series displayed in (c) is obtained in a region with HC-CDW structure. In (d) one can discern the CC-phase of the CDW in the background around the atoms.[5] Within each approach series, the atom marked with the star is not moved while a second Fe atom is positioned precisely with the STM tip in order to form the desired dimers. The exact arrangement of the dimer atoms relative to each other and within the CDW for both approach series are indicated in Fig. 5.7a,b. The star marks the location of the first (non-moved) atom. The position of the second atom is indicated by the numbers (where the numbers indicate the spacing between both atoms in terms of lattice sites). One can see that for the approach series within the HC-CDW (where the static atom is located on a CDW minimum, dark red site) the atoms have equal CDW positions only for an interatomic spacing of $3a$. It was shown in the previous chapter that such dimers indeed hybridize. For spacings of $4a, 2a, 1a$ the atoms forming the dimer do

[5] The only exception is the dimer with spacing $1a$ within the HC-series, where the CDW switched to the CC pattern upon manipulation as discernable in the right of the topography (right panel in Fig. 5.7c).

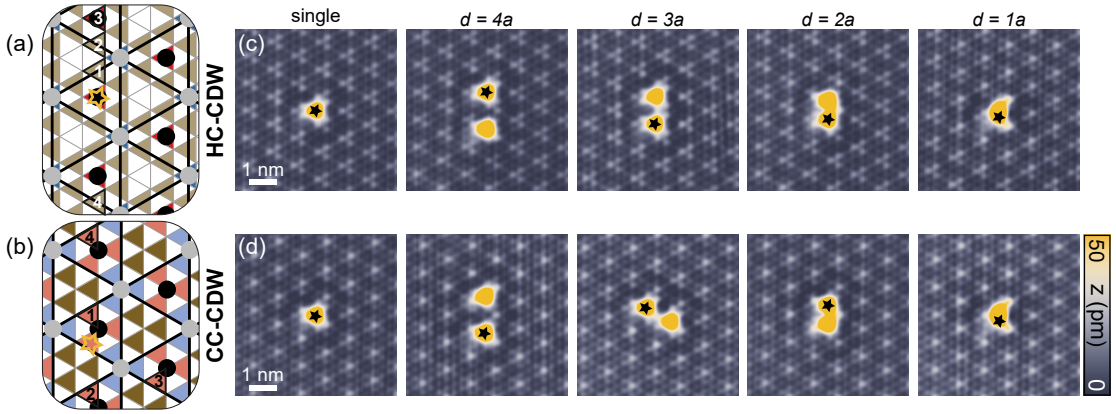

Fig. 5.7.: (a,b) Schematic illustrations of the different possible adsorption sites of HC adatoms within the HC- (c) and CC- (d) CDW structure using the same coloring as in Fig. 4.8b. The CDW is depicted by the black grid, where gray (black) dots indicate CDW maxima (minima). Additionally, the Se grid is overlaid in gray (Se atoms located at vertices of the triangles). Different atomic positions corresponding to the data in (c) and (d) are indicated by the star and the numbers. (c,d) Constant-current STM images showing a single Fe atom and dimers with different spacings as indicated above the panels (set point: $100\,\mathrm{pA}, 10\,\mathrm{mV}$, recorded with a Nb tip). The black star marks the atom which was not moved during the data acquisition. The CDW in the background is in the HC and CC phase in (c) and (d), respectively.

not sit on identical positions relative to the CDW and hence, their YSR energies and wave functions differ. For the approach series within the CC-structure one finds that creation of dimers with spacings from $4a \rightarrow 1a$ is possible with the dimer atoms placed on equal positions relative to the CDW (star and numbers on bright red sites). Results of these two different building sequences focusing on the dimers with separations of $2a, 3a$ and $4a$ are discussed and compared in the following two sections in terms of the impact of the CDW on the hybridization between the Fe atoms. Dimers with spacing of $1a$ are not placed in the dilute coupling limit, but interact directly via their d levels. Results obtained on such dimers are addressed in detail in section 6.3.

5.3.1 Different dimers in the HC-CDW structure

Figure 5.8a,b compiles data of the approach series within the HC-CDW structure (*c.f.* Fig. 5.7c). Note that all data of the single atom and the $3a$-dimer is reproduced from Fig. 5.5, but still presented here for better comparison. In (a) we plot spectra recorded centrally on the single atom and the dimer atoms with different separations as indicated for each set of traces. The black traces are recorded on the atom marked by the star in Fig. 5.7c and the red/brown data on the second dimer atom. A substrate trace is shown in gray in each panel. The colors are chosen to indicate the adsorption site of the second Fe atom within the CDW lattice (*c.f.* Fig. 5.7a). Figure 5.8b accommodates stacked spectra recorded along lines across all dimers (and the single atom) with the precise location of each line indicated in the inset topographies. Further, the position of

the spectra shown in (a) is indicated by the horizontal lines in the according color. As before, Δ_t is indicated by the gray box and the vertical dashed lines.

From the previous section we know that there is sizeable hybridization in the $3a$-dimer as identified by the symmetry in the line profile and the fingerprints of hybrid wave functions in the $\mathrm{d}I/\mathrm{d}V$ maps (*c.f.* Figs. 5.5 and 5.6). In this section, we do not aim to interpret every single YSR resonance in terms of their α- or β-characteristics as their identification is not straightforward (*c.f.* section 5.2.2). We rather exploit the $\mathrm{d}I/\mathrm{d}V$ maps with regard to the presence or absence of hybrid wave functions.

In Fig. 5.8a we see already that the spectra recorded on both dimer atoms are significantly different from each other within the $2a$- and $4a$-dimer (compare black and brown traces). Concomitant, we do not find horizontal mirror symmetry around the dimer center in the corresponding line spectra. A zoom (of both line spectra) to lower energies can be found in Fig. 5.9a,b. Note that in both dimers we find an increased number of resonances which could be missinterpreted as fingerprint of hybridization. These resonances rather originate from the long-range nature (several $\sim \mathrm{nm}$) of the YSR wave functions (of the single atoms) which is much larger than the dimer separations of $\approx 0.7\,\mathrm{nm}$ ($\approx 1.4\,\mathrm{nm}$) for the $2a$ ($4a$) dimer. Therefore, we find resonances of the second atom (brown) in the spectra of the first atom (and vice versa). This scenario is further supported by the $\mathrm{d}I/\mathrm{d}V$ data as discussed in the following.

Representative $\mathrm{d}I/\mathrm{d}V$ maps recorded on the $4a$- and $2a$-dimers are presented in Fig. 5.9c,d (topography in the left). The bias voltages at which the maps are recorded are given in the top of each panel and are indicated in the close-ups of the line spectra (vertical dotted lines). The horizontal dashed lines at the center of each dimer serve as guides to the eye. None of the patterns resembles symmetric or antisymmetric wave function combinations with a horizontal mirror axis or nodal plane (as observed for the $3a$-dimer, Fig. 5.6) which would hint towards hybridization. Thus, the patterns rather result from (long-ranged) YSR states emerging from the individual atoms within the dimer yielding the complex patterns.

Despite the lack of any fingerprint of hybrid wave functions, we note that the wave functions are still affected by the presence of the second impurity (*i.e.* we can not identify characteristic wave function patterns of the single HC atom on the minimum of the CDW in the data neither). The YSR energies are shifted with respect to the single-atom resonances.

These experimental findings can be rationalized within the scheme presented in section 5.1.2. The spins of both atoms within the dimer couple due to the RKKY interaction (with its magnitude and sign dictating the ground state). However, the hybridization between the YSR wave functions (creating the hybrid doublet phase) can be significantly reduced or completely suppressed as the YSR wave functions are detuned in energy (and also obey different symmetry) owing to their different positions relative to the CDW. Moreover, since

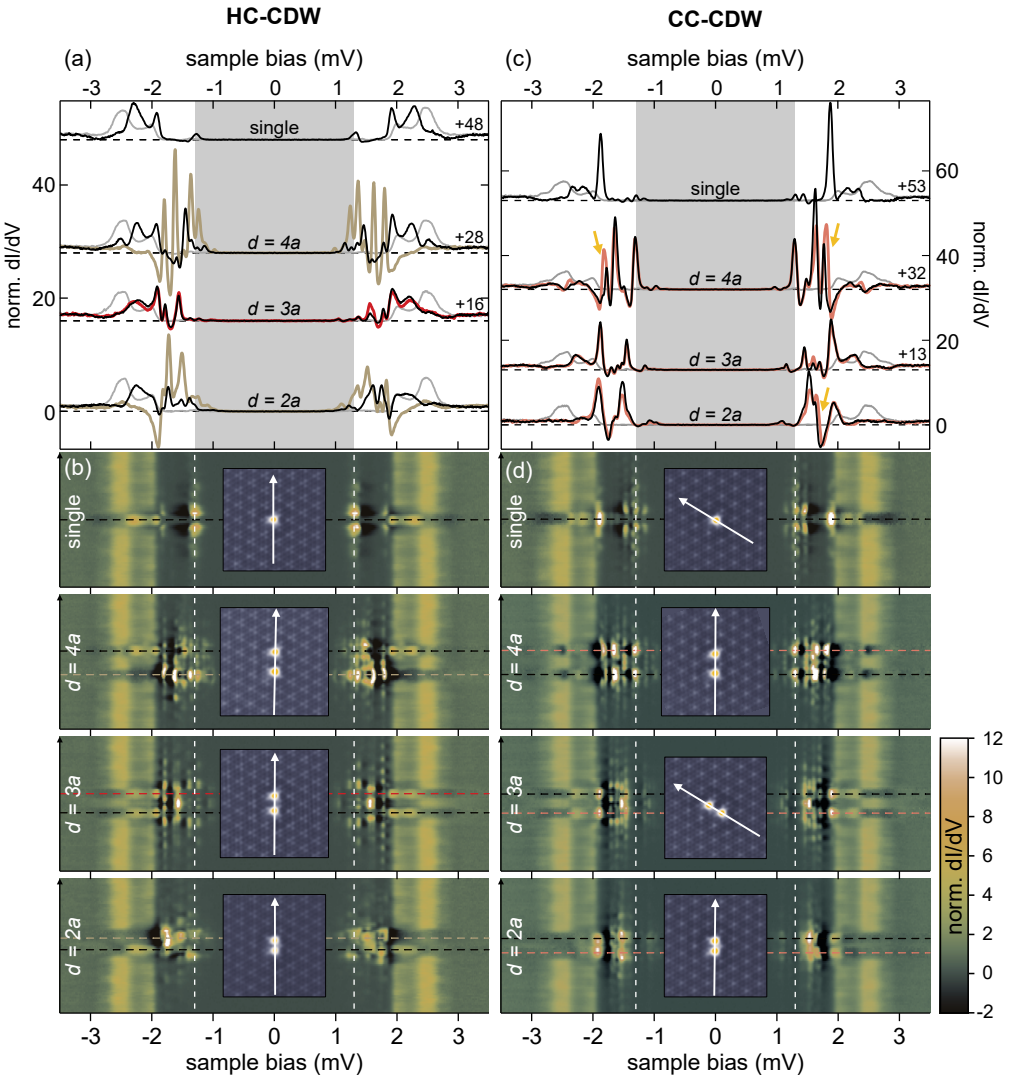

Fig. 5.8.: (a) Normalized differential conductance spectra recorded on the atom(s) of the monomer (top) and dimers with different spacings (lower traces) as indicated in the graph acquired in the HC-CDW structure. Data on atoms in black and color. A substrate spectrum is shown in gray. Offsets are indicated in the right of each set of traces. (b) Stacked $\mathrm{d}I/\mathrm{d}V$ spectra recorded across the monomer and the different dimers from (a) as illustrated in the inset topographies (topographies reproduced from Fig. 5.7c). (c,d) accommodate the analogue data set of (a,b) within the CC-CDW recorded on the atoms shown in Fig. 5.7d. Feedback was opened at $750\,\mathrm{pA}, 5\,\mathrm{mV}$ and a modulation of $15\,\mu\mathrm{V}$ was used. The (Nb) tip gap $\Delta_\mathrm{t} \approx 1.30\,\mathrm{meV}$ is indicated by the gray box/vertical lines. Horizontal dashed lines in (b,d) indicate the position of the spectra of (a,c). Yellow arrows highlight some features of the data as discussed in the text.

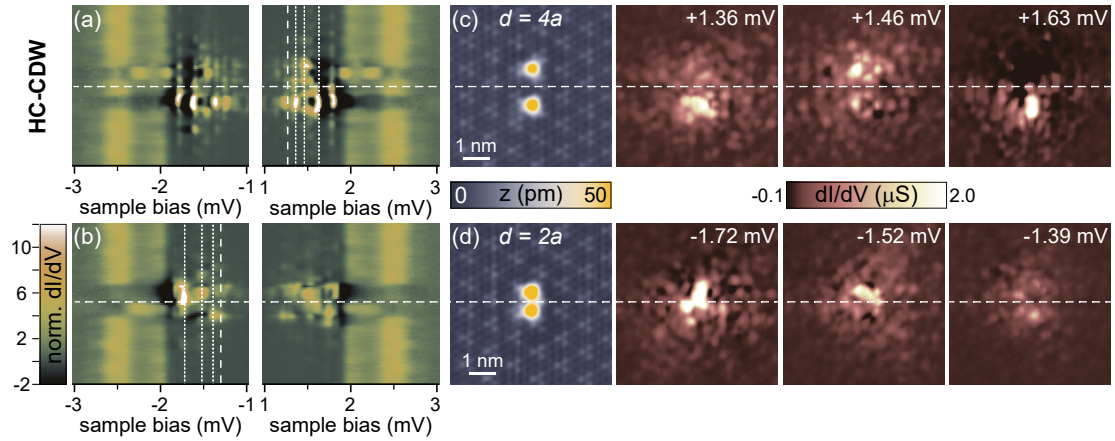

Fig. 5.9.: (a,b) Zoom into the line profiles already presented in Fig. 5.8b for dimers with a spacing of $4a$ (a) and $2a$ (b) in the HC-CDW. Vertical dotted lines indicate the bias voltage of the $\mathrm{d}I/\mathrm{d}V$ maps shown in (c,d). $\Delta_\mathrm{t} \approx 1.30\,\mathrm{meV}$ is indicated by white dashed lines. (c,d) STM topographies (constant-current mode with set point $100\,\mathrm{pA}, 10\,\mathrm{mV}$) of the $4a$ and the $2a$ dimer in the left. Corresponding constant-contour $\mathrm{d}I/\mathrm{d}V$ maps of selected YSR states of both dimers in the right. Constant-contour feedback was opened at $750\,\mathrm{pA}, 5\,\mathrm{mV}$ and a modulation of $15\,\mu\mathrm{V}$ was used. Horizontal dashed lines serve as guide to the eye.

one atom located on the CDW minimum (where the α-state is in the free-spin regime) is involved, both impurities can differ in the total spin S meaning that they can have different numbers of occupied quasiparticle states. The fact that the $\mathrm{d}I/\mathrm{d}V$ patterns seem to originate from the individual impurities indicates that the exchange coupling between each impurity and the substrate is stronger than the spin-spin interaction mediated by the RKKY interaction ($J, \Delta > I$) as otherwise (if the spins couple mainly among each other and then the total spin of the dimer interacts with the substrate) one would expect one single YSR wave function centered on the dimer.

Thus, we do not find clear evidence for hybridization in Fe dimers whose spacings do not match the CDW periodicity. Indeed, considering the different positions within the CDW lattice we know that the atoms exhibit different YSR energies and wave functions which can reduce or prevent sizeable hybridization within the atomic dimers. Hence, our study of such dimers underpins the importance of the position of the individual atoms relative to the CDW as prerequisite to effectively couple YSR wave functions in magnetic dimers on $NbSe_2$. In order to further confirm the CDW as the reason for absent hybridization we compare the results of this section to data of the analogue approach series within the CC-CDW, where the CDW should allow hybridization also for $2a$- and $4a$-dimers.

5.3.2 Different dimers in the CC-CDW structure

Figure 5.8c,d presents the analogue dataset as shown in (a,b), but the dimers are assembled within a region with CC-CDW structure (*c.f.* Fig. 5.7b,d). As before, the spectra recorded on the different dimers are very different. However, within each dimer, we notice that the spectra recorded on the individual atoms exhibit similar YSR states for

all separations. This is in contrast to the findings of the HC-approach series, where the spectra obtained one the individual atoms of the $4a$- and $2a$- dimers were very different. Also the line spectra inherit a large degree of symmetry (horizontal mirror axis) for all three different dimers. Enlarged views of the line spectra can be found in Fig. 5.10a-d. The intensity distribution along the line spectra points towards the presence of hybrid wave functions in all dimers as we find states which lack intensity and states with increased intensity centrally between both atoms.

Again, we inspect $\mathrm{d}I/\mathrm{d}V$ maps for further insight. We show representative maps (energies indicated by vertical dotted lines in the enlarged line spectra) for the single atom and for the different dimers in Fig. 5.10e-h (topography in the left and $\mathrm{d}I/\mathrm{d}V$ data in the right panels). Horizontal dashed lines through the dimer center serve as guide to the eyes. As before, we do not aim at a complete identification of all hybrid wave functions in terms of their origin (α- or β-like), but rather search for characteristics of hybrid wave functions in the data. For the single atom, we show the map of the characteristic β-state (*c.f.* Fig. 4.7a, atom IV). In the $4a$-dimer we clearly identify the antisymmetric combination of the single atom β-state at $+1.58\,\mathrm{mV}$ (one nodal plane). Due to residual intensity at the right vertex (of each atom) the state at $-1.48\,\mathrm{mV}$ could be attributed to the symmetric β-like linear combination (enhanced intensity between both atoms). However, this assignment is rather tentative. For the $3a$-dimer we also find symmetric ($+1.45\,\mathrm{mV}$ and $-1.52\,\mathrm{mV}$) and antisymmetric ($-1.70\,\mathrm{mV}$) wave functions in the data.[6] Similar findings hold for a spacing of $2a$, where we discern a symmetric (antisymmetric) state at $-1.50\,\mathrm{mV}$ ($+1.64\,\mathrm{mV}$). However, as can be seen in the single and stacked spectra (Figs. 5.8c and 5.10d), several YSR resonances accumulate within an energy window of $\approx 0.3\,\mathrm{mV}$ around $1.5\,\mathrm{mV}$ for the $2a$-dimer leading to a broad peak distribution. Therefore, also the signal of several resonances overlaps within one $\mathrm{d}I/\mathrm{d}V$ map yielding less pronounced features such as nodal planes in the data.

Thus, in contrast to the data acquired in the HC-CDW, we find signatures of hybridization for all three dimers with separations of $4a, 3a$ and $2a$. In fact, this is in agreement with the expectations from Fig. 5.7b. All atoms are located on equivalent positions within the CDW lattice (bright red sites, *c.f.* atom IV in section 4.4) and, hence, should facilitate efficient hybridization between the YSR wave functions. This confirms the CDW as origin of absent hybrid states in the $2a$- and $4a$-dimers in the HC-CDW as it detunes the YSR energies such that hybridization is avoided.

Yet, while the dimer with spacing of $3a$ exhibits perfect symmetry around the dimer's center (*c.f.* line spectra and maps Fig. 5.10c), there are few deviations from perfect mirror

[6] The careful reader might notice the similarity between the wave function patterns of the minimum-minimum dimer (Fig. 5.6) and the data in Fig. 5.10g. This is not surprising as the positions relative to the CDW of the atoms forming both dimers are not too different. In Fig. 5.6 the atoms are located on a CDW minimum (*c.f.* atom III in section 4.4) while they sit close to the CDW minimum (*c.f.* atom IV in section 4.4) in Fig. 5.10g.

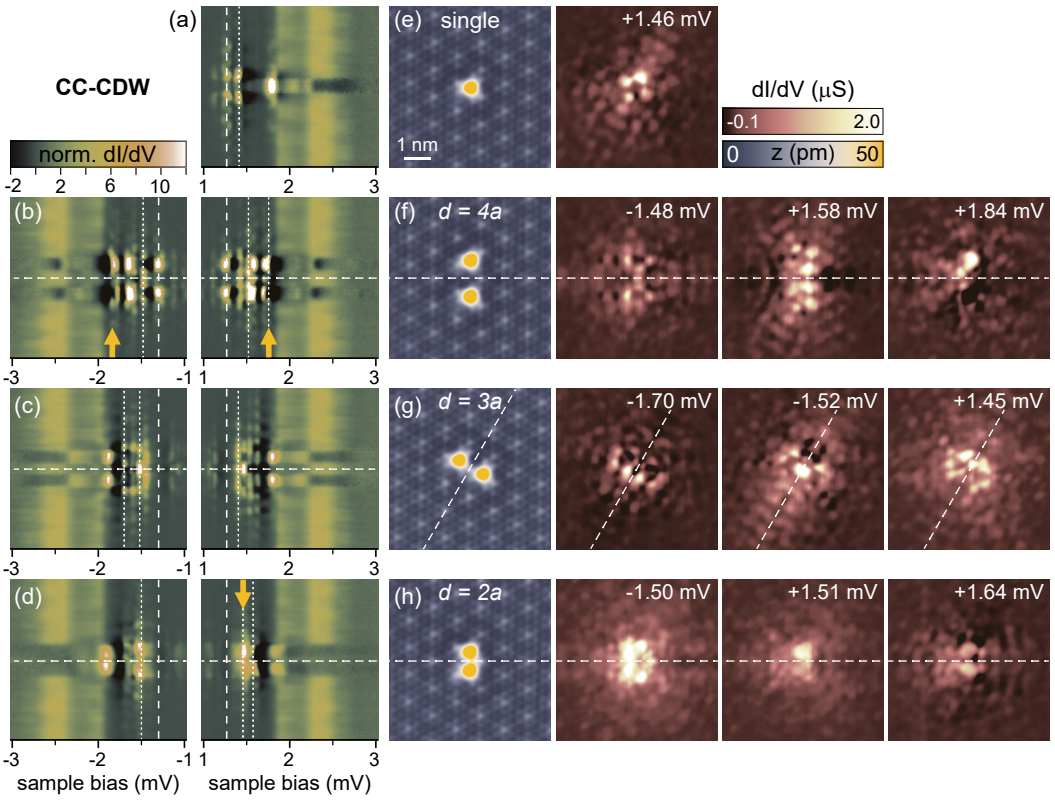

Fig. 5.10.: (a-e) Zoom into the line profiles already presented in Fig. 5.8d for the single atom (a) and dimers with spacings of $4a$ (b), $3a$ (c) and $2a$ (d) in the CC-CDW. Vertical dotted lines indicate the bias voltage of the $\mathrm{d}I/\mathrm{d}V$ maps shown in (e-h). $\Delta_\mathrm{t} \approx 1.30\,\mathrm{meV}$ is indicated by white dashed lines. (e-h) STM topographies (constant-current mode with set point $100\,\mathrm{pA}, 10\,\mathrm{mV}$) of the single atom and all dimers in the left. Corresponding constant-contour $\mathrm{d}I/\mathrm{d}V$ maps of selected YSR states in the right. Constant-contour feedback was opened at $750\,\mathrm{pA}, 5\,\mathrm{mV}$ and a modulation of $15\,\mu\mathrm{V}$ was used. Dashed lines serve as guide to the eye.

symmetry for spacings of $2a$ and $4a$ as highlighted with the yellow arrows in Figs. 5.8c and 5.10b,d. While being very pronounced on one of the dimer atoms, some YSR resonances seem to be suppressed by a strong NDC on the other atom. This can also be tagged in the $\mathrm{d}I/\mathrm{d}V$ maps at according energies. For example, the state at $+1.84\,\mathrm{mV}$ of the $4a$-dimer is very intense on the top atom, while its intensity is strongly suppressed by the NDC around the center of the bottom atom.[7] A further example of asymmetric intensities is presented along with the $2a$-dimer maps at $+1.51\,\mathrm{mV}$. Importantly, such asymmetric wave functions are not observed for any dimer with spacing of $3a$.

As already pointed out earlier, we notice a delicate interplay between Fe atoms and the CDW. On the one hand we find Fe atoms in many different positions relative to the CDW as exploited in section 4.4. On the other hand we observe manipulation-induced switches of the CDW. For example, attempts to place an Fe atom precisely in the third symmetric position of the HC-CDW structure (which is not found a-priori after deposition of Fe on the surface, *c.f.* Fig. 4.8b) induce a phase slip of the CDW relative to the crystal lattice. While dimers with spacing of $3a$ locally match the periodicity of the CDW other geometries could induce slight distortions in the CDW not discernable in the topographies which could cause the spectroscopic differences within the $2a$- and $4a$-dimers.

To close this chapter, we find that the position of the individual atoms forming a dimer within the CDW strongly affects the hybridization between the YSR wave functions. In detail, YSR hybridization is only facilitated when both atoms sit on equivalent sites relative to the CDW as their YSR wave functions and energies are otherwise too different to enable sizeable hybridization. Beside slight distortions, we observe hybridization in dimers with separations of $4a, 3a$ and $2a$ within the CC-CDW structure while the HC-structure restricts hybridization to dimers with a spacing of $3a$. Since both CDW-structures smoothly transform into each other, the CDW sets a smoothly varying energetic landscape. Hence, these findings are important prerequisites for the assembly of larger structures as addressed in the following chapter where we go far beyond atomic dimers and assemble magnetic chains.

[7] Note that the long-range pattern maintains the horizontal symmetry to some degree.

6 Beyond magnetic dimers - chains of magnetic impurities on $2H$-$NbSe_2$

This last chapter is dedicated to larger structures where we investigate adatom chains subject to different coupling mechanisms. First, we set the theoretical background. In 6.2 we track the formation of YSR bands in a dilute adatom chain and discuss the influence of the incommensurate CDW on the hybrid YSR-bands. Finally - starting again with the dimer - we exploit a different coupling regime in densely packed chains where the direct interaction between d levels dominates.

6.1 Theoretical models describing the interactions in atomic chains

In the first part of this section we study a very simple tight-binding model of a quantum wire in order to get a feeling how long-range interactions - as the RKKY interaction - could affect hybridization in assemblies with more than two atoms. Afterwards we introduce the full Hamiltonians for chains of magnetic atoms on superconductors.

6.1.1 Toy model of a freestanding chain

In this section we start with a simple discrete model of a quantum wire with N sites which allows us to study how additional on-site terms influence the eigenstates of the system. The Hamiltonian of such a chain reads:

$$\mathcal{H} = \sum_{i}^{N} (E_0 + V_i)\, c_i^\dagger c_i - t \sum_{i}^{N} (c_{i+1}^\dagger c_i + c_i^\dagger c_{i+1})\,, \tag{6.1}$$

where E_0 is the energy of the isolated state, t the hopping and $c_i^\dagger(c_i)$ create (annihilate) an electron at site i of the chain. There are additional site-dependent potential terms V_i which could effectively represent RKKY interactions[1] within a spin chain or long-range potential scattering terms. Depending on the site i, we account for nearest neighbor (NN) terms (V) as well as next nearest neighbor (NNN) contributions $(\tilde{V})$ and neglect longer-range interactions. By defining $\Psi = (c_1, c_2, ..., c_N)^T$ and applying $\mathcal{H} = \Psi^\dagger H \Psi$ we can pass over to matrix notation. Figure 6.1 shows Hamiltonians H_N for different chain lengths. The sketches of the chains and colors indicate the number of NN and NNN contributions for

[1] In section 5.1.1 we have seen that long-range oscillatory decay of the RKKY interaction can produce significant NNN contributions.

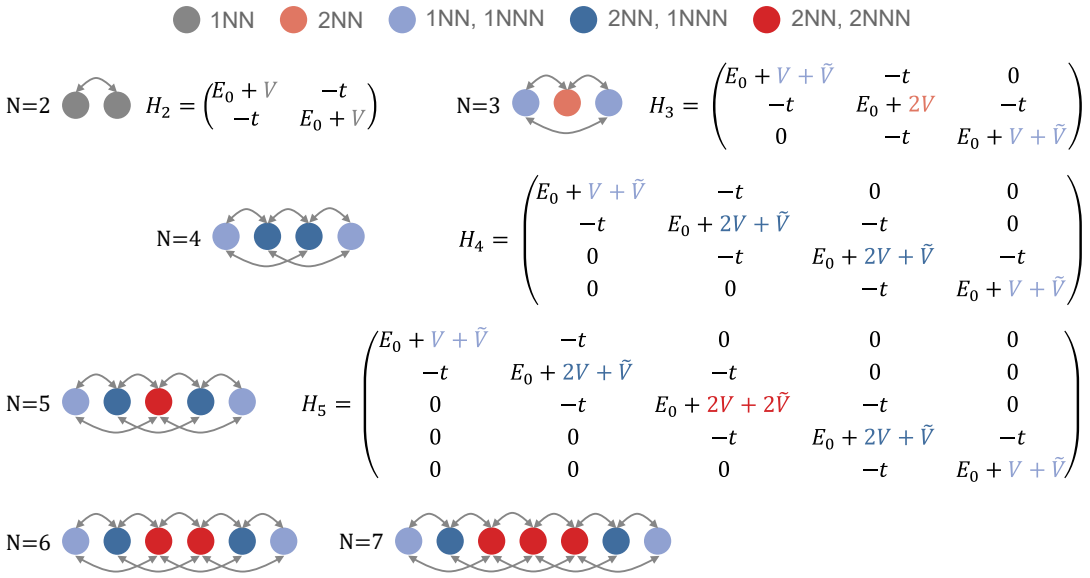

Fig. 6.1.: Schematic illustration of the influence of the NN and NNN potentials for atoms within chains of different lengths.

each site within the chain. For example, in the dimer, there are no NNNs and each atom has only one NN (gray). In the trimer, the two outer atoms have one NN and one NNN (bright blue) while the center atom has two NNs (bright red). Only beyond a chain length of 5 atoms there forms a uniform chain center with constant on-site potentials (dark red).

We now study the influence of the NN and NNN potentials. Therefore, we solve the eigenvalue problem for H_2 to H_{10} for exemplary values of V and $\tilde{V}$ and plot the results in Fig. 6.2. For all panels, $t = 0.05$ and $E_0 = -0.05$. Without additional on-site potentials (panel a) we see the usual hybridization-splitting of states (all levels are equidistant) and open a band of width $4t$ around E_0. Depending on the sign of t the corresponding eigenstates exhibit ascending or descending number of nodal planes with energy. In Fig. 6.1b we add NN contributions yielding an overall center of mass shift such that the band opens at $E > 0$. Furthermore, the energy splitting between levels is not equidistant anymore. In panel (c) we switch on the NNN potential of comparable size and different sign (which could arise from the oscillatory behavior of the RKKY interaction). As in part (b) both dimer levels are shifted above $E = 0$ due to V. The influence of $\tilde{V}$ which becomes relevant only for $N \geq 3$ reverses that trend such that the band opens around $E = 0$.

Note that NN and NNN potentials can lead to a reversed order within the eigenstates such that the states are not necessarily sorted by their number of nodal planes anymore. Further, there will be wave functions exhibiting enhanced and reduced spectral weight on the boundary atoms depending on the relative signs and magnitudes of V and $\tilde{V}$.

Importantly, we point out that this toy model is not capable to predict or fit energies of hybridized YSR states obtained from experiment. For deep in-gap states it might capture correct trends for the dimer and the bandwidth for large N. However, for intermediate

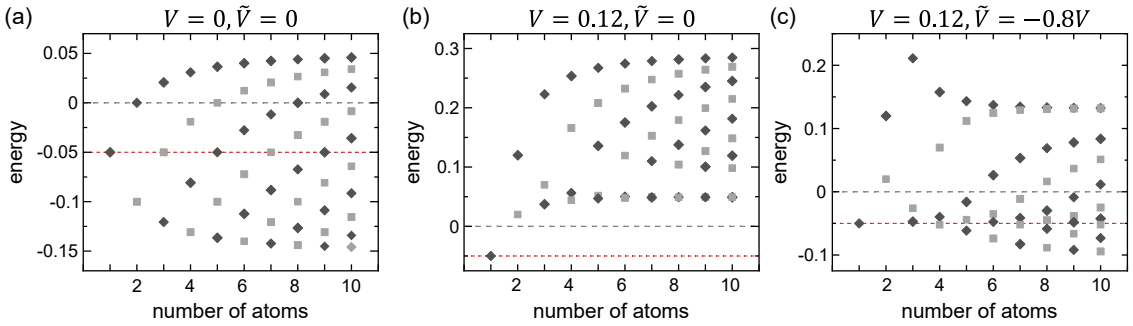

Fig. 6.2.: Eigenenergies of the Hamiltonian in Eq. 6.1 for different sets of parameters. (a) $V = \tilde{V} = 0$, (b) $V = 0.12$, $\tilde{V} = 0$ and (c) $V = 0.12$, $\tilde{V} = -0.8V$. For all panels $E_0 = -0.05$ (indicated by the red dashed line) and $t = 0.05$.

chain lengths $N = 3, 4, 5...$, the values of V and $\tilde{V}$ do not have to be constant upon chain elongation if the spin state of the atoms within the chain changes, *i.e.* if one or more YSR hybrid states cross zero energy from screened to free spin or vice versa. Moreover, we neglect possible long-range hopping terms and generally the hopping depends on the spin-order within the chain (*c.f.* section 6.1.2). Furthermore, the model does not capture all relevant physics of the system as the substrate is ignored. Especially, if YSR states are close to each other or close to the quasiparticle continuum these simple tight-binding scheme is not applicable. Nevertheless it gives us insight into possible effects of long-range interactions.

6.1.2 YSR chains as a platform for topological superconductivity

Chains of magnetic adatoms proximity-coupled to an s-wave superconductor are considered to be a promising route towards the experimental realization of Majorana bound states. In this section, after introducing the well-known model of the Kitaev chain [Kit01], we outline more sophisticated theoretical approaches modeling magnetic chains on superconductors in the dilute and the dense limit yielding topological phases following [Pen+15; PGO13; PGO14; Pie+15][2].

Kitaev chain

In 2001, A. Y. Kitaev introduced his famous model system of a spinless chain with pairing correlations between neighboring sites described by the following Hamiltonian [Kit01]:

$$\mathcal{H} = -\mu \sum_{i}^{N} c_i^\dagger c_i - t \sum_{i}^{N} (c_i^\dagger c_{i+1} + c_{i+1}^\dagger c_i) + \sum_{i}^{N} (\Delta c_i c_{i+1} + \Delta^* c_{i+1}^\dagger c_i^\dagger) \tag{6.2}$$

Above, t is the hopping amplitude between adjacent sites, μ is the chemical potential and Δ is the induced superconducting pairing. Note that the above equation describes a spinless system and hence, the induced gap is p-wave.

[2] There has been great theoretical effort focusing on topological superconductivity and Majorana physics arising from magnetic chains in proximity to an ordinary superconductor [Li+14; Nad+13; BS13; Kli+13; AS17] to name a few of them.

Now, one can formally construct two Majorana [MM06] operators from the fermionic creation and annihilation operators

$$\gamma_{i,a} = c_i + c_i^\dagger \quad \text{and} \quad \gamma_{i,b} = -\mathrm{i}(c_i - c_i^\dagger), \tag{6.3}$$

which satisfy the Majorana conditions:

$$\gamma_i^\dagger = \gamma_i \quad \text{and} \quad \gamma_i\gamma_j + \gamma_i\gamma_j = 2\delta_{ij} \quad \text{for} \quad i,j = 1,...,N \tag{6.4}$$

which imply the special properties of Majorana particles, namely being its own antiparticle and the special Majorana anticommutation relation. In principle, we artificially decomposed one fermionic operator of one site in two Majorana operators. Naturally, the Majorana operators pair up along the chain as sketched in Fig. 6.3a, top panel. However, if the chemical potential is within the hybrid band of width $4t$ there is a topological phase emerging with one unpaired Majorana operator at each end (Fig. 6.3a, bottom panel). These appear as zero-energy eigenstates at both chains ends - so-called Majorana zero modes (MZMs) - and are protected by the finite p-wave gap. If the chain is extended enough, the MZMs will not merge. As the Majorana operators do naturally not appear in any Hamiltonian preserving fermionic parity, the isolated MZMs are immune to any kind of perturbation.

YSR states - being linear combinations of spin-up holes and spin-down electrons (or vice versa) - are perfectly spin-polarized. Thus, we can transfer the Kitaev Hamiltonian to a Hamiltonian describing a chain of (hybridizing) YSR states. Therefore, we associate aboves fermionic operators $c_i^\dagger(c_i)$ with the creation (annihilation) of a quasiparticle in the YSR state at site i. Further, we identify the YSR energy E_0 to play the role of the chemical potential. Hence, we find that if the hybridization between the YSR states is strong enough that the resulting YSR band spans the Fermi level $|E_0| < 2t$ the induced pairing correlation will open up a p-wave gap within that band and we expect the system to be in a topological phase hosting MZMs at its ends [Pie+15].

Even though it governs the basic principles of the emergence of MZMs in magnetic chains with hybridizing YSR bound states, the Kitaev's model neglects relevant physics of a real system which are covered in more advanced models as outlined in the following.

Dilute chain

There are two routes to realize topological superconductivity within an adatom chain in proximity to an s-wave superconductor which depend on the long-range spin order along the chain mediated by the RKKY interaction. First, if the chain is ferromagnetically (FM) ordered, all YSR bound states are perfectly spin-polarized along the chain. Hence, the spin-singlet Cooper pair (CP) cannot proximity-couple to the dilute chain. We can generate superconducting pairing correlations within the chain by including Rashba spin-orbit coupling of the substrate which softens the singlet nature of the CPs and thus, enables the

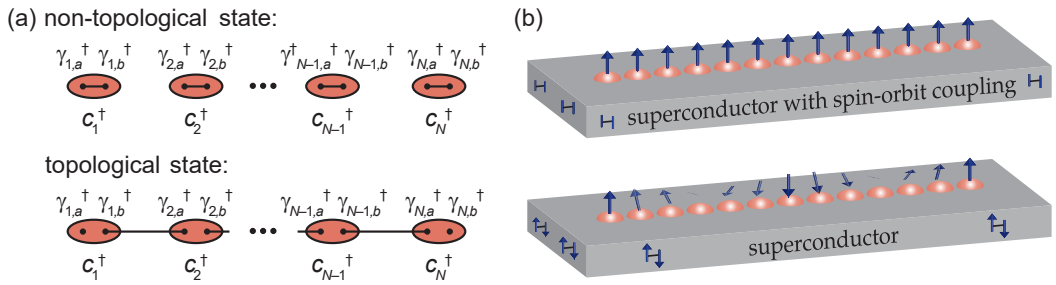

Fig. 6.3.: (a) 1D Kitaev chain with N electronic sites. Each site with creation operator $c_i^\dagger$ can be decomposed into Majorana operators $\gamma_a^\dagger$ and $\gamma_b^\dagger$. As discussed in the text, there is a trivial and a topological phase with no or one unpaired Majorana mode at each end, respectively. (b) Two possible realizations of topological superconductivity including a FM spin chain (top) in combination with Rashba spin-orbit coupling in the superconducting host and a spin-spiral (bottom). Figure taken and adapted from [Kle17].

CPs to enter the FM chain (Fig. 6.3b, top panel). The second option is that the atoms along the chain form a spin helix (Fig. 6.3b, bottom panel). Singlet CPs can proximity-couple to the chain's YSR states as long as the electron of a CP enter on different sites and thus, induce superconducting pairing within the chain. In the following we focus on the latter scenario [PGO13; PGO14; Pie+15].

The spin helix along a chain of (classical) magnetic moments of size S can be expressed as [PGO13]

$$\mathbf{S}_i = S(\sin\theta\cos\phi_i, \sin\theta\sin\phi_i, \cos\theta)\,, \quad \phi_i = 2k_\mathrm{h}x_i\,, \tag{6.5}$$

where we restricted the discussion to helices with fixed opening angle θ. $x_i = id$ denotes the position along the chain with interatomic separation of d.

If the atoms within the chain are sufficiently far apart from each other, direct hopping between d orbitals can be neglected. The d levels of atoms within the chain remain electronically inert and do not hybridize into d-bands. For YSR states deep inside the host's superconducting gap we can project out the quasiparticle continuum and describe the system by a Kitaev-like Hamiltonian [PGO13; Pie+15]:[3]

$$\mathcal{H} = E_0\sum_i^N c_i^\dagger c_i - \sum_{i\neq j}^N t_{ij}(c_j^\dagger c_i + c_i^\dagger c_j) + \sum_{i\neq j}^N \Delta_{ij}(c_j c_i + c_i^\dagger c_j^\dagger) \tag{6.6}$$

Details of the long-range hopping t_{ij} and long-range pairing Δ_{ij} amplitudes are goverened by the delocalized nature of the YSR wave functions (*c.f.* Eq. 4.18) and are further affected

[3] A detailed derivation starting with the BdG Hamiltonian can be found in [PGO13].

by the spin order of the system. For a planar spin helix (*i.e.* $\theta = \pi/2$) they can be expressed as [PGO13]:

$$t_{ij} = \Delta_0 \frac{\sin k_\mathrm{F} r_{ij}}{k_\mathrm{F} r_{ij}} e^{-r_{ij}/\zeta_0} \cos k_\mathrm{h} x_{ij} \,,$$
$$\Delta_{ij} = \mathrm{i}\Delta_0 \frac{\cos k_\mathrm{F} r_{ij}}{k_\mathrm{F} r_{ij}} e^{-r_{ij}/\zeta_0} \sin k_\mathrm{h} x_{ij} \,. \tag{6.7}$$

Here, Δ_0 is the superconducting paring strength of the host superconductor, k_F is the Fermi wave vector, $x_{ij} = (i-j)d$ and $r_{ij} = |x_{ij}|$ with d being the separation between atoms within the chain. The above model results in a more complex phase diagram which contains topological and trivial regions.

As one last aspect we point out that the helical spin-order along the chain can be mapped into a spin-orbit coupling-like term for FM aligned spins (by the unitary transformation $e^{\mathrm{i}k_\mathrm{h} x \sigma_z}$, which rotates the spin basis along the direction of the local impurity spins [Pie+15; Pen+15]). Hence, the physics of the FM chain with Rashba spin-orbit coupling and the chain with helical spin order are closely related.

Dense chain

When the atoms within the chain are densely spaced, direct hopping between d levels cannot be neglected and the above models are not applicable. We can rather describe the system by a linear chain of Anderson impurities (*c.f.* section 4.1.2) embedded in a superconducting host [Pen+15]:

$$\mathcal{H} = \mathcal{H}_0 + \mathcal{H}_d + \mathcal{H}_{sd} \,. \tag{6.8}$$

The first part describes the host superconductor

$$\mathcal{H}_0 = \sum_{\mathbf{k}\sigma} \xi_\mathbf{k} c^\dagger_{\mathbf{k}\sigma} c_{\mathbf{k}\sigma} + \sum_\mathbf{k} \Delta (c^\dagger_{\mathbf{k}\uparrow} c^\dagger_{-\mathbf{k}\downarrow} + c_{-\mathbf{k}\downarrow} c_{\mathbf{k}\uparrow}) \,. \tag{6.9}$$

The second term

$$\mathcal{H}_d = \sum_{i,\sigma} (\varepsilon_d - \mu) n_{i,\sigma} + U \sum_i n_{i\uparrow} n_{i\downarrow} - w \sum_{i,\sigma} (d^\dagger_{i+1,\sigma} d_{i,\sigma} + d^\dagger_{i,\sigma} d_{i+1,\sigma}) \tag{6.10}$$

contains an additional term accounting for the hopping w between d-levels of adjacent adatoms opening a spin-polarized d-band. $d^\dagger_{i,\sigma}(d_{i,\sigma})$ act on impurity site i and $n_{i,\sigma} = d^\dagger_{i,\sigma} d_{i,\sigma}$ The last term $\mathcal{H}_{sd}$ remains in principle unchanged compared to section 4.1.2 with the simplification of constant hybridization V between d level and substrate states

$$\mathcal{H}_{sd} = -V \sum_{i,\sigma} [d^\dagger_{i,\sigma} \psi_\sigma(\mathbf{R}_i) + \psi^\dagger_\sigma(\mathbf{R}_i) d_{i,\sigma}] \,, \tag{6.11}$$

with $\psi^\dagger_\sigma(\mathbf{R}_i)$ creating and electron at site $\mathbf{R}_i = id\hat{x}$ in the superconductor. Topological superconductivity requires one spin-polarized d-band to cross the Fermi energy opening a p-wave gap at the Fermi level.

Recent experiments of self-assembled (dense) Fe chains on Pb [Nad+14; Rub+15b; Fel+17; Paw+16] and artificially constructed Fe chains on Re [Kim+18; Sch+20; Sch+21a; Sch+21b; Mie+21] showed zero-energy end states that putatively arise from Majorana bound states. However, the emergence of MZMs sensitively depends on details of the material system and the dispersion of the spin-polarized d-bands. For example, while Fe chains on Pb exhibit MZMs no such states are found on Co chains on Pb [Rub+17].

Up to date extensive experiments studying dilute adatom chains are missing. Very recent experiments involve Mn chains on Nb [Sch+21a; Sch+21b], Cr chains on β-Bi_2Pd [Mie+21] and Fe chains on Ta(100) [Kam+18]. In the following section we present the experimental realization of an extended dilute chain which we assemble atom by atom tracking the formation of the YSR bands.

6.2 Experimental realization of a dilute YSR chain

Results presented in this section are published in [Lie+21].

In order to successfully hybridize YSR wave functions in longer chains ($\gg 2$ atoms) we first have to elucidate a suitable starting point. Since the CDW transforms from HC to CC structure within $\approx 10\,\mathrm{nm}$, one should choose a spacing which enables hybridization within both structures. Therefore, considering the findings of chapter 5, we choose an interatomic spacing of $3a$ because hybridization is absent for $2a$- and $4a$-spaced dimers in the HC-structure. In the following section we stepwise increase the number of atoms and trace the evolution of hybrid YSR states.

6.2.1 Linear trimer with spacing of $3a$

In section 5.2 we have seen that dimers with an interatomic spacing of $3a$ clearly form symmetric and antisymmetric hybrid wave functions which we can excite with single electron tunneling. We choose atoms located on CDW maxima (HC structure) as starting point for longer chains since their (hybrid) α- and β-states of the monomer and the dimer are energetically well separated (*c.f.* section 5.2.1). To recall, we expect an increase in the number of hybrid states upon chain elongation as each YSR state of the monomer leads to N hybrid states in a chain of N atoms.

We start by adding a third atom to the Fe dimer discussed in section 5.2.1 in order to from a linear trimer. The third atom is placed precisely $3a$ apart of the second atom such that all three atoms are located on a CDW maximum. Corresponding data are compiled in Fig. 6.4 which contains spectra recorded centrally on the three atoms in (a) and along a line across the trimer axis in (b). Part (c) accommodates zooms in the low-energy region

of (b). Compared to the dimer (Fig. 5.2), the data in turn show an increase in the number of YSR states, suggesting a larger number of hybrid states as expected for an increased number of atoms. However, the determination of the exact number of YSR states starts to be complicated as discussed in the following.

Starting at the Fermi level, we clearly find two resonances (per bias polarity) around $\pm 1.6\,\mathrm{mV}$. Furthermore, there is one broader resonance around $\pm 1.8\,\mathrm{mV}$. By close inspection of the oscillating decay in Fig. 6.4e, we find alternating intensity modulations in the long-range decay. This implies the presence of two states with different phases of their oscillating wave functions (*c.f.* Eq. 4.18). Thus, we discern two resonances being present in the narrow energy window around $\pm 1.8\,\mathrm{mV}$. The resonance at $\pm 2.0\,\mathrm{mV}$ is again well-separated from neighboring states. However, there is another state found at $\approx \pm 2.1\,\mathrm{mV}$ which already falls in the onset of the substrate coherence peaks and overlaps with YSR resonances at higher energies and is thus hard to disentangle from the background.

Therefore, searching for states in the energy region of the former α- and β-states we discern six different resonances at each bias polarity which matches the expectation for the trimer, *i.e.* three α- and three β-hybrid states. All resonances are indicated by the white dotted lines in Fig. 6.4c. Additionally, the line profile obeys again horizontal mirror symmetry around the center atom, further hinting towards the formation of hybrid wave functions delocalized over the linear trimer. All resonances are labeled in a similar nomenclature as done for the dimer in the top of the panels, *i.e.* according to the number of nodal planes, we label the states with $\alpha^{\mathrm{t0,t1,t2}}$ and $\beta^{\mathrm{t0,t1,t2}}$. In the following we investigate the $\mathrm{d}I/\mathrm{d}V$ maps in order to verify this assignment and to further corroborate hybrid trimer states as the origin of the observed resonances (Fig. 6.4d).

The corresponding topography is located in the left and only one bias polarity is shown (data of the other bias polarity can be found in Fig. A.12c). The energies at which the $\mathrm{d}I/\mathrm{d}V$ maps are acquired are marked in Fig. 6.4c by the dotted lines and are indicated on top of each map. Although the patterns are complex due to the oscillatory nature of the YSR states, we attempt to count the number of nodal planes perpendicular to the trimer axis as fingerprints of hybridization. The horizontal dotted line at the center of the trimer marks a nodal plane in the maps at $+1.84\,\mathrm{mV}$ and $+1.57\,\mathrm{mV}$. Two nodal planes, marked by dashed lines (centrally) between the Fe atoms, are clearly found in the map at $+2.02\,\mathrm{mV}$ and less pronounced at $+1.79\,\mathrm{mV}$. However, we note that the latter state is very close in energy to the state at $+1.84\,\mathrm{mV}$ and its shape may be partially obscured as both states overlap (*c.f.* corresponding maps at $V < 0$ in Fig. A.12c). We find two states without nodal planes at $-1.65\,\mathrm{mV}$ and $+2.11\,\mathrm{mV}$. While being obvious for the former, the latter is hard to disentangle from resonances at higher energies and the substrate quasiparticle peaks. Furthermore, it suffers from the strong negative differential conductance (NDC) of the adjacent resonance. Apart from these distortions, there is no clear evidence for a nodal plane neither in the short nor in the long-range patterns. Additionally, the maps recorded

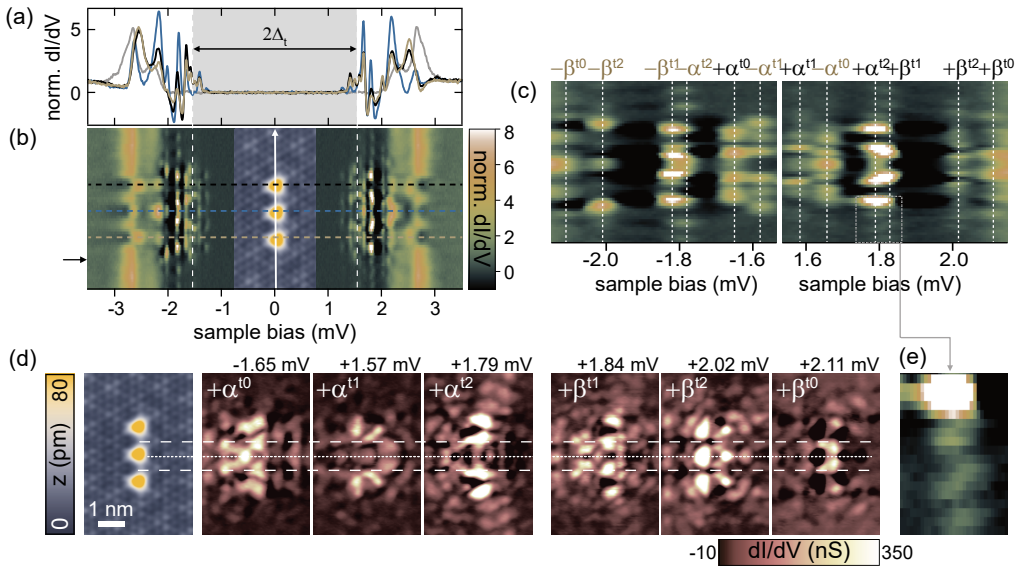

Fig. 6.4.: (a) Normalized differential conductance spectra recorded on the atoms of the trimer (black, blue, brown) and on the bare $NbSe_2$ (gray). Feedback was opened at $250\,\mathrm{pA}, 5\,\mathrm{mV}$ and a modulation of $15\,\mu\mathrm{V}$ was used. (b) Stacked spectra recorded along the trimer as illustrated in the inset topography (recorded in constant-current mode with set point $100\,\mathrm{pA}, 10\,\mathrm{mV}$). Horizontal dashed lines indicate the position of the spectra of (a). The (Nb) tip gap $\Delta_\mathrm{t} \approx 1.55\,\mathrm{meV}$ is indicated by the gray box (a) and dashed lines (b). (c) Zoom to lower bias voltages of (b). The hybrid α- and β-states are indicated by the vertical dotted lines and labeled on the top of each graph. (d) STM topography (constant-current mode with set point $100\,\mathrm{pA}, 10\,\mathrm{mV}$) of the linear trimer with spacing of $3a$ in the left. Right: Corresponding constant-contour $\mathrm{d}I/\mathrm{d}V$ maps of the hybridized YSR states recorded at the bias voltages indicated in (c) by the dotted lines and also above each image. Horizontal dashed and dotted lines serve as guides to the eye. Constant-contour feedback was opened at $250\,\mathrm{pA}, 5\,\mathrm{mV}$ and a modulation of $15\,\mu\mathrm{V}$ was used. (e) Close-ups of the oscillatory decay around $1.8\,\mathrm{mV}$ as indicated by the box in (c).

at the other bias polarity (Fig. A.12c) and data recorded with a different tip (showing less pronounced NDC effects) underpin the lack of a nodal plane for this state (*c.f.* Fig. A.13).

Beside the classification in terms of nodal planes we identify further similarities between the trimer wave functions and the monomer and dimer states. For example, the near-field structure of the state labeled $\beta^{\mathrm{t}2}$ closely resembles the shape of $\beta^{\mathrm{d}1}$ (compare Figs. 5.3b and 6.4d) with increased intensity at the right vertex (of each atom). This assignment is further supported by the long-range patterns (see also the other bias polarity in Fig. A.12c). Although the long-range oscillations are rather weak for $\beta^{\mathrm{t}0}$ (as it overlaps with the quasiparticle continuum) we can identify similar structures comparing it to $\beta^{\mathrm{d}0}$. Note that the YSR resonances within the coherence peaks (γ- and δ-like, *c.f.* section 4.5) are short-ranged and mainly localized on the atoms such that they should not contribute to the long-range pattern. From the other bias polarity and data recorded with a different tip with less pronounced NDCs we arrive at the same assignment for the $\beta^{\mathrm{t}0}$-state. Data and discussion are provided in Appendix A.5. Assuming that the three hybrid β-states should be found within the same energy corridor, the third β-state, $\beta^{\mathrm{t}1}$, is probably the one with one nodal plane of the strongly overlapping states around $\pm 1.8\,\mathrm{mV}$.

Consequently, we assign the other three states (which have none, one and two nodal planes) to be α-derived. Unfortunately, the near-field patterns (serving as strong indication for the assignment of the dimer states) do not inherit clear characteristics of the α-like wave functions. One might discern reminiscent fingerprints of the single-atom state at both outer atoms of $\alpha^{\mathrm{t}1}$ and $\alpha^{\mathrm{t}2}$. We suggest that $\alpha^{\mathrm{t}1}$ and $\alpha^{\mathrm{t}2}$ are again screened (as all β-states) and only $\alpha^{\mathrm{t}0}$ remains unscreened which is based on observations in longer chains and will become more clear section 6.2.2 when we study extended chains. Note already that the presence of wave functions which much spectral weight on both outer atoms points towards a strong influence of NNN potentials (*c.f.* ball model in Fig. 6.1).

We emphasize that the above assignment of α- and β-hybrid states is rather tentative. However, with this assignment we can go a step further and quantify the splitting D and center-of-mass shift C of the hybridized α- and β-states upon hybridization as described in the following. Results for monomer and dimer were already presented in Fig. 5.4a. For this, a precise determination of the YSR energies is necessary. As there are strong spatial intensity variations we deconvolve multiple spectra of the lines of Figs. 5.2b,d and 6.4b to obtain the local DOS of the monomer, dimer and trimer. The deconvolution procedure is described in sections 2.2.3 and A.1. Exemplary data is shown in Fig. 6.5a which contains all deconvolved spectra of Figs. 5.2a,c and 6.4a. To extract the YSR energies,

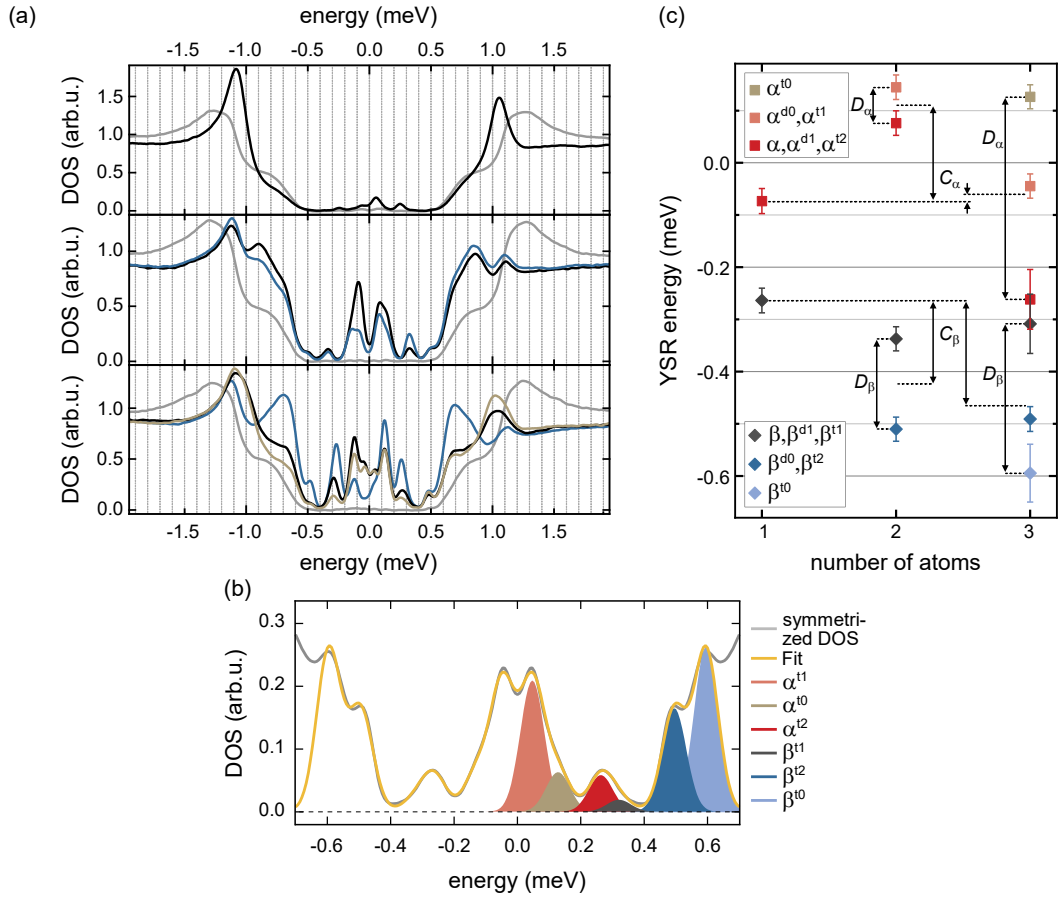

Fig. 6.5.: (a) Deconvolved data of Fig. 5.2a,c (top and middle panel) and of Fig. 6.4a (bottom panel). For the deconvolution $\Delta_t = 1.55\,\mathrm{meV}$ and a depairing factor of $\Gamma = 5\,\mu\mathrm{eV}$ was used. (b) Fit results for one exemplary deconvolved spectrum (position of the original spectrum marked by the black arrow in Fig. 6.4b). The graph contains the symmetrized DOS (gray), the total fit (yellow) and the individual Gaussian peaks (shown for one polarity only). (c) Energies of the (hybrid) α- and β-states of the monomer, dimer and trimer obtained by fitting multiple deconvolved DOS traces as described in the text. Errors are discussed in the text.

we then symmetrize the DOS in energy[4] and fit the low-energy range of all data with the appropriate number of Gaussians (similar to the analysis described along with Fig. 4.9):

$$\mathrm{DOS}(E) = \nu_0 + \sum_{i=1}^{N} \left(A_i\, e^{-(E\pm E_{\alpha_i})^2/(2\sigma^2)} + B_i\, e^{-(E\pm E_{\beta_i})^2/(2\sigma^2)} \right). \tag{6.12}$$

Here, ν_0 is an intensity offset, A_i (B_i) are the symmetric amplitudes of the α- (β-) resonances and σ is the width of the Gaussian peaks. N is the number of atoms, *i.e.* $N = 1, 2, 3$ for monomer, dimer and trimer.

While the fit results are reliable for the monomer and the dimer, the situation is more complicated for the trimer due to the presence of multiple peaks within the gap. An example of a fitted trace is shown in Fig. 6.5b (position of the original spectrum marked by

[4]The symmetrization halves the number of amplitudes as fit parameters, because the resonances found at different bias sides have in general different intensities.

	$\lvert D_\alpha(\mu\text{eV})\rvert$	$\lvert D_\beta(\mu\text{eV})\rvert$	$C_\alpha(\mu\text{eV})$	$C_\beta(\mu\text{eV})$
dimer	69 ± 33	173 ± 33	184 ± 29	-160 ± 29
trimer	388 ± 62	286 ± 79	14 ± 33	-201 ± 36

Tab. 6.1.: Results for the splits $D_{\alpha,\beta}$ and shifts $C_{\alpha,\beta}$ (relative to the monomer) of the hybrid α- and β-states of the dimer and trimer obtained from Fig. 6.5c.

the black arrow in Fig. 6.4b). The gray trace is the symmetrized DOS, the total fit is shown in yellow and the individual Gaussians are shown (for positive energies only) in color. The fit yields reliable values for α^{t0}, α^{t1} and β^{t2}. However, as discussed already, α^{t2} and β^{t1} strongly overlap within one broader resonance (full width half maximum of $\approx 100\,\mu$eV) reducing the reliability of the fit. Furthermore, note the flanks of the quasiparticle coherence peaks at the graphs boundaries just above β^{t0} obscuring its energetic position. Therefore, we added additional errors of $\pm 50\,\mu$eV for the latter three resonances. For all six states, errors accounting for the uncertainty of the tip energy gap, the lock-in modulation of the bias voltage and the sampling interval were added to the standard deviation of the fit. Figure 6.5c compiles the results for the monomer to trimer obtained by averaging over the energies extracted from the fits of multiple spectra across monomer, dimer and trimer. From these results we determine the energetic splittings $D_{\alpha,\beta}$ and shifts $C_{\alpha,\beta}$ (relative to the monomer) of the hybrid states. Results are summarized in Tab. 6.1.

We note that the energetic order of the hybrid α-states is as expected ($\alpha^{t2} \rightarrow \alpha^{t1} \rightarrow \alpha^{t0}$). However, the energetic order of the hybrid β-states does not follow the simple tight-binding rule of increasing energy with increasing number of nodal planes as we find β^{t2} in between β^{t0} and β^{t1}. As outlined in section 6.1.1, the energetic order depends on the sign of the hopping amplitude (sign of the overlap integral) and can further be affected by NN and NNN on-site contributions which can arise due to long-range RKKY interactions. Recalling Fig. 6.1, we see that such NNN contributions start to play a role for $N \geq 3$. Furthermore, the above assignment places the hybrid α- states on different sides of the Fermi level which could explain the absence of clear linear combinations in the wave function patterns as the excitation scheme is more complex.

To sum up the findings so far, we detect the correct number of resonances (six hybrid states) in the expected energy window. While the hybrid wave functions keep characteristics of the monomer states for both, α and β in the dimer (*c.f.* section 5.2.1), the situation in the trimer is more complicated. Here, the single wave function character is lost, except for β^{t0} and β^{t2}. Nonetheless, the data show clear characteristics of hybridization in terms of wave function symmetry and presence (absence) of nodal planes. Although the assignment in terms of α- or β-nature in the trimer is rather tentative, it is unlikely that the observed wave functions originate from non-hybridizing Fe atoms within the trimer. We should keep in mind that the excitation scheme of the α-states can be complex as we find not all hybrid state excitations on the same bias side. Also YSR resonances within the coherence peaks (γ and δ) are unlikely to be the origin of the observed wave functions

as they are short-ranged and mainly localized on the atoms. Thus, we expect only weak hybridization for them and no long-range oscillatory nature.

6.2.2 Band formation upon increasing atom number

Figure 6.6 shows the sequential extension of the Fe chain up to a length of 11 atoms. It contains stacked $\mathrm{d}I/\mathrm{d}V$ spectra recorded along the entire chains as indicated in the inset topographies. The last atom being added to the chain is marked by a red dot. The tip energy gap is indicated by the white dashed lines. The dotted lines are located at $\pm 2.15\,\mathrm{mV}$, $\pm 1.95\,\mathrm{mV}$ and $\pm 1.7\,\mathrm{mV}$ corresponding to energies of $\pm 0.6\,\mathrm{meV}$, $\pm 0.4\,\mathrm{meV}$ and $\pm 0.15\,\mathrm{meV}$ (after subtraction of $\Delta_\mathrm{t} \approx 1.55\,\mathrm{meV}$), respectively, and serve as guides to the eye. The data of monomer, dimer and trimer (a-c) is reproduced from from Figs. 5.2b,d and 6.4b, but still shown here for better comparison.

The spectra appear with a rich subgap structure. Being challenging for the trimer already (*c.f.* section 6.2.1) we cannot disentangle all individual peaks for more than three atoms anymore. However, a qualitative assessment of the characteristic subgap features gives valuable insights into hybridization. In the following we will go step-wise through the data and identify fingerprints of hybrid states and successive band formation of YSR states.

Upon attachment of one additional Fe atom to the three-atom chain, the subgap structure along the entire chain changes drastically (Fig. 6.6c,d). This points to the formation of new hybrid states, in agreement with the expectation of four hybrid states to arise from the α- and β-states each. Figure 6.7a contains exemplary $\mathrm{d}I/\mathrm{d}V$ maps recorded on the quadrumer (topography in the left). The energies are given in the top of each panel and indicated in Fig. 6.6d by the red arrows. In particular, the states at $-1.62\,\mathrm{mV}$ and $2.17\,\mathrm{mV}$ have no nodal plane. At $1.95\,\mathrm{mV}$ there is a state with one pronounced nodal plane centrally on the quadrumer. More data with different number of nodal planes can be found in Fig. A.14a. Thus, the new wave functions exhibit characteristics of continuing hybridization upon increasing the chain length. We can also identify similarities between the former trimer and new quadrumer states further pointing toward coherent hybridization over the entire chain length. For example, the states at $1.91\,\mathrm{mV}$ and $-1.62\,\mathrm{mV}$ resemble the trimer states at $1.84\,\mathrm{mV}$ and $-1.65\,\mathrm{mV}$, respectively (*c.f.* Fig. 6.4d). The state at $2.17\,\mathrm{mV}$ most likely originates from the highest β-like hybrid state. Similarities between trimer and quadrumer states are also present at other energies (see Figs. A.12c and A.14a for more data and discussion). As already mentioned above, we can not disentangle all expected eight hybrid states ($2N$) as they are strongly overlapping. For example, while we observe a pronounced nodal plane at $1.95\,\mathrm{mV}$, this nodal plane is not unambiguously present at $1.91\,\mathrm{mV}$ (*c.f.* blue arrow in Fig. 6.7a).

Attachment of a fifth atom again leads to a strong change of the hybrid states all along the chain (Fig. 6.6d,e). In particular, there is a delocalized state at zero energy (dashed

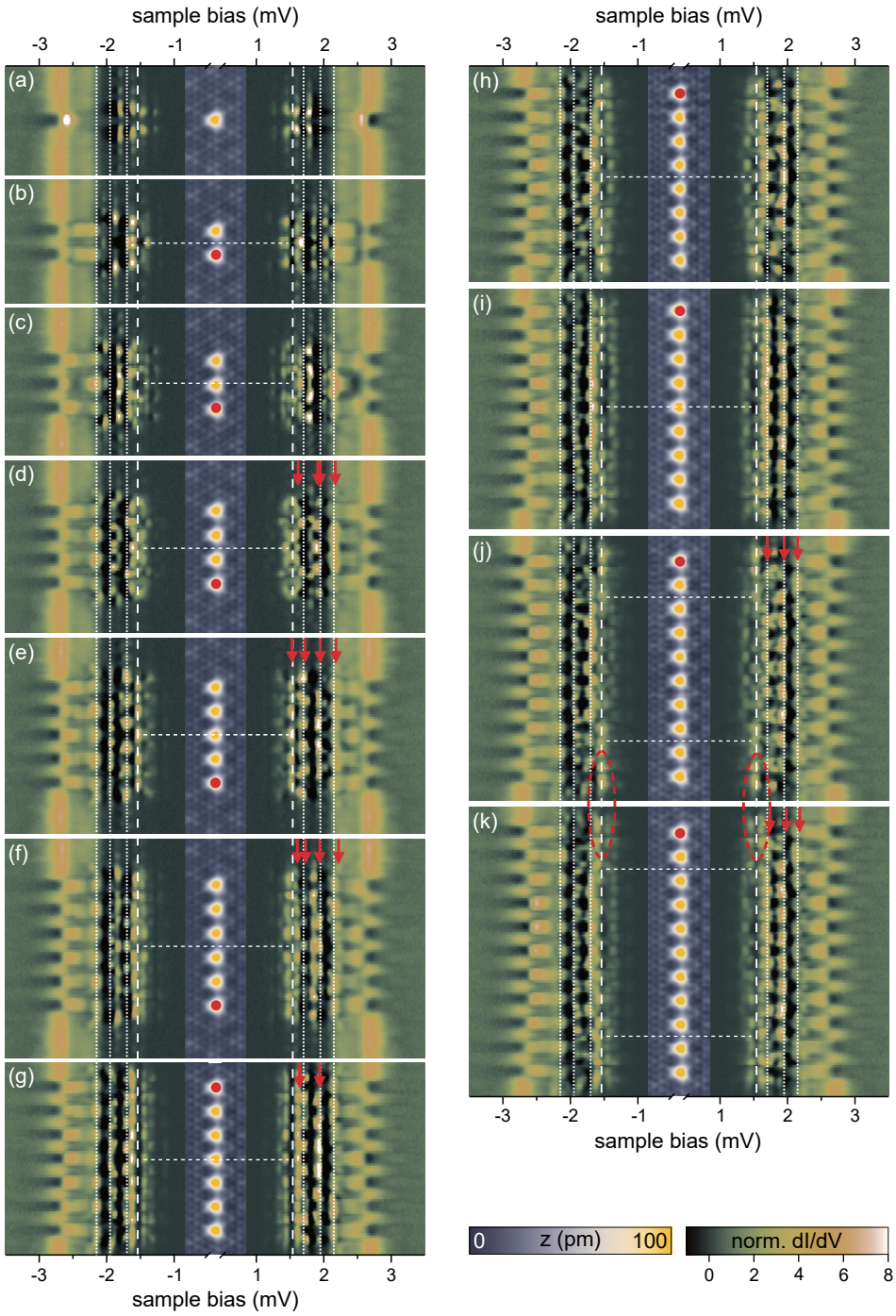

Fig. 6.6.: Stacked constant-height $\mathrm{d}I/\mathrm{d}V$ spectra (normalized) recorded along lines across the monomer, dimer, trimer (a-c) and chains containing 4-11 atoms (d-k) as illustrated in the inset topographies (constant-current mode with set point $100\,\mathrm{pA}, 10\,\mathrm{mV}$). Set point for spectra $250\text{-}700\,\mathrm{pA}, 5\,\mathrm{mV}$ and a modulation of $15\,\mu\mathrm{V}$ was used. The (Nb) tip gap $\Delta_\mathrm{t} \approx 1.55\,\mathrm{meV}$ is indicated by dashed lines. Dotted lines are at $\pm 2.15\,\mathrm{mV}$, $\pm 1.95\,\mathrm{mV}$ and $\pm 1.7\,\mathrm{mV}$ corresponding to energies of $\pm 0.6\,\mathrm{meV}$, $\pm 0.4\,\mathrm{meV}$ and $\pm 0.15\,\mathrm{meV}$, respectively. Data from (a-c) is reproduced from Figs. 5.2b,d and 6.4b, but still shown here for better comparison. Red dots highlight the atoms added last. Red arrows indicate the energies at which the $\mathrm{d}I/\mathrm{d}V$ maps of Fig. 6.7 are recorded. Red ellipses outline the presence (j) and absence (k) of a zero-energy end state. Horizontal dashed lines mark the chain center in (b-i) and the inner part of the chain in (j,k).

lines), with the strongest intensity in the very center of the chain and gradually decaying toward the terminations (no nodal plane, map at $1.53\,\mathrm{mV}$ in Fig. 6.7b). We further identify a couple of states at $\sim \pm 1.7\,\mathrm{mV}$ (inner pair of dotted lines in Fig. 6.6), where there were no quadrumer states. Among these states there is one with enhanced intensity at the chain ends ($\mathrm{d}I/\mathrm{d}V$ map at $1.72\,\mathrm{mV}$, Fig. 6.7b). The former quadrumer states that have been just below $1.95\,\mathrm{mV}$ are slightly shifted towards the gap edge. Here, we find a state being most intense at the three center atoms of the 5-atom chain ($1.95\,\mathrm{mV}$) which exhibits similar features as found on the corresponding quadrumer state (blue arrows in Fig. 6.7b). Such states with different intensity distributions along the chain in combination with different number of nodal planes are expected from the simple tight-binding model of the freestanding chain with additional NN and NNN contributions as introduced in section 6.1.1. However, a direct assessment of the number of nodal planes is difficult as several hybrid states are overlapping within our energy resolution. As before, we find fingerprints of the outermost β-state just above $\pm 2.15\,\mathrm{mV}$.

Upon addition of another Fe atom ($N = 6$, Fig. 6.6f), the zero-energy state disappears along the entire chain and is slightly shifted away from the Fermi level. The corresponding $\mathrm{d}I/\mathrm{d}V$ map is displayed in Fig. 6.7c ($1.61\,\mathrm{mV}$). While finding a state with reduced intensity on the chain center on the 5-atom chain, we can identify a state which is most intense centrally on the chain (between the four center atoms) at $1.73\,\mathrm{mV}$. Because of NDC effects, this state is overall less intense. Interestingly, we in turn find a hybrid state with similar signatures (blue arrows) at $1.95\,\mathrm{mV}$ which is also suppressed by a NDC, but the main features are still observable. In turn, we find outermost β-state just above $\pm 2.15\,\mathrm{mV}$.

As we further increase to a length of $N = 7$ (Fig. 6.6g) we observe again spectroscopic changes delocalized over the whole structure. For example, the former zero-energy state ($N = 5$) which is shifted away from the Fermi level for $N = 6$ is in turn slightly shifted to higher energy ($1.64\,\mathrm{mV}$, Fig. 6.7d). Around $1.95\,\mathrm{mV}$ we can again observe the similar signatures than before (blue arrows).

While we cannot characterize the states individually, the variations of YSR states along the entire chain upon increasing the chain length indicates their hybridization along the whole structure. This observation remains valid upon further chain extension. Furthermore, the linespectra exhibit perfect horizontal mirror symmetry around the chains center as indicated by the horizontal dashed lines in Fig. 6.6b-i (of course this symmetry is also present in the $\mathrm{d}I/\mathrm{d}V$ maps in Fig. 6.7a-d). Importantly, this holds for odd and even number of atoms within the chain. Starting from $N = 8$ (Fig. 6.6h-k), the rich variations of the hybrid states upon chain elongation observed for low atom numbers become less profound. Broader features seem to converge and fall into specific energy intervals around $\pm 1.7\,\mathrm{mV}$, $\pm 1.95\,\mathrm{mV}$ and $\pm 2.15\,\mathrm{mV}$ (dotted lines) and wave function patterns become more uniform in the interior of the chain (outlined by the horizontal dashed lines in Fig. 6.6j,k). Interestingly, $\mathrm{d}I/\mathrm{d}V$ maps recorded at these energies exhibit similar characteristics as can be found when comparing Fig. 6.7d-f. We ascribe this behavior to the onset of YSR band

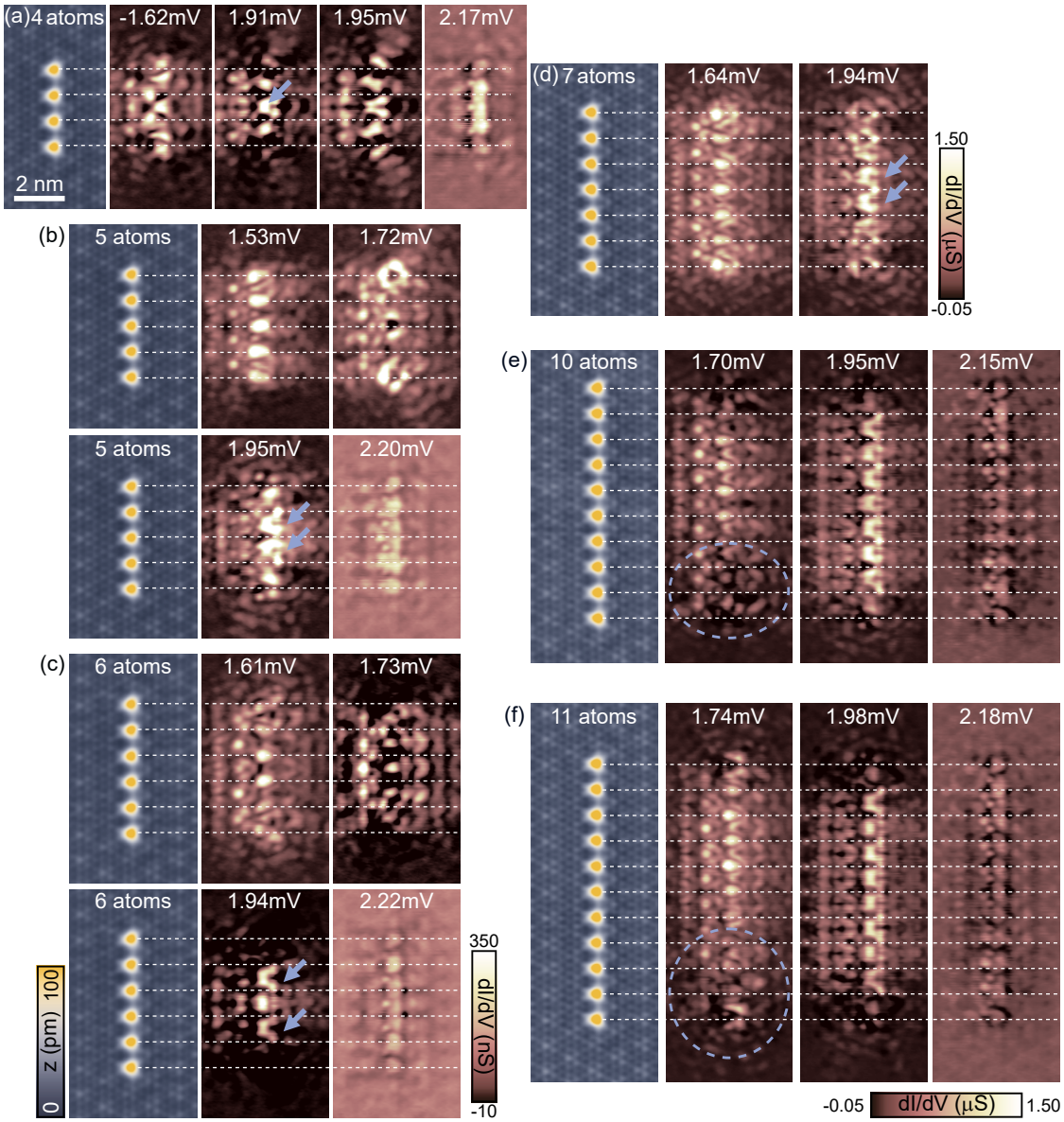

Fig. 6.7.: (a-f) STM topographies (constant-current mode with set point $100\,\mathrm{pA}, 10\,\mathrm{mV}$) of the 4-, 5-, 6-, 7-, 10- and 11-atom chains with spacing of $3a$ in the left. Corresponding constant-contour $\mathrm{d}I/\mathrm{d}V$ maps at selected bias voltages in the right. The energies are indicated in Fig. 6.6 as red arrows and within each panel ($\Delta_\mathrm{t} \approx 1.55\,\mathrm{meV}$). Constant-contour feedback was opened at $250\,\mathrm{pA}, 5\,\mathrm{mV}$ (a-c) or $700\,\mathrm{pA}, 5\,\mathrm{mV}$ (d-f) and a modulation of $15\,\mu\mathrm{V}$ was used. Blue circles/arrows highlight features in the data (see text).

formation of the original α- and β-states of the monomer. Indeed, these findings are in agreement with the considerations of section 6.1.1 expecting uniform wave functions in the chain's center to develop for $N \geq 6$ in the presence of NN and NNN RKKY terms (dark red circles in the sketch of Fig. 6.1).

We know that the highest β-state is always found around $\pm 2.15\,\mathrm{mV}$ (outer pair of dotted lines). Furthermore, the lowest energy β-state is found around $\pm 1.95\,\mathrm{mV}$ (second pair of dotted lines). Additionally, we observe resonances around the Fermi level at various chain lengths. This suggests that the α-derived band likely opens around the Fermi energy. One possible scenario is that the uppermost and lowermost α-states are located within the broad features around $\pm 1.7\,\mathrm{mV}$. Recall, that we found both α-dimer states at opposite bias in the free-spin regime (Fig. 6.5). This trend was partially reversed already in the (tentative) assignment of the trimer states (*c.f.* Fig. 6.5). The opening of the α-band around the Fermi level can be rationalized by the influence of NNN RKKY contributions which can reverse the shift from $N = 2 \rightarrow N >> 2$ as discussed within the model of the freestanding chain in section 6.1.1.

Thus, we suggest a β-derived hybrid band to form within the energy window in between the outer two pairs of dotted lines (*i.e.* within $\pm[1.95, 2.15]\mathrm{mV}$) and a α-derived band to form around the Fermi level (within $\pm[1.7, -1.7]\mathrm{mV}$). The situation is schematically depicted in Fig. 6.8. The quasiparticle continuum is indicated in gray. $\pm\varepsilon_1$, $\pm\varepsilon_2$ and $\pm\varepsilon_3$ correspond to the three pairs of dotted lines in Fig. 6.6. The particle- (hole-like) β-band is indicated by the solid (dashed) blue line. The corresponding α-bands are drawn in red. The enhanced DOS at the energies indicated by the dotted lines thus originates from van Hove-singularities at the band edges (flat dispersion) of the α- and β-band as schematically indicated in the right panel of Fig. 6.8. The bandwidth is determined by the hopping amplitudes as indicated in the sketch. Note that we draw the α- (β-) bands with the maximum (minimum) at $k = 0$ due to the reversed order of hybrid states with none and one nodal plane in the dimer indicating a different sign of the hopping.

One interesting observation is a zero-energy state localized at the chain ends at a length of ten atoms (Fig. 6.6j, red ellipse). Actually, the α-band spanning zero energy could open the desired p-wave gap around the Fermi level (*c.f.* section 6.1.2). However, this state is not a sought-after MZM as it disappears upon addition of another Fe atom (Fig. 6.6k, red circle). $\mathrm{d}I/\mathrm{d}V$ maps are provided in Fig. A.15. Hence, we ascribe it to a hybrid state that happens to have strong intensity at the chain terminations as already observed for shorter chain lengths.

We note that we carefully monitored the phase and stability of the CDW around the chain upon the build-up sequence (*c.f.* Fig. A.16) such that all atoms of the chain are found on maxima of the CDW. Hence, a change of the YSR states due to an altered CDW configuration around the chain can be excluded. However, we also note slight deviations from the horizontal mirror symmetry when the chain length reaches the order of $\approx 10\,\mathrm{nm}$, *c.f.* Fig. 6.7e,f (blue ellipses) as further addressed in the following section.

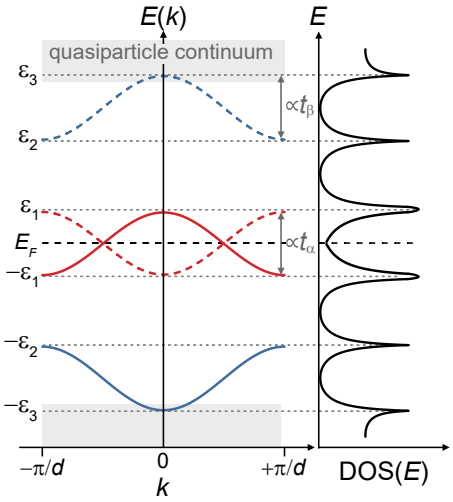

Fig. 6.8.: Schematic illustration of the formation of van Hove-singularities at the band edges of two YSR bands at different energies. $\pm\varepsilon_{1,2,3}$ correspond to the three pairs of dotted lines in Fig. 6.6.

6.2.3 Influence of the CDW on the YSR bands in Fe atom chains

It has been shown that the CDW can be pinned by crystal defects [Cos+18; Lan+14; FW15; Cha+15; Arg+14] which means that the long-range order of the CDW is dictated by the competition of crystal defects and natural periodicity of the CDW. Fe impurities (being surface defects) also interact with the CDW to some extent as discussed already. There is a slight mismatch between the periodicity of the chain ($3a$) and the periodicity of the CDW ($a_{\mathrm{CDW}} \gtrsim 3a$). Hence, the $3a$-chain acts on the CDW as a large scale defect. On short length scales, the Fe atoms seem to pin the CDW, such that all atoms coincide with a CDW maximum leading to the perfect horizontal mirror symmetry observed in Fig. 6.6 and Fig. 6.7 for chain lengths of $< 10\,\mathrm{nm}$. Beyond, the extent of the chain is comparable to the length scale on which the CDW naturally transforms between the HC and CC structure without the presence of defects. Thus, there is a competition between the $3a$-spacing of the chain and the natural long-range periodicity of the CDW being slightly larger. In the previous section we observed the onset of YSR band formation. In the following we will explore the interplay between the incommensurate CDW and the $3a$-chain upon further increase of the chain length and address the effect on the YSR bands.

The $\mathrm{d}I/\mathrm{d}V$ spectra recorded along a 27-atom chain (Fig. 6.9a) reveal spatial modulations of the YSR bands along this extended structure. This is most clearly expressed in the absence of the overall mirror symmetry with respect to the center of the chain, which had been preserved in the shorter chains. The white dashed and dotted lines mark the tip energy gap and $\pm 2.15\,\mathrm{mV}$, $\pm 1.95\,\mathrm{mV}$, $\pm 1.7\,\mathrm{mV}$, respectively (as in Fig. 6.6). Interestingly, within a wide region in the center of the chain, labeled as section 2, the spectra are similar to the ones in the 11-atom chain. This region contains the previous 11-atom chain as indicated by blue circles in the large scale topography in Fig. 6.9b. In particular, the bands originating from the α- and β-states (spanning the energies between the dotted lines) are

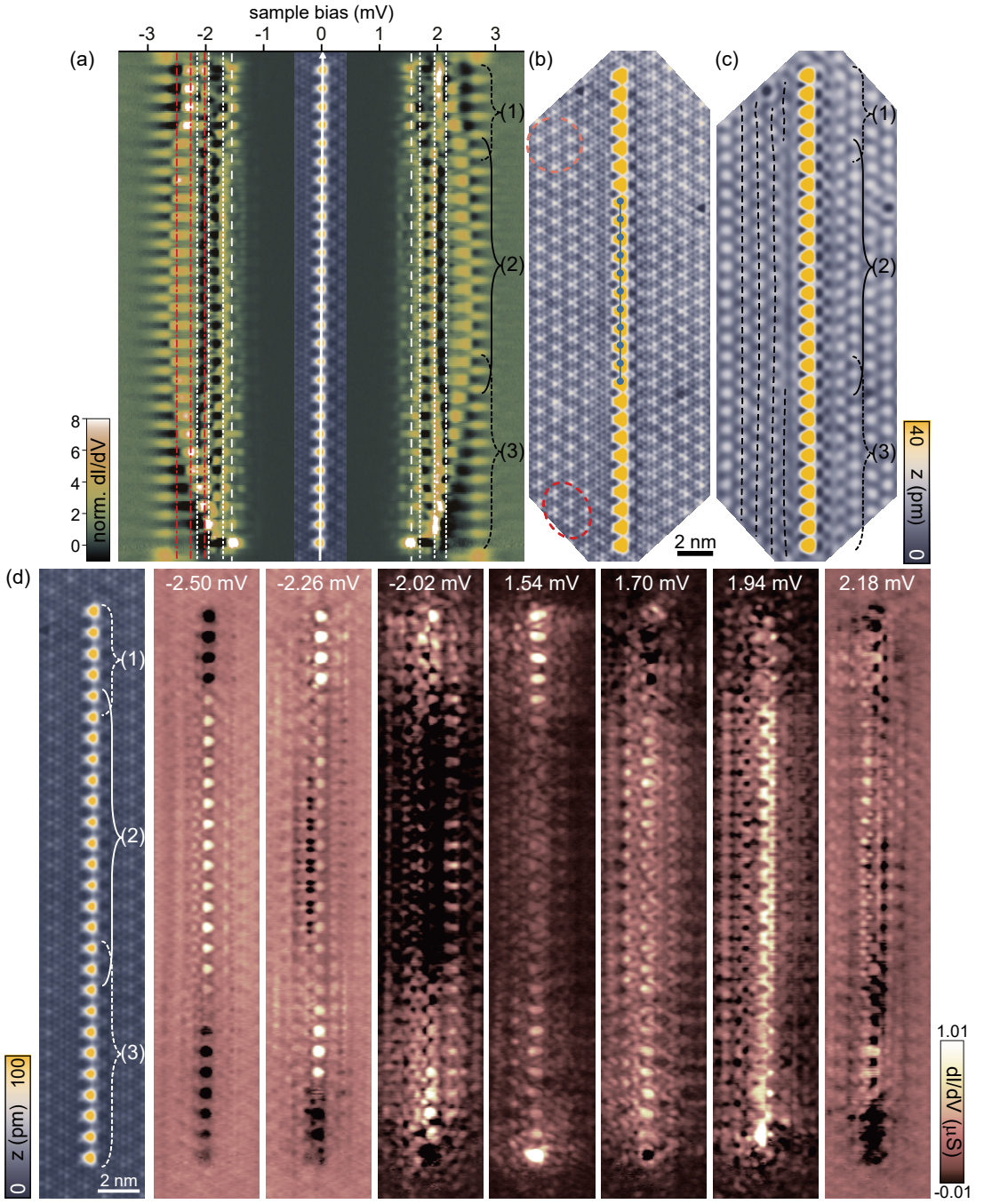

Fig. 6.9.: (a) Stacked constant-height $\mathrm{d}I/\mathrm{d}V$ spectra (normalized) recorded along a line across the 27-atom chain as illustrated in the inset topography. Set point for the spectra is $700\,\mathrm{pA}, 5\,\mathrm{mV}$ with a modulation of $15\,\mu\mathrm{V}$. The (Nb) tip gap $\Delta_\mathrm{t} \approx 1.55\,\mathrm{meV}$ is indicated by the white dashed lines. White dotted lines are at $\pm 2.15\,\mathrm{mV}$, $\pm 1.95\,\mathrm{mV}$ and $\pm 1.7\,\mathrm{mV}$. Different sections of the chain are labeled with (1)-(3). (b) Extended STM topography of the 27-atom chain. The position of the former 11-atom chain (Fig. 6.6k) is indicated in blue (constant-current set point is $100\,\mathrm{pA}, 10\,\mathrm{mV}$). One region with HC- (CC-) CDW is highlighted in dark (bright) red. (c) FFT-filtered topography of (b). Dashed lines serve as guide to the eye to illustrate CDW distortions in the background. (d) STM topography of the 27-atom chain in the left. Corresponding constant-contour $\mathrm{d}I/\mathrm{d}V$ maps at selected energies in the right. Constant-contour feedback was opened at $700\,\mathrm{pA}, 5\,\mathrm{mV}$ and a modulation of $15\,\mu\mathrm{V}$ was used. Maps recorded at energies not already covered by white dashed/dotted lines are indicated by the red dashed-dotted lines in (a). For clarity, there are more lines than maps as the white dotted lines point out the band edges of the two YSR bands.

visible with similar oscillatory behavior as on the shorter chain and remain at the same energy delocalized over the entire region 2 (and even further into region 3). This we can also identify in the $\mathrm{d}I/\mathrm{d}V$ maps at corresponding energies ($2.18\,\mathrm{mV}$, $1.94\,\mathrm{mV}$ and $1.70\,\mathrm{mV}$, Fig. 6.9c) where we find in region 2 similar patterns as already observed along the shorter chains (compare Figs. 6.9d and 6.7e-f).

In regions 1 and 3 these two bands slightly shift in energy leading to resonances at different energies. For example, the patterns of the the low energy band edge is found at the Fermi level (*c.f.* Fig. 6.9d, $1.54\,\mathrm{mV}$) in region 1. Additionally, the YSR bands within the superconducting coherence peaks in region 2, continuously shift toward the Fermi level at the lower end of the chain (region 3) and also at the top (region 1), but remain separated from the Fermi level in the latter. Figure 6.9d accomodates $\mathrm{d}I/\mathrm{d}V$ maps at selected energies ($-2.50\,\mathrm{mV}$, $-2.26\,\mathrm{mV}$, $-2.02\,\mathrm{mV}$, indicated as red dashed-dotted lines in Fig. 6.9a) which reflect this dispersion. A complete set of $\mathrm{d}I/\mathrm{d}V$ maps at various energies can be found in Figs. A.17 and A.18. For instance, the highest-energy band is found in region 2 in the map at $-2.50\,\mathrm{mV}$ while it appears in region 1 and the top of region 3 at $-2.26\,\mathrm{mV}$ before appearing localized at the terminations at $-2.02\,\mathrm{mV}$.

We further note the presence of zero-energy states, localized on the very last atom at the bottom of the chain and delocalized over region 1 in the top of the chain. While these could easily be interpreted as MZMs, we emphasize that the continuous shift of multiple YSR states toward zero energy disagrees with such an interpretation. Most probably, the spectral weight found at zero energy arises from (multiple) YSR-derived states/bands coinciding at this energy at the bottom end of the chain and is related to the α-band edge which appears at zero energy in the top of the chain.

To understand the energetic shifts of the YSR bands qualitatively, we investigate the phase of the CDW along the chain. Figure 6.9b shows an STM topography of a broader area around the chain. The CDW is smoothly transforming between the usual HC and CC patterns in the surrounding of the chain. Two small regions with the familiar HC (CC) structure are highlighted in dark (bright) red. For direct inspection of the CDW, we remove the atomic corrugation from the STM image by a Fourier-filter (Fig. 6.9c). The black dashed lines (guide to the eye) connect maxima of the CDW and immediately reflect its variation along the Fe chain. The CDW in region 1 is strongly distorted around the dark defect close to the chain at the very top. In region 2, the CDW is parallel and „in-phase“ with the chain's period of $3a$, which allows all Fe atoms to be located at identical CDW positions (maxima). Thus, the CDW seems to adapt the chain's periodicity in this section of the chain. The CDW in region 3 is not exactly parallel to the Fe chain. In particular, this manifests as an additional CDW maximum gradually appearing in the left of the chain (additional dashed line), resulting in different adsorption sites of the Fe atoms with respect to the CDW. Thus, beyond a certain chain length (of the order of $10\,\mathrm{nm}$), the positions of the Fe atoms relative to the CDW vary along the chain.

We can thus conclude that the changes in the YSR band structure are correlated with the spatial variation of the CDW with respect to the Fe atoms. The incommensurate nature of the CDW imposes a smoothly varying potential onto the YSR bands leading to the observed energy shifts. We have shown in section 4.4 that the YSR states of individual Fe atoms shift in energy due to the CDW-induced variation of the DOS and potential scattering (*c.f.* section 4.4, [Lie+20]). In particular, we observe the α- and β-resonances to shift towards the Fermi level when moving from a CDW maximum to minimum. This is in agreement with the general downshift of the YSR-bands identified here when the atoms do not coincide with the CDW maxima toward the chains ends (section 1 and 3). We note that YSR bands close to the superconducting gap edge seem to be more strongly affected by this additional potential, while the shift of bands deep inside the gap is more difficult to detect. In both cases the potential can effectively lead to bands at or close to zero energy. Due to their dispersive nature they seem to be localized in space at the chain ends and may thus be easily be misinterpreted as MZMs. While the dispersive nature already contradicts this interpretation, we extend the chain further in the next step and track the evolution of the bands. If the zero-energy feature was a MZM, it should move along with the chain's extension.

We have seen so far that the gradual shift of the CDW relative to the Fe atoms within the chain imposes smooth band bending along extended chains. Beyond a certain length, a different configuration of the CDW around the chain becomes energetically more favorable. In particular, we observe an abrupt change in the CDW background upon placement of the 31^{st} atom to the chain leaving the atoms in region 3 on minima of the CDW while the atoms in region 2 still sit on CDW maxima. We interpret this as the result of the sophisticated interplay between the extended Fe chain (spacing 3a) interfering with the natural periodicity of the CDW, further complicated by the presence of crystal defects in the vicinity of the chain. Importantly, the CDW configuration around the chain is stable upon chain elongation for $N < 30$ and for $N > 31$ (data of the transition can be found in Fig. A.19).

Therefore, we directly show the chain after its extension to a length of 51 atoms in Fig. 6.10a. Additional atoms have been placed regions 4 and 5, the previous 27(11)-atom chain is indicated in red (blue). In (b) we show the FFT-filtered version of (a) offering insight into the CDW background. We find that the atoms in region 4 which contains the former bottom end of the 27-atom chain (red arrow) are now located on CDW minima while the atoms in region 2 still coincide with CDW maxima. This is illustrated by the white grids which indicate CDW maxima around the chain (CDW maxima on crossings, CDW minima in triangles pointing upwards). In between the CDW distorts rather abruptly within $\approx 5\,\mathrm{nm}$ in region 3 as outlined by the black-dashed lines.

$\mathrm{d}I/\mathrm{d}V$ spectra recorded along the entire chain are presented in Fig. 6.10c. White dashed and dotted lines are at same energetic positions as before (tip gap and low-energy band edges). We note rich energy variations along the chain. Interestingly, the regions with

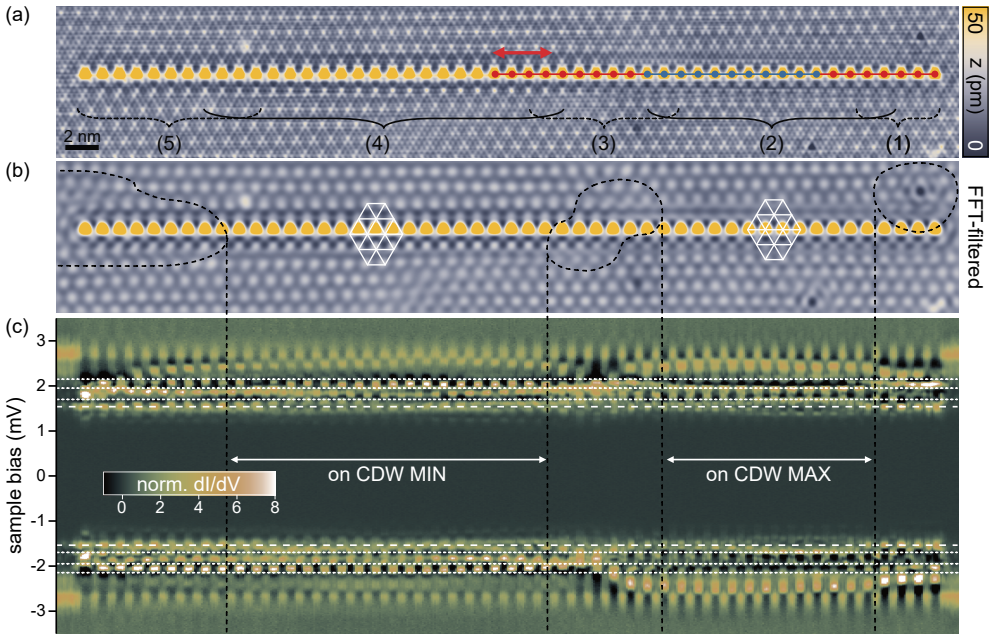

Fig. 6.10.: (a) STM topography (constant-current mode with set point $100\,\mathrm{pA}, 10\,\mathrm{mV}$) of the 51-atom chain. The position of the former 11(27)-atom chain (Figs. 6.6k and 6.9) is indicated in blue (red). The red arrow highlights the end of the former 27-atom chain, see text. Different sections of the chain are labeled with (1)-(5). Section (1) and (2) are identical to Fig. 6.9a-c. (b) FFT-filtered topography of (a). Dashed lines serve as guide to the eye to illustrate CDW distortions in the background. White grids indicate the CDW maxima. (c) Stacked constant-height $\mathrm{d}I/\mathrm{d}V$ spectra (normalized) recorded along a line across the 51-atom chain (set point $700\,\mathrm{pA}, 5\,\mathrm{mV}$ with a modulation of $15\,\mu\mathrm{V}$). The (Nb) tip gap $\Delta_\mathrm{t} \approx 1.55\,\mathrm{meV}$ is indicated by dashed lines. The dotted lines are located at $\pm 2.15\,\mathrm{mV}$, $\pm 1.95\,\mathrm{mV}$ and $\pm 1.7\,\mathrm{mV}$.

strongest energy shifts coincide with the regions of most pronounced CDW distortions in direct vicinity of the chain as highlighted by the black lines in Fig. 6.10b,c.

In section 1 and 2 spectra have not changed upon chain extension which is expected as the position of the atoms relative to the CDW has not changed in this regions. This can be identified in the $\mathrm{d}I/\mathrm{d}V$ maps (Fig. 6.11) which are recorded at the same energies as those presented in Fig. 6.9d for the 27-atom chain. In sections 1 and 2, where the CDW did not change upon chain elongation, we find very similar patterns as in Fig. 6.9d at all energies. Hence, the attachment of further Fe atoms does not affect the band structure, supporting the band limit of the original YSR states. On the contrary, we observe different spectra and wave function patterns in sections 4 and 5. We assign this strongly modified YSR band structure to hybridization of YSR states of atoms adsorbed in minima of the CDW in this section of the chain (region 4). Thus, in agreement with the findings on the 27-atom chain, we conclude that the dispersing YSR bands are correlated with the configuration of the CDW around the chain.

While the delocalized zero-energy mode is still present on one end (region 1, $1.54\,\mathrm{mV}$) we do not find its counterpart somewhere along the chain, contradicting a MZM as its

origin (as mentioned above already, this state most probably arises from the low-energy band appearing at zero energy in section 1). Therefore, we conclude that the zero-energy $\mathrm{d}I/\mathrm{d}V$ signal found on the ends of the 27-atom chain is imposed by the local potential of the CDW leading to dispersing states and not due to topological end states.

For this particular chain, the CDW causes atoms in section 2 to be on the maxima of the CDW while atoms in section 4 are located on CDW minima. Thus, the CDW divides the chain in two regions with different band structures, connected by a small region with strong band bending in section 3, where the CDW distorts rather abruptly in the background. Hence, we can view this chain as two subchains. This scenario is further supported by Fig. 6.12. It shows the same chain as in Fig. 6.11, but in section 3, where we observe the strong band bending connecting both parts of the chain, we removed three atoms (as the CDW starts to distort also on the left end, we also removed one atom there). Indeed, comparing the $\mathrm{d}I/\mathrm{d}V$ maps of Figs. 6.11 and 6.12, we find that the patterns in regions (1,2,4,5) are very similar and hence, not affected by the removal of atoms in section 3 - confirming the scenario of two independent subchains created by the CDW around the chain.

To close this section we observe the formation of YSR-bands in Fe chains with interatomic spacing of $3a$. Furthermore, the incommensurate CDW sets a smoothly varying potential landscape for extended chains leading to dispersing YSR-bands along the chain which occasionally can lead to localized zero-energy modes which should not be misinterpreted as MZMs as they are not robust upon chain increase. Therefore, the $3a$-chain investigated so far seems not to be in the right parameter regime to support a topological phase. The phase diagram of dilute chains is affected by the exact spin structure of the chain, namely if the spins are FM aligned or couple to a spin helix (*c.f.* section 6.1.2). In order to access the spin configuration, one could perform spin polarized STS using spin-polarized tips (see [Wie09; WZW11] for reviews). However, in weakly coupled systems, the energy scale of the RKKY interaction is of order of $100\,\mu\mathrm{eV}$. Considering the experimental temperature of $1.2\,\mathrm{K}$ and quantum fluctuations the spin-order might have very short lifetimes [Kha+12]. Thus, one usually needs an external magnetic field to stabilize the spin structure in the order of $0.5\,\mathrm{T}$ [Kha+12] which is large compared to the small first critical field of $NbSe_2$ ($B_{\mathrm{c1}} = 20\,\mathrm{mT}$). Of course, the presence of vortices affects (locally) superconductivity and also the spins of Fe atoms on the surface hindering spin-sensitive measurements.

In the next section we explore the interaction between closely spaced Fe atoms in neighboring HC sites which we have not addressed so far. Here, the interaction is not mediated entirely via the substrate anymore (dilute limit), but the atoms can interact via direct d level exchange - known as densely packed chains.

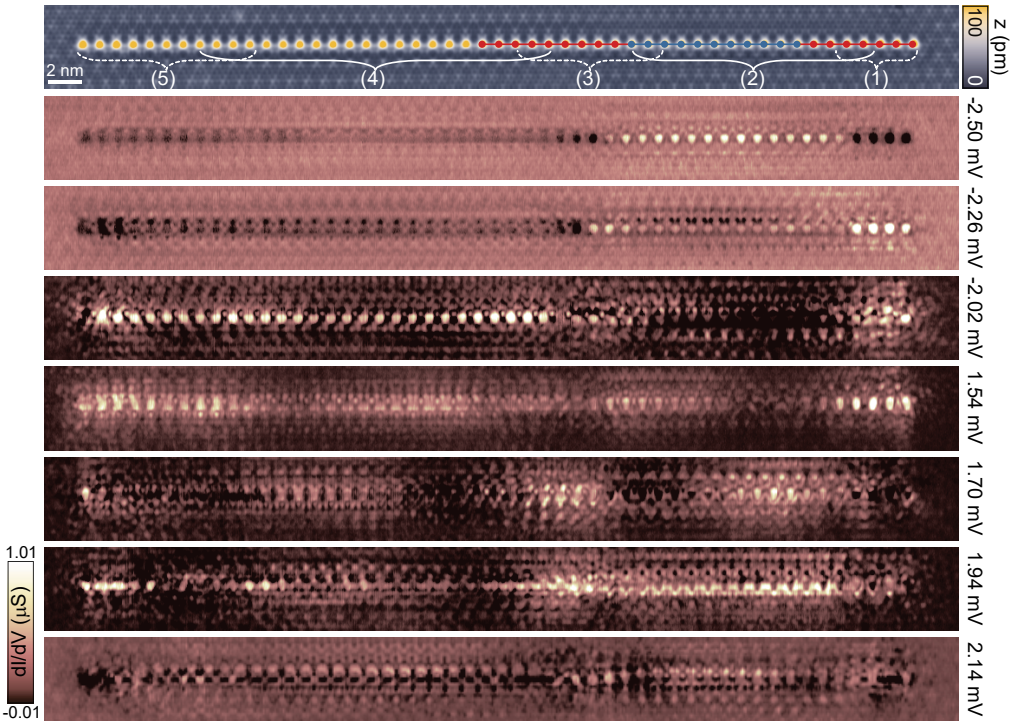

Fig. 6.11.: STM topography of the 51-atom chain in the top. Corresponding constant-contour $\mathrm{d}I/\mathrm{d}V$ maps at selected energies in the bottom. Constant-contour feedback was opened at $700\,\mathrm{pA}, 5\,\mathrm{mV}$ and a modulation of $15\,\mu\mathrm{V}$ was used. The (Nb) tip gap is $\Delta_\mathrm{t} \approx 1.55\,\mathrm{meV}$. Different sections of the chain are labeled with (1)-(5) as in Fig. 6.10a.

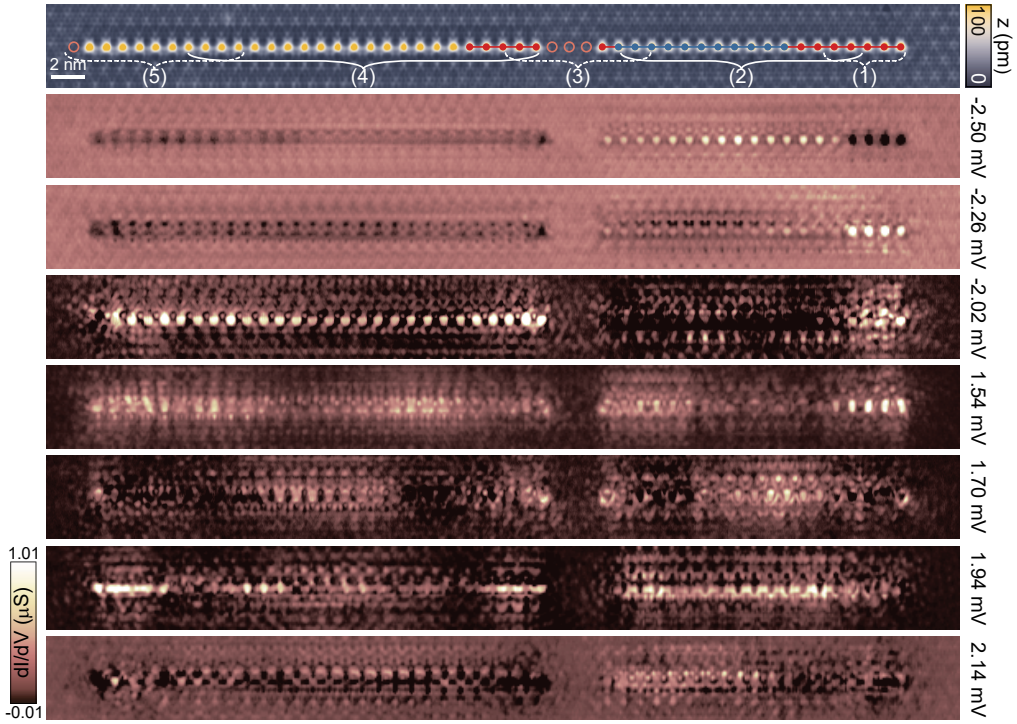

Fig. 6.12.: Analogous data set as in Fig. 6.11, but the former 51-atom chain was separated into a 19-atom and a 28-atom chain (topography in the top and $\mathrm{d}I/\mathrm{d}V$ maps in the lower panels, same parameters). Different sections (1)-(5) labeled identical to Fig. 6.11. Open circles mark the former position of atoms which have been removed.

6.3 Adatom chain with direct exchange

Omitted in section 5.3, we focus on the interaction between two Fe atoms with a spacing of $1a$ in the following. For dimers with interatomic distances of $\geq 2a$ we showed that the hybridization depends on the orientation of the atoms within the CDW. When the atoms are on equal positions relative to the CDW we find the YSR wave functions to form symmetric and antisymmetric hybrid states. In closely packed dimers we observe fundamentally different behavior. First, we focus on the YSR resonances before addressing findings at higher energies.

6.3.1 YSR resonances in densely packed structures

Figure 6.13a shows a topography of the 1a-dimer within the CC-CDW (same data than in Fig. 5.7d). The closely packed dimer appears as one protrusion (bright red trace, Fig. 6.13b). Even though we cannot resolve the individual atoms anymore, it was ensured that the orientation of the dimer within the CDW and the atomic lattice is well-controlled meaning that the maximum of the oval elevation is in the correct atomic row and in between two HC sites (see Fig A.20 for a topography with overlaid grids). The apparent height of the dimer compared to the monomer is only slightly increased by $\approx 20\,\mathrm{pm}$ (*c.f.* dark and bright red curves in Fig. 6.13b). Low-energy spectroscopy (Fig. 6.13c) on the positions of the two Fe atoms within the 1a-dimer (black, bright red) and the substrate (gray) reveals strongly altered YSR characteristics. Fig. 6.13d accomodates the corresponding stacked spectra measured across the dimer (white arrow in Fig. 6.13a). Importantly, there are no intense in-gap YSR resonances. We observe only very faint asymmetries within the range of the coherence peaks directly on the dimer. This is in contrast to findings for single HC atoms and all HC dimers with spacings $\geq 2a$ which showed intense and long-ranged in-gap YSR resonances (*c.f.* Fig. 5.8). The absence of YSR states is also reflected in the $\mathrm{d}I/\mathrm{d}V$ maps which exhibit very faint features compared to the long-ranged oscillating wave functions observed before (note the largely reduced $\mathrm{d}I/\mathrm{d}V$ magnitude). Note that the remaining in-gap resonances at $\pm 1.68\,\mathrm{mV}$ originate from another nearby Fe atom as can be seen in Fig. 6.13e (right panel). Thus, intense low-energy YSR resonances are absent on the $1a$-dimer.

As for the $3a$-chain studied in detail in the previous section, we increase the number of atoms in order to investigate longer chains in the dense limit. In the left panel of Fig. 6.14a we show a chain consisting of six atoms with separations of $1a$ between adjacent atoms. The circles indicate the location of the individual atoms along the chain. The chain appears as three oval elevations, *i.e.* three dimers along the chain as outlined by the black circles which are either connected to each other or stay separated. This is in contrast to previous observations in many systems of densely-packed atom chains which formed uniform chains [Rub+15b; Nad+14; Paw+16; Nad+14; Fel+17] and artificially constructed chains [Kim+18; Sch+20; Sch+21a; Sch+21b; Mie+21].

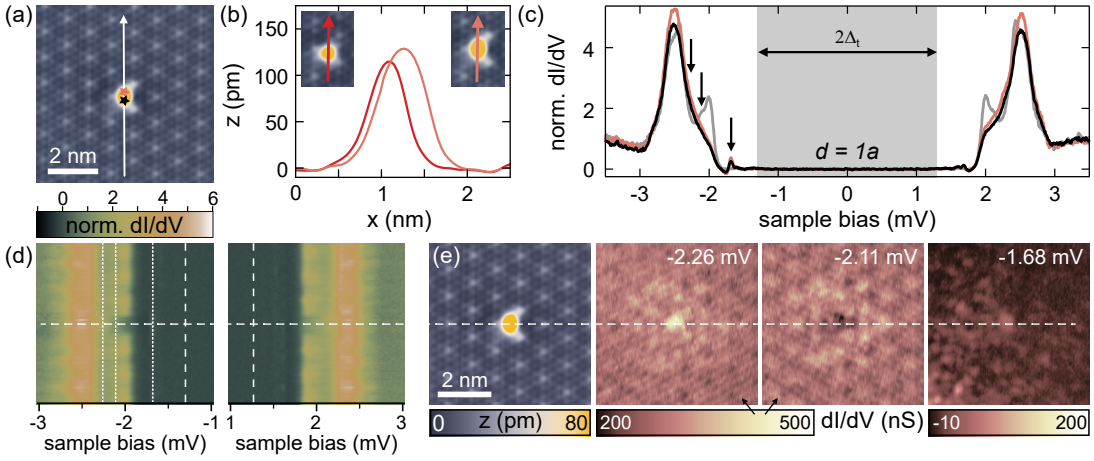

Fig. 6.13.: (a) Constant-current topography (set point $100\,\mathrm{pA}, 10\,\mathrm{mV}$) of the dimer with spacing of 1a (data reproduced from Fig. 5.7d, right panel). The stars mark the positions of the two atoms within the dimer. (b) Height profiles from the single Fe atom (Fig. 5.7d, left panel) and the 1a-dimer in dark and bright red as indicated in the inset topographies. (c) Normalized constant-height $\mathrm{d}I/\mathrm{d}V$ spectra recorded on the atoms of the 1a-dimer (black, bright red). Substrate spectrum in gray. (d) Stacked $\mathrm{d}I/\mathrm{d}V$ spectra recorded across the 1a-dimer as indicated by the white arrow in (a). Feedback was opened at $750\,\mathrm{pA}, 5\,\mathrm{mV}$ and a modulation of $15\,\mu\mathrm{V}$ was used. The (Nb) tip gap $\Delta_\mathrm{t} \approx 1.30\,\mathrm{meV}$ is indicated by the gray box/vertical lines (c,d). (e) Constant-contour $\mathrm{d}I/\mathrm{d}V$ maps of the 1a-dimer (corresponding topography in the left). Bias voltage given in each panel and indicated by the white dotted lines in (d) and the arrows in (c). Horizontal dashed line serves as guide to the eye. Same feedback parameters as in (c,d).

When adding a 7^{th} atom (here to the bottom end, 2^{nd} panel of Fig. 6.14a) we find three dimers and one *single end* (red arrow) as again indicated by the black circles. Interestingly, by applying bias pulses in the order of $\sim 1\,\mathrm{V}$ at the dimerized end we can reversibly switch the single end between both extremities of the chain[5] (3^{rd} panel). Adding the 8^{th} atom at the dimerized end (here bottom) results in two single ends with 3 dimers in the center of the chain. This configuration is not stable upon measurements at higher voltages and easily switches to the fully dimerized chain consisting of 4 dimers. While single ends can be „normally“ manipulated, $1a$-dimers are much more stable and cannot easily be separated (with usual manipulation parameters[6]).

These findings suggest a pairwise coupling of Fe atoms within the $1a$-chain and hold for all chain lengths: If the number N of atoms within the chain is odd, the chain appears as $(N-1)/2$ dimers with one single end. For an even number of atoms, the fully dimerized configuration ($N/2$) appears to be stable. The dimerization was observed independent of the CDW structure in the background, *i.e.* there is no difference between HC and CC structure.

Spectroscopy on these different chains reveals that whenever there is a single end there are intense YSR resonances while the YSR states largely disappear where atoms appear

[5] This switching was tested to a chain length of 10 atoms.
[6] Separation of $1a$-dimers was possible with a very reactive tip, but with the majority of tips it is not achieved with the standard manipulation parameters.

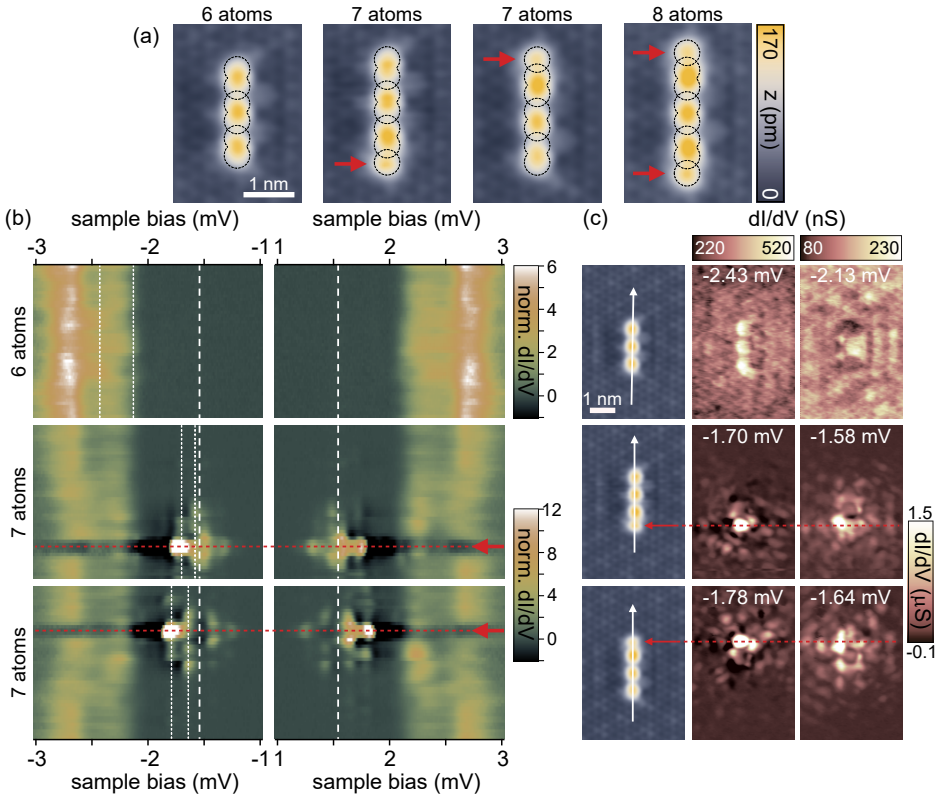

Fig. 6.14.: (a) Constant-current topographies (set point $100\,\mathrm{pA}, 10\,\mathrm{meV}$) of the 6-atom chain, the same chain elongated to 7 atoms with different dimerizations and the 8-atom chain with two single ends. Red arrows point at the single end(s). Black dashed lines serve as guide to the eye indicating the atoms' position within the chain. (b) Normalized $\mathrm{d}I/\mathrm{d}V$ spectra measured across the 6-atom and 7-atom chain with the single end on different sides (feedback opened at $700\,\mathrm{pA}, 5\,\mathrm{mV}$; modulation of $15\,\mu\mathrm{V}$). The exact position of the lines is indicated in the topographies in the left of (c). The tip gap ($\Delta_\mathrm{t} \approx 1.55\,\mathrm{meV}$) is indicated by the white dashed lines. (c) Constant-contour $\mathrm{d}I/\mathrm{d}V$ maps recorded at the energies given in each panel (also indicated by the white dotted lines in part (b). Topographies with the same area as the $\mathrm{d}I/\mathrm{d}V$ maps in the left. The single ends are marked in red (arrows and lines) in (b,c).

dimerized in the topographies. This can be seen in Fig. 6.14b,c which contain line spectra and $\mathrm{d}I/\mathrm{d}V$ maps at selected energies. On the (fully dimerized) 6-atom chain and the dimerized parts of the 7-atom chain we observe only faint YSR resonances within the substrates coherence peaks. On the contrary, we observe intense long-ranged YSR states on the 7-atom chain emerging from the single end of the chain (indicated by red arrows). Note that due to their long-range nature (several nm) the YSR states arising from the chain ends significantly leak into the chain and are spread over several atoms (chain length of 7-atom chain: $6a \approx 2\,\mathrm{nm}$), but their extent is comparable to the YSR states on single atoms.

We can unambiguously identify the single end as origin of these intense wave functions on longer chains. Fig. 6.15a,c shows the chain extended to 37 atoms with the single end at the bottom of the chain (red arrow). Both, line spectra (a) and $\mathrm{d}I/\mathrm{d}V$ maps (c) unveil the single end as the origin of the intense YSR states with their long-range oscillatory decay. Along the rest of the chain as well as for chain with even number of atoms (fully dimerized), we find the faint patterns within the substrates coherence peaks as already pointed out before. Exemplarily, we show the 44-atom chain in Fig. 6.15b,d (Note the strongly reduced $\mathrm{d}I/\mathrm{d}V$ scale in order to resolve the patterns).

To summarize so far, Fe atoms with spacing of $1a$ appear as one single protrusion. While single Fe atoms exhibit intense in-gap YSR states, we find only very faint YSR signatures in the closely packed dimers. For more than 2 atoms within a $1a$-chain, the Fe atoms appear dimerized in the topographies for all chain lengths. The appearance of intense YSR resonances is always linked to the single end in the topographies (for odd numbers of atoms within the chain). Hence, the longer chains directly reflect the characteristics observed on single atoms and $1a$-dimers: intense YSR states on single ends or absence of YSR resonances in the dimerized sections. Thus, the data suggests that atoms forming a dimer interact stronger than adjacent dimers (and than single end to adjacent dimer for odd atom numbers within the chain).

YSR resonances indicate the existence of spin [Hat+17; Kez+19; Kez+20a; Kez+18; Cho+17a; Rub+16; Hom+20] giving insight into the spin state of the magnetic adsorbate. Hence, the disappearance of the YSR resonances could hint toward a different spin state of the Fe atoms within the dimers compared to the single Fe atom. In section 4.4.4 we noted that the CDW has only slight influence on the d level resonances (Fig. 4.10). In the next step we monitor the evolution of the d levels upon decreasing the distance between HC Fe atoms in order to gain insight into the coupling mechanism within the closely packed Fe atoms.

6.3.2 Direct exchange between d orbitals

All dimers so far ($d \geq 2a$) have been considered in the dilute coupling scheme where the interaction is purely mediated by the substrate via the RKKY interaction. However,

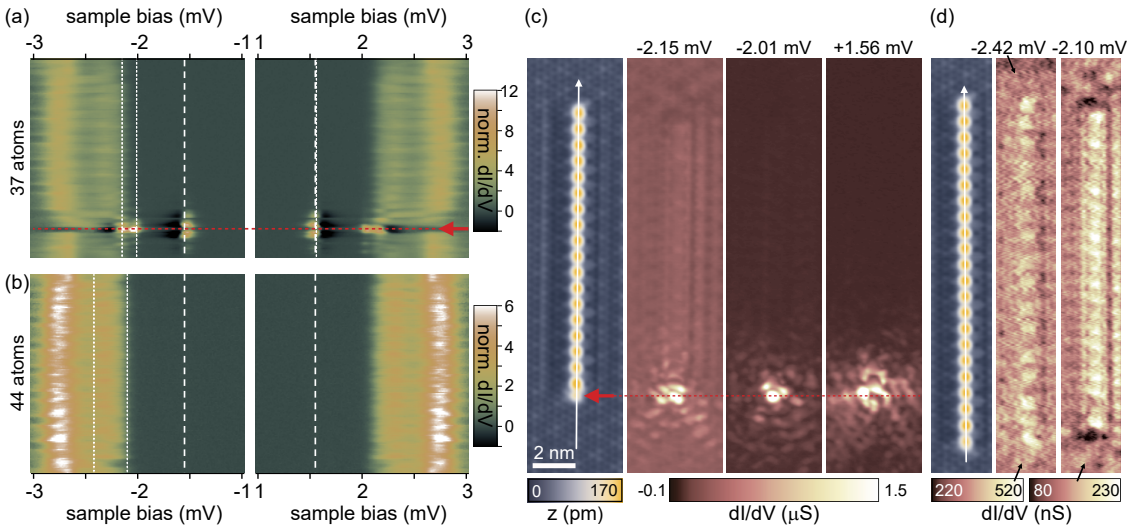

Fig. 6.15.: (a,b) Normalized $\mathrm{d}I/\mathrm{d}V$ spectra measured across a 37-atom (a) and a 44-atom (b) chain (feedback opened at $700\,\mathrm{pA}, 5\,\mathrm{mV}$; modulation of $15\,\mu\mathrm{V}$; $\Delta_\mathrm{t} \approx 1.55\,\mathrm{meV}$ indicated by the white dashed lines). The exact position of the lines is indicated in the topographies in the left of (c,d). (c,d) Constant-current topographies (set point $100\,\mathrm{pA}, 10\,\mathrm{meV}$) of the 37-atom (c) and the 44-atom (d) in the left. The right panels are constant-contour $\mathrm{d}I/\mathrm{d}V$ maps recorded at the energies given above each panel (also indicated by the white dotted lines in (a,b). The single end of the 37-atom chain is marked in red (arrows and lines) in (a,c).

when the atoms are placed very close to each other, direct exchange between d orbitals becomes relevant.

Figure 6.16a shows topographies of dimers with different separations within the CC-CDW (analogue to Fig. 5.7d). The black star denotes the atom that was not moved during data acquisition. Constant-current $\mathrm{d}I/\mathrm{d}V$ spectra covering the positive bias range of a single Fe atom (red trace) can be found in Fig. 6.16b showing the d level resonances as discussed in section 4.3 (Fig. 4.5c). A substrate curve is given in gray. Data of the different energy ranges, $[-2\,\mathrm{V}, -0.2\,\mathrm{V}]$ and $[-0.5\,\mathrm{V}, 0.5\,\mathrm{V}]$ are compiled Fig. A.21.

At this point we like to point out that we observe different resonances with different Nb tips. While the YSR resonances are unaffected the Nb tips may exhibit non-flat DOS at higher energies yielding additional resonances due to the convolution of tip and sample DOS (*c.f.* section 2.2.1). Spectroscopic differences are less pronounced between different Pb tips, but Pb tips are not capable of atom manipulation. Future measurements with several Nb tips (more statistics) could be performed to unambiguously discern the different d levels. Hence, the interpretation provided here has to be viewed as preliminary. In the following, we do not aim at a complete identification of all d-resonances in the spectra, but outline the key findings and interpret the data with regards to possible coupling mechanisms between the atoms in closely packed dimers.

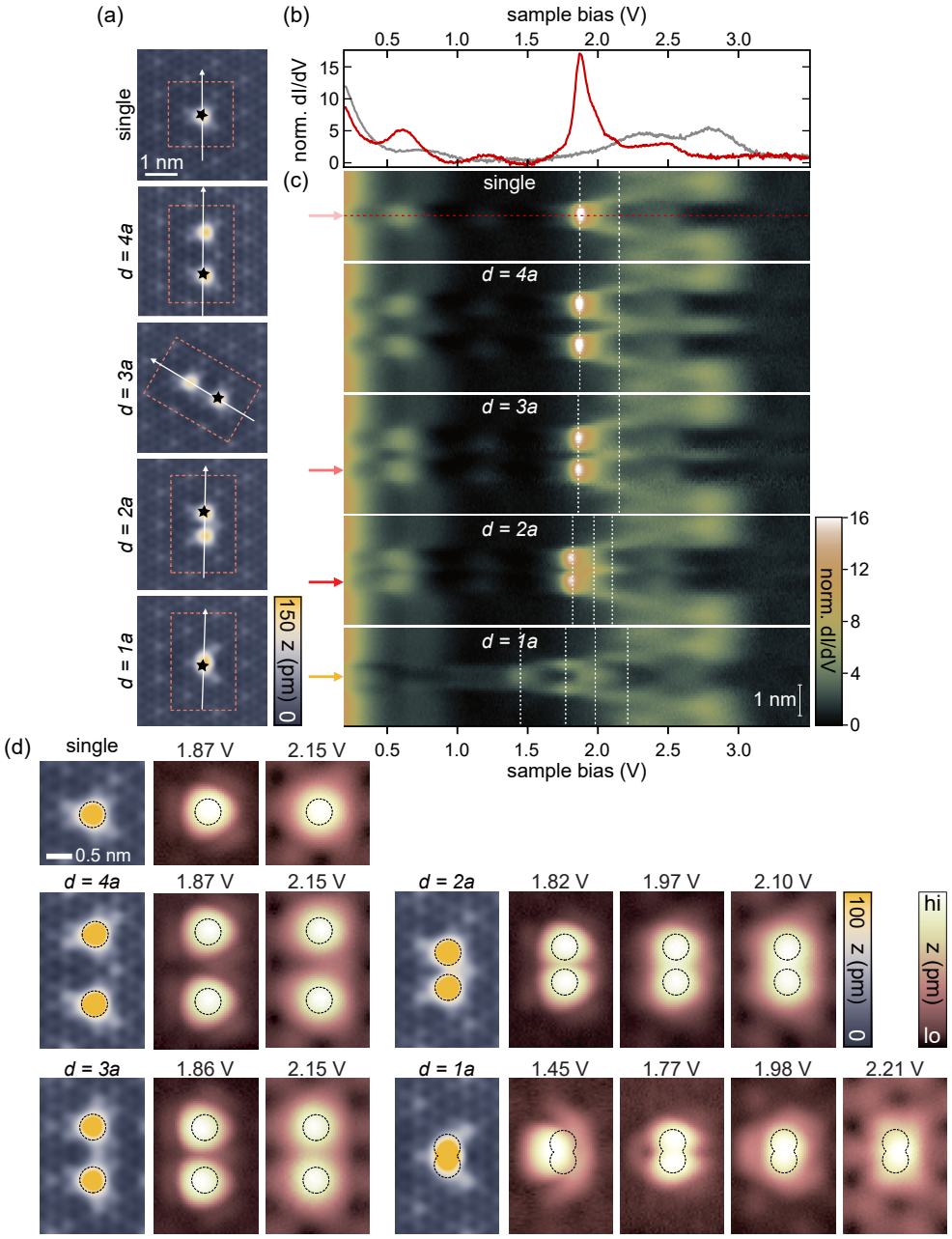

Fig. 6.16.: (a) Topographies (constant-current mode with set point $100\,\mathrm{pA}, 10\,\mathrm{meV}$) of a single Fe atom and Fe dimers with spacings between $4a$ and $1a$. The black star marks the atom which was not moved during the approach series. The white arrows mark the position of the linespectra in (c). The pink boxes indicate the area of the constant-$\mathrm{d}I/\mathrm{d}V$ maps in (d). (b) Normalized constant-current $\mathrm{d}I/\mathrm{d}V$ spectra recorded on a single Fe atom (red) and the substrate (gray) ($200\,\mathrm{pA}$; modulation of $5\,\mathrm{meV}$). (c) Stacked $\mathrm{d}I/\mathrm{d}V$ spectra recorded across the Fe atom and all dimers as indicated in each panel. The position of the spectrum shown in (a) is indicated in red. White dashed lines show the energy of the constant-$\mathrm{d}I/\mathrm{d}V$ maps in (d). The colored arrows in the left mark the position of the spectra shown in Fig. 6.17a,c. (d) Constant-DOS images acquired with a modulation of $30\,\mathrm{meV}$. The bias set point is indicated above each panel. Corresponding topography in the left. Black circles serve as guide to the eye for the atoms' center.

Importantly, the resonances at $0.6\,\mathrm{V}$, $1.87\,\mathrm{V}$ and $2.15\,\mathrm{V}$ have been observed with all Pb and Nb tips[7] (*c.f.* Fig. 6.16b and Fig. 4.10). Note that the resonance at $2.15\,\mathrm{V}$ is very broad and overlaps with the substrate bands at 2-3 V. The resonance around $1.2\,\mathrm{V}$ is not observed with the majority of tips. Thus we assign this resonance to a tip state and will ignore it in the following (analysis). Remember, that the resonances at positive voltage arise from tunneling via singly occupied or empty d orbitals (*c.f.* section 4.3).

Discarding a complete analysis we can compare the data from different dimers recorded with the very same tip apex. In Fig. 6.16c we show stacked spectra recorded across the single atom and the different dimers as indicated in the corresponding topographies in (a) by the white arrows. The position of the spectrum of Fig. 6.16b is indicated as red dashed line. Comparing the different panels in Fig. 6.16c one finds that there are no major differences between the LDOS of the single Fe atom and of the individual Fe atoms within the $4a$-, $3a$- and $2a$-dimers. They all exhibit similar resonances. We detect a slight shift to lower energies ($\approx 50\,\mathrm{mV}$) in the $2a$-dimer for the intense resonance around $1.87\,\mathrm{V}$ (left dashed line) which is in the same order of magnitude than the small shifts observed for different adsorption sites relative to the CDW (*c.f.* Fig. 4.10). Furthermore, the resonances of adjacent atoms start to overlap in the $2a$-dimer leading to slightly enhanced DOS in between the atoms at $1.97\,\mathrm{V}$ (middle dotted line) which could indicate the inset of direct overlap between the d levels.

In strong contrast, the LDOS acquired across the $1a$-dimer shows drastic changes compared to the single Fe LDOS and all dimers with $d \geq 2a$. The resonances previously observed at $0.6\,\mathrm{V}$ and $1.87\,\mathrm{V}$ are clearly not present on the $1a$-dimer. Especially, there is no resonance of similar intensity than the one at $1.87\,\mathrm{V}$. For the faint resonance above $2\,\mathrm{V}$ the situation is not as clear. Interestingly, we find a several resonances at different energies across the $1a$-dimer in the energy window $[1.4\,\mathrm{V}, 2.3\,\mathrm{V}]$. We note that these resonances exhibit different intensity distributions along the dimer, with increased (at $1.45\,\mathrm{V}$ and $1.98\,\mathrm{V}$) or reduced (at $1.77\,\mathrm{V}$ and $2.21\,\mathrm{V}$) intensity on the center of the dimer.[8]

In order to study the spatial distribution of the LDOS in more detail we performed constant-$\mathrm{d}I/\mathrm{d}V$ imaging.[9] Focusing on the energy interval $[1.4\,\mathrm{V}, 2.3\,\mathrm{V}]$ we show constant-$\mathrm{d}I/\mathrm{d}V$ images obtained for the single Fe and the different dimers in Fig. 6.16d (voltages indicated by the dotted lines in (c) and above each panel). The map area is outlined in (a) by the pink frames. Black circles serve as guide to the eye to indicate the atoms' size and position within the maps. The resonance at $1.87\,\mathrm{V}$ exhibits one intense triangular lobe centrally on the atom flanked by three faint stripes at its sides. The resonance at $2.15\,\mathrm{V}$ is mainly characterized by a circular lobe. The patterns in the surrounding are

[7] The fourth resonance at positive bias at $0.15\,\mathrm{V}$ is also detected with all different tips. This energy is not covered in the energy range of Fig. 6.16. See Fig. A.21 for extended data of the other energy ranges.

[8] Further changes in the spectroscopy can also be discerned at lower (and negative energies, Fig. A.21), but the resonances are unintense, broad and thus hard to disentangle from the background.

[9] Lock-In signal at a certain voltage used as feedback for tip position, for details of the measurement mode see section 2.2.1.

related to the CDW as this resonance is in the energy range of the substrate bands above $2\,\mathrm{V}$. In agreement with the line profiles (Fig. 6.16c) we find similar shapes on the single atom and on the atoms of the $4a$- to $2a$-dimers. In the $2a$-dimer the spatial overlap of the states leads to a resonance at $1.97\,\mathrm{V}$ which inherits fingerprints of both other states. As expected from the line profiles, this changes for the $1a$-dimer, where the constant-$\mathrm{d}I/\mathrm{d}V$ maps reveal different shapes. The state at $1.45\,\mathrm{V}$ exhibits one bright lobe with its main intensity shifted to the left of the dimer axis (black circles indicate the atoms' position) and a less intense delocalized lobe spanning the right side of the dimer fading out at the top and bottom. Remarkably, the state at $1.77\,\mathrm{V}$ exhibits reduced intensity on the horizontal axis centrally on the dimer, *i.e.* seems to have a nodal plane. The resonance at $1.98\,\mathrm{V}$ is characterized by one oval protrusion centrally on the dimer, also with faint lobes around. Finally, the resonance at $2.21\,\mathrm{V}$ shows a more rectangular shape also centrally on the dimer. In the line spectra in Fig. 6.16c (constant-current mode) we observe the presence of a nodal plane also for this resonance. Here, one has to consider the measuring method of the constant-$\mathrm{d}I/\mathrm{d}V$ maps and the line spectra. On the one hand, as the constant-$\mathrm{d}I/\mathrm{d}V$ images are a convolution of the topography and the DOS, the nodal plane can be obscured in the maps. On the other hand, the presence of a nodal plane may be exaggerated in the constant-current spectra because the tip is closer to the surface at the edge of the dimer than on its center [Zie+09]. Therefore, we can not unambiguously conclude about the presence or absence of a nodal plane at this energy.

Thus, the $1a$-dimer reveals abrupt changes of the d levels with respect to the single atom and dimers with $d \geq 2a$ including resonances at different energies, different intensities and different spatial appearance which could originate from the formation of bonding and antibonding hybrid d orbitals. Note already, that this abrupt change in the d-resonances appears in combination with the disappearance of the YSR states as discussed in the previous section.

Before offering possible explanations, let us first study the high energy states in longer chains with even and odd number of atoms. Selected constant-current spectra and line spectra across a 6- and 7-atom chain can be found in Fig. 6.17a,b (data covering other energy ranges can be found in Fig. A.21). The position of the spectra of (a) is indicated in the line spectra in the according color, a substrate trace is displayed in black. The position of the line spectra are indicated in the topographies in the left panels in (b). For comparison, we plot a spectrum recorded on the single $1a$-dimer in yellow (position indicated by the yellow arrow in Fig. 6.16c, bottom panel). Comparing the brown and yellow traces we find similar resonances for the freestanding dimer and the dimer within the 6-atom chain.

Along the 6-atom chain one can identify periodic patterns which are symmetric around the center of the chain (horizontal mirror axis). In the dimerized part of the 7-atom chain

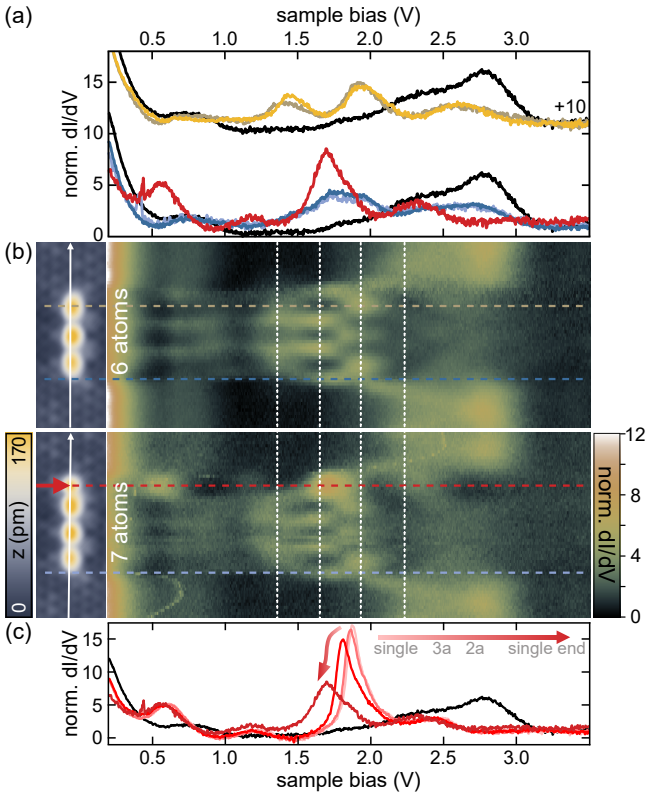

Fig. 6.17.: (a) Normalized constant-current $\mathrm{d}I/\mathrm{d}V$ spectra recorded on the 6- and 7-atom chain as indicated by the colored dashed lines in (b). For comparison, spectrum on a single dimer (yellow, position as indicated in the left of Fig. 6.16c, bottom panel). Substrate in black. Spectra offset as indicated in the right. (b) Stacked $\mathrm{d}I/\mathrm{d}V$ spectra recorded across the 6-atom and 7-atom chain (constant-current set point: $200\,\mathrm{pA}$ and $30\,\mathrm{pA}$ for the 6-atom and the 7-atom chain, respectively; modulation $5\,\mathrm{meV}$). Topographies (constant-current mode with set point $100\,\mathrm{pA}, 10\,\mathrm{meV}$) in the left show the position along the chain. Data covering other energy ranges can be found in Fig. A.21. (c) Normalized constant-current $\mathrm{d}I/\mathrm{d}V$ spectra recorded on the single end of the 7-atom chain (dark red, reproduced from panel a) and on one Fe atom of the dimers with spacings of $2a$, $3a$ (medium red) and on the single Fe atom (bright red) from Fig. 6.16c. The positions of the spectra are highlighted by the arrows in Fig. 6.16c. Substrate spectrum in black.

one can realize the same periodic patterns while the LDOS at the single end is significantly different than in the dimerized part.[10]

In Fig. 6.17c we compare spectra acquired on the single Fe atom (bright), on one atom of the $3a$- and $2a$- dimers (medium red) and on the single end of the 7-atom chain (dark red). We already noted a slight downshift of the resonance at $1.87\,\mathrm{V}$ upon decreasing the separation ($4a \rightarrow 2a$) above (Fig. 6.16c). This trend continues for the data acquired on the single end which is placed at a distance of $1a$ to the next dimer of the 7-atom chain. Furthermore, we observe broadening of the intense resonance. Beside these slight deviations the LDOS at the single end exhibits similar resonances as the single Fe atom. Broadening and shifting of states may result from different screening by or hybridization with the substrate and adjacent atoms which can be different for different orbitals. Moreover, at the outermost dimer of the 6-atom chain there are states at similar energies (blue traces in Fig. 6.17a) that spatially overlap with the intense state at the single end which could feign the broadening.

Let us investigate the constant-$\mathrm{d}I/\mathrm{d}V$ maps acquired on the 6- and 7-atom chains (Fig. 6.18). Energies are indicated by the white dashed lines in Fig. 6.17b and above each panel. Comparing the maps of the 6-atom chain to the maps recorded on the 1a-dimer (Fig. 6.16d, bottom right panel) one can identify the 1a-dimer states appearing three times in a row along the 6-atom chain (slightly shifted in energy). In particular, the dimer state at $1.45\,\mathrm{V}$ exhibiting asymmetric DOS with intense lobe left of the dimer axis and the faint lobe spanning from top to bottom at the right side of the dimer can be identified at $1.36\,\mathrm{V}$. Also the ($1a$-)dimer state with the nodal plane at $1.77\,\mathrm{V}$ can be found at $1.65\,\mathrm{V}$ along the 6-atom chain exhibiting nodal planes centered on each of the three dimers. Similar findings hold for the resonances at $1.93\,\mathrm{V}$ and $2.23\,\mathrm{V}$ of the 6-atom chain which reveal similar spatial fingerprints than the dimer maps at $1.98\,\mathrm{V}$ and $2.21\,\mathrm{V}$. This behavior can also be discerned in the constant-current line spectra. A detailed graphic illustrating the repetition of dimer states along the chain can be found in Appendix Fig. A.22. Generally, one expects increasing number of hybrid orbitals with increasing number of atoms ultimately resulting in the formation of d-bands in a chain with uniform coupling (*c.f.* section 6.1.2). Hence, as already pointed out earlier, this hints toward small or negligible coupling between adjacent dimers.

For completeness, Fig. 6.18b shows constant-$\mathrm{d}I/\mathrm{d}V$ maps acquired on the 7-atom chain. During data acquisition the single end occasionally switched to the other side of the chain. That is why some maps are acquired with the single end on top and others with the single atom at the bottom of the chain as indicated by the topographies in the left of the panels (and by red arrows). It was assured that no switch of the single end occured during acquisition of each map presented here (by recording topographic images directly before and after each constant-$\mathrm{d}I/\mathrm{d}V$ map). In the dimerized part of the chain we identify

[10] In order to avoid switching of the single end during the measurement, the spectra on the 7-atom chain has to be recorded at a very low current set point, i.e. the data is in general more noisy.

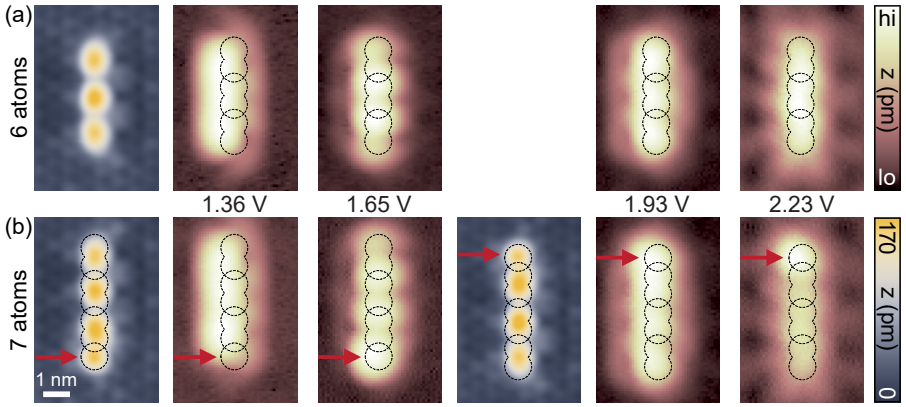

Fig. 6.18.: (a) Constant-$\mathrm{d}I/\mathrm{d}V$ maps acquired in the area of the topographies (constant-current mode with set point $100\,\mathrm{pA}, 10\,\mathrm{meV}$) shown in the left for the 6-atom chain (a) and the 7-atom chain (b). The bias set point is indicated between the top and bottom panels ($30\,\mathrm{meV}$ modulation) and by the white dashed lines in Fig. 6.17b. The single end of the 7-atom chain switched in between recording the images (it was ensured that there is no switch during one map). Arrows point out the single ends. Black dashed circles serve as guide to the eye.

the same patterns as observed on the 6-atom chain. In contrast, we find (in agreement with the line spectra) increased (reduced) signal at the bottom end of the chain at $1.65\,\mathrm{V}$ ($1.36\,\mathrm{V}$) as there is a (no) resonance at the single end. Similar findings, although not as clear hold for the top end at both higher energies (and also for the resonances at lower energies, not shown).

To summarize, the findings at higher energies reveal striking changes in the d-orbital structure when Fe atoms are brought close together. A spacing of $1a$ corresponds to a distance of $3.44\,\text{Å}$ [Mar+72] between the atoms which facilitates direct exchange between the d orbitals and hence, they can form bonding and antibonding linear combinations. Indeed, the constant-$\mathrm{d}I/\mathrm{d}V$ maps inherit signatures of such hybrid orbitals. Interestingly, the pronounced changes in the d level spectroscopy coincide with the quenching of intense YSR resonances. Thus, the data further confirms the dimerization between two adjacent Fe atoms within longer $1a$-chains. In the following section we discuss different coupling mechanisms that could explain the findings in both energy ranges.

6.3.3 Possible mechanisms of d orbital coupling

In the previous sections we presented extensive data covering the superconducting energy range and the d-orbital physics. For all spacings $d \geq 2a$ between two Fe atoms we find similar d-orbital structure and intense long-range YSR states. When reducing the distance to $d = 1a$ we find an abrupt change in the d orbitals accompanied with largely quenched YSR states (only faint YSR fingerprints within the substrates coherence peaks). We further find the Fe atoms appear dimerized in larger structures $N \geq 3$. For odd numbers of atoms the single atom attributes (intense YSR states and d levels) are recovered at the

single end of the chain while the dimerized parts show similar features as observed on the single $1a$-dimer.

Recalling Eq. 4.14, the YSR excitation energy contains the spin S and the exchange coupling J. The abrupt disappearance of YSR states can have several origins: (1) Quenching of the magnetic moment in the $1a$-dimer, (2) reduced exchange coupling J between the (singly occupied) d levels and the substrate in the dimers and (3) purely antiferromagnetic (AFM) RKKY coupling between the $1a$-spaced Fe atoms. In the following we discuss all mechanisms.

Recalling section 5.1.1, the RKKY interaction is an indirect spin-spin interaction mediated by the conduction electrons. In the dense limit, the d orbitals overlap and direct exchange between them should dominate the interaction in the $1a$-dimers. This is in agreement with the observed changes in the d levels for $d = 1a$. Furthermore, the RKKY interaction should be uniform along the chain, independent of the number of atoms. Hence, the dimerization with the presence of single ends rules out purely AFM RKKY interaction to be the origin of the diminished YSR signatures. Moreover, the recovery of the single atom attributes at single ends and the constant number of hybrid orbitals discerned on the dimer and 6-atom chain (being similar to three dimers in a row) hint toward small or negligible hopping between adjacent dimers (or between a dimer and a single end). Further, the dimer d orbitals inherit signatures of bonding and antibonding hybrid orbitals and manipulation experiments show (relatively) strong bonding within the dimer. Hence, we interpret the dimers in terms of formation of covalent bonds between two Fe atoms, *i.e.* the formation of Fe_2 molecules on the $NbSe_2$ surface with no or very weak interaction between adjacent molecules (or between a molecule and a single atom next to it).

In the following we address points (1) and (2) of above. In gas phase all d orbitals are degenerate and split in bonding and antibonding hybrid orbitals upon molecule formation. Here, it is straightforward that the molecule is stable only if more electrons occupy bonding orbitals than antibonding ones. The situation including two degenerate levels is sketched in Fig. 6.19c. Albeit, we observe not only orbitals with antibonding character, but also orbitals which seem to be bonding at $V > 0$. Remember, that all orbitals found at positive bias correspond to empty of half filled levels.

Importantly, we should consider that the Fe_2 molecules form on the surface of $NbSe_2$. Hence, the starting point is the non-degenerate d levels split by the crystal field. Figure 6.19a images the $1a$-dimer (from Fig. 6.16a) in a 3D view. The red triangles indicate two adjacent HC sites, *i.e.* the adsorption configuration of an Fe_2 molecule. The x- and y-axis point along and perpendicular to the dimer axis, respectively. Figure 6.19b presents the crystal field split d levels within a trigonal-pyramidal (ML_3) adsorption configuration (*c.f.* Fig. 4.1e) and a 3D representation of the d-block within the same coordinate system as in Fig. 6.19a [Jea05]. We now focus on two orbitals of the d-block: one with two lobes pointing along the x-axis (red ellipse) and one with all lobes directed in the yz-plane (blue ellipse). We expect strong splitting upon hybridization in the Fe_2 molecule for the former

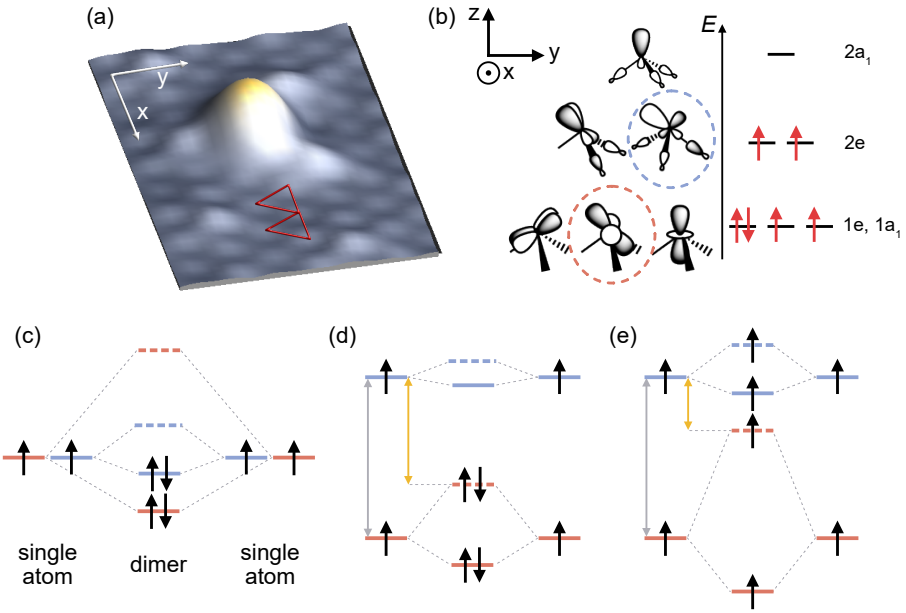

Fig. 6.19.: (a) 3D topographic view of the $1a$-dimer (constant-current mode with set point $100\,\mathrm{pA}, 10\,\mathrm{meV}$). Axis are indicated in white and red triangles outline two adjacent HC sites. (b) Crystal field split d orbitals (pyramidal ML_3 crystal field) with a 3D representation in the left. Images taken and adapted from [Jea05]. (c) Schematic illustration of two singly occupied degenerate d levels with different hybridization strengths. All electrons occupy bonding states in the molecule. (d,e) Schematic illustration of two non-degenerate levels and their possible occupation with electrons. In (c) doubly occupation is favored. In (d) the energy gain due to parallel spin wins.

orbital (σ-bond) while the hybridization would be weak due to small overlap for the latter. Remember, that this splitting due to hybridization happens within the crystal field. As the separation of the atoms forming the Fe_2 molecule is only one lattice site ($a = 3.44\,\text{Å}$), we expect the splitting upon dimerization to be in the same order than the crystal field splitting.

Considering only these two orbitals we schematically illustrate one possible scenario in Fig. 6.19d that can lead to the presence of unoccupied bonding levels. In the monomer (left), both levels are singly occupied due to Hund's energy gain (which exceeds the energy splitting indicated by the gray arrow). In the molecule the electrons of the blue monomer level can lower their energy by doubly occupying the red antibonding orbital (energy gain of twice the yellow arrow). Thus, we find the bonding level of the blue level among the empty orbitals. This corresponds to point (1) of above implying that the disappearance of the YSR states originates from a quenched total spin $S = 0$ within an Fe_2 molecule. Hence, the orbitals detected at positive energies would correspond to unoccupied levels in this scenario.

However - to address the third possible scenario - the hybrid orbitals detected at positive bias could also be singly occupied when the spins are aligned as sketched in Fig. 6.19e. In this case the energy gain by doubly occupying the red level (yellow arrow) is smaller than the energy gain by aligning the spins (Hund's ernegy). In this case, the Fe dimers carry a

non-zero spin and the resonances at $V > 0$ would correspond to singly occupied levels. If the spin is carried by hybrid orbitals which point away from the surface, the exchange coupling J with the substrate would be small and thus, YSR resonances can appear as weak features at energies within the substrates coherence peaks (free-spin regime).

Dimerization along self-assembled Co chains on Cu(111) [Zak+13] was observed. DFT calculations suggest FM exchange between two Co atoms to be the driving mechanism for the dimerization along the chain. Hence, the Co atoms within the dimer both keep the high-spin configuration of the single Co atoms.

In the simple examples of Fig. 6.19d,e we considered only two orbitals, generally explaining the appearance of bonding orbitals at positive energy. In reality, of course, a mixed version with some resonances probed at positive bias being empty and some being singly occupied is realistic. Concluding, experiments reveal the formation of (nearly) noninteracting/independent covalently bonded Fe_2 molecules within $1a$-spaced atomic chains on $NbSe_2$.

As discussed before we are not able to unambiguously identify the complete set of d orbitals in the data. Future measurements with different tips could enable a more complete interpretation (in order to unambiguously distinguish orbital states from possible tip states). Also the use of functionalized tips (*e.g.* attaching a single CO molecule to the tip apex) [Gro+11] could enhance the resolution enough to discern the different d level geometries. However, resonances at negative energies (corresponding to the filled states) are generally hard to discover by STS. Supporting DFT calculations could provide more insight into the exact adsorption configuration (trigonal planar or trigonal-pyramidal ML_3, *c.f.* Fig. 4.1) of a single HC atom and the $1a$-dimer which we cannot access with our STM measurements and provide the d level splitting within the crystal field and the expected spin configuration of monomer and dimer.

In order to access the spin configuration of the Fe_2 molecules, one could perform spin polarized STS using spin-polarized tips (see [Wie09; WZW11] for reviews) and search for FM contrast on the dimerized chain. For example, the orbital character of the minority and majority spin channels of Co atoms on a Mn layer on W(110) could be resolved with a spin-polarized tip in [Ser+10]. However, such experiments are quite demanding as they require preparation and calibration of the spin-polarized tip on the surface and may be not easily realized in our material system (requirement of a particular tip for atomic manipulation).

Additionally, one can search for different magnetic fingerprints. Examples involve spin-flip excitations or Kondo anomalies[11] (in the non-superconducting state). Spin-excitations can appear as symmetric steps/peaks outside the superconducting energy gap ($\sim$ meV-range) which result from tunneling processes involving an inelastic spin-flip channel [LLH10; Hei+04; Kez+19]. The Kondo effect arises from the local screening of the

[11] Preliminary data show broad Kondo features on single HC Fe atoms, not shown in this thesis.

impurity spin by the surrounding conduction electrons and manifests as a resonance at the Fermi level which is characterized by a particular (Fano-) lineshape (*c.f.* section 4.1.2 [Hew93]). The presence of either one would imply a non-vanishing spin of $S \geq 1$ for the former and $S \geq 1/2$ for the latter. However, the disappearance of a Kondo resonance upon dimer formation does not necessarily imply a quenched dimer spin as shown for FM closely spaced Co-dimers on Cu(100) [Wah+07] and Au(111) [Che+99]. Also, spin excitations might be flattened out due to strong scattering between the magnetic impurity and the metallic host and thus not be resolved. Different measurements methods such as XMCD (X-ray magnetic circular dichroism) spectroscopy performed on samples with different coverage of Fe atoms could help to access the spin configuration. However, this method is an averaging technique and lacks spatial resolution.

Closing the chapter, even though the actual spin configuration (complete d level occupation) of the $1a$-dimers remains an open question to be addressed in future experiments, the data shows the formation of (nearly) non-interacting Fe_2 molecules within the chain. The position of the single end is stable, but reversibly switchable by bias pulses and could thus be used at a single bit data storage. In case of FM dimers the molecules within the chain could act as „spin-isolated“ units [Zak+13] along the chain which might be controllable by placing magnetic atoms at a certain distance nearby exploiting dipolar or RKKY interactions.

7 Conclusion and Outlook

In this thesis we investigated Fe atoms adsorbed on the surface of $2H$-$NbSe_2$ by means of scanning tunneling microscopy and spectroscopy. The coexistence of superconductivity and a charge density wave (CDW) at low temperature provides a complex platform for the study of Yu-Shiba-Rusinov (YSR) states. Atomic manipulation facilitates the assembly of customized adatom arrangements which we exploit in order to study the interaction between Fe atoms in various different dimers and larger structures such as adatom chains.

Tunneling spectroscopy performed on the clean surface exploiting the superior energy resolution of superconducting tips reveals a peculiar quasiparticle density of states (DOS). In a combined STM and *ab initio* study [San+21] this quasiparticle DOS could be well reproduced. In the study, first-principles simulations reveal the highly anisotropic nature of superconductivity in $NbSe_2$ ruling out the scenario of multiband superconductivity. The calculations further shine light onto the complex interplay between the CDW and superconductivity - both being charge-ordered phases driven by electron-phonon coupling.

We successfully employed $2H$-$NbSe_2$ as a superconducting substrate for the investigation of YSR states induced by Fe atoms, which adsorb in the two hollow sites of the terminating Se layer (HC and MC). For both species, the strong 2D electronic character of $NbSe_2$ yields long-ranged YSR wave functions. The incommensurate CDW induces local variations of the DOS. We found that the exact position of the Fe atoms relative to the CDW affects the YSR energy and governs the symmetry of the wave function. By investigating various HC atoms we could track the evolution of the two YSR states deepest within the gap, referred to as α- and β- state, along one period of the CDW. The correlation between the YSR excitation energies and the CDW-induced DOS suggests a screened-spin ground state for both (α-, β-) states at the maximum of the CDW. For adatoms coinciding with the minimum of the CDW, the deepest in-gap resonance, α, undergoes the quantum phase transition to the free-spin regime. The experimental findings were qualitatively reproduced within a phenomenological mean-field description of the CDW incorporated in a simple tight-binding model of $NbSe_2$ [Lie+20; Ace20]. Thus, the CDW creates a variety of inequivalent sites and, hence, provides a novel mechanism to tune YSR energies of magnetic adsorbates across the surface.

Besides the CDW-induced variations of the YSR energies we find spatial variations of the YSR energies in the vicinity of MC atoms. Possible origins involve slight movement of the atoms within the adsorption site due to van der Waals forces between tip and adatom or the electric field present in the tunnel junction. At this stage, we are not able

to unambiguously discern the underlying mechanism. The number of YSR resonances of both species (MC and HC) is in agreement with a high-spin configuration $S_{\mathrm{imp}} = 2$ of the Fe atoms. Fingerprints of magnetic-anisotropy-split YSR excitations could be revealed.

During this thesis, manipulation of Fe atoms on $NbSe_2$ with superconducting Nb tips could be successfully established. This allows the assembly of customized adatom arrangements while retaining the high energy resolution of a SC tip. The large extent of the YSR wave functions allows hybridization in dimers with interatomic separations of several lattice sites - referred to as dilute coupling limit.

Based on the knowledge of the effect of the CDW on the YSR states of single HC atoms we assembled and investigated various atomic dimers within the rich landscape provided by the incommensurate CDW. Dilute dimers with interatomic separations ranging from two to four lattice sites have been explored. We find that the hybridization between YSR states sensitively depends on the position of the individual atoms forming the dimer relative to the CDW. In particular, the incommensurate nature of the CDW allows the comparison between dimers with equal separation, but with both constituents on equal or different CDW positions. If the prerequisite of identical positions relative to the CDW of both constituents and hence, similar YSR energies is met, we observe hybridization between YSR states which is absent otherwise.

Dimers consisting of HC atoms with a separation of three lattice sites $(3a)$ almost match the CDW periodicity $(a_{\mathrm{CDW}} \approx 3.05a)$. On dimers with both atoms on adjacent CDW maxima, we found a dimerization-induced quantum phase transition of the α-derived hybrid states. This transition is probably driven by the RKKY interactions and not be explained classically. The larger gain in RKKY energy overcompensates the energy required to drive the hybrid α-states (deepest within the gap) from the screened-spin to the free-spin regime.

A separation of $3a \approx 1\,\mathrm{nm}$ between adjacent HC atoms should facilitate coupling within the landscape set by the incommensurate CDW on larger scales as neighboring atoms sit on nearly identical CDW positions. In order to realize an extended YSR chain in the dilute coupling limit we stepwise increase the number of atoms (keeping the separation of $3a$) and track the formation of the YSR bands. We find that for intermediate chain lengths ($\lesssim 10\,\mathrm{nm}$) the CDW adopts the periodicity of the chain yielding uniform hybrid bands along the entire structure. For increased chain lengths the natural long-range periodicity $\gtrsim 3a$ of the CDW imposes a smoothly varying background potential along the chain inducing band bending of the YSR bands. Up to a chain length of 51 atoms we do not find evidence of Majorana end states.

Beside the systematic investigation of hybridization between YSR states within various atomic dimers and the realization of a extended chain in the dilute coupling limit we studied closely packed dimers. Here, Fe atoms are located on adjacent HC sites and d orbitals directly overlap. We find that atoms within linear structures with more than two

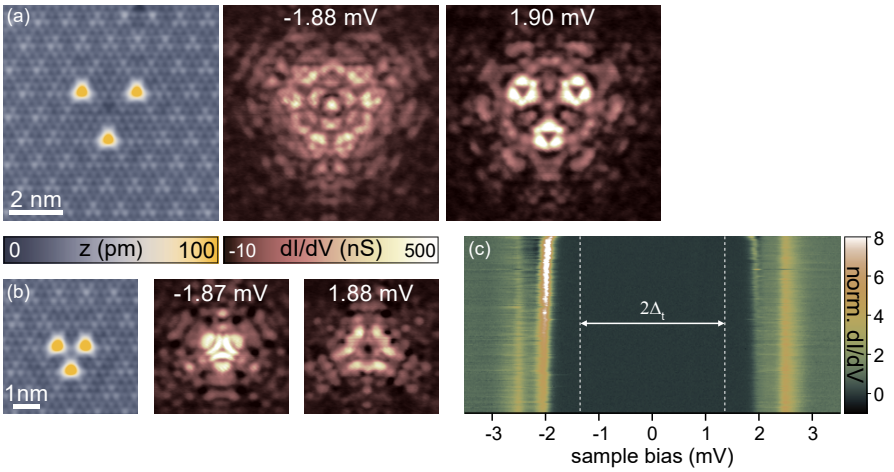

Fig. 7.1.: (a,b) STM topographies (constant-current mode with set point $100\,\mathrm{pA}, 10\,\mathrm{mV}$) of three Fe atoms arranged in a triangle with sides of $6a$ (a) and $3a$ (b). Exemplary constant-contour $\mathrm{d}I/\mathrm{d}V$ maps of the hybrid YSR states. Constant-contour feedback was opened at $250\,\mathrm{pA}, 5\,\mathrm{mV}$ and a modulation of $15\,\mu\mathrm{V}$ was used. Bias voltages are given above each panel. The Nb tip gap is $\Delta_\mathrm{t} \approx 1.55\,\mathrm{meV}$. (c) Stacked normalized constant-height $\mathrm{d}I/\mathrm{d}V$ spectra recorded centrally on various MC Mn atoms. Spectra are sorted by the energy of the intense YSR resonance. Feedback was opened at $200\,\mathrm{pA}, 4\,\mathrm{mV}$ and a modulation of $15\,\mu\mathrm{V}$ was used. The (Pb) tip gap of $\Delta_\mathrm{t} \approx 1.35\,\mathrm{meV}$ is indicated by the white dotted lines.

atoms appear dimerized in the topographies accompanied by the disappearance of intense YSR resonances and an abrupt change of the d level resonances. These observations indicate the formation of covalently bonded Fe_2 molecules on the $NbSe_2$ surface. Further studies (STM and DFT) should be performed to reveal the spin state of the Fe_2 molecules and to discern the full electronic structure of the d shell.

The findings of this thesis put forward $NbSe_2$ as a well-suited substrate for the investigation of coupled YSR states and pave the way for various following experiments. We can go beyond the 0D (atom) and 1D (chain) nanostructures and study wave function hybridization within 2D arrangements of adatoms. For example, in the dense structures one could create frustrated spins in closed loops consisting of an odd number of Fe atoms. Further, closed loops of dilute assembled Fe atoms could mimic infinite YSR chains. First exemplary $\mathrm{d}I/\mathrm{d}V$ maps of two triangular structures with side lengths of $6a$ and $3a$ are presented in Fig. 7.1a,b showing auspicious wave function patterns.

On the one hand the CDW constitutes a rich energetic landscape for the assembly of diverse atom assemblies. But it also limits the extent of YSR chains with constant-energy YSR bands due to its incommensurate nature. Possibilities to overcome this limitation would be the use of a different adatom species that is less sensitive to the CDW-induced variations of the DOS. Here, first experiments with Mn atoms on $NbSe_2$ showed promising results as can be seen in Fig. 7.1c. It shows a plot of stacked $\mathrm{d}I/\mathrm{d}V$ spectra recorded on the centers of various MC Mn atoms on multiple positions relative to the CDW. Mn atoms

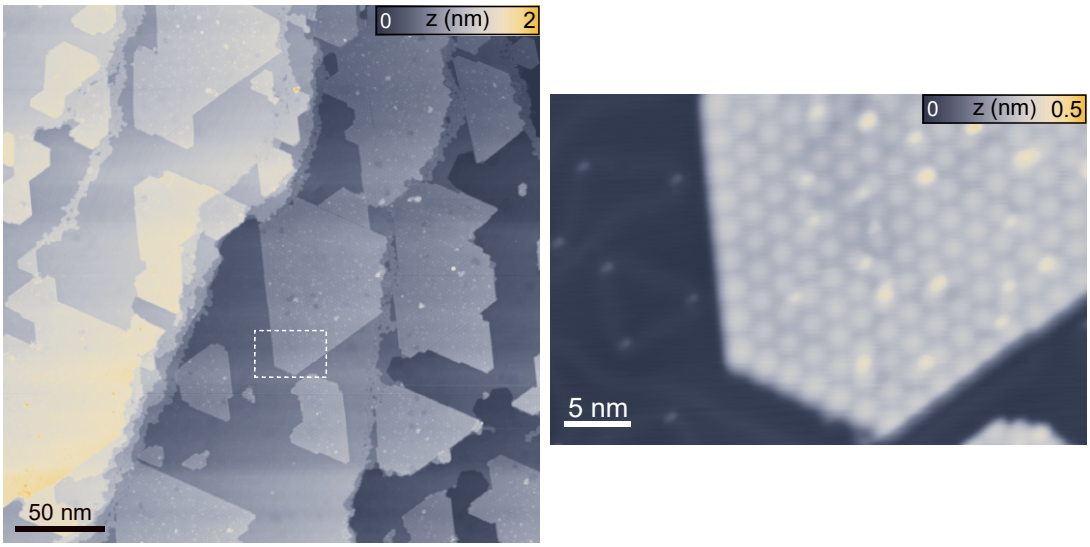

Fig. 7.2.: Large scale constant-current topography (left) and close-up view of a smaller area (right) of NbS_2 islands grown on a Au(111) surface (set point: $100\,\mathrm{pA}, 1\,\mathrm{V}$).

exhibit only one pronounced YSR resonance. We find only slight variations within the multiple MC Mn atoms.

Further, one could employ NbS_2 as a substrate which has - beside the lack of a CDW - very similar physical properties as $NbSe_2$ [Gui+08b; Fen+16; Hei+17]. Recently, there was progress in the development of the growth of bulk NbS_2 crystals such that sufficiently large samples for the investigation by scanning tunneling microscopy are commercially available. One could also implement the growth procedure of single-layer NbS_2 in order to obtain truly 2D superconductivity [Sta+19; Zha+19]. First experimental attempts to grow NbS_2 on a Au(111) have shown promising results as can be seen in the topographies in Fig. 7.2, where one finds large monolayer-NbS_2 islands. However, at $1.2\,\mathrm{K}$ we do not find evidence of a superconducting energy gap. One could avoid hybridization with the Au surface by employing a decoupling layer as graphene, on which superconducting single layers of $NbSe_2$ have been successfully grown [Uge+16; Xin+17]. Another possibility is to implement the growth process on a superconducting or semiconducting substrate.

Appendix

A

A.1 Details of the numerical deconvolution

As described in section 2.3.3, the characterization of the SC tips on the corresponding crystal before changing to the $NbSe_2$-substrate gives us already a good estimate of the tip's energy gap Δ_t and the depairing factor Γ (*c.f.* Eq. 2.20).

In order to assure that the tip properties did not change during sample exchange from Pb/Nb samples to $NbSe_2$, we checked the accurateness of the tip's energy gap by deconvolution and recalculation of spectra on several Fe adatoms for each sample and tip preparation. If a slightly inaccurate value of the energy gap is assumed for the tip, the energies of the thermally excited YSR resonances are found in a wrong position in the recalculated trace as can be seen in Fig. A.1a (red arrows). Before deconvolving all spectra are normalized and smoothed using a Savitzky-Golay filter.

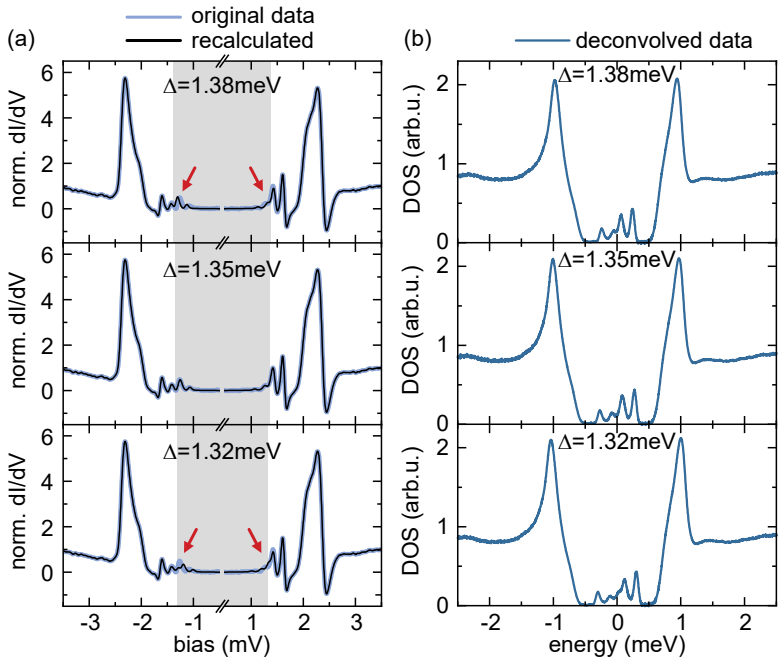

Fig. A.1.: (a) Original and recalculated data of a atom I of section 4.4. (b) Deconvoluted data. The deconvolution is performed with different values for the tip gap as indicated in the panels. Already for slightly inaccurate tip gaps the thermal peaks start to deviate when we recalculate the data.

A.2 Additional data and discussion to section 3.2.2

Intensity variations on the scale of the CDW can be identified by comparing the dark, medium and bright traces of each color corresponding to minimum, local minimum and maximum of the CDW in the HC (red) and CC (brown) phase as indicated by colored stars in the topography. The bottom trace is the average of all six spectra and is used for the comparison with the simulations in Fig. 3.8c in section 3.2.2. The intensity variations are of similar magnitude than the atomic scale variations (*c.f.* Fig. 3.6).

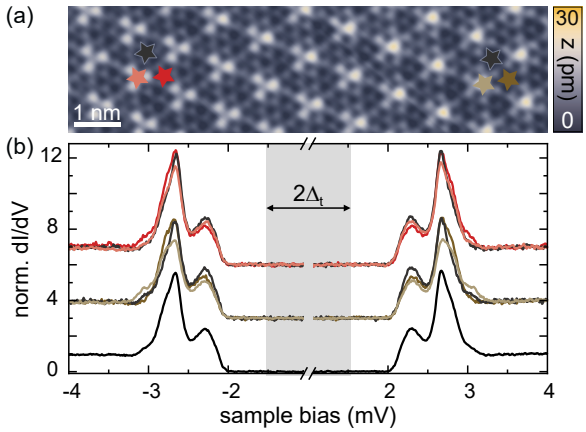

Fig. A.2.: (a) Constant-current image of a clean $NbSe_2$ surface (recorded with a set point of $100\,\mathrm{pA}, 10\,\mathrm{mV}$). (b) Constant height $\mathrm{d}I/\mathrm{d}V$ spectra taken on the $NbSe_2$ surface at the positions indicated with the colored stars in (a) recorded with a Nb tip (feedback was opened at the position of the bright brown spectrum for all traces shown at $250\,\mathrm{pA}, 5\,\mathrm{mV}$ and a modulation of $V_{\mathrm{rms}} = 15\,\mu\mathrm{eV}$ was used). The black curve is the average between all six colored spectra and is used in Fig. 3.8c. Spectra offset for clarity.

A.3 Additional data and discussion to section 4.4

A.3.1 Additional $\mathrm{d}I/\mathrm{d}V$ maps and the influence of the NDC

Figure A.3 accommodates the complete set of the $\mathrm{d}I/\mathrm{d}V$ maps of the $\pm\alpha$- and $\pm\beta$-resonances of atoms I-VI. The positive bias voltage panels were already presented in section 4.4, Fig. 4.7a, but are still presented here for better comparison. Their negative counterparts are depicted in the lower two rows. As introduced in section 4.2.1, opposite bias polarities image the $|u|^2$ and $|v|^2$ components of the YSR wave function, respectively [Rus69].

As expected, the $|u|^2$ and $|v|^2$ components lead to distinct scattering patterns. As discussed in section 4.3, the convolution of tip and sample density of states can lead to the appearance of a negative $\mathrm{d}I/\mathrm{d}V$ signal. Its spatial variations can induce distortions of the intensity of individual YSR states, culminating in their suppression in the NDC region of a nearby state. Consequently, also the $\mathrm{d}I/\mathrm{d}V$ maps at the energy of a specific YSR state may be affected by a close-lying YSR state.

In particular, the $\pm\beta$-states of atom II, IV and V are strongly affected by the NDC of the $\pm\alpha$-resonances, which are close in energy (Fig. A.3). In order to grasp the effect of NDC, we investigate the $\mathrm{d}I/\mathrm{d}V$ maps of thermally excited YSR states. As mentioned in section 4.3, thermal excitation of quasiparticles leads to additional resonances within the energy gap of the tip (for example, *c.f.* Figs. 4.5 and 4.6, grey shaded area). Whereas the original resonances are found at a bias voltage of $eV_{\pm\alpha,\pm\beta} = \pm|\Delta_\mathrm{t} + E_{\alpha,\beta}|$, the thermally excited states are located at $eV_{\pm\alpha^\star,\pm\beta^\star} = \mp|\Delta_\mathrm{t} - E_{\alpha,\beta}|$ [Rub+15c].

The thermally excited YSR states are of much less intensity and, therefore, exhibit small or negligible regions of NDC. Figure A.4 shows the $\mathrm{d}I/\mathrm{d}V$ maps recorded at the corresponding voltages of the thermally excited YSR states for atoms I-VI arranged in a manner that the thermal duplicates can be found at the same position within the array as in Fig. A.3. In these maps the similarity of the $\pm\beta^\star$ states of atoms I, II and IV is more striking than in the original maps of $\pm\beta$.

To further illustrate the impact of the NDC from the $\pm\alpha$-YSR resonances on the $\pm\beta$ state, we *simulate* the map of $\pm\beta$ by subtracting a fraction of the $\pm\alpha$ maps (mimicking the NDC) from the thermal $\pm\beta^\star$ maps (Fig. A.5a,b). The result (Fig. A.5c) shows remarkable similarity to the original $\pm\beta$-states (Fig. A.5d), illustrating the impact of NDC on the observed wave function patterns.

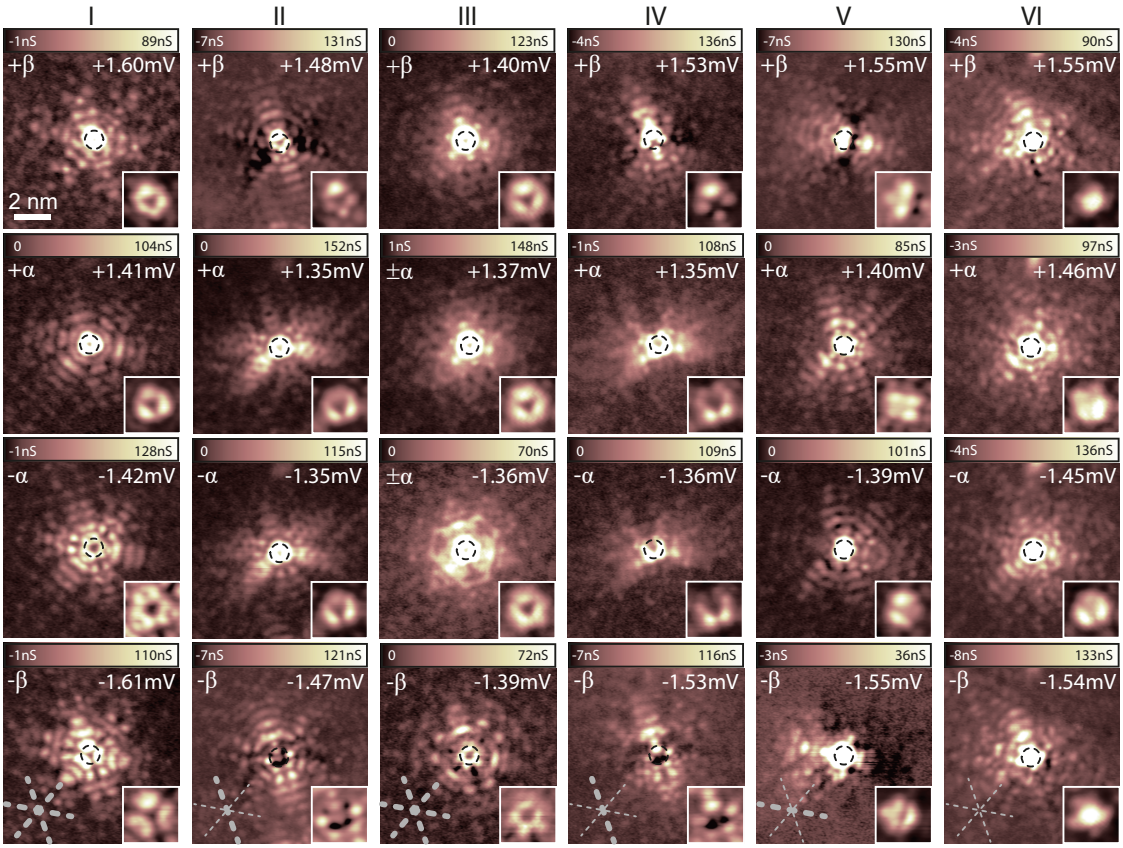

Fig. A.3.: Constant-contour $\mathrm{d}I/\mathrm{d}V$ maps ($9.5\,\mathrm{nm} \times 9.5\,\mathrm{nm}$) of the YSR $(\pm\alpha, \pm\beta)$ states of HC atoms I-VI (set point: $200\,\mathrm{pA}, 4\,\mathrm{mV}$; $V_{\mathrm{rms}} = 15\text{-}25\,\mu\mathrm{eV}$; V_{bias} as indicated in the images). The insets show a $2\,\mathrm{nm} \times 2\,\mathrm{nm}$ close-up view around the center of the atoms. Black dashed circles (diameter $1\,\mathrm{nm}$) outline the atoms' position. The grey dashed lines in the bottom map of each atom indicate the crystal's symmetry axes. Thick lines indicate mirror axes present in the $\mathrm{d}I/\mathrm{d}V$ map. Data is partially reproduced from Fig. 4.7.

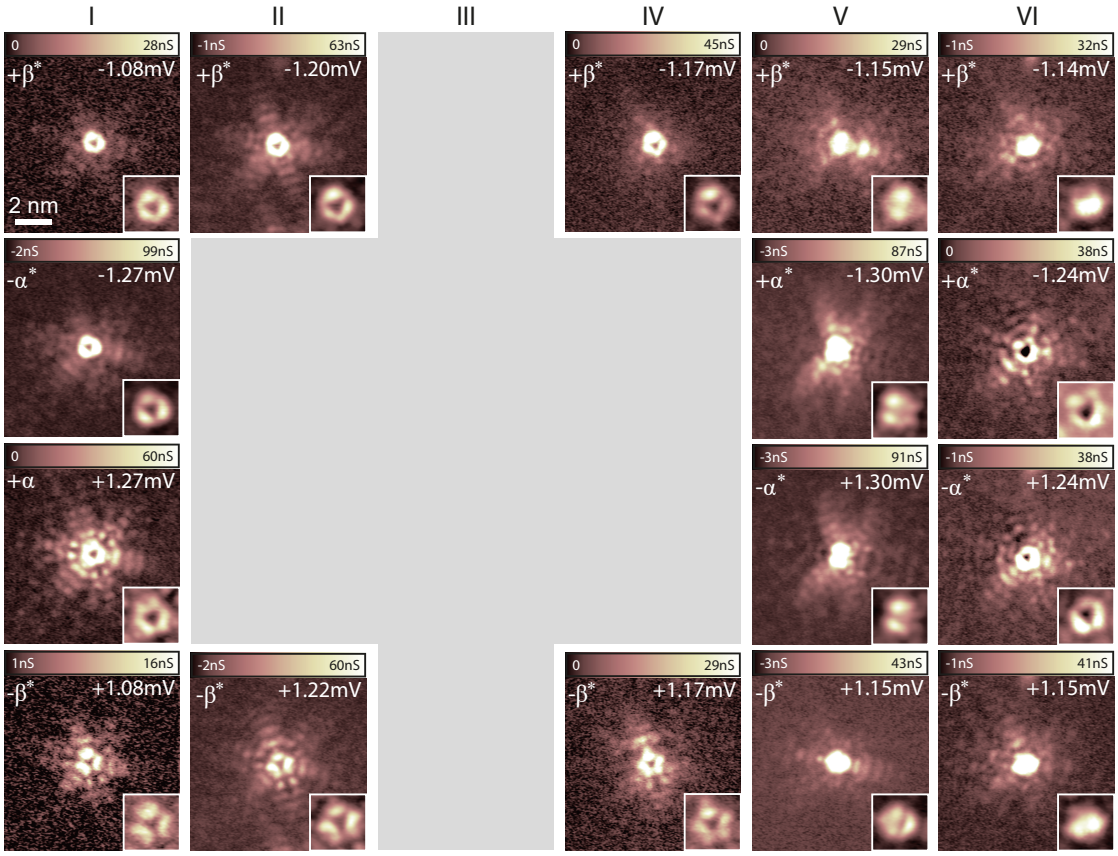

Fig. A.4.: Constant-contour $\mathrm{d}I/\mathrm{d}V$ maps ($9.5\,\mathrm{nm} \times 9.5\,\mathrm{nm}$) of the thermally excited YSR ($\pm\alpha^*, \pm\beta^*$) states (set point: $200\,\mathrm{pA}, 4\,\mathrm{mV}$; $V_{\mathrm{rms}} = 15\text{-}25\,\mu\mathrm{eV}$; V_{bias} as indicated in the images). The insets show a $2\,\mathrm{nm} \times 2\,\mathrm{nm}$ close-up view around the center of the atoms. The images are arranged in the same way as in Fig. A.3, *i.e.* the maps of the thermally excited YSR states can be found in the same position within the array as in Fig. A.3. For YSR resonances at zero energy (*i.e.* $eV_{+\alpha,\beta} = eV_{-\alpha,\beta} = \Delta_{\mathrm{t}}$) there are no thermal duplicates (grey area).

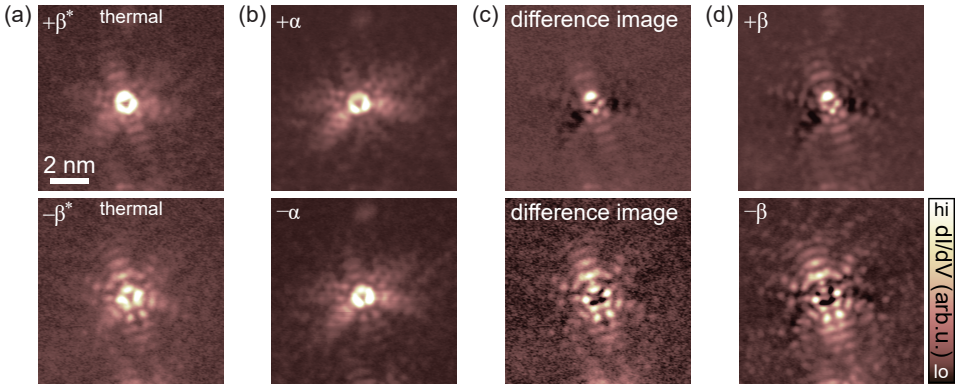

Fig. A.5.: Constant-contour $\mathrm{d}I/\mathrm{d}V$ maps of (a) $+\beta^\star$ (top) and $-\beta^\star$ (bottom) of atom II, and (b) $+\alpha$ (top) and $-\alpha$ (bottom) of atom II. (c) Difference images: $+\alpha$ ($-\alpha$) map subtracted with a factor of 0.7 (1.0) from the map $+\beta^\star$ ($-\beta^\star$). (d) $\mathrm{d}I/\mathrm{d}V$ map of the $+\beta$ (top) and $-\beta$ (bottom) resonance. Panels (c) and (d) exhibit very similar patterns. Data in (a) is reproduced from Fig. A.4. Data in (b,d) is reproduced from Fig. A.3.

A.3.2 Possible alignments between the atomic lattice and the incommensurate CDW

As seen in Fig. A.6 and Fig. 4.9 in section 4.4, some regions along the CDW cannot be probed by Fe adatoms (gray areas). To understand the absence of data in these regions, we illustrate the phase change of the CDW (black rhombi with gray and black dots representing CDW maxima and minima, respectively) with respect to the atomic lattice (gray lattice) along one main symmetry axis in detail in Fig. A.6. One HC adsorption site of an Fe atom is marked by a colored triangle in the atomic lattice. The green triangles indicate observed lattice sites, whereas the red triangles indicate that we did not find these adsorption sites relative to the CDW. The latter cases correspond to configurations, where the maximum of the CDW is located on top of a MC site. As discussed in section 3.2.1, this CDW structure, where the CDW maxima coincide with the Nb atoms (*i.e.* MC sites) are energetically unfavored as shown by DFT calculations and hence, are not observed across the surface [GOY19; Zhe+18; Gus+19; LSD18; Cos+18]. Therefore, the corresponding positions of HC sites relative to the CDW cannot be found either. This explains the absence of data points in the gray areas with only one exception as indicated by the red box in Fig. A.6b. Here, the atomic HC adsorption site would exactly coincide with the local minimum of the CDW corresponding to the third high symmetry position. As already discussed in section 4.4, Fe atoms on such a site were not found in experiment. We attribute this to the delicate interplay between the CDW and the Fe atoms. It seems that the energy landscape of the CDW and hence, its configuration across the surface is affected by the Fe adatoms for this specific adsorption site.

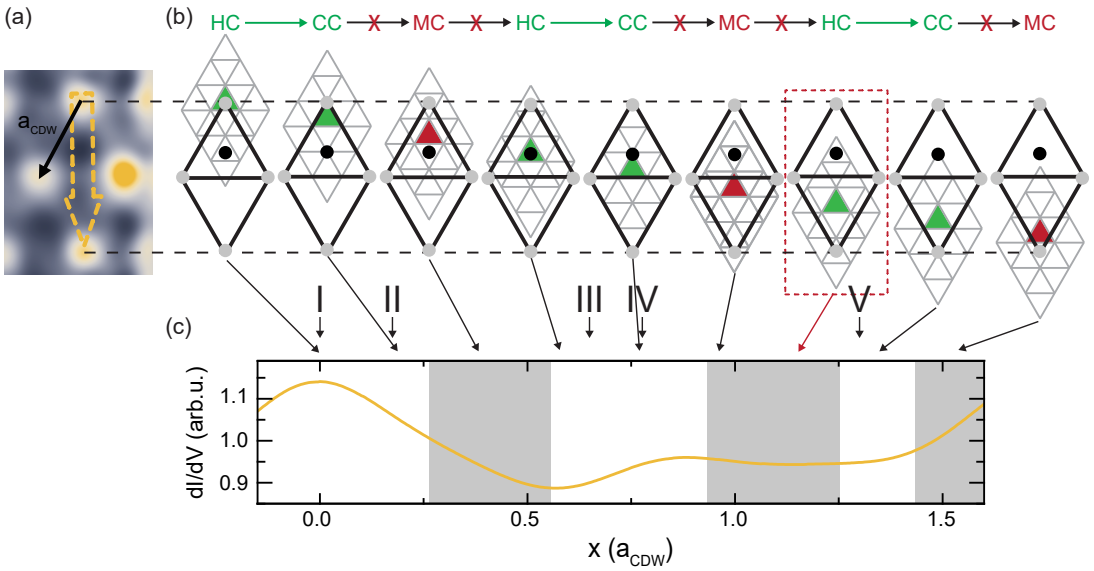

Fig. A.6.: (a) FFT-filtered topography already presented in Fig. 4.9a in section 4.4. (b) Illustration of the alignemt between CDW and atomic lattice following a symmetry axis of the CDW. The CDW is depicted by the black grid, where gray (black) dots indicate CDW maxima (minima). The Se grid is overlaid in gray (Se atoms located at vertices of the triangles). The HC (MC) adsorption sites correspond to triangles pointing up (down). One HC site is marked in color. Green/red indicates if the relative orientation of both lattices relative to each other can be found in experiment. (c) Connection to the linecut along the symmetry axis of the CDW (reproduced from Fig. 4.9e).

A.4 Additional data and discussion to section 4.6

Figure A.7a,b provides large topographies of both MC atoms of type (i) and (ii), respectively, overlaid with CDW grid as in Fig. 4.8 for HC atoms. Atom (i) is located near a CDW maximum and atom (ii) near a CDW minimum. In (c), their adsoprtion sites are marked with the thick triangles in corresponding color. Note that in Fig. A.7a the CDW is distorted in the left of the atom due to the defect visible in the edge of the topography.

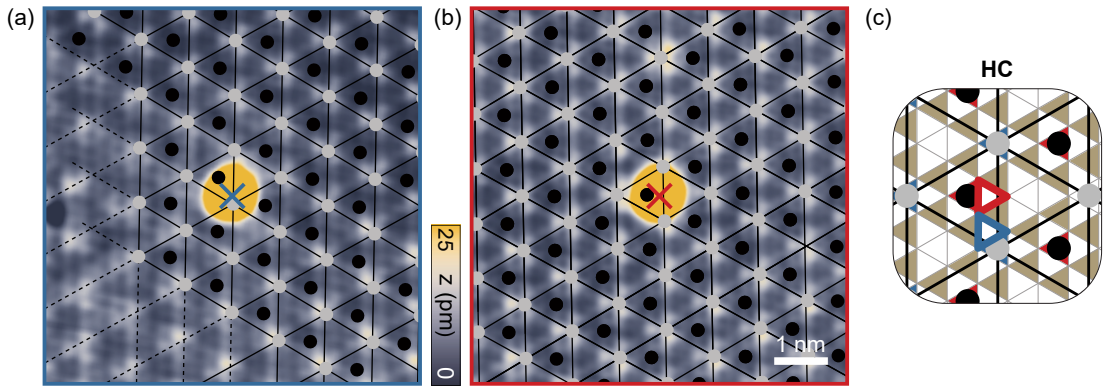

Fig. A.7.: (a,b) Constant-current topographies (set point $100\,\mathrm{pA}, 10\,\mathrm{mV}$) of both atoms from Fig. 4.13. Atom (i) in (a), atom (ii) in (b). Analogue to Fig. 4.8, the CDW is depicted by the black grid, where gray (black) dots indicate CDW maxima (minima). The center of each atom is marked by the blue (red) cross. Atom (i) is located near a CDW maximum, atom (ii) near a CDW minimum. (c) Adsorption positions (MC sites) relative to the CDW of both atoms in the scheme of Fig. 4.8b indicated by the thick triangles in blue and red for atom (i) and (ii), respectively.

Fig. A.8a,b shows data of atoms located in similar positions close to the CDW maximum and minimum as presented in section 4.6, Fig. 4.13c,d acquired using Pb tips. The data shows that also Pb tips induce spatial variations of the YSR excitations comparable to the Nb tips. As discussed in the main text, the magnitude of the observed shifts depends rather on the shape of the tip apex than on the tip material.

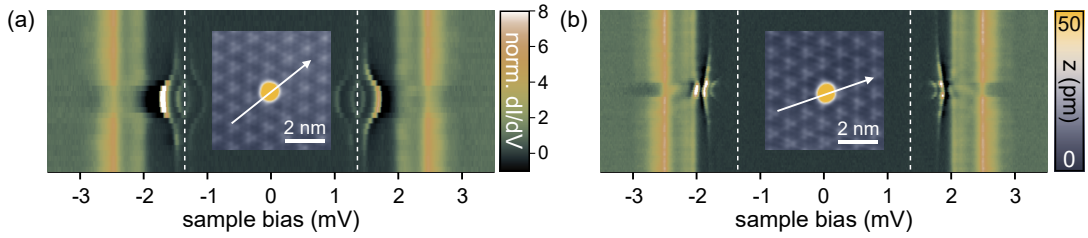

Fig. A.8.: (a,b) Stacked $\mathrm{d}I/\mathrm{d}V$ spectra recorded across MC atoms on similar CDW positions as in Fig. 4.13c,d as illustrated in the inset topographies (constant-current mode with set point $200\,\mathrm{pA}, 4\,\mathrm{mV}$) using a Pb tip. Feedback was opened at $200\,\mathrm{pA}, 4\,\mathrm{mV}$ and a modulation of $15\,\mu\mathrm{V}$ was used. The Pb tip gap of $\Delta_\mathrm{t} \approx 1.35\,\mathrm{meV}$ is indicated by the vertical dashed lines.

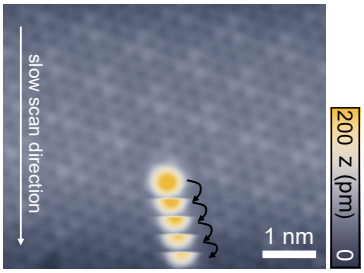

Fig. A.9.: z-channel of a constant-contour $\mathrm{d}I/\mathrm{d}V$ map recorded over an MC atom. Feedback parameters of $250\,\mathrm{pA}, 5\,\mathrm{mV}$ are used. The atom is dragged by the tip during data acquisition.

As discussed in section 4.6 MC atoms are less stable than HC atoms. With some (Nb) tips the MC atoms had to be measured with reduced set point ($100\,\mathrm{pA}, 10\,\mathrm{mV}$ instead of $250\,\mathrm{pA}, 5\,\mathrm{mV}$) as they tend to follow the tip otherwise. An example is shown in Fig. A.9 which shows the z-channel of a constant-contour $\mathrm{d}I/\mathrm{d}V$ map. During this long-term measurement (several hours) the atom followed the tip continuously. Importantly, such occasional manipulations do not happen for HC atoms. This illustrates that the usual set point parameters correspond to a regime with strong enough vdW forces close to the manipulation regime of MC atoms while the HC atoms are more stable.

Figures A.10 and A.11 complement Fig. 4.15 and compile $\mathrm{d}I/\mathrm{d}V$ maps at various voltages of the type (i) and type (ii) atom. The dispersing YSR excitations manifest as ring-shaped features as discussed in the main text. When the YSR resonances saturate in energy the rings continuously transform into typical oscillating YSR wave functions. As discussed in the main text there is not only one intense in-gap resonance per atom. On atom (i) the intense one is saturating to $\approx 1.5\,\mathrm{mV}$ while the second less intense resonance saturates to $\lesssim 1.4\,\mathrm{mV}$. Interestingly, the maps reveal very similar wave functions at these energies differing only in the intensity. This suggests that these excitations correspond to a magnetic anisotropy split doublet. We find a similar doublet, although the second resonance being very unintense (not discernable in the line spectra of Fig. 4.13d) also for the atom (ii), where both excitations saturate to $\approx 1.7\,\mathrm{mV}$ and $\approx 1.4\,\mathrm{mV}$ as can be seen in the corresponding $\mathrm{d}I/\mathrm{d}V$ channels.

We further note that the maps recorded on both atoms reveal similar wave functions appearing at different energies as for the HC atoms. We also note the presence of one mirror symmetry axis in each map as expected for MC sites. The axis is indicated in the topography in the top left panel in each figure.

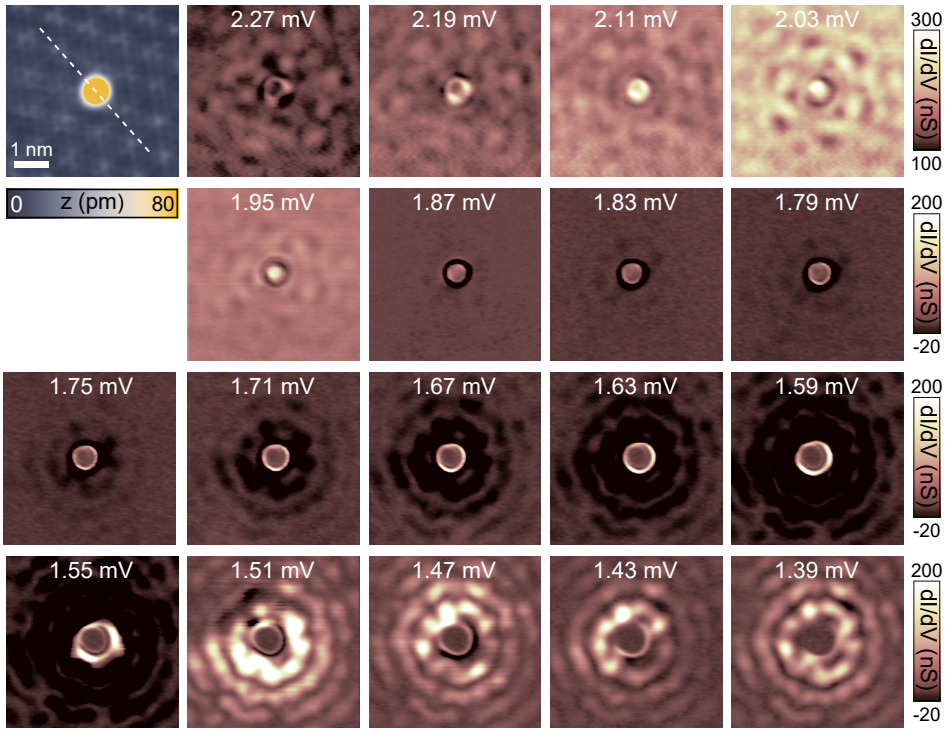

Fig. A.10.: Complementary data to Fig. 4.15a, *i.e.* atom (i) which is close to the maximum of the CDW. Same parameters as in Fig. 4.15.

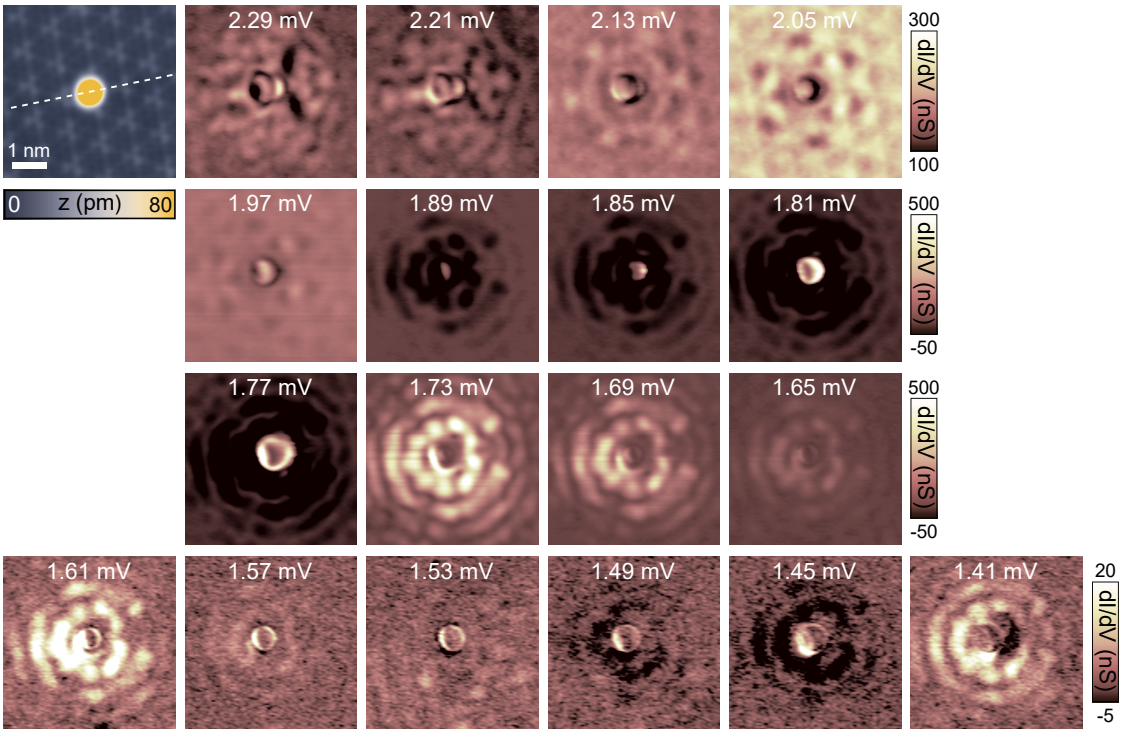

Fig. A.11.: Complementary data to Fig. 4.15b, *i.e.* atom (ii) which is close to the minimum of the CDW. Same parameters as in Fig. 4.15.

A.5 Additional data and discussion to sections 5.2.1 and 6.2.1

Figure A.12a-c accommodates the $\mathrm{d}I/\mathrm{d}V$ maps of the (hybrid) α- and β-resonances recorded at the opposite bias polarity than in Figs. 5.3a,b (monomer, dimer) and 6.4d (trimer). In Fig. A.12a we identify the familiar patterns of the α- and β-states at negative bias voltages (*c.f.* Figs. 4.11b and A.3, atom I). In the following we address features of the data supporting the assignment of α- and β-like states of sections 5.2.1 and 6.2.1.

In Fig. A.12d,e we plot the thermally activated duplicates of the α-states of dimer and trimer. The panels are arranged in a manner that the thermally excited states appear in the same order than the original wave functions. Generally, the thermal maps show the same patterns as the original states, however, since they are less intense they are less/not affected by NDC effects. For example, while being strongly obscured by the NDC of α^{d1} in the original maps (Fig. 5.3b), we can identify the symmetric α-like linear combination in the corresponding thermal map $\alpha^{\mathrm{d0}*}$ at $1.39\,\mathrm{mV}$. Moreover, both original α-resonances found at negative bias, $-\alpha^{\mathrm{d0}}$ and $-\alpha^{\mathrm{d1}}$ (Fig. A.12b) do not inherit the characteristic near-field shape of the $+\alpha$-resonance found at positive bias on the monomer (*c.f.* Fig. 5.3a) underpinning the QPT of both α-states in the dimer.

Turning towards the β-resonances, both β-dimer states show a simililar long-range oscillatory decay as the monomer wave function as exemplary indicated in Fig. A.12a,b by the white arrows. Similar features between dimer and trimer states (in particular β^{t2} and β^{t0}) are highlighted by circles. Note that as β^{t0} already overlaps with the coherence peaks the features are very faint. Moreover, data recorded on a different linear trimer, also with spacing of $3a$ and with all atoms on the CDW maximum, using a different Nb tip is shown in Fig. A.13. This tip exhibits different NDC signatures. Note that considering the slightly smaller tip energy gap and the natural variations of YSR energies (*c.f.* Fig. 4.9c) we find the trimer states at nearly the same energies than on the trimer presented above. Also the spatial resolution is slightly different between both tips, but the overall wave function patterns nicely agree. The data with the different tip unambiguously underpins the correct assigment of the β^{t0} state of the main text. We clearly discern the typical β-like near-field patterns with intensity at vertices and sides (*c.f.* Fig. 5.3c) on all three trimer atoms without any nodal plane revealing this state as trimer version of the totally symmetric linear combination of the monomer β-state.

The two nodal planes of α^{t2} which are partially obscured by the nearby β^{t1}-resonance at positive bias are nicely discernable at negative bias. As discussed in the main text, the assignment of β^{t1} and all α-trimer states remains tentative.

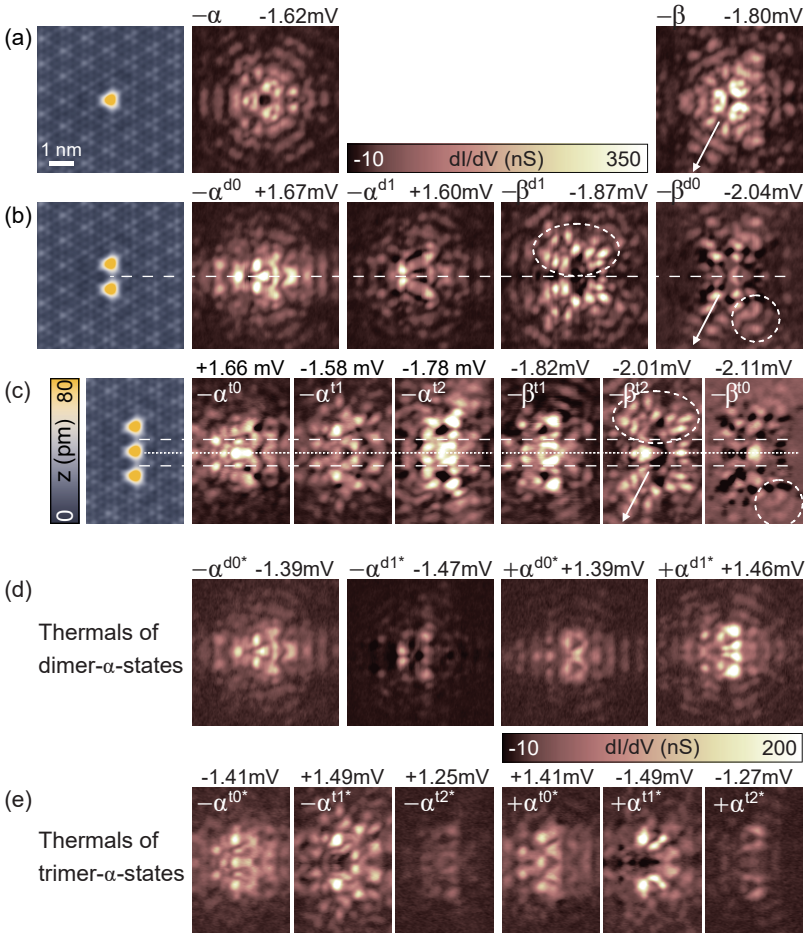

Fig. A.12.: Complementary data of Figs. 5.3 and 6.4. (a-c) STM topographies (constant-current mode with set point $100\,\mathrm{pA}, 10\,\mathrm{mV}$) of one to three Fe atoms with spacing of $3a$ in the left. Corresponding constant-contour $\mathrm{d}I/\mathrm{d}V$ maps of the (hybridized) YSR states in the monomer (a), dimer (b) and trimer (c). Bias voltages are given above each panel ($\Delta_\mathrm{t} \approx 1.55\,\mathrm{meV}$). Constant-contour set point is $250\,\mathrm{pA}, 5\,\mathrm{mV}$ and the modulation is $15\,\mu\mathrm{V}$. White lines serve as guides to the eye. (d,e) Constant-contour maps (same parameters as in a-c) of the thermally activated α-states of the dimer (d) and the trimer (e) at $V_\mathrm{bias} = \mp|\Delta_\mathrm{t} - E_\mathrm{YSR}|/e$. White arrows and circles indicate similarities in the data as discussed in the text.

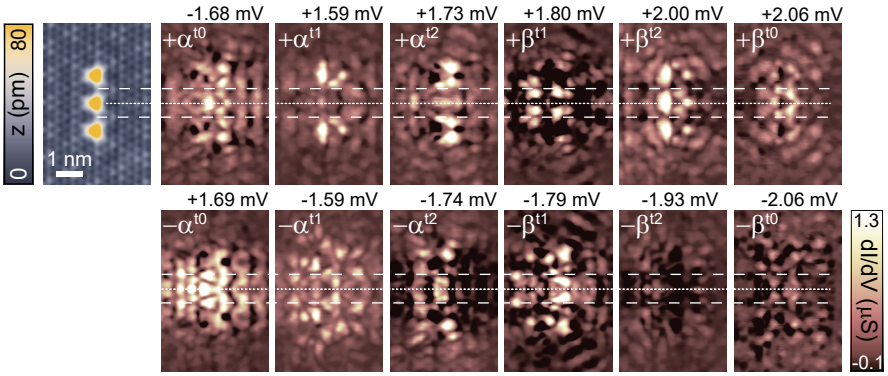

Fig. A.13.: Constant-contour $\mathrm{d}I/\mathrm{d}V$ maps of a linear trimer with interatomic spacing of $3a$ recorded with a different Nb tip (all atoms on CDW maxima). Topography (constant-current mode with set point $100\,\mathrm{pA}, 10\,\mathrm{mV}$) in the left. Bias voltages are given above each panel ($\Delta_\mathrm{t} \approx 1.52\,\mathrm{meV}$). Constant-contour set point is $700\,\mathrm{pA}, 5\,\mathrm{mV}$ and the modulation is $15\,\mu\mathrm{V}$. White lines serve as guide to the eye.

A.6 Additional data and discussion to section 6.2.2

Figures A.14 and A.15 show complementary data to Fig. 6.7 of the linear $3a$-chain at different lengths. The maps capture the diversity of hybrid wave functions with different intensity distributions along the chain. Note that the set of $\mathrm{d}I/\mathrm{d}V$ maps is not complete and is rather a selection in order to get some insight into similarities and differences between hybrid states between chains with different lenghts. A complete set of $\mathrm{d}I/\mathrm{d}V$ maps recorded at various equidistant energies is presented below for the 27-atom chain (Figs. A.17 and A.18).

As mentioned in the main text there is a zero-energy end state ($\Delta_\mathrm{t} \approx 1.55\,\mathrm{mV}$) at the 10-atom chain. However, as can also be nicely discerned in the line spectra (*c.f.* Fig. 6.6j,k), this state is shifted to slightly higher energies at the 11-atom chain ($1.58\,\mathrm{meV}$) similarily to states appearing at the Fermi level for shorter lengths.

Figure A.16 presents topographies of the build-up sequence of the $3a$-chain up to $N = 11$. The red lines mark the atoms' center. Close inspection reveals that all atoms sit on CDW maxima within our resolution. Thus, as discussed in the main text, the CDW adopts the periodicity of the chain up to a certain chain length. Beyond, the CDW does not maintain the periodicity of the chain as it conflicts with the natural CDW periodicity ($\gtrsim 3a$) which induces the smooth variation between HC and CC phases. Although not discernable in the topographies, slight distrotions of the CDW manifest in the loss of perfect mirror symmetric hybrid wave functions observable from chain lengths of $\gtrsim 10\,\mathrm{nm}$ (*c.f.* Fig. A.15 and Fig. 6.7).

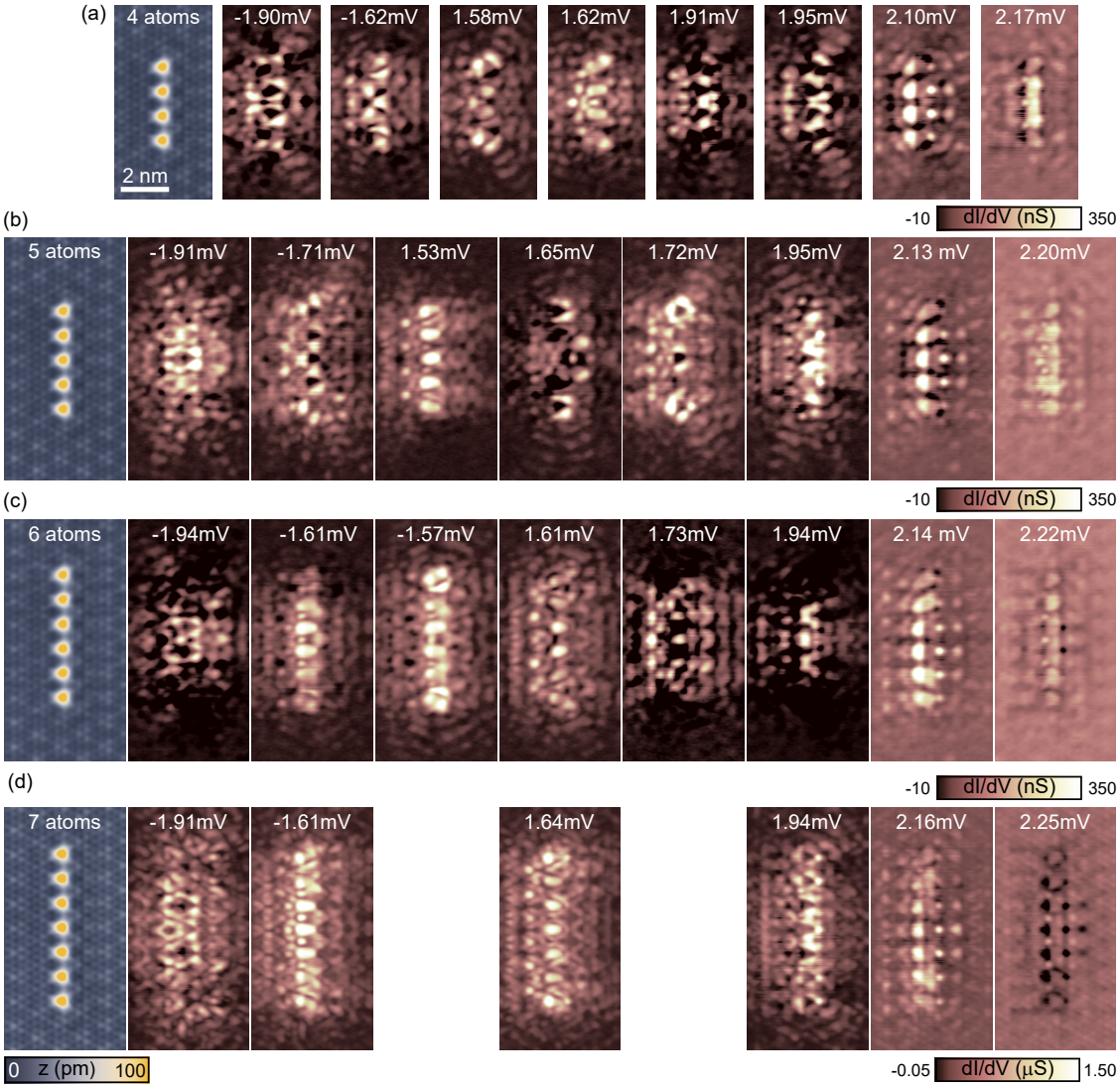

Fig. A.14.: (a-d) Complementary data of Figs. 6.7a-d. STM topographies (constant-current mode with set point $100\,\mathrm{pA}, 10\,\mathrm{mV}$) of 4- to 7-atom chain with spacing of $3a$ in the left. Corresponding constant-contour $\mathrm{d}I/\mathrm{d}V$ maps in the right. Bias voltages are given in each panel ($\Delta_t \approx 1.55\,\mathrm{meV}$). Constant-contour feedback set point is $250\,\mathrm{pA}, 5\,\mathrm{mV}$ (a-c) $700\,\mathrm{pA}, 5\,\mathrm{mV}$ (d) and the modulation is $15\,\mu\mathrm{V}$.

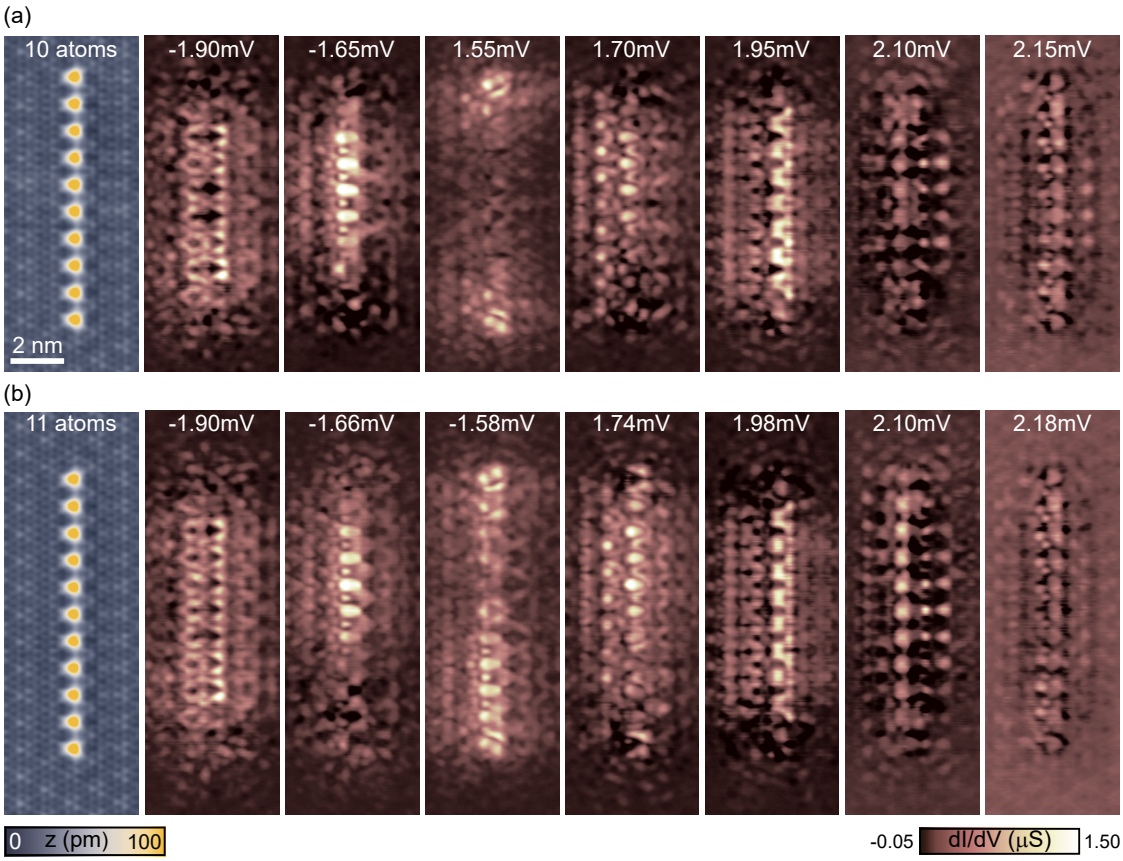

Fig. A.15.: (a,b) Complementary data of Fig. 6.7e,f. STM topographies (constant-current mode with set point $100\,\mathrm{pA}, 10\,\mathrm{mV}$) of the 10- and 11-atom chain with spacing of $3a$ in the left. Corresponding constant-contour $\mathrm{d}I/\mathrm{d}V$ maps in the right. Bias voltages are given in each panel ($\Delta_\mathrm{t} \approx 1.55\,\mathrm{meV}$). Constant-contour feedback set point is $700\,\mathrm{pA}, 5\,\mathrm{mV}$ and the modulation is $15\,\mu\mathrm{V}$.

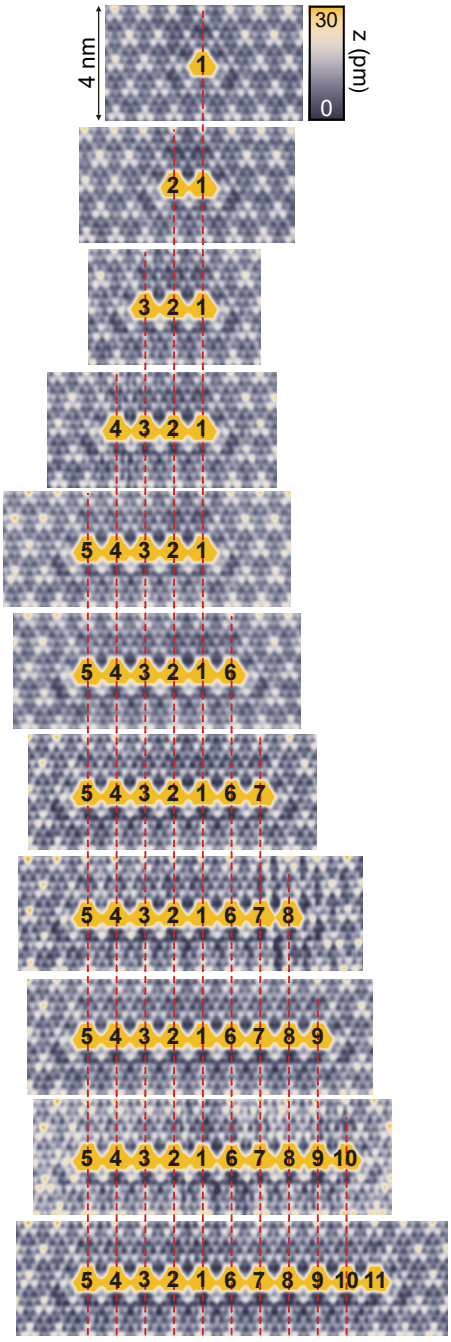

Fig. A.16.: Constant-current topographies (set point $100\,\mathrm{pA}, 10\,\mathrm{mV}$). Red lines serve as guide to the eye. The CDW in the background is „in phase“ with the atoms elongation of the chain, such that all atoms sit on a CDW maximum. Atoms are labeled according to the build-up sequence.

A.7 Additional data and discussion to section 6.2.3

Figures A.17 and A.18 complement the data of the $\mathrm{d}I/\mathrm{d}V$ maps of the 27-atom chain (Fig. 6.9d of the main text) showing in detail the energetic and spatial evolution of the YSR bands as discussed in the main text.

As outlined in the main text, we observe manipulation-induced instabilities of the CDW. Importantly, during the manipulation and extension of the chain up to a chain length of $N = 30$ atoms, the CDW did not change abruptly. In contrast, upon attachment of the 31^{st} atom, an abrupt change occurred in the CDW as visible comparing Figs. A.19a,b. The sections (1-3) are indicated as well as the former 27(11)-atom chains in red (blue). By close inspection we note that in the former region 3 of the 27-atom chain the atoms now sit on CDW minima (white arrow). This change becomes very clear in the corresponding $\mathrm{d}I/\mathrm{d}V$ spectra recorded along the 30- and 31-atom chains (Fig. A.19c,d). While the 30-atom chain exhibits the smooth variations of van Hove singularities toward the chain's terminations, the 31-atom chain shows two distinct areas of YSR bands. These observations suggest that the Fe atoms favor adsorption sites on the maxima or minima of the CDW and thus push the CDW into the respective phase. However, when too much energy is stored in the locked CDW, stress is released by an abrupt switch of the CDW. All atoms attached to the 31-atom chain are located on/close to CDW minima up the chain length of 51 atoms (*c.f.* Fig. 6.10). For this extended chain we note that the CDW starts to distort at the left termination of the chain probably being close to the occurence of another abrupt switch upon further chain elongation leading to three subchains (atoms again on CDW maxima in the third subchain).

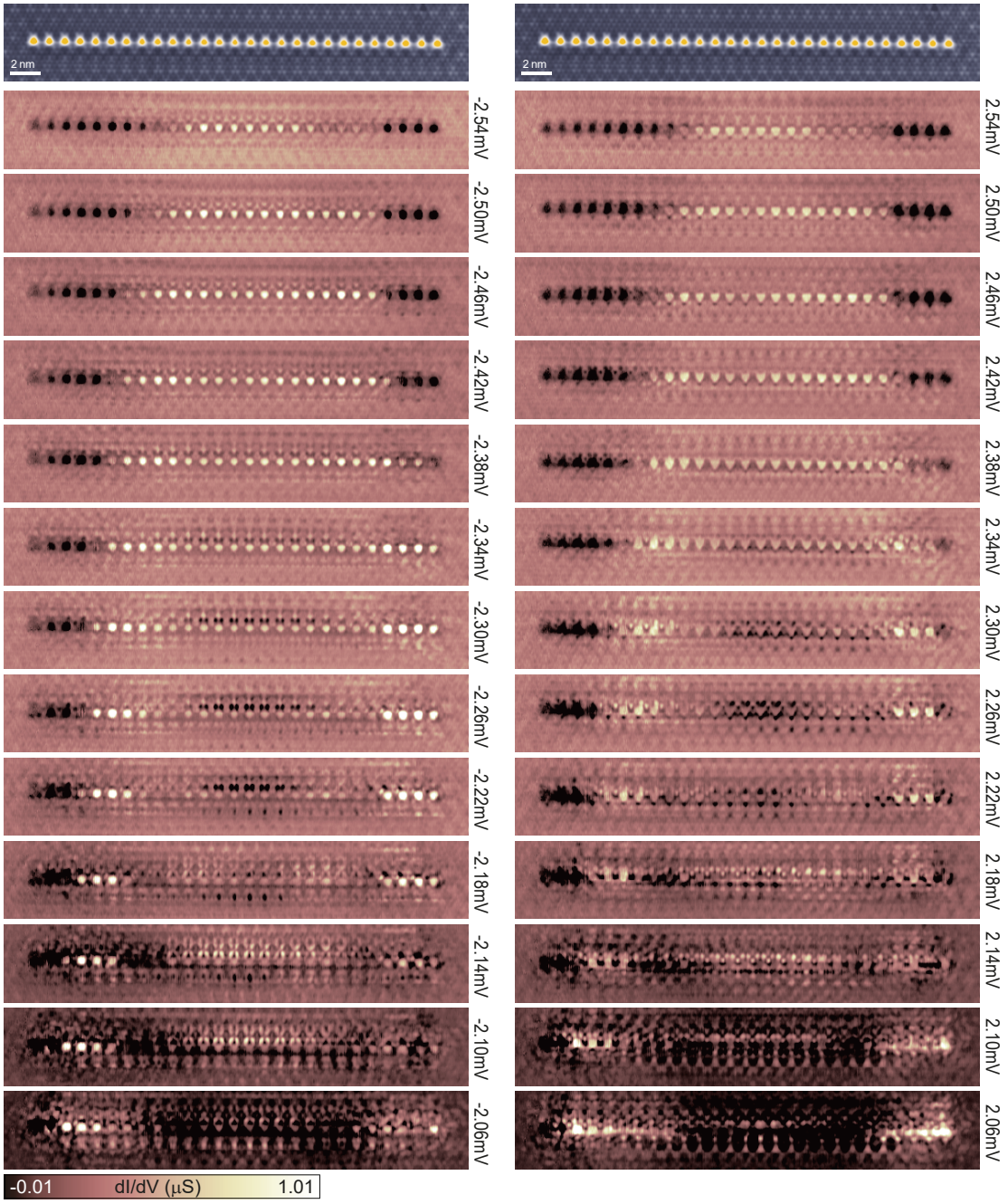

Fig. A.17.: Additional $\mathrm{d}I/\mathrm{d}V$ maps of the 27-atom chain (Fig. 6.9) at various energies. Constant-contour feedback was opened at $700\,\mathrm{pA}, 5\,\mathrm{mV}$ and a modulation of $15\,\mu\mathrm{V}$ was used. The energies are given beside each panel. STM topography in the top (constant-current set point $100\,\mathrm{pA}, 10\,\mathrm{mV}$).

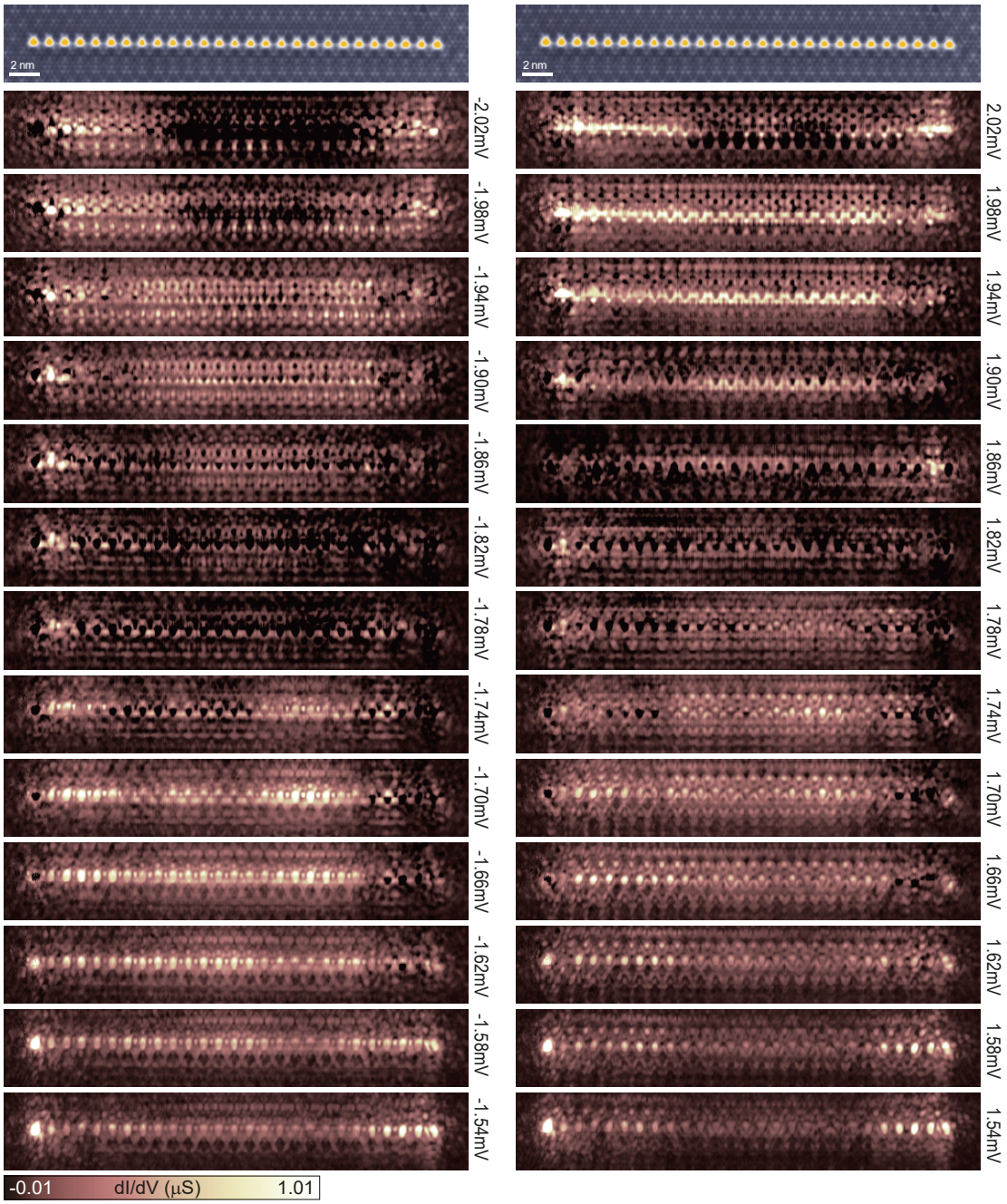

Fig. A.18.: Additional $\mathrm{d}I/\mathrm{d}V$ maps of the 27-atom chain (Fig. 6.9) at various energies. Constant-contour feedback was opened at $700\,\mathrm{pA}, 5\,\mathrm{mV}$ and a modulation of $15\,\mu\mathrm{V}$ was used. The energies are given beside each panel. STM topography in the top (constant-current set point $100\,\mathrm{pA}, 10\,\mathrm{mV}$).

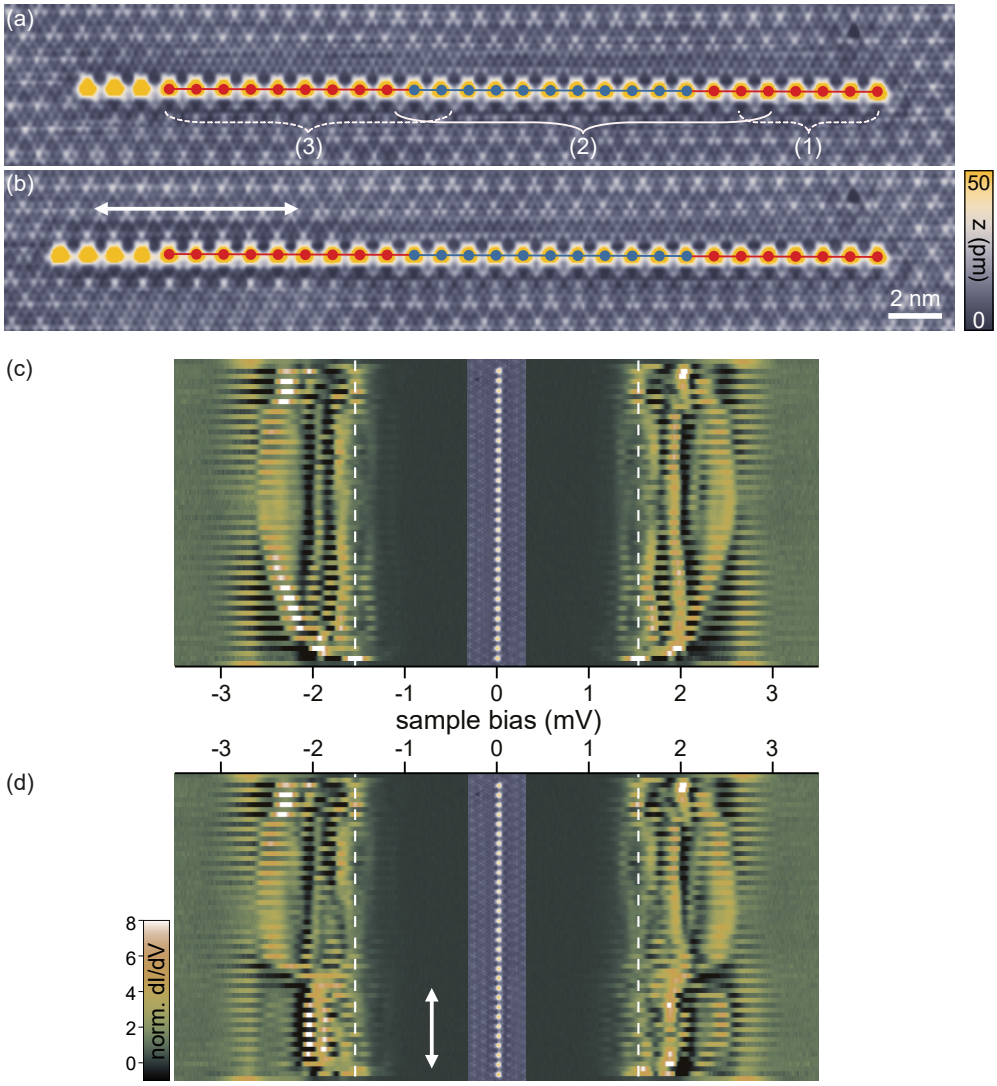

Fig. A.19.: (a,b) STM topographies (constant-current set point is $100\,\mathrm{pA}, 10\,\mathrm{mV}$) of the 30- and 31-atom chains. The position of the former 11(27)-atom chain is indicated in blue (red). (c,d) Stacked constant-height $\mathrm{d}I/\mathrm{d}V$ spectra (normalized) recorded along a line across the 30- and 31-atoms chain as illustrated in the inset topography. Set point for the spectra is $700\,\mathrm{pA}, 5\,\mathrm{mV}$ with a modulation of $15\,\mu\mathrm{V}$. The (Nb) tip gap $\Delta_\mathrm{t} \approx 1.55\,\mathrm{meV}$ is indicated by dashed lines. Furthermore the different sections (*c.f.* Fig. 6.9) are indicated. The arrow indicates the region of the CDW slip in the background (atoms on CDW minima).

A.8 Additional data and discussion to section 6.3

Figure A.20 shows an enlarged STM topography of the 1a-dimer discussed in the section 6.3 (Fig. 6.13). The black grids denote the Se grid with triangles pointing to the left indicating HC adsorption sites. The neighboring HC sites corresponding to the adsorption sites of both Fe atoms within the dimer are marked in gray. As discussed in the main text (*c.f.* Fig. 6.13a,b) the $1a$-dimer appears as one oval elevation, hence we do not resolve the individual Fe atom within the dimer. The red cross marks the center of the $1a$-dimer. Within our resolution we conclude that the dimer is centered exactly in between the two HC sites marked in gray and furthermore located in the correct atomic row. We checked various $1a$-dimers yielding equal results. Thus, the assembly of $1a$-dimers with Nb tips is reliably and reproducible.

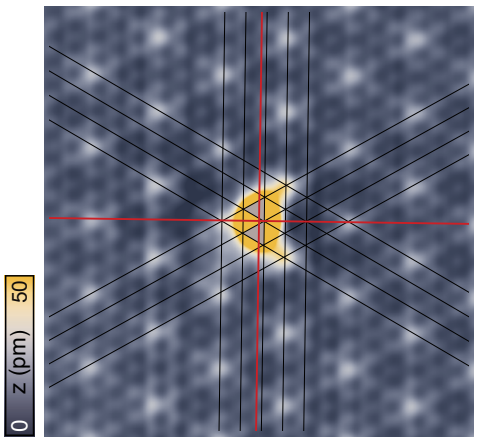

Fig. A.20.: Enlarged topography (constant-current set point is $100\,\mathrm{pA}, 10\,\mathrm{mV}$) of the $1a$-dimer of Fig. 6.13a. The atomic grid is overlaid in black and both dimer axes in red. The semi-major axis (vertical red line) is parallel to the atomic rows. The semi-minor axis (horizontal red line) is exactly in between two adjacent HC sites (gray triangles).

Figure A.21 shows constant-current data of other voltage ranges complementary to Fig. 6.16b,c in panels (a,b,e,f) and to Fig. 6.17b in panels (c,d,g,h). There are differences between the $1a$-dimer and dimers with spacings of $\geq 2a$ discernable and also between the single end of the 7-atom chain and the dimerized part of the chain. However, as the resonances are broad these changes are more subtile than for the bias range addressed in the main text.

In Fig. A.22 the data of the dimer and the 6-atom chain is arranged in a manner that one can compare the similarity between the spectra recorded on a lonestanding $1a$-dimer and the three dimers within the 6-atom chain. This was already discussed by comparing the constant-$\mathrm{d}I/\mathrm{d}V$ maps in the main text (Figs. 6.16d and Fig. 6.18a). White lines are all parallel and indicate the energy shift of the levels. Red and yellow lines serve as guide to the eye.

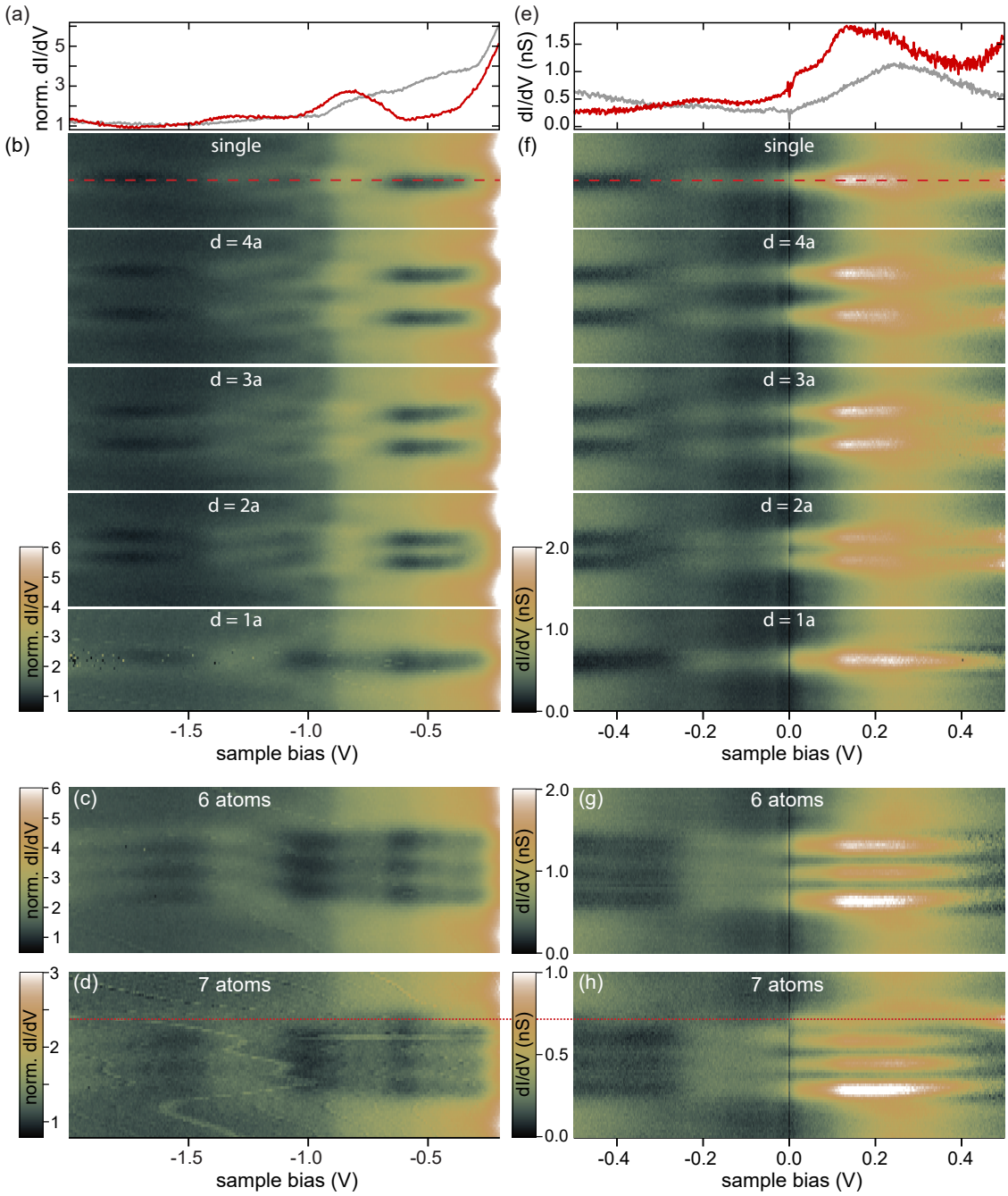

Fig. A.21.: Complemented data to Fig. 6.16b,c and Fig. 6.17b covering different voltage ranges. (a) Constant-current $\mathrm{d}I/\mathrm{d}V$ spectrum at the single Fe atom (red) and substrate (gray). (b,c,d) Spectra measured across the single atom and the dimers with different separations (b), the 6-atom chain (c) and the 7-atom chain (d). Constant-current set point of $1\,\mathrm{nA}$ (a,b) and $200\,\mathrm{pA}$ (c) and $70\,\mathrm{pA}$ (d) with a modulation of $5\,\mathrm{mV}$. (e) Constant-height spectrum at the single Fe atom (red) and substrate (gray). (f,g,h) Spectra measured across the single atom and the dimers with different separations (f), the 6-atom chain (g) and the 7-atom chain (h). Constant-height set point $200\,\mathrm{pA}$, $-0.5\,\mathrm{V}$ (e,f,g) and $100\,\mathrm{pA}$, $-0.5\,\mathrm{V}$ (h) with a modulation of $2\,\mathrm{mV}$. The red dashed lines mark the position of the traces in (a,e) within the line spectra (b,f). The single end of the 7-atom chain is marked by the red dotted line in (d,h).

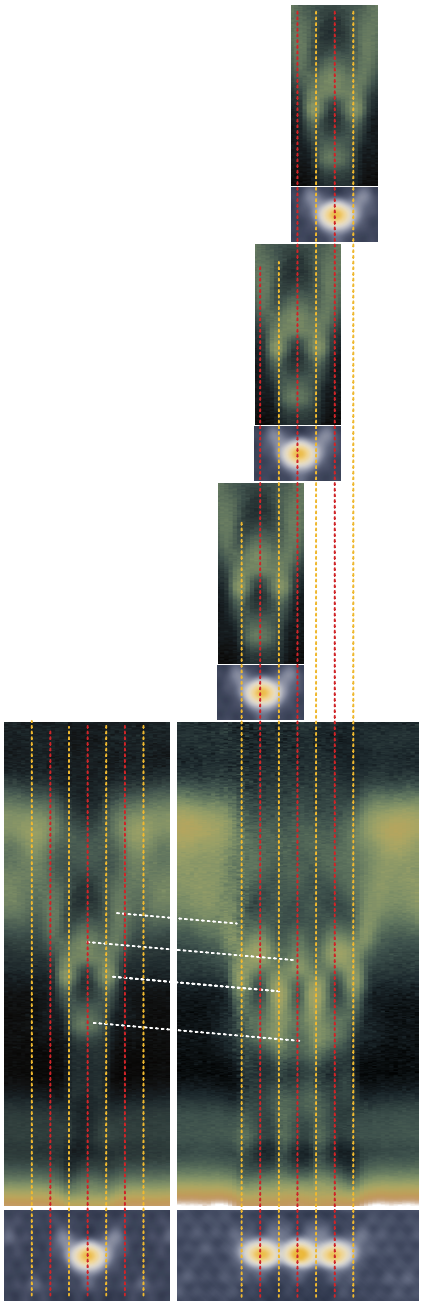

Fig. A.22.: Same data than in Fig. 6.16c (bottom panel) of the isolated $1a$-dimer and Fig. 6.17b (top panel) of the three dimer within the 6-atom chain arranged such that one can compare the dimer and the chain. Dashed lines serve as guide to the eye.

Bibliography

[Abr57] A. A. Abrikosov. "The magnetic properties of superconducting alloys". *J. Phys. Chem. Solids* 2 (1957), pp. 199–208. DOI: 10.1016/0022-3697(57)90083-5 (cited on page 24).

[Ace20] S. Acero González. "Topological State Engineering". PhD thesis. Freie Universität Berlin, 2020 (cited on pages 49, 54, 55, 60, 137).

[Ali12] J. Alicea. "New directions in the pursuit of Majorana fermions in solid state systems". *Rep. Prog. Phys.* 75 (2012), p. 076501. DOI: 10.1088/0034-4885/75/7/076501 (cited on page 4).

[AM07] N. W. Ashcroft and N. D. Mermin. *Festkörperphysik*. Vol. 3. Oldenbourg Wissenschaftsverlag GmbH, 2007 (cited on page 75).

[AMY97] D. Aristov, S. Maleyev, and A. Yashenkin. "RKKY interaction in layered superconductors with anisotropic pairing". *Z. Phys. B* 102 (1997), pp. 467–471 (cited on page 76).

[And61] P. W. Anderson. "Localized Magnetic States in Metals". *Phys. Rev.* 124 (1961), pp. 41–53. DOI: 10.1103/PhysRev.124.41 (cited on page 40).

[Arg+14] C. J. Arguello, S. P. Chockalingam, E. P. Rosenthal, L. Zhao, C. Gutiérrez, J. H. Kang, W. C. Chung, R. M. Fernandes, S. Jia, A. J. Millis, R. J. Cava, and A. N. Pasupathy. "Visualizing the charge density wave transition in $2H$-$NbSe_2$ in real space". *Phys. Rev. B* 89 (2014), p. 235115. DOI: 10.1103/PhysRevB.89.235115 (cited on pages 29, 30, 53, 114).

[Arn98] R. G. Arns. "The other transistor: early history of the metal-oxide semiconductor field-effect transistor". *Eng. Sci. Educ. J.* 7 (1998), pp. 233–240. DOI: 10.1049/esej:19980509 (cited on page 3).

[AS17] G. M. Andolina and P. Simon. "Topological properties of chains of magnetic impurities on a superconducting substrate: Interplay between the Shiba band and ferromagnetic wire limits". *Phys. Rev. B* 96 (2017), p. 235411. DOI: 10.1103/PhysRevB.96.235411 (cited on pages 6, 99).

[Bar61] J. Bardeen. "Tunnelling from a Many-Particle Point of View". *Phys. Rev. Lett.* 6 (1961), pp. 57–59. DOI: 10.1103/PhysRevLett.6.57 (cited on pages 9, 10).

[BCS57a] J. Bardeen, L. N. Cooper, and J. R. Schrieffer. "Microscopic Theory of Superconductivity". *Phys. Rev.* 106 (1957), pp. 162–164. DOI: 10.1103/PhysRev.106.162 (cited on page 23).

[BCS57b] J. Bardeen, L. N. Cooper, and J. R. Schrieffer. "Theory of Superconductivity". *Phys. Rev.* 108 (1957), pp. 1175–1204. DOI: 10.1103/PhysRev.108.1175 (cited on page 23).

[Bec+21] P. Beck, L. Schneider, L. Rózsa, K. Palotás, A. Lászlóffy, L. Szunyogh, J. Wiebe, and R. Wiesendanger. “Spin-orbit coupling induced splitting of Yu-Shiba-Rusinov states in antiferromagnetic dimers”. *Nat. Commun.* 12 (2021), p. 2040. DOI: 10.1038/s41467-021-22261-6 (cited on pages 5, 76, 78).

[BH13] B. A. Bernevig and T. L. Hughes. *Topological insulators and topological superconductors*. Princeton University Press, 2013 (cited on page 28).

[Bin+82a] G. Binnig, H. Rohrer, C. Gerber, and E. Weibel. “Tunneling through a controllable vacuum gap”. *Appl. Phys. Lett.* 40 (1982), pp. 178–180. DOI: 10.1063/1.92999 (cited on pages 4, 9).

[Bin+82b] G. Binnig, H. Rohrer, C. Gerber, and E. Weibel. “Surface Studies by Scanning Tunneling Microscopy”. *Phys. Rev. Lett.* 49 (1982), pp. 57–61. DOI: 10.1103/PhysRevLett.49.57 (cited on pages 4, 9).

[BMR97] L. Bartels, G. Meyer, and K.-H. Rieder. “Basic Steps of Lateral Manipulation of Single Atoms and Diatomic Clusters with a Scanning Tunneling Microscope Tip”. *Phys. Rev. Lett.* 79 (1997), pp. 697–700. DOI: 10.1103/PhysRevLett.79.697 (cited on page 12).

[Boa+03] E. Boaknin, M. A. Tanatar, J. Paglione, D. Hawthorn, F. Ronning, R. W. Hill, M. Sutherland, L. Taillefer, J. Sonier, S. M. Hayden, and J. W. Brill. “Heat Conduction in the Vortex State of $NbSe_2$: Evidence for Multiband Superconductivity”. *Phys. Rev. Lett.* 90 (2003), p. 117003. DOI: 10.1103/PhysRevLett.90.117003 (cited on page 31).

[Bog58] N. N. Bogoliubov. “On a New Method in the Theory. of Superconductivity”. *Nuovo Cimento* 7 (1958), pp. 794–805 (cited on pages 26, 27).

[BS13] B. Braunecker and P. Simon. “Interplay between Classical Magnetic Moments and Superconductivity in Quantum One-Dimensional Conductors: Toward a Self-Sustained Topological Majorana Phase”. *Phys. Rev. Lett.* 111 (2013), p. 147202. DOI: 10.1103/PhysRevLett.111.147202 (cited on pages 4, 99).

[BY01] C. Buzea and T. Yamashita. “Review of the superconducting properties of MgB_2”. *Supercond. Sci. Technol.* 14 (2001), pp. R115–R146. DOI: 10.1088/0953-2048/14/11/201 (cited on page 32).

[Cao+18] Y. Cao, V. Fatemi, S. Fang, K. Watanabe, T. Taniguchi, E. Kaxiras, and P. Jarillo-Herrero. “Unconventional superconductivity in magic-angle graphene superlattices”. *Nature* 556 (2018), pp. 43–50. DOI: 10.1038/nature26160 (cited on page 60).

[Cha+15] U. Chatterjee, J. Zhao, M. Iavarone, R. Di Capua, J. P. Castellan, G. Karapetrov, C. D. Malliakas, M. G. Kanatzidis, H. Claus, J. P. C. Ruff, F. Weber, J. van Wezel, J. C. Campuzano, R. Osborn, M. Randeria, N. Trivedi, M. R. Norman, and S. Rosenkranz. “Emergence of coherence in the charge-density wave state of $2H$-$NbSe_2$”. *Nat. Commun.* 6 (2015), p. 6313. DOI: 10.1038/ncomms7313 (cited on pages 30, 53, 114).

[Cha+21] D. Chatzopoulos, D. Cho, K. M. Bastiaans, G. O. Steffensen, D. Bouwmeester, A. Akbari, G. Gu, J. Paaske, B. M. Andersen, and M. P. Allan. “Spatially dispersing Yu-Shiba-Rusinov states in the unconventional superconductor $FeTe_{0.55}Se_{0.45}$”. *Nat. Commun.* 12 (2021), p. 298. DOI: 10.1038/s41467-020-20529-x (cited on pages 45, 70).

[Che+99] W. Chen, T. Jamneala, V. Madhavan, and M. F. Crommie. “Disappearance of the Kondo resonance for atomically fabricated cobalt dimers”. *Phys. Rev. B* 60 (1999), pp. R8529–R8532. DOI: 10.1103/PhysRevB.60.R8529 (cited on page 135).

[Che93] C. J. Chen. *Introduction to Scanning Tunneling Microscopy*. Vol. 4. Oxford University Press, 1993 (cited on page 13).

[Cho+17a] D.-J. Choi, C. Rubio-Verdú, J. De Bruijckere, M. M. Ugeda, N. Lorente, and J. I. Pascual. "Mapping the orbital structure of impurity bound states in a superconductor". *Nat. Commun.* 8 (2017), p. 15175. DOI: 10.1038/ncomms15175 (cited on pages 4, 17, 46, 47, 50, 62, 124).

[Cho+17b] T. Choi, W. Paul, S. Rolf-Pissarczyk, A. J. Macdonald, F. D. Natterer, K. Yang, P. Willke, C. P. Lutz, and A. J. Heinrich. "Atomic-scale sensing of the magnetic dipolar field from single atoms". *Nat. Nanotechnol.* 12 (2017), pp. 420–424. DOI: 10.1038/nnano.2017.18 (cited on page 75).

[Cho+18a] K. Cho, M. Kończykowski, S. Teknowijoyo, M. A. Tanatar, J. Guss, P. B. Gartin, J. M. Wilde, A. Kreyssig, R. J. McQueeney, A. I. Goldman, V. Mishra, P. J. Hirschfeld, and R. Prozorov. "Using controlled disorder to probe the interplay between charge order and superconductivity in $NbSe_2$". *Nat. Commun.* 9 (2018), p. 2796. DOI: 10.1038/s41467-018-05153-0 (cited on page 31).

[Cho+18b] D.-J. Choi, C. G. Fernández, E. Herrera, C. Rubio-Verdú, M. M. Ugeda, I. Guillamón, H. Suderow, J. I. Pascual, and N. Lorente. "Influence of Magnetic Ordering between Cr Adatoms on the Yu-Shiba-Rusinov States of the β-Bi_2Pd Superconductor". *Phys. Rev. Lett.* 120 (2018), p. 167001. DOI: 10.1103/PhysRevLett.120.167001 (cited on pages 5, 78).

[Coo56] L. N. Cooper. "Bound Electron Pairs in a Degenerate Fermi Gas". *Phys. Rev.* 104 (1956), pp. 1189–1190. DOI: 10.1103/PhysRev.104.1189 (cited on page 23).

[Cos+18] F. Cossu, A. G. Moghaddam, K. Kim, H. A. Tahini, I. Di Marco, H.-W. Yeom, and A. Akbari. "Unveiling hidden charge density waves in single-layer $NbSe_2$ by impurities". *Phys. Rev. B* 98 (2018), p. 195419. DOI: 10.1103/PhysRevB.98.195419 (cited on pages 30, 32, 38, 53, 114, 146).

[De 99] P.-G. De Gennes. *Superconductivity of Metals and Alloys*. CRC Press, 1999 (cited on page 27).

[Dem16] W. Demtröder. *Experimentalphysik 3: Atome, Moleküle und Festkörper*. Springer-Verlag, 2016 (cited on page 37).

[Din+21] H. Ding, Y. Hu, M. T. Randeria, S. Hoffman, O. Deb, J. Klinovaja, D. Loss, and A. Yazdani. "Tuning interactions between spins in a superconductor". *PNAS* 118 (2021), p. e2024837118. DOI: 10.1073/pnas.2024837118 (cited on pages 5, 76, 78, 82, 83).

[Dvi+18] T. Dvir, M. Aprili, C. H. Quay, and H. Steinberg. "Tunneling into the Vortex State of $NbSe_2$ with van der Waals Junctions". *Nano Lett.* 18 (2018), pp. 7845–7850. DOI: 10.1021/acs.nanolett.8b03605 (cited on page 35).

[DXW08] D. Dai, H. Xiang, and M.-H. Whangbo. "Effects of spin-orbit coupling on magnetic properties of discrete and extended magnetic systems". *Journal of computational chemistry* 29 (2008), pp. 2187–2209. DOI: 10.1002/jcc.21011 (cited on page 40).

[Dzy57] I. E. Dzyaloshinskii. "Thermodynamic theory of 'weak' ferromagnetism in antiferromagnetic substances". *Sov. Phys. JETP* 5 (1957), pp. 1259–1262 (cited on page 76).

[Eas70] D. E. Eastman. "Photoelectric Work Functions of Transition, Rare-Earth, and Noble Metals". *Phys. Rev. B* 2 (1970), pp. 1–2. DOI: 10.1103/PhysRevB.2.1 (cited on page 69).

[ELR91] D. M. Eigler, C. P. Lutz, and W. E. Rudge. “An atomic switch realized with the scanning tunnelling microscope”. *Nature* 352 (1991), pp. 600–603. DOI: 10.1038/352600a0 (cited on page 12).

[ES90] D. M. Eigler and E. K. Schweizer. “Positioning single atoms with a scanning tunnelling microscope”. *Nature* 344 (1990), pp. 524–526. DOI: 10.1038/344524a0 (cited on page 12).

[Fan61] U. Fano. “Effects of Configuration Interaction on Intensities and Phase Shifts”. *Phys. Rev.* 124 (1961), pp. 1866–1878. DOI: 10.1103/PhysRev.124.1866 (cited on page 42).

[Far+18] L. Farinacci, G. Ahmadi, G. Reecht, M. Ruby, N. Bogdanoff, O. Peters, B. W. Heinrich, F. von Oppen, and K. J. Franke. “Tuning the Coupling of an Individual Magnetic Impurity to a Superconductor: Quantum Phase Transition and Transport”. *Phys. Rev. Lett.* 121 (2018), p. 196803. DOI: 10.1103/PhysRevLett.121.196803 (cited on pages 44, 45, 58, 71).

[Far19] L. Farinacci. “Tuning the Interactions of Magnetic Molecules on a Superconductor”. PhD thesis. Freie Universität Berlin, 2019 (cited on pages 20, 44).

[FB97] M. E. Flatté and J. M. Byers. “Local Electronic Structure of a Single Magnetic Impurity in a Superconductor”. *Phys. Rev. Lett.* 78 (1997), pp. 3761–3764. DOI: 10.1103/PhysRevLett.78.3761 (cited on pages 5, 46).

[FBM12] E. Fortunato, P. Barquinha, and R. Martins. “Oxide Semiconductor Thin-Film Transistors: a Review of Recent Advances”. *Adv. Mater.* 24 (2012), pp. 2945–2986. DOI: 10.1002/adma.201103228 (cited on page 3).

[Fee94] R. M. Feenstra. “Tunneling spectroscopy of the (110) surface of direct-gap III-V semiconductors”. *Phys. Rev. B* 50 (1994), pp. 4561–4570. DOI: 10.1103/PhysRevB.50.4561 (cited on page 69).

[Fel+17] B. E. Feldman, M. T. Randeria, J. Li, S. Jeon, Y. Xie, Z. Wang, I. K. Drozdov, B. A. Bernevig, and A. Yazdani. “High-resolution studies of the Majorana atomic chain platform”. *Nat. Phys.* 13 (2017), pp. 286–291. DOI: 10.1038/nphys3947 (cited on pages 5, 103, 121).

[Fen+12] Y. Feng, J. Wang, R. Jaramillo, J. van Wezel, S. Haravifard, G. Srajer, Y. Liu, Z.-A. Xu, P. B. Littlewood, and T. F. Rosenbaum. “Order parameter fluctuations at a buried quantum critical point”. *PNAS* 109 (2012), pp. 7224–7229. DOI: 10.1073/pnas.1202434109 (cited on page 29).

[Fen+16] A. Fente, E. Herrera, I. Guillamón, H. Suderow, S. Mañas-Valero, M. Galbiati, E. Coronado, and V. G. Kogan. “Field dependence of the vortex core size probed by scanning tunneling microscopy”. *Phys. Rev. B* 94 (2016), p. 014517. DOI: 10.1103/PhysRevB.94.014517 (cited on page 140).

[Fer+12] I. Fernández-Torrente, D. Kreikemeyer-Lorenzo, A. Stró żecka, K. J. Franke, and J. I. Pascual. “Gating the Charge State of Single Molecules by Local Electric Fields”. *Phys. Rev. Lett.* 108 (2012), p. 036801. DOI: 10.1103/PhysRevLett.108.036801 (cited on page 70).

[FK08] L. Fu and C. L. Kane. “Superconducting Proximity Effect and Majorana Fermions at the Surface of a Topological Insulator”. *Phys. Rev. Lett.* 100 (2008), p. 096407. DOI: 10.1103/PhysRevLett.100.096407 (cited on page 4).

[FK75] B. Fischer and M. W. Klein. “Magnetic and nonmagnetic impurities in two-dimensional metals”. *Phys. Rev. B* 11 (1975), pp. 2025–2029. DOI: 10.1103/PhysRevB.11.2025 (cited on page 76).

[Fle+07] J. D. Fletcher, A. Carrington, P. Diener, P. Rodière, J. P. Brison, R. Prozorov, T. Olheiser, and R. W. Giannetta. “Penetration Depth Study of Superconducting Gap Structure of $2H$-$NbSe_2$”. *Phys. Rev. Lett.* 98 (2007), p. 057003. DOI: 10.1103/PhysRevLett.98.057003 (cited on page 31).

[Flo+07] A. Floris, A. Sanna, S. Massidda, and E. K. U. Gross. “Two-band superconductivity in Pb from ab initio calculations”. *Phys. Rev. B* 75 (2007), p. 054508. DOI: 10.1103/PhysRevB.75.054508 (cited on pages 21, 32).

[FM73] S. Foner and E. J. McNiff Jr. “Upper critical fields of layered superconducting $NbSe_2$ at low temperature”. *Phys. Lett. A* 45 (1973), pp. 429–430. DOI: 10.1016/0375-9601(73)90693-2 (cited on page 35).

[FR00] M. E. Flatté and D. E. Reynolds. “Local spectrum of a superconductor as a probe of interactions between magnetic impurities”. *Phys. Rev. B* 61 (2000), pp. 14810–14814. DOI: 10.1103/PhysRevB.61.14810 (cited on pages 5, 76, 78).

[FSP11] K. J. Franke, G. Schulze, and J. I. Pascual. “Competition of Superconducting Phenomena and Kondo Screening at the Nanoscale”. *Science* 332 (2011), pp. 940–944. DOI: 10.1126/science.1202204 (cited on pages 5, 16, 45, 58).

[FW15] F. Flicker and J. van Wezel. “Charge order from orbital-dependent coupling evidenced by $NbSe_2$”. *Nat. Commun.* 6 (2015), p. 7034. DOI: 10.1038/ncomms8034 (cited on pages 30, 53, 114).

[Gir+93] C. Girard, C. Joachim, C. Chavy, and P. Sautet. “The electric field under a STM tip apex: implications for adsorbate manipulation”. *Surf. Sci.* 282 (1993), pp. 400–410. DOI: 10.1016/0039-6028(93)90944-F (cited on pages 69–71).

[GL02] V. M. Galitski and A. I. Larkin. “Spin glass versus superconductivity”. *Phys. Rev. B* 66 (2002), p. 064526. DOI: 10.1103/PhysRevB.66.064526 (cited on page 76).

[GL09] V. L. Ginzburg and L. D. Landau. “On the Theory of Superconductivity”. In: *On Superconductivity and Superfluidity*. Springer, 2009, pp. 113–137 (cited on page 23).

[GM12] R. Gross and A. Marx. *Festkörperphysik*. De Gruyter, 2012 (cited on pages 24–26, 46).

[GOY19] G. Gye, E. Oh, and H. W. Yeom. “Topological Landscape of Competing Charge Density Waves in $2H$-$NbSe_2$”. *Phys. Rev. Lett.* 122 (2019), p. 016403. DOI: 10.1103/PhysRevLett.122.016403 (cited on pages 30, 32, 47, 53, 146).

[Gro+11] L. Gross, N. Moll, F. Mohn, A. Curioni, G. Meyer, F. Hanke, and M. Persson. “High-Resolution Molecular Orbital Imaging Using a p-Wave STM Tip”. *Phys. Rev. Lett.* 107 (2011), p. 086101. DOI: 10.1103/PhysRevLett.107.086101 (cited on page 134).

[GSV06] D. Gatteschi, R. Sessoli, and J. Villain. *Molecular nanomagnets*. Vol. 5. Oxford University Press, 2006 (cited on page 40).

[Gui+08a] I. Guillamón, H. Suderow, F. Guinea, and S. Vieira. “Intrinsic atomic-scale modulations of the superconducting gap of $2H$-$NbSe_2$”. *Phys. Rev. B* 77 (2008), p. 134505. DOI: 10.1103/PhysRevB.77.134505 (cited on page 31).

[Gui+08b] I. Guillamón, H. Suderow, S. Vieira, L. Cario, P. Diener, and P. Rodière. "Superconducting Density of States and Vortex Cores of $2H$-NbS_2". *Phys. Rev. Lett.* 101 (2008), p. 166407. DOI: 10.1103/PhysRevLett.101.166407 (cited on pages 31, 140).

[Gus+19] B. Guster, C. Rubio-Verdú, R. Robles, J. Zaldívar, P. Dreher, M. Pruneda, J. Á. Silva-Guillén, D.-J. Choi, J. I. Pascual, M. M. Ugeda, P. Ordejón, and E. Canadell. "Coexistence of Elastic Modulations in the Charge Density Wave State of $2H$-$NbSe_2$". *Nano Lett.* 19 (2019), pp. 3027–3032. DOI: 10.1021/acs.nanolett.9b00268 (cited on pages 30, 32, 47, 53, 146).

[Hat+15] N. Hatter, B. W. Heinrich, M. Ruby, J. I. Pascual, and K. J. Franke. "Magnetic anisotropy in Shiba bound states across a quantum phase transition". *Nat. Commun.* 6 (2015), p. 8988. DOI: 10.1038/ncomms9988 (cited on pages 4, 45, 47, 64).

[Hat+17] N. Hatter, B. W. Heinrich, D. Rolf, and K. J. Franke. "Scaling of Yu-Shiba-Rusinov energies in the weak-coupling Kondo regime". *Nat. Commun.* 8 (2017), p. 2016. DOI: 10.1038/s41467-017-02277-7 (cited on page 124).

[Hat16] N. Hatter. "Fundamental Properties of Molecules on Surfaces - Molecular Switching and Interaction of Magnetic Molecules with Superconductors". PhD thesis. Freie Universität Berlin, 2016 (cited on page 19).

[Hei+04] A. J. Heinrich, J. A. Gupta, C. P. Lutz, and D. M. Eigler. "Single-Atom Spin-Flip Spectroscopy". *Science* 306 (2004), pp. 466–469. DOI: 10.1126/science.1101077 (cited on page 134).

[Hei+17] C. Heil, S. Poncé, H. Lambert, M. Schlipf, E. R. Margine, and F. Giustino. "Origin of Superconductivity and Latent Charge Density Wave in NbS_2". *Phys. Rev. Lett.* 119 (2017), p. 087003. DOI: 10.1103/PhysRevLett.119.087003 (cited on page 140).

[Hei35] O. Heil. *Improvements in or relating to electrical amplifiers and other control arrangements and devices*. U.K. Patent 439457. 1935 (cited on page 3).

[Hew93] A. C. Hewson. *The Kondo Problem to Heavy Fermions*. Cambridge University Press, 1993 (cited on pages 40, 42, 43, 135).

[Hla05] S.-W. Hla. "Scanning tunneling microscopy single atom/molecule manipulation and its application to nanoscience and technology". *J. Vac. Sci. Technol., B* 23 (2005), pp. 1351–1360. DOI: 10.1116/1.1990161 (cited on page 12).

[HMK15] A. Heimes, D. Mendler, and P. Kotetes. "Interplay of topological phases in magnetic adatom-chains on top of a Rashba superconducting surface". *New J. Phys.* 17 (2015), p. 023051. DOI: 10.1088/1367-2630/17/2/023051 (cited on pages 76, 77).

[Hof+15] S. Hoffman, J. Klinovaja, T. Meng, and D. Loss. "Impurity-induced quantum phase transitions and magnetic order in conventional superconductors: Competition between bound and quasiparticle states". *Phys. Rev. B* 92 (2015), p. 125422. DOI: 10.1103/PhysRevB.92.125422 (cited on pages 5, 76).

[Hom+20] J. Homberg, A. Weismann, R. Berndt, and M. Gruber. "Inducing and Controlling Molecular Magnetism through Supramolecular Manipulation". *ACS Nano* 14 (2020), pp. 17387–17395. DOI: 10.1021/acsnano.0c07574 (cited on page 124).

[HRW90] H. F. Hess, R. B. Robinson, and J. V. Waszczak. "Vortex-core structure observed with a scanning tunneling microscope". *Phys. Rev. Lett.* 64 (1990), pp. 2711–2714. DOI: 10.1103/PhysRevLett.64.2711 (cited on pages 31, 35).

[Hua+20] H. Huang, R. Drost, J. Senkpiel, C. Padurariu, B. Kubala, A. L. Yeyati, J. C. Cuevas, J. Ankerhold, K. Kern, and C. R. Ast. "Quantum phase transitions and the role of impurity-substrate hybridization in Yu-Shiba-Rusinov states". *Communications Physics* 3.1 (2020), pp. 1–9 (cited on pages 45, 71).

[Ino+08] D. S. Inosov, V. B. Zabolotnyy, D. V. Evtushinsky, A. A. Kordyuk, B. Büchner, R. Follath, H. Berger, and S. V. Borisenko. "Fermi surface nesting in several transition metal dichalcogenides". *New J. Phys.* 10 (2008), p. 125027. DOI: 10.1088/1367-2630/10/12/125027 (cited on page 54).

[Ino+09] D. S. Inosov, D. V. Evtushinsky, V. B. Zabolotnyy, A. A. Kordyuk, B. Büchner, R. Follath, H. Berger, and S. V. Borisenko. "Temperature-dependent Fermi surface of $2H$-$TaSe_2$ driven by competing density wave order fluctuations". *Phys. Rev. B* 79 (2009), p. 125112. DOI: 10.1103/PhysRevB.79.125112 (cited on page 54).

[Jea05] Y. Jean. *Molecular Orbitals of Transition Metal Complexes*. Oxford University Press, 2005 (cited on pages 37, 38, 48, 132, 133).

[Ji+08] S.-H. Ji, T. Zhang, Y.-S. Fu, X. Chen, X.-C. Ma, J. Li, W.-H. Duan, J.-F. Jia, and Q.-K. Xue. "High-Resolution Scanning Tunneling Spectroscopy of Magnetic Impurity Induced Bound States in the Superconducting Gap of Pb Thin Films". *Phys. Rev. Lett.* 100 (2008), p. 226801. DOI: 10.1103/PhysRevLett.100.226801 (cited on pages 4, 5, 46, 78).

[JM08] M. D. Johannes and I. I. Mazin. "Fermi surface nesting and the origin of charge density waves in metals". *Phys. Rev. B* 77 (2008), p. 165135. DOI: 10.1103/PhysRevB.77.165135 (cited on page 29).

[JMH06] M. D. Johannes, I. I. Mazin, and C. A. Howells. "Fermi-surface nesting and the origin of the charge-density wave in $NbSe_2$". *Phys. Rev. B* 73 (2006), p. 205102. DOI: 10.1103/PhysRevB.73.205102 (cited on page 29).

[Kam+18] A. Kamlapure, L. Cornils, J. Wiebe, and R. Wiesendanger. "Engineering the spin couplings in atomically crafted spin chains on an elemental superconductor". *Nat. Commun.* 9 (2018), p. 3253. DOI: 10.1038/s41467-018-05701-8 (cited on page 103).

[Kam08] H. Kamerlingh Onnes. "The liquefaction of helium". *Koninklijke Nederlandse Akademie von Wetenschappen, Proceedings* 11 (1908), pp. 1908–1909 (cited on page 23).

[Kas56] T. Kasuya. "A Theory of Metallic Ferro-and Antiferromagnetism on Zener's Model". *Prog. Theor. Phys.* 16 (1956), pp. 45–57. DOI: 10.1143/PTP.16.45 (cited on page 75).

[Kez+18] S. Kezilebieke, M. Dvorak, T. Ojanen, and P. Liljeroth. "Coupled Yu-Shiba-Rusinov States in Molecular Dimers on $NbSe_2$". *Nano Lett.* 18 (2018), pp. 2311–2315. DOI: 10.1021/acs.nanolett.7b05050 (cited on pages 5, 6, 78, 124).

[Kez+19] S. Kezilebieke, R. Žitko, M. Dvorak, T. Ojanen, and P. Liljeroth. "Observation of Coexistence of Yu-Shiba-Rusinov States and Spin-Flip Excitations". *Nano Lett.* 19 (2019), pp. 4614–4619. DOI: 10.1021/acs.nanolett.9b01583 (cited on pages 124, 134).

[Kez+20a] S. Kezilebieke, V. Vaňo, M. N. Huda, M. Aapro, S. C. Ganguli, P. Liljeroth, and J. L. Lado. "Moiré-enabled topological superconductivity". *arXiv Preprint* (2020). arXiv: 2011.09760 (cited on pages 60, 124).

[Kez+20b] S. Kezilebieke, M. N. Huda, V. Vaňo, M. Aapro, S. C. Ganguli, O. J. Silveira, S. Głodzik, A. S. Foster, T. Ojanen, and P. Liljeroth. "Topological superconductivity in a van der Waals heterostructure". *Nature* 588 (2020), pp. 424–428. DOI: 10.1038/s41586-020-2989-y (cited on page 60).

[Kha+12] A. A. Khajetoorians, J. Wiebe, B. Chilian, S. Lounis, S. Blügel, and R. Wiesendanger. "Atom-by-atom engineering and magnetometry of tailored nanomagnets". *Nat. Phys.* 8 (2012), pp. 497–503. DOI: 10.1038/nphys2299 (cited on pages 76, 119).

[Kim+18] H. Kim, A. Palacio-Morales, T. Posske, L. Rózsa, K. Palotás, L. Szunyogh, M. Thorwart, and R. Wiesendanger. "Toward tailoring Majorana bound states in artificially constructed magnetic atom chains on elemental superconductors". *Sci. Adv.* 4 (2018), p. eaar5251. DOI: 10.1126/sciadv.aar5251 (cited on pages 5, 103, 121).

[Kis+07] T. Kiss, T. Yokoya, A. Chainani, S. Shin, T. Hanaguri, M. Nohara, and H. Takagi. "Charge-order-maximized momentum-dependent superconductivity". *Nat. Phys.* 3 (2007), pp. 720–725. DOI: 10.1038/nphys699 (cited on pages 29, 31).

[Kit01] A. Y. Kitaev. "Unpaired Majorana fermions in quantum wires". *Phys. Usp.* 44 (2001), pp. 131–136. DOI: 10.1070/1063-7869/44/10s/s29 (cited on page 99).

[Kle+73] J. Klein, A. Léger, M. Belin, D. Défourneau, and M. J. L. Sangster. "Inelastic-Electron-Tunneling Spectroscopy of Metal-Insulator-Metal Junctions". *Phys. Rev. B* 7 (1973), pp. 2336–2348. DOI: 10.1103/PhysRevB.7.2336 (cited on page 21).

[Kle17] M. H. Kleinert. "Magnetic Impurities on a Superconductor: from Single Atoms to Coupled Chains". PhD thesis. Freie Universität Berlin, 2017 (cited on pages 27, 101).

[Kli+13] J. Klinovaja, P. Stano, A. Yazdani, and D. Loss. "Topological Superconductivity and Majorana Fermions in RKKY Systems". *Phys. Rev. Lett.* 111 (2013), p. 186805. DOI: 10.1103/PhysRevLett.111.186805 (cited on pages 4, 6, 76, 99).

[Kon64] J. Kondo. "Resistance Minimum in Dilute Magnetic Alloys". *Prog. Theor. Phys.* 32 (1964), pp. 37–49. DOI: 10.1143/PTP.32.37 (cited on page 42).

[Krö+04] J. Kröger, L. Limot, H. Jensen, R. Berndt, and P. Johansson. "Stark effect in Au(111) and Cu(111) surface states". *Phys. Rev. B* 70 (2004), p. 033401. DOI: 10.1103/PhysRevB.70.033401 (cited on pages 70, 71).

[KTK18] S. Körber, B. Trauzettel, and O. Kashuba. "Collective Yu-Shiba-Rusinov states in magnetic clusters at superconducting surfaces". *Phys. Rev. B* 97 (2018), p. 184503. DOI: 10.1103/PhysRevB.97.184503 (cited on page 78).

[LA91] I.-W. Lyo and P. Avouris. "Field-Induced Nanometer- to Atomic-Scale Manipulation of Silicon Surfaces with the STM". *Science* 253 (1991), pp. 173–176. DOI: 10.1126/science.253.5016.173 (cited on page 12).

[Lan+14] M. Langer, M. Kisiel, R. Pawlak, F. Pellegrini, G. E. Santoro, R. Buzio, A. Gerbi, G. Balakrishnan, A. Baratoff, E. Tosatti, and E. Meyer. "Giant frictional dissipation peaks and charge-density-wave slips at the $NbSe_2$ surface". *Nat. Mater.* 13 (2014), pp. 173–177. DOI: 10.1038/nmat3836 (cited on pages 30, 53, 114).

[Ler+15] M. Leroux, I. Errea, M. Le Tacon, S.-M. Souliou, G. Garbarino, L. Cario, A. Bosak, F. Mauri, M. Calandra, and P. Rodière. "Strong anharmonicity induces quantum melting of charge density wave in $2H$-$NbSe_2$ under pressure". *Phys. Rev. B* 92 (2015), p. 140303(R). DOI: 10.1103/PhysRevB.92.140303 (cited on pages 29, 31).

[LF12] M. Leijnse and K. Flensberg. “Introduction to topological superconductivity and Majorana fermions”. *Semicond. Sci. Technol.* 27 (2012), p. 124003. DOI: 10.1088/0268-1242/27/12/124003 (cited on page 4).

[Li+14] J. Li, H. Chen, I. K. Drozdov, A. Yazdani, B. A. Bernevig, and A. H. MacDonald. “Topological superconductivity induced by ferromagnetic metal chains”. *Phys. Rev. B* 90 (2014), p. 235433. DOI: 10.1103/PhysRevB.90.235433 (cited on page 99).

[Lie+20] E. Liebhaber, S. Acero González, R. Baba, G. Reecht, B. W. Heinrich, S. Rohlf, K. Rossnagel, F. von Oppen, and K. J. Franke. “Yu-Shiba-Rusinov States in the Charge-Density Modulated Superconductor $NbSe_2$”. *Nano Lett.* 20 (2020), pp. 339–344. DOI: 10.1021/acs.nanolett.9b03988 (cited on pages 49, 54, 55, 60, 62, 117, 137).

[Lie+21] E. Liebhaber, L. M. Rütten, G. Reecht, J. F. Steiner, S. Rohlf, K. Rossnagel, F. von Oppen, and K. J. Franke. “Quantum spins and hybridization in artificially-constructed chains of magnetic adatoms on a superconductor”. *arXiv Preprint* (2021). arXiv: 2107.06361 (cited on pages 79, 103).

[Lil30] J. E. Lilienfeld. *Method and apparatus for controlling electric currents*. U.S. Patent 1745175. 1930 (cited on page 3).

[Lil32] J. E. Lilienfeld. *Amplifier for electric currents*. U.S. Patent 1877140. 1932 (cited on page 3).

[Lil33] J. E. Lilienfeld. *Device for controlling electric current*. U.S. Patent 1900018. 1933 (cited on page 3).

[Lim+03] L. Limot, T. Maroutian, P. Johansson, and R. Berndt. “Surface-State Stark Shift in a Scanning Tunneling Microscope”. *Phys. Rev. Lett.* 91 (2003), p. 196801. DOI: 10.1103/PhysRevLett.91.196801 (cited on page 70).

[LL35] F. London and H. London. “The electromagnetic equations of the supraconductor”. *Proc. R. Soc. London, Ser. A* 149 (1935), pp. 71–88. DOI: 10.1098/rspa.1935.0048 (cited on page 23).

[LLH10] S. Loth, C. P. Lutz, and A. J. Heinrich. “Spin-polarized spin excitation spectroscopy”. *New J. Phys.* 12 (2010), p. 125021. DOI: 10.1088/1367-2630/12/12/125021 (cited on page 134).

[LRT05] N. Lorente, R. Rurali, and H. Tang. “Single-molecule manipulation and chemistry with the STM”. *J. Phys.: Condens. Matter* 17 (2005), pp. S1049–S1074. DOI: 10.1088/0953-8984/17/13/003 (cited on page 12).

[LSD10] R. M. Lutchyn, J. D. Sau, and S. Das Sarma. “Majorana Fermions and a Topological Phase Transition in Semiconductor-Superconductor Heterostructures”. *Phys. Rev. Lett.* 105 (2010), p. 077001. DOI: 10.1103/PhysRevLett.105.077001 (cited on page 4).

[LSD18] C.-S. Lian, C. Si, and W. Duan. “Unveiling Charge-Density Wave, Superconductivity, and Their Competitive Nature in Two-Dimensional $NbSe_2$”. *Nano Lett.* 18 (2018), pp. 2924–2929. DOI: 10.1021/acs.nanolett.8b00237 (cited on pages 29–32, 48, 53, 60, 146).

[LSW16] Y. Liu, P. Stradins, and S.-H. Wei. “Van der Waals metal-semiconductor junction: Weak Fermi level pinning enables effective tuning of Schottky barrier”. *Sci. Adv.* 2 (2016), p. e1600069. DOI: 10.1126/sciadv.1600069 (cited on page 69).

[MAD75] D. E. Moncton, J. D. Axe, and F. J. DiSalvo. “Study of Superlattice Formation in $2H$-$NbSe_2$ and $2H$-$TaSe_2$ by Neutron Scattering”. *Phys. Rev. Lett.* 34 (1975), pp. 734–737. DOI: 10.1103/PhysRevLett.34.734 (cited on page 29).

[Mal+18] L. Malavolti, M. Briganti, M. Hänze, G. Serrano, I. Cimatti, G. McMurtrie, E. Otero, P. Ohresser, F. Totti, M. Mannini, R. Sessoli, and S. Loth. “Tunable Spin-Superconductor Coupling of Spin $1/2$ Vanadyl Phthalocyanine Molecules”. *Nano Lett.* 18 (2018), pp. 7955–7961. DOI: 10.1021/acs.nanolett.8b03921 (cited on pages 45, 58, 71).

[Mar+08] F. Marczinowski, J. Wiebe, F. Meier, K. Hashimoto, and R. Wiesendanger. “Effect of charge manipulation on scanning tunneling spectra of single Mn acceptors in InAs”. *Phys. Rev. B* 77 (2008), p. 115318. DOI: 10.1103/PhysRevB.77.115318 (cited on page 70).

[Mar+72] M. Marezio, P. D. Dernier, A. Menth, and G. W. Hull Jr. “The crystal structure of $NbSe_2$ at 15°K”. *J. Solid State Chem.* 4 (1972), pp. 425–429. DOI: 10.1016/0022-4596(72)90158-2 (cited on pages 28, 131).

[McE+93] M. McEllistrem, G. Haase, D. Chen, and R. J. Hamers. “Electrostatic sample-tip interactions in the scanning tunneling microscope”. *Phys. Rev. Lett.* 70 (1993), pp. 2471–2474. DOI: 10.1103/PhysRevLett.70.2471 (cited on page 69).

[McM76] W. L. McMillan. “Theory of discommensurations and the commensurate-incommensurate charge-density-wave phase transition”. *Phys. Rev. B* 14 (1976), pp. 1496–1502. DOI: 10.1103/PhysRevB.14.1496 (cited on page 29).

[Mei+08] F. Meier, L. Zhou, J. Wiebe, and R. Wiesendanger. “Revealing Magnetic Interactions from Single-Atom Magnetization Curves”. *Science* 320 (2008), pp. 82–86. DOI: 10.1126/science.1154415 (cited on page 76).

[Mén+15] G. C. Ménard, S. Guissart, C. Brun, S. Pons, V. S. Stolyarov, F. Debontridder, M. V. Leclerc, E. Janod, L. Cario, D. Roditchev, P. Simon, and T. Cren. “Coherent long-range magnetic bound states in a superconductor”. *Nat. Phys.* 11 (2015), pp. 1013–1016. DOI: 10.1038/nphys3508 (cited on pages 5, 6, 45, 46, 50, 54).

[Mic77] H. B. Michaelson. “The work function of the elements and its periodicity”. *J. Appl. Phys.* 48 (1977), pp. 4729–4733. DOI: 10.1063/1.323539 (cited on page 69).

[Mie+21] C. Mier, J. Hwang, J. Kim, Y. Bae, F. Nabeshima, Y. Imai, A. Maeda, N. Lorente, A. Heinrich, and D.-J. Choi. “Atomic manipulation of in-gap states in the β-Bi_2Pd superconductor”. *Phys. Rev. B* 104 (2021), p. 045406. DOI: 10.1103/PhysRevB.104.045406 (cited on pages 5, 103, 121).

[MK13] C. D. Malliakas and M. G. Kanatzidis. “Nb–Nb Interactions Define the Charge Density Wave Structure of $2H$-$NbSe_2$”. *JACS* 135 (2013), pp. 1719–1722. DOI: 10.1021/ja3120554 (cited on pages 29, 48, 60).

[MM06] E. Majorana and L. Maiani. “A symmetric theory of electrons and positrons”. In: *Ettore Majorana Scientific Papers*. Springer, 2006, pp. 201–233 (cited on pages 4, 100).

[MO33] W. Meissner and R. Ochsenfeld. “Ein neuer Effekt bei Eintritt der Supraleitfähigkeit”. *Naturwissenschaften* 21 (1933), pp. 787–788 (cited on pages 4, 23).

[Moc+08] C. P. Moca, E. Demler, B. Jankó, and G. Zaránd. “Spin-resolved spectra of Shiba multiplets from Mn impurities in MgB_2”. *Phys. Rev. B* 77 (2008), p. 174516. DOI: 10.1103/PhysRevB.77.174516 (cited on pages 46, 62).

[Mor60] T. Moriya. “Anisotropic Superexchange Interaction and Weak Ferromagnetism”. *Phys. Rev.* 120 (1960), pp. 91–98. DOI: 10.1103/PhysRev.120.91 (cited on page 76).

[Mou+12] V. Mourik, K. Zuo, S. M. Frolov, S. R. Plissard, E. P. A. M. Bakkers, and L. P. Kouwenhoven. “Signatures of Majorana Fermions in Hybrid Superconductor-Semiconductor Nanowire Devices”. *Science* 336 (2012), pp. 1003–1007. DOI: 10.1126/science.1222360 (cited on page 4).

[Nad+13] S. Nadj-Perge, I. K. Drozdov, B. A. Bernevig, and A. Yazdani. “Proposal for realizing Majorana fermions in chains of magnetic atoms on a superconductor”. *Phys. Rev. B* 88 (2013), p. 020407(R). DOI: 10.1103/PhysRevB.88.020407 (cited on pages 4, 6, 99).

[Nad+14] S. Nadj-Perge, I. K. Drozdov, J. Li, H. Chen, S. Jeon, J. Seo, A. H. MacDonald, B. A. Bernevig, and A. Yazdani. “Observation of Majorana fermions in ferromagnetic atomic chains on a superconductor”. *Science* 346 (2014), pp. 602–607. DOI: 10.1126/science.1259327 (cited on pages 4, 5, 103, 121).

[Noa+10] Y. Noat, T. Cren, F. Debontridder, D. Roditchev, W. Sacks, P. Toulemonde, and A. San Miguel. “Signatures of multigap superconductivity in tunneling spectroscopy”. *Phys. Rev. B* 82 (2010), p. 014531. DOI: 10.1103/PhysRevB.82.014531 (cited on page 31).

[Noa+15] Y. Noat, J. A. Silva-Guillén, T. Cren, V. Cherkez, C. Brun, S. Pons, F. Debontridder, D. Roditchev, W. Sacks, L. Cario, P. Ordejón, A. García, and E. Canadell. “Quasiparticle spectra of $2H$-$NbSe_2$: Two-band superconductivity and the role of tunneling selectivity”. *Phys. Rev. B* 92 (2015), p. 134510. DOI: 10.1103/PhysRevB.92.134510 (cited on page 31).

[NQH05] G. V. Nazin, X. H. Qiu, and W. Ho. “Charging and Interaction of Individual Impurities in a Monolayer Organic Crystal”. *Phys. Rev. Lett.* 95 (2005), p. 166103. DOI: 10.1103/PhysRevLett.95.166103 (cited on page 70).

[Odo+19] A. B. Odobesko, S. Haldar, S. Wilfert, J. Hagen, J. Jung, N. Schmidt, P. Sessi, M. Vogt, S. Heinze, and M. Bode. “Preparation and electronic properties of clean superconducting Nb(110) surfaces”. *Phys. Rev. B* 99 (2019), p. 115437. DOI: 10.1103/PhysRevB.99.115437 (cited on page 21).

[Odo+20] A. Odobesko, D. Di Sante, A. Kowalski, S. Wilfert, F. Friedrich, R. Thomale, G. Sangiovanni, and M. Bode. “Observation of tunable single-atom Yu-Shiba-Rusinov states”. *Phys. Rev. B* 102 (2020), p. 174504. DOI: 10.1103/PhysRevB.102.174504 (cited on page 45).

[OF21] F. von Oppen and K. J. Franke. “Yu-Shiba-Rusinov states in real metals”. *Phys. Rev. B* 103 (2021), p. 205424. DOI: 10.1103/PhysRevB.103.205424 (cited on pages 47, 64, 66, 67).

[OPP17] F. von Oppen, Y. Peng, and F. Pientka. “Topological superconducting phases in one dimension”. *Topological Aspects of Condensed Matter Physics: Lecture Notes of the Les Houches Summer School* 3 (2017), pp. 387–447. DOI: 10.1093/acprof:oso/9780198785781.001.0001 (cited on pages 28, 43, 44).

[ORO10] Y. Oreg, G. Refael, and F. von Oppen. “Helical Liquids and Majorana Bound States in Quantum Wires”. *Phys. Rev. Lett.* 105 (2010), p. 177002. DOI: 10.1103/PhysRevLett.105.177002 (cited on page 4).

[Paw+16] R. Pawlak, M. Kisiel, J. Klinovaja, T. Meier, S. Kawai, T. Glatzel, D. Loss, and E. Meyer. “Probing atomic structure and Majorana wavefunctions in mono-atomic Fe chains on superconducting Pb surface”. *npj Quantum Inf.* 2 (2016), p. 16035. DOI: 10.1038/npjqi.2016.35 (cited on pages 5, 103, 121).

[Pen+15] Y. Peng, F. Pientka, L. I. Glazman, and F. von Oppen. “Strong Localization of Majorana End States in Chains of Magnetic Adatoms”. *Phys. Rev. Lett.* 114 (2015), p. 106801. DOI: 10.1103/PhysRevLett.114.106801 (cited on pages 99, 102).

[PGO13] F. Pientka, L. I. Glazman, and F. von Oppen. “Topological superconducting phase in helical Shiba chains”. *Phys. Rev. B* 88 (2013), p. 155420. DOI: 10.1103/PhysRevB.88.155420 (cited on pages 4, 6, 28, 43, 44, 99, 101, 102).

[PGO14] F. Pientka, L. I. Glazman, and F. von Oppen. “Unconventional topological phase transitions in helical Shiba chains”. *Phys. Rev. B* 89 (2014), p. 180505(R). DOI: 10.1103/PhysRevB.89.180505 (cited on pages 6, 99, 101).

[Pie+15] F. Pientka, Y. Peng, L. Glazman, and F. von Oppen. “Topological superconducting phase and Majorana bound states in Shiba chains”. *Phys. Scr.* 2015 (2015), p. 014008. DOI: 10.1088/0031-8949/2015/T164/014008 (cited on pages 99–102).

[Pra+05] N. A. Pradhan, N. Liu, C. Silien, and W. Ho. “Atomic Scale Conductance Induced by Single Impurity Charging”. *Phys. Rev. Lett.* 94 (2005), p. 076801. DOI: 10.1103/PhysRevLett.94.076801 (cited on page 70).

[Rah+12] D. J. Rahn, S. Hellmann, M. Kalläne, C. Sohrt, T. K. Kim, L. Kipp, and K. Rossnagel. “Gaps and kinks in the electronic structure of the superconductor $2H$-$NbSe_2$ from angle-resolved photoemission at 1 K”. *Phys. Rev. B* 85 (2012), p. 224532. DOI: 10.1103/PhysRevB.85.224532 (cited on pages 22, 29, 31, 54, 76).

[Ree+17] G. Reecht, B. W. Heinrich, H. Bulou, F. Scheurer, L. Limot, and G. Schull. “Imaging isodensity contours of molecular states with STM”. *New J. Phys.* 19 (2017), p. 113033. DOI: 10.1088/1367-2630/aa969a (cited on page 15).

[RK54] M. A. Ruderman and C. Kittel. “Indirect Exchange Coupling of Nuclear Magnetic Moments by Conduction Electrons”. *Phys. Rev.* 96 (1954), pp. 99–102. DOI: 10.1103/PhysRev.96.99 (cited on page 75).

[Rol18] D. Rolf. “Fundamental Properties of Atoms and Molecules on Surfaces - a Combined STM and Shot-Noise Study”. PhD thesis. Freie Universität Berlin, 2018 (cited on page 12).

[Ros+01] K. Rossnagel, O. Seifarth, L. Kipp, M. Skibowski, D. Voß, P. Krüger, A. Mazur, and J. Pollmann. “Fermi surface of $2H$-$NbSe_2$ and its implications on the charge-density-wave mechanism”. *Phys. Rev. B* 64 (2001), p. 235119. DOI: 10.1103/PhysRevB.64.235119 (cited on page 29).

[Ros+05] K. Rossnagel, E. Rotenberg, H. Koh, N. V. Smith, and L. Kipp. “Fermi surface, charge-density-wave gap, and kinks in $2H$-$TaSe_2$”. *Phys. Rev. B* 72 (2005), p. 121103(R). DOI: 10.1103/PhysRevB.72.121103 (cited on page 54).

[Ros11] K. Rossnagel. “On the origin of charge-density waves in select layered transition-metal dichalcogenides”. *J. Phys.: Condens. Matter* 23 (2011), p. 213001. DOI: 10.1088/0953-8984/23/21/213001 (cited on page 29).

[RS35] J. N. Rjabinin and L. W. Shubnikow. “Magnetic Properties and Critical Currents of Supra-conducting Alloys”. *Nature* 135 (1935), pp. 581–582. DOI: 10.1038/135581a0 (cited on page 23).

[Rub+15a] M. Ruby, B. W. Heinrich, J. I. Pascual, and K. J. Franke. “Experimental Demonstration of a Two-Band Superconducting State for Lead Using Scanning Tunneling Spectroscopy”. *Phys. Rev. Lett.* 114 (2015), p. 157001. DOI: 10.1103/PhysRevLett.114.157001 (cited on pages 12, 21, 32).

[Rub+15b] M. Ruby, F. Pientka, Y. Peng, F. von Oppen, B. W. Heinrich, and K. J. Franke. “End States and Subgap Structure in Proximity-Coupled Chains of Magnetic Adatoms”. *Phys. Rev. Lett.* 115 (2015), p. 197204. DOI: 10.1103/PhysRevLett.115.197204 (cited on pages 5, 103, 121).

[Rub+15c] M. Ruby, F. Pientka, Y. Peng, F. von Oppen, B. W. Heinrich, and K. J. Franke. “Tunneling Processes into Localized Subgap States in Superconductors”. *Phys. Rev. Lett.* 115 (2015), p. 087001. DOI: 10.1103/PhysRevLett.115.087001 (cited on pages 47, 143).

[Rub+16] M. Ruby, Y. Peng, F. von Oppen, B. W. Heinrich, and K. J. Franke. “Orbital Picture of Yu-Shiba-Rusinov Multiplets”. *Phys. Rev. Lett.* 117 (2016), p. 186801. DOI: 10.1103/PhysRevLett.117.186801 (cited on pages 4, 5, 46, 47, 50, 62, 124).

[Rub+17] M. Ruby, B. W. Heinrich, Y. Peng, F. von Oppen, and K. J. Franke. “Exploring a Proximity-Coupled Co Chain on Pb(110) as a Possible Majorana Platform”. *Nano Lett.* 17 (2017), pp. 4473–4477. DOI: 10.1021/acs.nanolett.7b01728 (cited on pages 5, 103).

[Rub+18] M. Ruby, B. W. Heinrich, Y. Peng, F. von Oppen, and K. J. Franke. “Wave-Function Hybridization in Yu-Shiba-Rusinov Dimers”. *Phys. Rev. Lett.* 120 (2018), p. 156803. DOI: 10.1103/PhysRevLett.120.156803 (cited on pages 5, 76, 78, 79, 83).

[Rus69] A. I. Rusinov. “Superconcductivity near a Paramagnetic Impurity”. *JETP Lett.* 9 (1969), p. 85 (cited on pages 4, 43–45, 143).

[RV04] J. G. Rodrigo and S. Vieira. “STM study of multiband superconductivity in $NbSe_2$ using a superconducting tip”. *Physica C* 404 (2004), pp. 306–310. DOI: 10.1016/j.physc.2003.10.030 (cited on page 31).

[SA17] M. Sato and Y. Ando. “Topological superconductors: a review”. *Rep. Prog. Phys.* 80 (2017), p. 076501. DOI: 10.1088/1361-6633/aa6ac7 (cited on page 4).

[San+21] A. Sanna, C. Pellegrini, E. Liebhaber, K. Rossnagel, K. J. Franke, and E. K. U. Gross. “Real-space anisotropy of the superconducting gap in the charge-density wave material $2H$-$NbSe_2$”. *Submitted* (2021) (cited on pages 29–34, 60, 137).

[SBS97] M. I. Salkola, A. V. Balatsky, and J. R. Schrieffer. “Spectral properties of quasiparticle excitations induced by magnetic moments in superconductors”. *Phys. Rev. B* 55 (1997), pp. 12648–12661. DOI: 10.1103/PhysRevB.55.12648 (cited on pages 5, 46).

[Sch+20] L. Schneider, S. Brinker, M. Steinbrecher, J. Hermenau, T. Posske, M. dos Santos Dias, S. Lounis, R. Wiesendanger, and J. Wiebe. “Controlling in-gap end states by linking nonmagnetic atoms and artificially-constructed spin chains on superconductors”. *Nat. Commun.* 11 (2020), p. 4707. DOI: 10.1038/s41467-020-18540-3 (cited on pages 5, 103, 121).

[Sch+21a] L. Schneider, P. Beck, J. Neuhaus-Steinmetz, T. Posske, J. Wiebe, and R. Wiesendanger. "Controlled length-dependent interaction of Majorana modes in Yu-Shiba-Rusinov chains". *arXiv Preprint* (2021). arXiv: 2104.11503 (cited on pages 5, 103, 121).

[Sch+21b] L. Schneider, P. Beck, T. Posske, D. Crawford, E. Mascot, S. Rachel, R. Wiesendanger, and J. Wiebe. "Topological Shiba bands in artificial spin chains on superconductors". *Nat. Phys.* (2021), pp. 1–6 (cited on pages 5, 103, 121).

[SE91] J. A. Stroscio and D. M. Eigler. "Atomic and Molecular Manipulation with the Scanning Tunneling Microscope". *Science* 254 (1991), pp. 1319–1326. DOI: 10.1126/science.254.5036.1319 (cited on page 12).

[Sen+19] J. Senkpiel, C. Rubio-Verdú, M. Etzkorn, R. Drost, L. M. Schoop, S. Dambach, C. Padurariu, B. Kubala, J. Ankerhold, C. R. Ast, and K. Kern. "Robustness of Yu-Shiba-Rusinov resonances in the presence of a complex superconducting order parameter". *Phys. Rev. B* 100 (2019), p. 014502. DOI: 10.1103/PhysRevB.100.014502 (cited on pages 50, 62).

[Ser+10] D. Serrate, P. Ferriani, Y. Yoshida, S.-W. Hla, M. Menzel, K. Von Bergmann, S. Heinze, A. Kubetzka, and R. Wiesendanger. "Imaging and manipulating the spin direction of individual atoms". *Nat. Nanotechnol.* 5 (2010), pp. 350–353. DOI: 10.1038/nnano.2010.64 (cited on page 134).

[Shi68] H. Shiba. "Classical Spins in Superconductors". *Prog. Theor. Phys.* 40 (1968), pp. 435–451. DOI: 10.1143/PTP.40.435 (cited on pages 4, 43).

[Sho84] W. Shockley. "The path to the Conception of the junction transistor". *IEEE Trans. Electron Devices* 31 (1984), pp. 1523–1546. DOI: 10.1109/T-ED.1984.21749 (cited on page 3).

[SK93] J. A. Stroscio and W. J. Kaiser. *Scanning Tunneling Microscopy*. Vol. 27. Academic press, 1993 (cited on pages 10, 11).

[SKD85] N. V. Smith, S. D. Kevan, and F. J. DiSalvo. "Band structures of the layer compounds 1T-TaS_2 and 2H-$TaSe_2$ in the presence of commensurate charge-density waves". *J. Phys. C: Solid State Phys.* 18 (1985), pp. 3175–3189. DOI: 10.1088/0022-3719/18/16/013 (cited on page 54).

[SOP94] T. Shimada, F. S. Ohuchi, and B. A. Parkinson. "Work Function and Photothreshold of Layered Metal Dichalcogenides". *Jpn. J. Appl. Phys., Part 1* 33 (1994), pp. 2696–2698. DOI: 10.1143/JJAP.33.2696 (cited on page 69).

[Sou+13] A. Soumyanarayanan, M. M. Yee, Y. He, J. van Wezel, D. J. Rahn, K. Rossnagel, E. W. Hudson, M. R. Norman, and J. E. Hoffman. "Quantum phase transition from triangular to stripe charge order in $NbSe_2$". *PNAS* 110 (2013), pp. 1623–1627. DOI: 10.1073/pnas.1211387110 (cited on pages 29, 31).

[Sta+19] R.-M. Stan, S. K. Mahatha, M. Bianchi, C. E. Sanders, D. Curcio, P. Hofmann, and J. A. Miwa. "Epitaxial single-layer NbS_2 on Au(111): Synthesis, structure, and electronic properties". *Phys. Rev. Mater.* 3 (2019), p. 044003. DOI: 10.1103/PhysRevMaterials.3.044003 (cited on page 140).

[SW66] J. R. Schrieffer and P. A. Wolff. "Relation between the Anderson and Kondo Hamiltonians". *Phys. Rev.* 149 (1966), pp. 491–492. DOI: 10.1103/PhysRev.149.491 (cited on page 42).

[Tei+08] K. Teichmann, M. Wenderoth, S. Loth, R. G. Ulbrich, J. K. Garleff, A. P. Wijnheijmer, and P. M. Koenraad. "Controlled Charge Switching on a Single Donor with a Scanning Tunneling Microscope". *Phys. Rev. Lett.* 101 (2008), p. 076103. DOI: 10.1103/PhysRevLett.101.076103 (cited on page 70).

[Ter+08] M. Ternes, C. P. Lutz, C. F. Hirjibehedin, F. J. Giessibl, and A. J. Heinrich. "The Force Needed to Move an Atom on a Surface". *Science* 319 (2008), pp. 1066–1069. DOI: 10.1126/science.1150288 (cited on page 71).

[TH83] J. Tersoff and D. R. Hamann. "Theory and Application for the Scanning Tunneling Microscope". *Phys. Rev. Lett.* 50 (1983), pp. 1998–2001. DOI: 10.1103/PhysRevLett.50.1998 (cited on pages 9–11).

[TH85] J. Tersoff and D. R. Hamann. "Theory of the scanning tunneling microscope". *Phys. Rev. B* 31 (1985), pp. 805–813. DOI: 10.1103/PhysRevB.31.805 (cited on pages 9–11).

[THS08] M. Ternes, A. J. Heinrich, and W.-D. Schneider. "Spectroscopic manifestations of the Kondo effect on single adatoms". *J. Phys.: Condens. Matter* 21 (2008), p. 053001. DOI: 10.1088/0953-8984/21/5/053001 (cited on page 42).

[Tin04] M. Tinkham. *Introduction to Superconductivity*. Courier Corporation, 2004 (cited on pages 24–27, 46).

[Tra71] S. Trasatti. "Work function, electronegativity, and electrochemical behaviour of metals: II. Potentials of zero charge and "electrochemical" work functions". *J. Electroanal. Chem. Interfacial Electrochem.* 33 (1971), pp. 351–378 (cited on page 69).

[Uge+16] M. M. Ugeda, A. J. Bradley, Y. Zhang, S. Onishi, Y. Chen, W. Ruan, C. Ojeda-Aristizabal, H. Ryu, M. T. Edmonds, H.-Z. Tsai, A. Riss, S.-K. Mo, D. Lee, A. Zettl, Z. Hussain, Z.-X. Shen, and M. F. Crommie. "Characterization of collective ground states in single-layer $NbSe_2$". *Nat. Phys.* 12 (2016), pp. 92–97. DOI: 10.1038/nphys3527 (cited on pages 31, 140).

[Val+04] T. Valla, A. V. Fedorov, P. D. Johnson, P.-A. Glans, C. McGuinness, K. E. Smith, E. Y. Andrei, and H. Berger. "Quasiparticle Spectra, Charge-Density Waves, Superconductivity, and Electron-Phonon Coupling in $2H$-$NbSe_2$". *Phys. Rev. Lett.* 92 (2004), p. 086401. DOI: 10.1103/PhysRevLett.92.086401 (cited on page 29).

[Val58] J. G. Valatin. "Comments on the theory of superconductivity". *Il Nuovo Cimento* 7 (1958), pp. 843–857 (cited on page 26).

[VF13] M. M. Vazifeh and M. Franz. "Self-Organized Topological State with Majorana Fermions". *Phys. Rev. Lett.* 111 (2013), p. 206802. DOI: 10.1103/PhysRevLett.111.206802 (cited on page 4).

[Wah+07] P. Wahl, P. Simon, L. Diekhöner, V. S. Stepanyuk, P. Bruno, M. A. Schneider, and K. Kern. "Exchange Interaction between Single Magnetic Adatoms". *Phys. Rev. Lett.* 98 (2007), p. 056601. DOI: 10.1103/PhysRevLett.98.056601 (cited on page 135).

[Web+11] F. Weber, S. Rosenkranz, J.-P. Castellan, R. Osborn, R. Hott, R. Heid, K.-P. Bohnen, T. Egami, A. H. Said, and D. Reznik. "Extended Phonon Collapse and the Origin of the Charge-Density Wave in $2H$-$NbSe_2$". *Phys. Rev. Lett.* 107 (2011), p. 107403. DOI: 10.1103/PhysRevLett.107.107403 (cited on page 29).

[Wei+09] A. Weismann, M. Wenderoth, S. Lounis, P. Zahn, N. Quaas, R. G. Ulbrich, P. H. Dederichs, and S. Blügel. "Seeing the Fermi Surface in Real Space by Nanoscale Electron Focusing". *Science* 323 (2009), pp. 1190–1193. DOI: 10.1126/science.1168738 (cited on page 50).

[Wei62] P. K. Weimer. "The TFT A New Thin-Film Transistor". *Proc. IRE* 50 (1962), pp. 1462–1469. DOI: 10.1109/JRPROC.1962.288190 (cited on page 3).

[Wie09] R. Wiesendanger. "Spin mapping at the nanoscale and atomic scale". *Rev. Mod. Phys.* 81 (2009), pp. 1495–1550. DOI: 10.1103/RevModPhys.81.1495 (cited on pages 76, 119, 134).

[Wil66] R. G. Wilson. "Vacuum Thermionic Work Functions of Polycrystalline Nb, Mo, Ta, W, Re, Os, and Ir". *J. Appl. Phys.* 37 (1966), pp. 3170–3172. DOI: 10.1063/1.1703180 (cited on page 69).

[Wu+04] S. W. Wu, G. V. Nazin, X. Chen, X. H. Qiu, and W. Ho. "Control of Relative Tunneling Rates in Single Molecule Bipolar Electron Transport". *Phys. Rev. Lett.* 93 (2004), p. 236802. DOI: 10.1103/PhysRevLett.93.236802 (cited on page 70).

[WZW11] J. Wiebe, L. Zhou, and R. Wiesendanger. "Atomic magnetism revealed by spin-resolved scanning tunnelling spectroscopy". *J. Phys. D: Appl. Phys.* 44 (2011), p. 464009. DOI: 10.1088/0022-3727/44/46/464009 (cited on pages 75, 76, 119, 134).

[Xi+15] X. Xi, L. Zhao, Z. Wang, H. Berger, L. Forró, J. Shan, and K. F. Mak. "Strongly enhanced charge-density-wave order in monolayer $NbSe_2$". *Nat. Nanotechnol.* 10 (2015), pp. 765–769. DOI: 10.1038/nnano.2015.143 (cited on page 31).

[Xin+17] Y. Xing, K. Zhao, P. Shan, F. Zheng, Y. Zhang, H. Fu, Y. Liu, M. Tian, C. Xi, H. Liu, J. Feng, X. Lin, S. Ji, X. Chen, Q.-K. Xue, and J. Wang. "Ising Superconductivity and Quantum Phase Transition in Macro-Size Monolayer $NbSe_2$". *Nano Lett.* 17 (2017), pp. 6802–6807. DOI: 10.1021/acs.nanolett.7b03026 (cited on page 140).

[Yaf87] Y. Yafet. "Ruderman-Kittel-Kasuya-Yosida range function of a one-dimensional free-electron gas". *Phys. Rev. B* 36 (1987), pp. 3948–3949. DOI: 10.1103/PhysRevB.36.3948 (cited on page 76).

[Yan+18] Y. Yang, S. Fang, V. Fatemi, J. Ruhman, E. Navarro-Moratalla, K. Watanabe, T. Taniguchi, E. Kaxiras, and P. Jarillo-Herrero. "Enhanced superconductivity upon weakening of charge density wave transport in $2H$-TaS_2 in the two-dimensional limit". *Phys. Rev. B* 98 (2018), p. 035203. DOI: 10.1103/PhysRevB.98.035203 (cited on page 31).

[Yan+20] X. Yang, Y. Yuan, Y. Peng, E. Minamitani, L. Peng, J.-J. Xian, W.-H. Zhang, and Y.-S. Fu. "Observation of short-range Yu-Shiba-Rusinov states with threefold symmetry in layered superconductor 2H-NbSe 2". *Nanoscale* 12 (2020), pp. 8174–8179. DOI: 10.1039/D0NR01383H (cited on pages 38, 48).

[Yao+14a] N. Y. Yao, L. I. Glazman, E. A. Demler, M. D. Lukin, and J. D. Sau. "Enhanced Antiferromagnetic Exchange between Magnetic Impurities in a Superconducting Host". *Phys. Rev. Lett.* 113 (2014), p. 087202. DOI: 10.1103/PhysRevLett.113.087202 (cited on pages 5, 76).

[Yao+14b] N. Y. Yao, C. P. Moca, I. Weymann, J. D. Sau, M. D. Lukin, E. A. Demler, and G. Zaránd. "Phase diagram and excitations of a Shiba molecule". *Phys. Rev. B* 90 (2014), p. 241108. DOI: 10.1103/PhysRevB.90.241108 (cited on pages 5, 77, 78, 82).

[Yaz+97] A. Yazdani, B. A. Jones, C. P. Lutz, M. F. Crommie, and D. M. Eigler. “Probing the Local Effects of Magnetic Impurities on Superconductivity”. *Science* 275 (1997), pp. 1767–1770. DOI: 10.1126/science.275.5307.1767 (cited on pages 4, 43).

[Yok+01] T. Yokoya, T. Kiss, A. Chainani, S. Shin, M. Nohara, and H. Takagi. “Fermi Surface Sheet-Dependent Superconductivity in $2H$-$NbSe_2$”. *Science* 294 (2001), pp. 2518–2520. DOI: 10.1126/science.1065068 (cited on page 31).

[Yos57] K. Yosida. “Magnetic Properties of Cu-Mn Alloys”. *Phys. Rev.* 106 (1957), pp. 893–898. DOI: 10.1103/PhysRev.106.893 (cited on page 75).

[Yu65] L. Yu. “Bound State in Superconductors With Paramagnetic Impurities”. *Acta Phys. Sin.* 21 (1965), pp. 75–91. DOI: 10.7498/aps.21.75 (cited on pages 4, 43).

[Zak+13] N. Zaki, C. A. Marianetti, D. P. Acharya, P. Zahl, P. Sutter, J. Okamoto, P. D. Johnson, A. J. Millis, and R. M. Osgood. “Experimental observation of spin-exchange-induced dimerization of an atomic one-dimensional system”. *Phys. Rev. B* 87 (2013), p. 161406. DOI: 10.1103/PhysRevB.87.161406 (cited on pages 134, 135).

[ŽBP11] R. Žitko, O. Bodensiek, and T. Pruschke. “Effects of magnetic anisotropy on the subgap excitations induced by quantum impurities in a superconducting host”. *Phys. Rev. B* 83 (2011), p. 054512. DOI: 10.1103/PhysRevB.83.054512 (cited on pages 46, 64).

[ZH09] H. J. W. Zandvliet and A. van Houselt. “Scanning Tunneling Spectroscopy”. *Annu. Rev. Anal. Chem.* 2 (2009), pp. 37–55. DOI: 10.1146/annurev-anchem-060908-155213 (cited on page 11).

[Zha+15] Y. Zhao, J. Wyrick, F. D. Natterer, J. F. Rodriguez-Nieva, C. Lewandowski, K. Watanabe, T. Taniguchi, L. S. Levitov, N. B. Zhitenev, and J. A. Stroscio. “Creating and probing electron whispering-gallery modes in graphene”. *Science* 348 (2015), pp. 672–675. DOI: 10.1126/science.aaa7469 (cited on page 69).

[Zha+19] Z. Zhang, P. Yang, M. Hong, S. Jiang, G. Zhao, J. Shi, Q. Xie, and Y. Zhang. “Recent progress in the controlled synthesis of 2D metallic transition metal dichalcogenides”. *Nanotechnology* 30 (2019), p. 182002. DOI: 10.1088/1361-6528/aaff19 (cited on page 140).

[Zhe+18] F. Zheng, Z. Zhou, X. Liu, and J. Feng. “First-principles study of charge and magnetic ordering in monolayer $NbSe_2$”. *Phys. Rev. B* 97 (2018), p. 081101(R). DOI: 10.1103/PhysRevB.97.081101 (cited on pages 29–32, 48, 60, 146).

[Zhe+94] J. F. Zheng, X. Liu, N. Newman, E. R. Weber, D. F. Ogletree, and M. Salmeron. “Scanning tunneling microscopy studies of Si donors (Si_{Ga}) in GaAs”. *Phys. Rev. Lett.* 72 (1994), pp. 1490–1493. DOI: 10.1103/PhysRevLett.72.1490 (cited on page 69).

[Zho+10] L. Zhou, J. Wiebe, S. Lounis, E. Vedmedenko, F. Meier, S. Blügel, P. H. Dederichs, and R. Wiesendanger. “Strength and directionality of surface Ruderman–Kittel–Kasuya–Yosida interaction mapped on the atomic scale”. *Nat. Phys.* 6 (2010), pp. 187–191. DOI: 10.1038/nphys1514 (cited on page 76).

[Zhu+15] X. Zhu, Y. Cao, J. Zhang, E. W. Plummer, and J. Guo. “Classification of charge density waves based on their nature”. *PNAS* 112 (2015), pp. 2367–2371. DOI: 10.1073/pnas.1424791112 (cited on page 29).

[Zie+09] M. Ziegler, N. Néel, A. Sperl, J. Kröger, and R. Berndt. “Local density of states from constant-current tunneling spectra”. *Phys. Rev. B* 80 (2009), p. 125402. DOI: 10.1103/PhysRevB.80.125402 (cited on page 128).

[ZW10] M. Zehetmayer and H. W. Weber. “Experimental evidence for a two-band superconducting state of $NbSe_2$ single crystals”. *Phys. Rev. B* 82 (2010), p. 014524. DOI: 10.1103/PhysRevB.82.014524 (cited on page 35).

Webseiten

[Int] Intel. *Intel’s First Microprocessor - Its invention, introduction, and lasting influence*. URL: https://www.intel.com/content/www/us/en/history/museum-story-of-intel-4004.html (visited on May 14, 2021) (cited on page 3).

[SRS] SRS. *About Lock-In Amplifiers - Application Note #3*. Stanford Research Systems, Inc., Sunnyvale, CA, USA. URL: https://www.thinksrs.com/downloads/pdfs/applicationnotes/AboutLIAs.pdf (visited on May 14, 2021) (cited on page 18).

Curriculum Vitae

Der Lebenslauf ist aus Gründen des Datenschutzes in der Onlineversion nicht enthalten.
For reasons of data protection, the curriculum vitae is not published in the electronic version.

List of publications

Publications related to this thesis:

- E. Liebhaber, L. M. Rütten, G. Reecht, J. F. Steiner, S. Rohlf, K. Rossnagel, F. von Oppen and K. J. Franke. "Quantum spins and hybridization in artificially-constructed chains of magnetic adatoms on a superconductor". *arXiv Preprint* (2021). arXiv: 2107.06361.
- A. Sanna, C. Pellegrini, E. Liebhaber, K. Rossnagel, K. J. Franke and E. K. U. Gross. "Real-space anisotropy of the superconducting gap in the charge-density wave material $2H$-$NbSe_2$". *Submitted* (2021).
- E. Liebhaber, S. Acero González, R. Baba, G. Reecht, B. W. Heinrich, S. Rohlf, K. Rossnagel, F. von Oppen and K. J. Franke. "Yu-Shiba-Rusinov States in the Charge-Density Modulated Superconductor $NbSe_2$". *Nano Lett.* 20 (2020), pp. 339-344.

Publications not related to this thesis:

- J. Wiedenmann, E. Liebhaber, J. Kübert, E. Bocquillon, P. Burset, Pablo C Ames, H. Buhmann, T. M. Klapwijk and L. W. Molenkamp. "Transport spectroscopy of induced superconductivity in the three-dimensional topological insulator HgTe". *Phys. Rev. B* 96 (2017), p. 165302.

Conference contributions

2016:

- **Poster** - “Superconducting Point Contacts on the 3D Topological Insulator Mercury Telluride”; 628^{th} WE-Heraeus Seminar: Trends in Mesoscopic Superconductivity, November 2016, Bad Honnef, Germany.

2017:

- **Poster** - “Influence of the Charge Density Wave Order on Quasiparticle Excitations in $2H$-$NbSe_2$”; DPG Spring Meeting of the Condensed Matter Section, March 2017, Dresden, Germany.
- **Poster** - “Yu-Shiba-Rusinov states of magnetic adatoms on the quasi 2D superconductor $2H$-$NbSe_2$”; SPICE - Spin Phenomena Interdisciplinary Center: Exotic New States in Superconducting Devices: The Age of the Interface, September 2017, Mainz, Germany.
- **Poster** - “Yu-Shiba-Rusinov states of magnetic adatoms on the quasi 2D superconductor $2H$-$NbSe_2$”; 654^{th} WE-Heraeus Seminar - Topical Insights into Nanoscience using Scanning Probes, November 2017, Bad Honnef, Germany.

2018:

- **Talk** - “Yu-Shiba-Rusinov states of magnetic adatoms on the quasi 2D superconductor $2H$-$NbSe_2$”; DPG Spring Meeting of the Condensed Matter Section, March 2018, Berlin, Germany.
- **Poster** - “Yu-Shiba-Rusinov states of Fe adatoms on the quasi 2D superconductor $2H$-$NbSe_2$”; MPI International Focus Workshop: New Platforms for Topological Superconductivity with Magnetic Atoms, April 2018, Dresden, Germany.
- **Poster** - “Yu-Shiba-Rusinov states of magnetic adatoms on the quasi 2D superconductor $2H$-$NbSe_2$”; SPSTM-7 LTSPM-1: Advances in High-Precision and Low-Temperature Scanning Probe Microscopy, July 2018, Nijmegen, The Netherlands.

2019:

- **Talk** - “Yu-Shiba-Rusinov states of Fe atoms on $2H$-$NbSe_2$”; DPG Spring Meeting of the Condensed Matter Section, April 2019, Regensburg, Germany.
- **Talk** - “Influence of a charge density wave on Yu-Shiba-Rusinov states”; MPI International Focus Workshop: Bound states in superconductors and interfaces, April 2019, Dresden, Germany.

2021:

- **Talk** - “Coupling of Yu-Shiba-Rusinov states on $2H$-$NbSe_2$”; Virtual DPG Spring Meeting of the Condensed Matter Section, March 2021, Germany.

Acknowledgements

Die Danksagung ist aus persönlichen Gründen in der Onlineversion nicht enthalten.
For personal reasons, the acknowledgements are not published in the electronic version.

This thesis was typeset with LaTeX 2$_\varepsilon$. It uses the *Clean Thesis* style developed by Ricardo Langner. The design of the *Clean Thesis* style is inspired by user guide documents from Apple Inc.

Download the *Clean Thesis* style at `http://cleanthesis.der-ric.de/`.

Selbstständigkeitserklärung

Name: Rudisch
Vorname: Eva-Maria

Ich erkläre gegenüber der Freien Universität Berlin, dass ich die vorliegende Dissertation selbstständig und ohne Benutzung anderer als der angegebenen Quellen und Hilfsmittel angefertigt habe. Die vorliegende Arbeit ist frei von Plagiaten. Alle Ausführungen, die wörtlich oder inhaltlich aus anderen Schriften entnommen sind, habe ich als solche kenntlich gemacht. Diese Dissertation wurde in gleicher oder ähnlicher Form noch in keinem früheren Promotionsverfahren eingereicht.

Mit einer Prüfung meiner Arbeit durch ein Plagiatsprüfungsprogramm erkläre ich mich einverstanden.

Berlin, den